Fall 2021

Hydrodeoxygenation of Biomass Derived Sugar Alcohols To Platform Chemicals Using Heterogeneous Catalysts

Blake MacQueen

HYDRODEOXYGENATION OF BIOMASS DERIVED SUGAR ALCOHOLS TO PLATFORM CHEMICALS USING HETEROGENEOUS CATALYSTS

by

Blake MacQueen

Bachelor of Science
The University of Alabama, 2017

Submitted in Partial Fulfillment of the Requirements

For the Degree of Doctor of Philosophy in

Chemical Engineering

College of Engineering and Computing

University of South Carolina

2021

Accepted by:

Jochen Lauterbach, Major Professor

Andreas Heyden, Committee Member

William Mustain, Committee Member

Yomaira Pagán-Torres, Committee Member

Melissa Moss, Committee Member

Tracey L. Weldon, Interim Vice Provost and Dean of the Graduate School

DEDICATION

To my family and to the pursuit of happiness. For all the struggles along the journey, it was all worth it. May I continue to use my setbacks and accomplishments as motivation for a better and brighter future.

ACKNOWLEDGEMENTS

I would like to thank my advisor, Prof. Jochen Lauterbach. Thank you for the guidance, mentorship and support over the years. I truly appreciate you helping me to think outside the box and helping me develop into the scientist and leader I am today. I am ever grateful for our experiences over the years and truly see you as part of my family. Thank you for all that you have done for me.

To Prof. Nakorn Tippayawong, thank you for taking me into your lab as a visiting scholar and mentoring me. I am very thankful for the hospitality you and your group showed me.

To Prof. Yomaira Pagán Torres, thank you for the guidance over the years and for providing me significant insight into various topics. I am appreciative of you taking me into your lab to help work on our collaborations and your mentorship.

I would like to thank my committee members Prof. Andreas Heyden, Prof. William Mustain, Prof. Yomaira Pagán-Torres, and Prof. Melissa Moss for their continued guidance and support.

I would like to thank the past and present group members of SAGE for all of the help and guidance over the years. To Michael Royko, thank you for the support, guidance, comedic relief, and friendship over the years. To Nicole Cordonnier, thanks for always helping me see the brighter side of things. To Dr. Juan Jimenez, thank you for the guidance and pushing me to be the best scientist I could be. To Katie McCullough, thank you for helping me see different perspectives and supporting me. To Dr. Elizabeth Barrow, thank

you for your mentorship and helping me establish myself as a scientist. To Dr. Benjamin Ruiz-Yi, thank you for insightful conversations and always being there for me. To the other past and present SAGE members not listed, thank you for your continued support.

I would like to thank Chris DeSoiza for his mentorship and insight. Thank you for helping me see the bigger picture and guiding me to success.

I would also like to acknowledge and thank Phi Kappa Sigma International Fraternity. Thank you for helping me develop as a leader, establishing a commitment to lifelong learning, and supporting me along my journey. I would like to especially thank Steve Richey, Lou Semrad, and Jesse Wells for their mentorship over the years.

Lastly, I would like to thank and acknowledge my family. To my family, thank you for your continued support and dedication. To my Mother, thank you for showing me that I can persevere anything life throws my way. I appreciate your constant support and guidance. To my Father and Step Mother, thank you for the sacrifices that you have made to help me accomplish my dreams. To my Grandfather Alden Dubois, thank you for showing me what it is like to be a truly good person and care about others. I deeply value the way you treat others and the countless stories you have shared with me. To my other family members who have helped and supported me along the way, thank you.

ABSTRACT

This work set out to investigate biomass derived sugar alcohol upgrading via the removal of oxygen and hydroxyl groups via the hydrodeoxygenation reaction utilizing heterogeneous catalysts. The importance of reaction conditions, catalyst meal loadings, catalyst structure and properties were probed using techniques such as design of experiments, and spectroscopic techniques including Raman and DRIFTS. The state of the art simultaneous hydrodeoxygenation (S-HDO) catalyst ReO_x-Pd/CeO_2 was investigated and optimized for various sugar alcohol substrates. The kinetics and associated mass transfer were also investigated to give further insight into the reaction over the ReO_x-Pd/CeO_2 catalyst.

First, the effects of reaction temperature, pressure and Re loading in the ReO_x-Pd/CeO_2 catalyst on S-HDO conversion and selectivity for 1,4-anhydroerythritol and xylitol as substrates was investigated. Simplistic L9 Taguchi design of experiments were utilized to elucidate the associated relationships. The designs showed the significance of reaction temperature on the yield of the reaction and also elucidated a zero-order relation with hydrogen pressure. The zero-order relation with pressure was evaluated and confirmed down to 10 bar H_2. Optimum reaction conditions for both the 1,4-anhydroerythritol and xylitol S-HDO reactions were elucidated.

Second, the general reaction kinetics and associated mass transfer of the xylitol S-HDO over a ReO_x-Pd/CeO_2 catalyst was investigated. It was determined that the xylitol concentration was zero-order in the S-HDO reaction to 1,2-dideoxypentitol and 1,2,5-

pentanetriol. Over the 120-170 °C temperature range, it was elucidated that a sub-Arrhenius relationship was present for this reaction, in which activation energy was a function of temperature. The activation energy ranged from 10.2–51.8 kJ/mol over the temperature range evaluated and the non-Arrhenius behavior was fully modeled to account for the quantum tunneling present in the reaction. Internal and external mass transfer were investigated through evaluating the Weisz–Prater criterion and the effect of varying stirring rate on the reaction rate, respectively and no limitations were found.

Third, the effects of reaction temperature, pressure and Re loading for sorbitol S-HDO was investigated using an L9 Taguchi design and a Box-Behnken design of experiment. The designs were directly compared to determine if the more simplistic Taguchi design could deliver comparable results to the more complex and experimentally intensive Box-Behnken design. The Taguchi design predicted an optimal reaction condition of 170 °C, 10 bar H_2, and a 4 wt% Re catalyst, which was experimentally validated. The structure of the ReO_x on the catalyst was also investigated as a function of temperature and Re loading using in-situ Raman spectroscopy.

Lastly, the structure of ReO_x supported on CeO_2 was investigated using in-situ ^{18}O isotopic exchange Raman and DRIFTS spectroscopy. The isotope exchange was utilized to help deconvolute the vibrational bands by tracking the resulting red shifted substituted bands. The ReO_x was found to exist in four distinct structures including a di-oxo structure, a mono-oxo species, a mono-oxo species that contains a hydroxyl group, and a cross-linked oligomeric ReO_x species. The effect of temperature and Re weight loading on the structure of ReO_x was also investigated.

TABLE OF CONTENTS

LIST OF TABLES

LIST OF FIGURES

LIST OF SYMBOLS

d	Distance between diffraction planes or deformation parameter
n	Diffraction order
λ	X-ray wavelength
θ	Incident angle
hkl	Miller indices
k	Reaction rate constant
A	Pre-exponential factor
E_a	Activation energy
R	Universal gas constant
T	Temperature
B	Quadratic constant
C	Quadratic constant or catalyst weight loading
E_0	Barrier height
v^*	Penetration frequency
h	Planck's constant
C_{WP}	Weisz Prater criterion
r_A	Reaction rate
ρ_c	Density
R	Radius
D_e	Effective diffusivity

C_{AS}	Concentration at surface
α	Significance level
S	Standard error of regression
R^2	Coefficient of determination
P	Pressure

LIST OF ABBREVIATIONS

ASME ..... American Society of Mechanical Engineers

BET ..... Brunauer–Emmett–Teller

CAS ..... Chemical Abstracts Service

CI ..... Confidence Interval

DFT ..... Density Functional Theory

DODH ..... Deoxydehydration

DOE ..... Design of Experiments

DRIFTS ..... Diffuse Reflectance Infrared Fourier Transform Spectroscopy

EDS ..... Energy Dispersive Spectroscopy

FID ..... Flame Ionization Detector

FTIR ..... Fourier-Transform Infrared Spectroscopy

GC ..... Gas Chromatography

HDO ..... Hydrodeoxygenation

ICP-OES ..... Inductively Coupled Plasma - Optical Emission Spectroscopy

MBA 2-Methyl-2-butanol

MBE 2-Methyl-3-buten-2-ol

MBY 2-Methyl-3-butyn-2-ol

MCT ..... Mercury Cadmium Telluride

NPT ..... National Pipe Taper

PID ..... Proportional–Integral–Derivative

PTFE ..... Polytetrafluoroethylene

PVDF ..... Polyvinylidene Fluoride

SEM ..... Scanning Electron Microscopy

S-HDO ..... Simultaneous Hydrodeoxygenation

SNR ..... Signal to Noise Ratio

SS ..... Stainless Steel

THF ..... Tetrahydrofuran

TPR ..... Temperature Programmed Reduction

UHP ..... Ultra High Purity

XRD ..... X-ray Diffraction

XRF ..... X-ray Fluorescence

CHAPTER 1

INTRODUCTION

1.1 OVERVIEW

Heterogeneous catalysts are used in chemical reactions to lower the activation barrier of the reaction and increase the reaction rate. This leads to faster reactions which require less energy to proceed and can allow for scaling of many chemical reactions. Heterogeneous catalysis deals with reactants and the catalyst which are in different phases including liquid and solid, gas and solid, or gas and liquid combinations [1]. The chemical reactions occur on the catalyst interface, such as the internal pores of the catalyst [2]. On a solid heterogeneous catalyst, the reactants would first adsorb on the catalyst surface. Then if there is sufficient energy, the reaction will proceed and reaction intermediates can form according to the reaction mechanism based on the most energetically favorable path of the reaction. Once the reaction mechanism has produced the adsorbed product, the product would then desorb and diffuse back into the reactant phase away from the catalyst. This allows for the reaction to then proceed again on the same site once the next reactant molecule adsorbs to the catalyst surface. The use of heterogeneous catalysts can allow for reactions to be conducted at high conversion and high selectivity to targeted products. In this dissertation, the upgrading of biomass derived sugar alcohols to various platform chemicals using heterogeneous catalysts is discussed in great detail. The catalysts were used to lower the energy barrier for the hydrodeoxygenation reaction, which removes

hydroxyl groups from the sugars and can produce large market commercial chemicals. In this work, heterogeneous catalysts were used to selectively target high value products, increase reaction rates, and to determine fundamental information about the reaction and reaction mechanisms. The catalysts were also characterized to determine the structure of the catalyst and determine various fundamental information that gave insight into the catalysts properties. The catalysts and reaction conditions used in this dissertation were optimized utilizing statistical design of experiments to determine the optimal settings for the various parameters to make the hydrodeoxygenation reaction as active and selective as possible.

1.2 BIOMASS CHEMICAL UPGRADING

With an ever-growing demand for energy and chemical production [3], new technologies must be investigated to help meet the growing demand [4]. A promising pathway to meet this demand includes the utilization of alternative and renewable fuels and renewable chemical production processes to help meet the demand and also alleviate the dependence on fossil resources [5]. Biomass is a renewable resource that can help sustainably replace a portion of this energy demand as well as serve as a resource for green chemical production. Biomass can be upgraded into liquid biofuels [6]–[8] or burnable products through processes such as torrefaction [9]–[12] to produce energy or the biomass can be upgraded to platform chemicals to help replace many chemicals commonly produced by fossil fuel processes [13]–[16]. Though the demand for liquid biomass-derived fuels is high as shown by The Department of Energy forecast of biofuels increasing 200% by 2035 due to the Federal Renewable Fuels Standard, there is a shortage of inexpensive feedstock that wouldn't compete with resources needed for food production to

make this achievable [17]. However, if biomass was used instead to produce platform chemicals in order to replace fossil resource chemical production many of the problems associated with fuel production can be avoided [18]. The majority of chemical production currently utilizes fossil fuel feedstock for production [19], but it has been shown that on a per mass basis, biomass far outperforms crude oil in terms of mass balance for chemical production [20]. The direct comparison is shown in Figure 1.1. For each kg of crude oil, 32 MJ of fuels and 0.2 kg of chemicals can be produces. For biomass, for every kg either 6 MJ of fuels or 0.80 kg of chemicals can be produced. Thus biomass on a per mass basis shows a four times higher production of chemicals on a per mass basis as compared to crude oil.

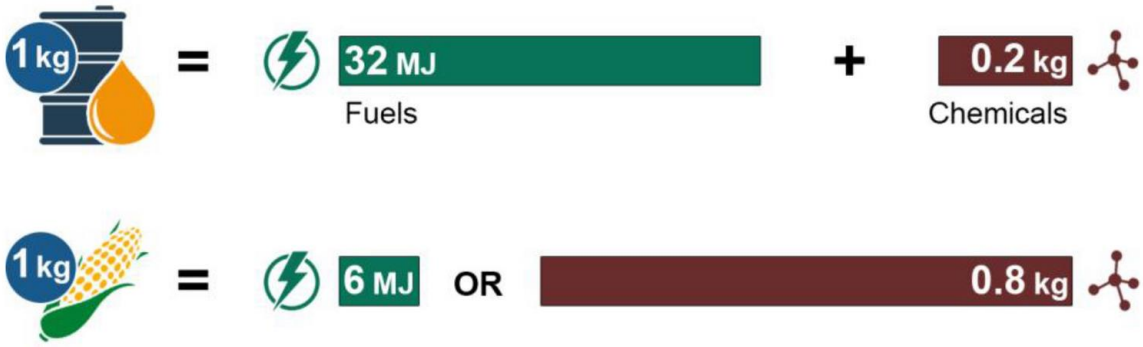

Figure 1.1. Energy and mass balances on crude oil and biomass as feedstock for energy and chemical production. Adapted from [20]

Biomass upgrading to platform chemicals would allow for high value-added chemical production to be targeted which would diminish the economic challenges of large scale development [18]. A promising source to meet the large scale need of biomass to produce fuels or value-added chemicals is lignocellulosic biomass [21], [22].

Lignocellulosic biomass is derived from plant cell walls and contains three main components, cellulose, lignin, and hemicellulose [17], [23]. Agricultural residues, waste streams, wood, and various energy crops provide renewable sources of lignocellulosic

biomass [17], [24]. Cellulose can undergo fermentation processes, acid catalyzed dehydrations, and hydrodeoxygenations (HDO) to make various chemicals such as sorbitol, erythritol, glycerol, and olefins [23], [25]–[29]. Lignin is used to make various aromatic compounds through catalytic transfer hydrogenolysis to make chemicals such as benzene, toluene, phenol, and styrene [23], [30]–[32]. Hemicellulose can be upgraded to various biofuels and chemicals such as xylitol, succinic acid, and furfural through hydrolysis and HDO [23], [33]–[37]. Some of the various products that can be made from lignocellulosic biomass chemical upgrading and the structures of cellulose, lignin, and hemicellulose are shown in Figure 1.2. Lignocellulosic biomass upgrading allows for the renewable production of platform chemicals, fuels, and the potential utilization of waste streams. HDO is one specific pathway in which biomass-derived compounds can be chemically upgraded.

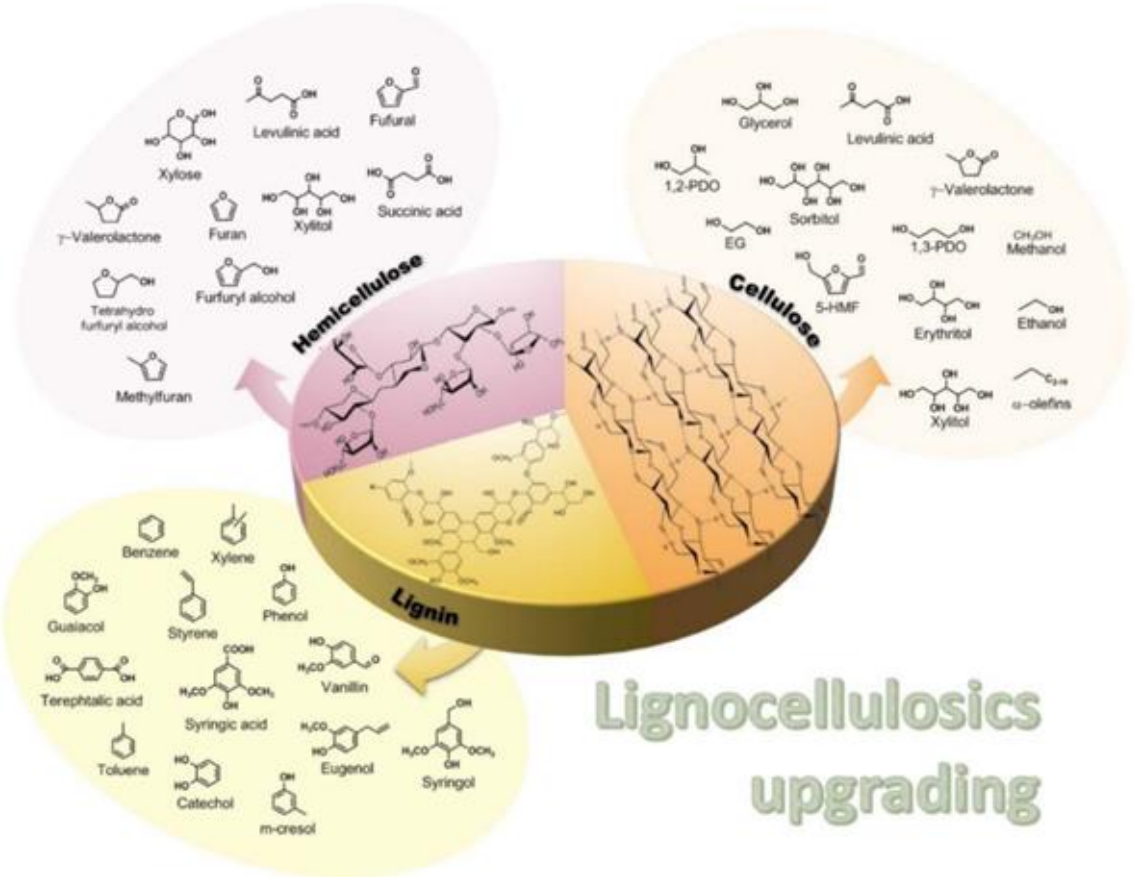

Figure 1.2 Lignocellulosic biomass components and potential upgrading products. Adapted from [23]

1.3 HYDRODEOXYGENATION OF SUGAR ALCOHOLS

The sugar alcohols that are derived from lignocellulosic biomass, such as 1,4-anhydroerthritol (AHERY), xylitol, and sorbitol can either undergo several upgrading paths using heterogeneous catalysts [38]. One potential path is deoxydehydration (DODH), which cleaves two vicinal hydroxyl groups and forms a double bond between the carbons which originally had the hydroxyl groups bonded to them [39], [40]. Another potential path is hydrodeoxygenation (HDO) to remove either singular or vicinal hydroxyl groups (through a simultaneous hydrodeoxygenation (S-HDO)), leaving behind a single bond

either between the respective carbons or with a hydrogen atom due to a hydrogenation step [41]. The deoxydehydration typically uses a state of the art ReO_x-Au/CeO_2 catalyst, and the HDO uses either a WO_x-Pd/ZrO_2 catalyst to remove a single hydroxyl group or a ReO_x-Pd/CeO_2 catalyst to simultaneously remove two vicinal hydroxyl groups [29], [38], [42]–[44]. The latter reaction is a simultaneous hydrodeoxygenation (S-HDO) and proceeds via deoxydehydration followed by a hydrogenation step that allows for the simultaneous removal of two vicinal hydroxyl groups, shown in Figure 1.3. Literature has shown that ReO_x-Pd/CeO_2 is a better catalyst for the S-HDO of AHERY as compared to ReO_x-Pd on other oxide supports, including SiO_2, Al_2O_3, ZrO_2, TiO_2, MgO, CaO, La_2O_3, and Y_2O_3 as well as activated carbon [45]. It has also been shown that Re is superior to other active metals including W, Mo, Cr, Nb, Mn, and V. Pd was determined to be the best promoter for the S-HDO reaction as compared to Co, Ni, Cu, Ru, Rh, Ir, and Pt [46]. The S-HDO of AHERY produces tetrahydrofuran (THF) which is a commonly used industrial solvent which had a $3.2 billion dollar market in 2018 [47]. AHERY S-HDO was used as a model reaction for sugar alcohol S-HDO since it has two vicinal cis-hydroxyl groups. AHERY was used to allow for the monitoring of HDO, DODH, and S-HDO products throughout the reaction in a more simplistic manner due to fewer potential products as compared to compounds with more hydroxyl groups. AHERY is ideal to use for a model reaction for S-HDO since it can only occur once on this compound.

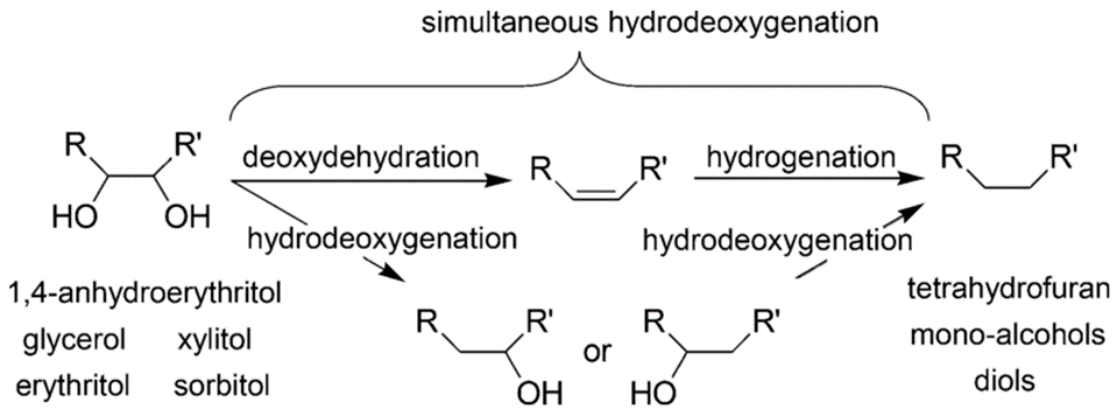

Figure 1.3. Simultaneous hydrodeoxygenation of sugar alcohols reaction schematic. Adapted from [45]

HDO reactions have been conducted over a wide range of conditions depending on the feedstock and catalyst used, including pressures that exceed 75 bar H_2 and temperatures over 350 °C [48]–[60]. The reactions conditions for typical HDO reactions involve either high pressure, high temperature or both high pressure and temperature which poses economic concerns. These harsh conditions challenge the scaling of HDO reactions for commercial viability. Milder conditions for these HDO reactions would allow for these processes to be conducted in a more economically desirable fashion for pilot scale production and beyond. The AHERY S-HDO reaction have been conducted in literature at 80 bar H_2 and 180 °C in a high-pressure batch system [45]. Xylitol and Sorbitol S-HDO were conducted at 80 bar H_2 at 160 °C in the same system. For a batch process, these conditions would pose major problems at an industrial level regarding economic viability specifically regarding the hydrogen pressure needed. A pressure of 80 bar H_2 greatly surpasses the safety rating for many commonly used industrial batch reactors and would pose a large reactant cost for these reactions, and require high grade gas compressors. In this dissertation, the feasibility of running S-HDO reactions at milder conditions using design of experiments to probe various reaction parameters was investigated. Our goal was

to determine the main effects of pressure, temperature, and catalyst loading on the yield of the various S-HDO reactions and to elucidate more economic operating conditions while also gaining fundamental insight into the reaction and relations between the factors and the yield of the reaction.

1.4 SIMULTANEOUS HYDRODEOXYGENATION MECHANISMS

The S-HDO reaction has been evaluated both experimentally through kinetic investigations and theoretically via Density Functional Theory (DFT) calculations. However, the proposed reaction mechanisms over a ReO_x-Pd/CeO_2 or ReO_x/CeO_2 catalyst have only been evaluated using theoretical DFT calculations. There are two studies which have proposed varying mechanisms for the S-HDO reaction. The first study by Ota et al. [45] suggested a mechanism based off of the mechanism proposed for the DODH of 1,4-anhydroerythritol to 2,5-dihydrofuran using a CH_3ReO_3 catalyst [61]. The proposed S-HDO mechanism over a ReO_x-Pd/CeO_2 catalyst is shown in Figure 1.4. The mechanism proposed starts with a di-oxo (O=Re=O) rhenium species which is reduced to a low valent di-oxo hydroxyl species (HO-Re-OH) in which the substrate coordinates with. After the coordination of the substrate, the elimination of the alkene occurs, followed by the hydrogenation of the alkene, and the rhenium species ends up in the di-oxo speciation allowing the mechanism to occur again in a cyclic manner.

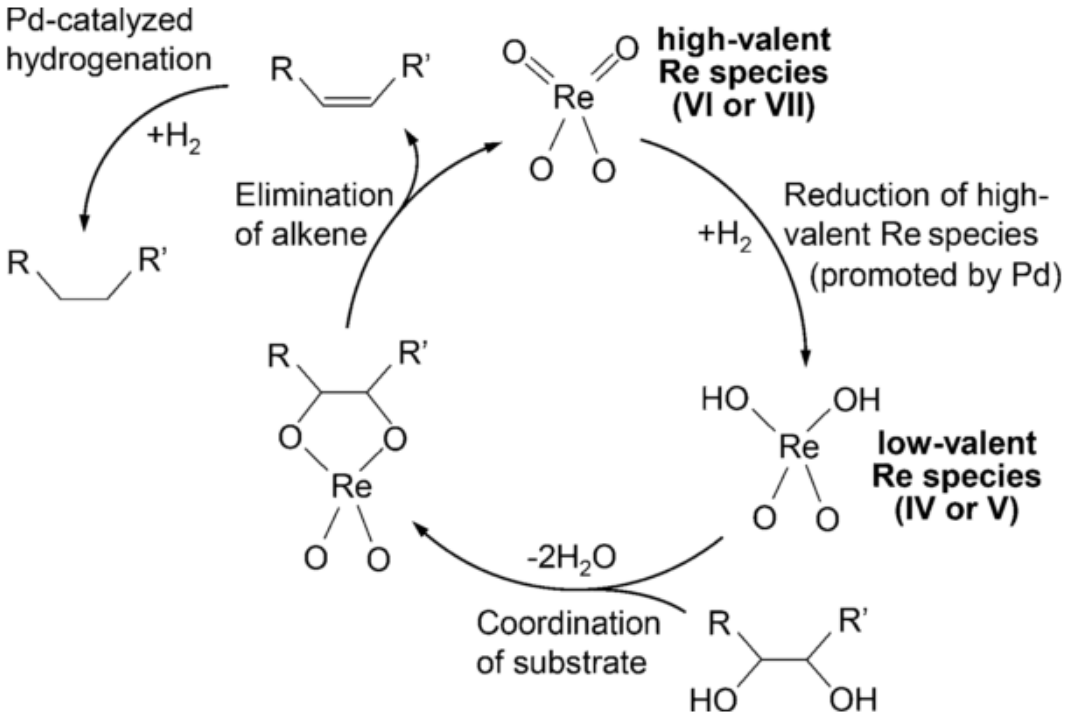

Figure 1.4. Original simultaneous hydrodeoxygenation mechanism over ReO_x-Pd/CeO_2 proposed. Adapted from [45]

After further investigation into the S-HDO reaction using DFT studies, the mechanism proposed in Figure 1.4 was updated based on the resulting DFT calculations. The new mechanism, shown in Figure 1.5, proposed the relative speeds of each step and proposed different speciation of the rhenium during the various steps in the mechanism. The rhenium oxide would first reduce from a tri-oxo speciation to a di-oxo species, which is promoted by the hydrogen dissociated on the surface of the catalyst. This reduction of the rhenium was proposed to be a fast step in the mechanism. The di-oxo rhenium would then have the coordination of the substrate in a fast step, forming a diolate structure with one terminal double bonded oxygen to the Re atom and four single bounded oxygen atoms (two to the substrate and two to the CeO_2 support). From the diolate the elimination of the

alkene would occur in the rate limiting step followed by the fast hydrogenation of the alkene to an alkane. The rhenium oxide would then end up in a tri-oxo speciation and the mechanism could repeat in a cyclic manner. This updated mechanism suggests that the rhenium is in a 6+ and 4+ oxidation state throughout the mechanism rather than the 6+ or 7+ and 4+ or 5+ oxidation states previously suggested.

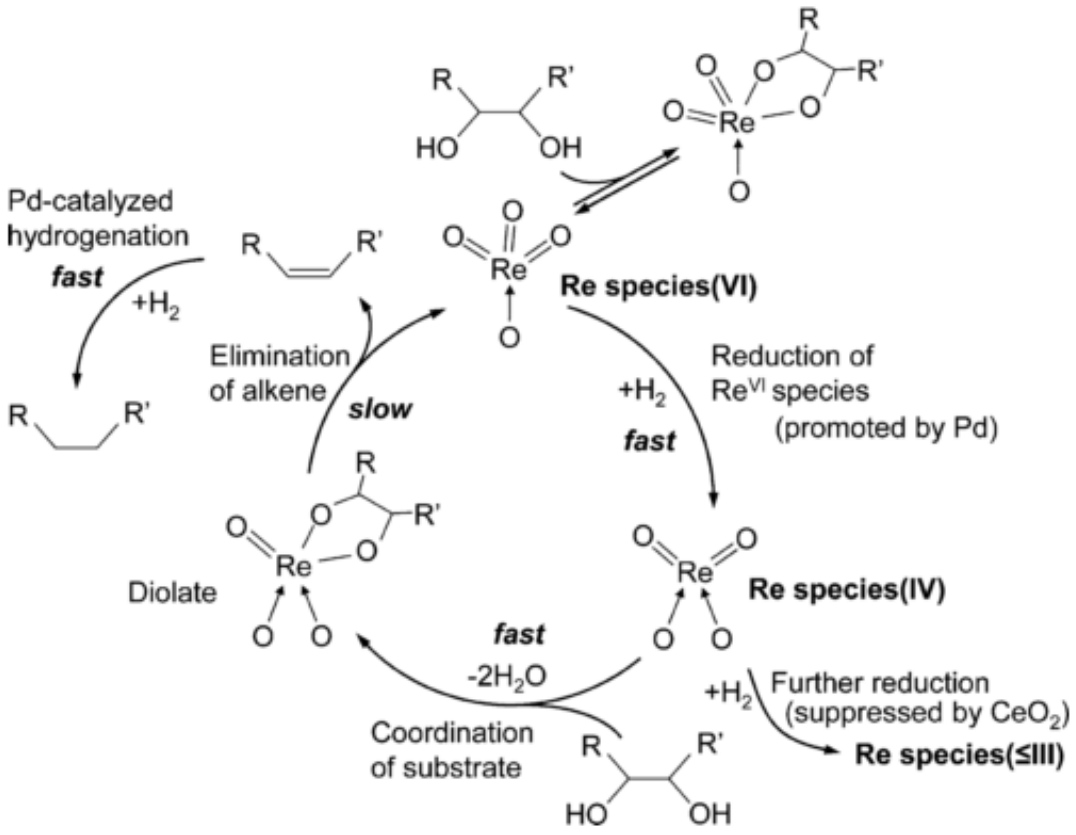

Figure 1.5. Updated simultaneous hydrodeoxygenation mechanism over a ReO_x-Pd/CeO_2 catalyst based on density functional theory calculations. Adapted from [38]

An alternative mechanism to the Ota mechanism has been proposed by Xi based on a ReO_x-Pd/CeO_2 catalyst using DFT calculations based on a support surface of four O-Ce-O trilayers for a fully hydroxylated CeO_2 for the (111) plane of CeO_2 [62]. Based on the DFT calculations performed, Xi et al. found that the mono-oxo structure (Re=O) of

rhenium oxide was the most energetically favorable on the catalyst surface. This finding along with supporting calculations resulted in the proposed mechanism shown in Figure 1.6. For the proposed mechanism, the mono-oxo rhenium would first have the coordination of the substrate occur (also referred to as the condensation step of the DODH). The coordination would be followed by the desorption of the alkene, resulting in a di-oxo rhenium oxide species. A neighboring hydrogen atom would then migrate to one of the terminal oxygen atoms of the rhenium oxide and create a hydrogen vacancy. This vacancy would then be filled by another hydrogen on the surface which is then followed by the formation and removal of water, resulting in the formation of a mono-oxo rhenium oxide species. The hydrogen vacancies are then replenished by the dissociate adsorption of H_2 and the mechanism can then repeat in a cyclic manner similar to the other proposed mechanisms. From their calculations, Xi et al. were also able to determine that the Pd promoter had no direct interaction with the Re species. However, the Pd was found to dissociate hydrogen spillover on the CeO_2 which allows for the regeneration of the Re catalyst.

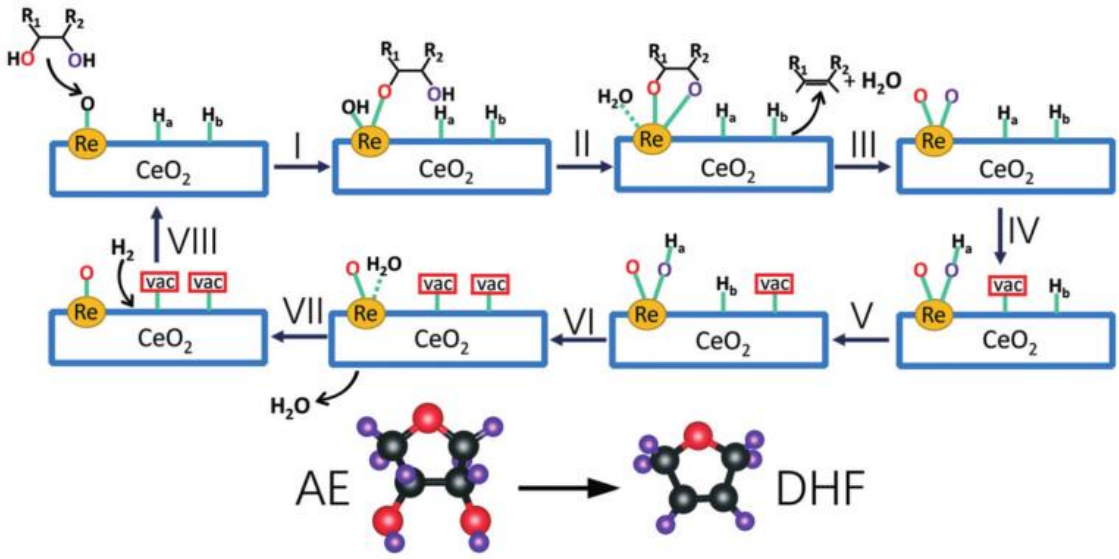

Figure 1.6. Proposed deoxydehydration reaction mechanism for a ReO_x/CeO_2 and ReO_x-Pd/CeO_2 catalyst based on density function theory calculations. Adapted from [62]

With the varying mechanisms in the literature, the active species of rhenium oxide for the S-HDO reaction is in question. It has been proposed via the various mechanisms that the rhenium oxide could exist in a mono-oxo, di-oxo, tri-oxo, or hydroxylated species on the ReO_x-Pd/CeO_2 catalyst. It is possible that both the mono-oxo and di-oxo active site mechanisms could occur or even compete if there are multiple speciation's of rhenium present on the catalyst surface. However, if only one speciation of rhenium oxide exists on the surface, only one of the mechanisms would proceed. The structure of the rhenium oxide has not been directly elucidated via vibrational spectroscopic methods which would allow for further insight into the active species. Thus to gain further insight into the starting point of the reaction mechanism for this reaction and to determine the possible structures of ReO_x present on the catalyst, various in-situ vibrational spectroscopy methods were employed in this dissertation.

1.5 ReO_x STRUCTURES ON OXIDE SUPPORTS

Since multiple structures have been proposed for ReO_x supported on CeO_2, it is important to evaluate the structures of ReO_x on other oxide supports. The structure of ReO_x on oxide supports including Al_2O_3, ZrO_2, SiO_2 and TiO_2 have been investigated utilizing various *in-situ* vibration spectroscopy techniques using various isotope exchange experiments [63]–[67].

On Al_2O_3, it was determined through DFT and complementary Raman studies that ReO_x exists in two different di-oxo (O=Re=O) species that were both isolated, monomeric, and tetra-coordinated [65]. The different structures were due to the difference in the bonding on basic and acidic Al sites. It was also found that the tetra-coordinated mono-oxo, penta-coordinated di-oxo, and tetra-coordinated tri-oxo structures of ReO_x were either not stable or were significantly less stable than the tetra-coordinated di-oxo species on Al_2O_3. However, a previous study using various characterization techniques and DFT suggests that the rhenium oxide exists in a Re(VII) isolated tri-oxo species as well as in nanoclusters [68]. Thus, there is debating assignments for the speciation of rhenium oxide on Al_2O_3 in the literature. However, the spectral evidence presented for the di-oxo speciation is strong and gives significant evidence that the di-oxo speciation is present on the catalyst surface.

On ZrO_2, ReO_x was found to exist in a mono-oxo (Re=O) species evident by the intense symmetric vibration at around 1005 cm^{-1} in the associated Raman spectrum [63]. The ReO_x was also found to form an oligomeric Re_2O_7 species at high metal loadings, evident by the asymmetric vibration between the oxygen bridge between the Re atoms observed at roughly 890 cm^{-1} in Raman. Thus, two structures of ReO_x were present when supported on the ZrO_2 support, one monomeric and one oligomeric species.

On SiO_2, the rhenium oxide (ReO_4) was found to exist exclusively in a tri-oxo species $(O=)_3Re\text{-}O\text{-}Si$. The tri-oxo speciation was determined through isotopic oxygen exchange and the quadruplet band splitting that was observed in the resulting Raman spectrum [66]. However, this species was found to be volatile and deposits as well as reduced signal were observed after prolonged exposure to the isotopic vapor. The tri-oxo species observed on SiO_2 is the only experimentally observed tri-oxo species of ReO_x on an oxide support.

On TiO_2, the rhenium oxide was found to exist as two major species instead of one speciation. Both the mono-oxo and di-oxo structures were found to be present on the P25 TiO_2 through vibrational spectroscopy investigations [67]. However, a reversible temperature dependence on the speciation was found for the dispersed rhenium oxide. It was found that the mono-oxo species was favored at higher temperature while keeping the coverage constant. However, the di-oxo species was favored at higher coverages at constant temperature. This finding shows that ReO_x can exist in multiple structures on the same support and that the structure of ReO_x can be a function of both temperature and coverage.

The structure of ReO_x supported on CeO_2 has been theorized but not confirmed by vibrational spectroscopic methods. Since ReO_x has been shown to exist as a mono-oxo, di-oxo, tri-oxo, and oligomeric species on other oxide supports, it is important to consider all of these speciation's as possible structures. It is also important to consider that multiple of these structures could be present on the CeO_2 and that the structures could change as a function of temperature similar to what has been observed for rhenium oxide on TiO_2. Determining the structure or structures of ReO_x present when supported on CeO_2 can give

further insight into the ReO_x active site and reaction mechanism for the DODH and S-HDO reactions that can occur on this catalyst. In this dissertation, structural determination utilizing in-situ isotope exchange vibrational spectroscopy techniques along with temperature and coverage investigations were conducted to fill the knowledge gap.

CHAPTER 2

METHODOLOGY

2.1 REACTOR SYSTEM

2.1.1 REACTOR DESCRITION

All kinetic and activity studies were and will be performed in a homebuilt 150 ml stainless steel high-pressure batch reactor. The reactor schematic can be seen in Figure 2.1. The 150 ml reactor was machined from a 3” diameter rod of 316 SS. The base of the reactor has a 2” diameter and leaves 0.5” as a wall and the bottom of the reactor. The reactor has eight tapped holes that are used for a bolted closure as well as having a groove for the placement of an O-ring to ensure the reactor is properly sealed. The lid assembly was machined from a 4” diameter and 0.5” thick piece of 316 SS. The lid assembly was tapped with six 0.25” NPT fittings. One of the fittings is used for a pressure gauge to monitor the reaction pressure. The other five fittings use bore through adapters using a male 0.25” NPT and a 0.125” male tube fitting. These fittings are used for a gas sampling/venting valve, a liquid sampling valve, a gas inlet valve, a thermocouple well and one free fitting to be used for a liquid inlet if needed. One major benefit of the lid assembly of the reactor is that it allows for both liquid and gas sampling in which the samples are taken during reaction without the need for cooling or depressurization. The reactor is heated in an oil bath and is coupled with a PID controller to maintain the desired reaction temperature. The temperature of the reactor is monitored with a K-type thermocouple that is inserted into the thermocouple well and sits at the center of the reactor. Aluminum foil is used as insulation

and cover the reactor and the oil bath to ensure consistent heating. The homebuilt reactor was tested up to 100 bar and temperatures in excess of 180 °C. However, as a safety measure, a spring assisted actuated pressure release valve was attached to the gas inlet, and the gas sampling valve is equipped with a check valve to prevent air from entering the reactor after it has been purged. The reactor is mixed using a 1.5” magnetic stir bar that is coupled with a magnetic stir plate on which the reactor and oil bath sit.

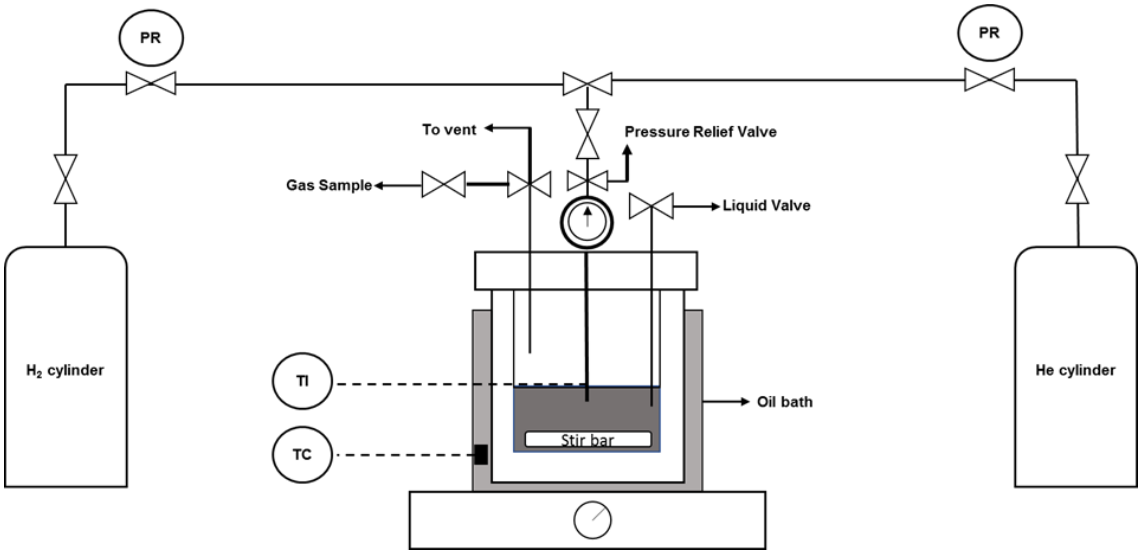

Figure 2.1. High-pressure batch reactor system schematic[69].

2.1.2 EXPERIMENTAL PROCEDURE

The following procedure is followed for each reaction conducted in our reactor. The desired amount of reactant, catalyst, and solvent are measured and weighed accordingly. Then the reactant, catalyst, solvent, and a 1.5” magnetic stir bar are added to the base of the reactor. The reactor base is then moved to the center of the magnetic stir plate. A PTFE O-ring is the placed in the groove on the top of the reactor base and flattened by pressing down uniformly around the grove. The magnetic stir plate is then set to the

desired stir rate, and the mixture is checked visually to ensure the stir bar is spinning, and the reaction solution is mixing. The K-type thermocouple is then inserted fully into the well, and the reader is turned on to monitor the temperature. The reactor lid assembly is then positioned on the top of the reactor by positioning the pressure gauge facing forward and lining up the tapped bolt closure taps. The eight tapped bolt closures are then filled with 10-24 inch alloy steel ASME B18.3 socket head cap screws with each having a size #10 18-8 stainless steel washer underneath. The bolts are then tightened by turning each down to a hand tight position and then slowly tightening the screws with an Allen key while frequently alternating the bolts being tightened to ensure a level and uniform tightening of the lid assembly to the base of the reactor. After the bolts are securely tightened, the reactor is then leaked checked. To leak check the reactor the gas inlet valve is opened, and the gas selector valve is opened to the helium line. The helium tank is then opened followed by opening the regulator so that gas can flow into the reactor. The regulator is then increased to slightly over the desired reaction pressure. After the desired pressure is reached the gas inlet and selector valves, the gas regulator and the helium tank are all closed, and the helium regulator is decreased fully. All of the fitting and reactor connections are tested for leaks using a leak detector that contains an FID detector. If any leaks are found, then the gas is released using the gas venting valve and the bolts are further tightened, and the leak detection procedure is refollowed until there are no leaks. Once no leaks are found the reactor is then purged of gas and the reactor is placed in the oil bath and centered on the stir plate. Additional oil is added to the oil bath until the oil reaches the top of the heating element. After the oil bath is at the proper level, aluminum foil is wrapped around the oil bath, reactor, and lid assembly with two layers to ensure uniform

heating and minimal heat losses due to the environment. For reactions of over 10bar in pressure, the appropriate amount of hydrogen needed according to the ideal gas law is then added. The hydrogen gas is added to the reactor by opening the gas inlet valve and selecting the hydrogen line on the gas selector valve and then opening the hydrogen tank and regulate and increasing the regulator to the desired pressure. After the desired pressure is reached the gas inlet and selector valves, the gas regulator and the helium tank are all close, and the hydrogen regulator is decreased fully. For reactions of 10bar and below, the hydrogen is introduced into the reactor once the desired reaction temperature is reached and the hydrogen line is left open to allow for constant pressure. The oil bath is then set above the desired reaction temperature, usually 5-10 °C depending on the temperature, and the oil bath begins ramping to the set temperature. Once the oil bath is at temperature any further adjustments can be made to ensure the reactor is at the desired temperature. For reactions above 10 bar, the reaction time starts once the reactor is at the desired temperature. For reactions of 10 bar and below, the reaction time starts once the hydrogen gas is introduced into the reactor. Liquid samples are then taken intermittently throughout the reaction by using the liquid sampling valve. The sampling valve is opened and a small amount of liquid is collected and discarded to ensure the tube is clear of any previous samples. If the sampling valve is clogged due to the sugar alcohols re-solidifying a heat gun is used to heat the sampling tube/ valve and the respective connections until liquid can flow. After the small amount of liquid is cleared, reaction samples are collected in a 0.5-dram vial filling the vial with roughly 1ml of liquid sample. Once the reaction is completed, the gas lines are closed, and the remaining gas is purged. Then the oil bath controller is set to 0 °C to allow for the oil bath to cool and the aluminum foil is removed from the reactor to expedite

the cooling process. Once the reactor is cooled the reactor is removed from the oil bath, the bolts are removed, the O-ring is discarded after cleaning, the reaction solution is discarded into a chemical waste container, and the reactor is cleaned. To clean the outside of the reactor paper towels are used to clear off any excess oil on still on the reactor. To clean the inside of the reactor and the liquid sampling port acetone is used. The reactor is filled with acetone, and then the lid assembly is attached and sealed using the previously described procedure. Helium is used to pressurize the reactor so that the acetone can flow through the sampling valve once it's open. Once the acetone is flushed through the sampling valve the gas is purged and then the lid assembly is removed. The remaining acetone in the base of the reactor is then discarded into a chemical waste container, and the reactor is cleaned in the sink with soap and water using a sponge. The reactor is then dried using paper towels, and a compressed air line is used to clear any liquid out of the bolt taps.

2.1.3 ANALYSIS PROCEDURE

To analyze the reaction samples a Shimadzu GC-2010 Plus that contains an FID detector, an RTX-1701 column (length of 30.0 m, Inner diameter of 0.32 mm), and an AOC-5000 auto-injector is used. Samples are diluted to ensure that the detector doesn't saturate and to ensure that the concentration ranges will be within the calibrations for the various reaction products and reactants. The calibrations are made by the user using external standards and then running a calibration methodology in the GC. For the S-HDO reactions, 240 µl of reaction sample is pipetted into a 10ml volumetric flask and then diluted in methanol to 10 ml. The volumetric flask is then sonicated in a water bath for 1 minute to ensure proper mixing. The volumetric flask is then removed and poured into a 10ml beaker. A 3 ml luer lock syringe is then used to extract sample from the beaker. The

luer lock tip is then removed, and a 0.20 µm PVDF filter is put on the syringe, and the sample is pushed through the filter into a GC autosampler vial until it is at the top fill line. The rest of the sample is discarded into a chemical waste container, and the beaker and volumetric flask are washed with methanol. Once all samples have followed the above procedure, the autosampler vials are placed in the AOC-5000 auto-injector tray in numerical order following an acetone and methanol vials used for reference. The GC software and batch file are the set up respectively, and the auto-injector is set to the appropriate sampling range and started once the GC is ready for operation. The GC spectra are then collected automatically and saved to the appropriate folders.

For reach run of sample in the GC, the injection port temperature is set to 250 °C, and the FID is set to 260 °C. The column uses helium as the carrier gas and is set to split injection mode with a split ratio of 10.0. The total flow is set to 30.5 mL/min, the column flow is set to 2.5 mL/min, and then linear velocity is set to 38.9 cm/s. The column temperature program is set to hold at 40 °C for 3 min and then ramp to 260 °C at 10.0 °C/min. Once the temperature of the column has reached 260 °C, it is set to hold for 20 min. The total program time per run is 45 min.

Calibration curves of the various chemicals used and produced in this dissertation were made by running prepared external standards of known concentration diluted in methanol in the GC methodology. 1,4-Anhydroerythritol and tetrahydrofuran were calibrated using an 11-point calibration with standards ranging from 132-2105 ppm, and 84-1348 ppm respectively. Xylitol, 1,2-pentanediol, 1-pentanol, and 3-pentanol were calibrated using an 8-point calibration with standards ranging from 215.5-17241 ppm, 194.2-15536 ppm, 81.4-6512 ppm, and 163-13040 ppm respectively. 1,2,5-pentanetriol

was calibrated using a 6-point calibration with standards ranging from 211.3-42264 ppm. 1,2-Dideoxypentitol was calibrated for using the 1,2,5-pentanetriol calibration. Sorbitol, 1,2-hexane diol, 1,6-hexanediol, and hexane were calibrated using an 8-point calibration ranging from 100-8000 ppm.

To analyze the GC spectra, Microsoft Excel and the calibration curves are used. The calibration curves for the various chemicals relate GC peak area to ppm concentration at specific retention times. The peak areas are converted into ppm's, and then the concentration is adjusted for the dilution of the sample and then converted to moles. The selectivity of the products is then calculated by dividing the moles of the product of interest by the total number of moles of products. The conversion of the reaction is calculated by dividing the initial moles of reactant minus the moles of reactant at the final reaction time divided by the initial moles of reactant.

2.2 CATALYST SYNTHESIS

The ReO_x/CeO_2 and ReO_x-Pd/CeO_2 catalysts used in this work were synthesized using a wet impregnation procedure [45], [69]–[71]. The CeO_2 support was weighed and then transferred to a heating crucible and calcined in air at 600 °C for 3 h with a ramping rate of 10 °C/min in an oven, before any metals were impregnated. Following the support calcination, the ReO_x was then impregnated onto the CeO_2 via wet impregnation using the desired amount of ammonium perrhenate (NH_4ReO_4) (based on the nominal weight loading of Re desired) dissolved in an aqueous solution while being mixed on a stir plate at 300 rpm. Once the solution was adequately mixed, it was dried at 110 °C for 12 h to allow the water to evaporate from the solution and leave only the ReO_x/CeO_2. For the ReO_x-Pd/CeO_2 catalysts, the palladium was impregnated via wet impregnation using an aqueous solution

of the desired amount of palladium (II) nitrate ($Pd(NO_3)_2$) in the same manner as the ReO_x was impregnated. The solution was then dried at 110 °C for 12 h. The respective ReO_x/CeO_2, and ReO_x-Pd/CeO_2 catalysts were then collected from the beakers and transferred to a heating crucible. The catalysts were then subjected to calcination in air at 500 °C for 3 h with a ramping rate of 10 °C/min. After cooling to room temperature, the resulting ReO_x/CeO_2, and ReO_x-Pd/CeO_2 catalysts were ground into a fine powder using a mortar and pestle. The various catalysts utilized had varying Re weight loadings based on what was being investigated. The same synthesis methodology was applied to all catalysts made and only the amount of metal precursors used was altered. All of the ReO_x-Pd/CeO_2 catalysts that were made maintained a nominal molar ratio of Pd to Re of Pd/Re = 0.25, which was reported to be optimal for this catalyst system of interest [38], [45].The ammonium perrhenate (NH_4ReO_4) and palladium (II) nitrate ($Pd(NO_3)_2$) used in the impregnations were obtained from Sigma-Aldrich, and the cerium (IV) oxide (CeO_2) support was donated by Daiichi Kigenso Kagaku Kogyo Co., Ltd. Osaka, Japan.

2.3 CHARACTERIZATION TECHNIQUES

To gain more fundamental insight into the structure and properties of the catalysts prepared and utilized in this work, various characterization techniques were utilized. X-ray Diffraction (XRD), X-ray Fluorescence (XRF) spectroscopy, Temperature Programmed Reduction (TPR), Scanning Electron Microscopy (SEM), Inductively Coupled Plasma-Optical Emission Spectrometry (ICP-OES), Raman spectroscopy, Fourier Transform Infrared Spectroscopy (FTIR), and Brunauer-Emmett-Teller (BET) nitrogen adsorption were utilized.

2.3.1 X-RAY DIFFRACTION (XRD)

X-ray diffraction is a technique that utilizes x-rays to irradiate a material and measures the resulting scattering/diffraction angles and the intensity of the diffraction. XRD takes advantage of the elastic scattering of the monochromatic X-rays, which allows for fundamental information such as the distance between diffraction planes (d) to be elucidated. Bragg's law, shown below, can be utilized to calculate the d spacing using the diffraction order (n), the X-ray wavelength (λ), and the incident angel (θ).

$$n\lambda = 2d \sin\theta$$

The diffractions observed can give insight into the long range ordering and crystal phases of the sample being evaluated. From the d spacing calculated using Bragg's law, the lattice spacing (a) and Miller Indices (*hkl*) can be determined using the various selection rules for different Bravais lattices and the following relation:

$$d = \frac{a}{\sqrt{h^2 + k^2 + l^2}}$$

From the determination of the Miller Indices for the various diffractions, we can determine which cubic structure the material is oriented in and then identify which species in our material it is based on XRD data bases and expected diffractions based on the known material. XRD can also be utilized to calculate the crystallite size in powder samples using Scherrer constants and equation [72], [73]. Utilizing these methods, the particle sizing and phases of the various elements or materials present in the sample can be determined [74]–[76], and if the elements are undetectable, it can be assumed that they are very well dispersed on the support material since peaks become too broad and have a low intensity for particle sizes below 3 nm [77].

XRD was utilized in this work to be able to determine if any long range ordering was present for the Re or Pd impregnated on the CeO_2 to evaluate if the particles were well dispersed or if larger agglomerates were forming during the synthesis methodology.

2.3.2 X-RAY FLOURESCENCE SPECTROSCOPY (XRF)

X-ray fluorescence spectroscopy is a technique that can be utilized to determine the elemental composition of a sample in terms of weight percentage utilizing X-rays. In XRF, the sample is irradiated with X-rays which then excites and ejects the inner shell (usually K and L shell) electrons of the atoms, which results in a vacancy [78], [79]. The resulting vacancy is filled by the electrons from higher energy shells and the difference in energy between the higher shell and the lower shell vacancy is emitted via radiation in the form of fluorescence. Each element has a characteristic radiation in XRF which is independent of the chemical bonding. The composition of the sample can be determined using the characteristic radiation for the elements of interest, and the intensity of the fluorescence, which is directly proportional to the concentration of the respective element in the sample [80].

XRF can be utilized as a fast method to analyze the composition of catalyst powders without the need for dissolving the sample in acid or other destructive preparation or analysis [81]. XRF can also allow for 2D compositional mapping of the sample, allowing for insight into uniformity of the sample [82], [83]. This technique allows for the quick determination of homogeneity and composition of prepared catalysts. However, XRF has a large spot size ranging from a few hundred micrometers to millimeters in diameter. Thus XRF samples a large area of the sample with each scan.

XRF was utilized in this work to investigate the actual loadings of the ReO_x-Pd/CeO_2 catalysts and to be able to 2D map the various elements to determine if the synthesis technique made homogenous catalyst or if there was significant localization of the various metals impregnated on the ceria.

2.3.3 TEMPERATURE PROGRAMMED REDUCTION (TPR)

Temperature programmed reduction utilizing hydrogen as the reductant, is a technique which can give insight into the oxidation state of a catalyst and help determine the temperature needed to fully reduce a metal in a catalyst [84]. In TPR, the catalyst is loaded into a sample tube at room temperature and a thermocouple is placed in the catalyst for accurate temperature measurements. The sample tube is then evacuated of air using an inert gas flow. Once the sample has been evacuated the gas flow is switched to a mixture of hydrogen (or another reducer) in an inert and the sample is heated at a fixed rate. While the sample is being heated in the reducing environment, measurements of the hydrogen concentration in the exiting gas is measured. As the catalyst reduces and consumes hydrogen, the concentration of the hydrogen in the exit gas decreases. This can also be measured by tracking the concentration of water, since water should form during the reduction of the species. Samples can have multiple reduction events occur during the analysis. Supported catalysts can have reduction events occurring from the support, impregnated active materials and promoters [85], [86]. Thus it is important to be able to separate these events to determine which events are occurring at the various temperatures to discerns which species are important to reduce or might be reducing under reaction conditions. TPR can be utilized to help see the effects of promoters or supports on the

reduction temperature and events of various supported active metals in catalysts [87]. This can give further insight into how the promoters, supports, and active metals interact.

TPR was utilized in this work to investigate the reduction events corresponding to the ReO_x and the CeO_2 present in the ReO_x/CeO_2 and ReO_x-Pd/CeO_2 catalysts used in this work. The TPR was also used to determine if the ReO_x was reducing in the reaction under reaction temperatures evaluated in this work.

2.3.4 SCANNING ELECTRON MICROSCOPY (SEM)

Scanning electron microscopy is a technique that utilizes electron beams to image a sample at very high magnifications and allows for the sample morphology to be investigated on the micrometer, nanometer, and angstrom scales [88], [89]. SEM uses a secondary electron detector to analyze the sample. The electrons are first produced by an electron source which then passes the electrons through an anode before they pass through a condenser lens [90]. After the passing through the condenser lens the electrons are passed through an objective lens and focused on the sample. The secondary electrons from the surface of the sample are then collected by the detector and an image is processed.

SEM can be utilized to be able to investigate heterogeneous catalyst morphology and particle size [91]. SEM can be used to investigate the effects of thermal treatments, reactions, synthesis parameters, and cycling effects on the catalyst particle sizing and morphology [92]. Thus SEM can help visually show what changes are occurring on the catalyst as a response to the various parameters mentioned. In this work, SEM was used to determine the particle size of the CeO_2, ReO_x/CeO_2 and ReO_x-Pd/CeO_2 to evaluate if the additional metal and metal oxides impregnated on the ceria changed the morphology or particle size.

2.3.5 INDUCTIVELY COUPLED PLASMA-OPTICAL EMISSION SPECTROMETRY (ICP-OES)

Inductively coupled plasma-optical emission spectrometry is a technique that utilizes electromagnetic radiation to determine the concentration of particular elements within a sample. ICP-OES uses plasma to excite the electrons of the various elements in the sample. When the electrons return to their respective ground state, electromagnetic radiation in the form of light is emitted at specific wavelengths that are characteristic to each respective element. The light is then measured and the concentration of each element present in the sample can be determined via an internal or external calibration. The intensity of the emission is directly related to the number of atoms of each respective element present in the sample [93]. The samples for ICP-OES are first dissolved in strong acids such as hydrochloric acid or aqua regia and then diluted in DI water for analysis [94]. The resulting solution is then fed through a peristaltic pump and through a nebulizer which sprays the sample into the plasma.

ICP-OES is a powerful tool which allows for the actual weight loadings of catalysts to be determined with high precision and accuracy [95], [96]. Being able to determine the actual loadings of the prepared catalysts allows for a quality check in the synthesis methodology and also allows for the total amount of metals to be known. Knowing the actual metal loadings can allow for kinetic measurements to be updated based on the actual loading of active metals. ICP-OES can also be utilized to determine if any leaching of impregnated elements is occurring during reaction, or if there is any contaminates in the catalyst sample post reaction. ICP-OES was utilized to determine the actual weight

loadings of Re and Pd in the ReO_x/CeO_2 and ReO_x-Pd/CeO_2 catalysts used throughout this work, and to ensure that the synthesis methodology was consistent.

2.3.6 RAMAN SPECTROSCOPY

Raman spectroscopy is a technique that can be used to determine the various vibration modes of a sample using the inelastic scattering of photons. For a vibrational mode to be observed in Raman spectroscopy, it must exhibit a change in polarizability. From the vibrational modes, the structure of metal oxides and various elements can be elucidated based on the observed vibrations and theoretical calculations. Raman utilizes a monochromatic light in the form of a laser to excite the samples electrons to a virtual energy state. Once the relaxation occurs there are three possibilities. First the electron can return to its original energy state (Rayleigh scattering) sue to an elastic scattering. Alternatively, the electron can return to a higher energy state (Stokes Raman scattering) or a lower energy state (anti-Stokes Raman scattering) due to inelastic scattering. The Stokes scattering results in a scattered photon with less energy than the incident photon and the anti-Stokes scattering results in a scattered photon with a more energy than the incident photon. The Rayleigh scattering is filtered out by the detector and only Stokes and anti-Stokes scattering is detected and analyzed. However, the probability of inelastic scattering occurring is extremely low (roughly 1 in every million scattering events) which results in a very low intensity as compared to the laser.

Raman can be used to directly elucidate the vibrational modes of metal oxides on oxide supports [97]. By determining the number and types of vibrations present, the structures of the metal oxides can be directly determined [98]. This can allow for further insight into the active sights of various catalyst and can help give further insight into

reaction mechanisms [99], [100]. From the vibrations present, it can also be determined if species are in monomeric or oligomeric structures and if one or more structures of the metal oxides are present on the catalyst. In this work Raman spectroscopy was utilized to determine the structures of ReO_x in ReO_x/CeO_2 and ReO_x-Pd/CeO_2 and to monitor the structures under different gas environments and temperatures to simulate reaction conditions.

2.3.7 FOURIER TRANSFORM INFRARED SPECTROSCOPY (FTIR)

Fourier transform infrared spectroscopy is a technique which measures the absorption spectrum of a sample which has infrared radiation applied to it. FTIR can be used to determine the various types of chemical bonds present in a sample and their relative quantities. Vibrations can be observed in FTIR if they can exhibit a change in the molecular dipole moment. Similar to Raman spectroscopy, this technique can be utilized to determine the various structures present on a catalyst and can be a complementary technique to Raman [101]. However, based on the selection rules, some peaks observed in Raman might not be observed in FTIR. In this work we specifically utilized Diffuse Reflectance Infrared Fourier Transform Spectroscopy (DRFITS). DRIFTS is a powerful tool in being able to analyze powders in a gas phase environment at elevated temperatures to conduct in-situ studies. DRIFTS focuses the infrared light onto the powder catalyst sample, which then has the light diffuse or scattered and the resulting light is collected by the detector. The signal from the detector is then analyzed using a Fourier transform which results in the spectrum as a function of absorbance or transmission vs wavenumber. A huge advantage of DRIFTS is the ability to take time resolves spectra [101], [102] which can allow for the tracking of in-situ reactions [103], [104], isotope exchanges [105], or pretreatment and

thermal effects [106] on the catalyst to be monitored with relative ease and without damaging the sample.

In this work, in-situ DRIFTS was utilized to determine the Re-O and Re=O vibrations present in the ReO_x/CeO_2 catalysts and to complement the Raman findings. DRIFTS was also utilized to get a time resolved analysis of the isotopic exchange of ^{18}O within the ReO_x/CeO_2 catalysts to gain further insight into which species exchange faster and to determine kinetic related parameters of the exchange.

2.3.8 BRUNAUER-EMMETT-TELLER (BET) NITROGEN ADSORPTION

Brunauer-Emmett-Teller nitrogen adsorption is a technique that uses physisorption of nitrogen on the surface and in pores of a material to measure the surface area and pore size distribution using Langmuir principles [107]. In BET the sample is first degassed by pulling a vacuum on the sample tube while also heating the tube. After the degassing of the sample, the sample is then cooled in liquid nitrogen to further evacuate and remaining gas in the sample tube. Then nitrogen is flowed into the sample tube while maintaining a constant temperature to allow for the nitrogen to physisorb on the sample. In BET, it is assumed that there are no lateral interactions between adsorbed molecules and that the molecules in the first monolayer act as sites for the second monolayer and so on [107], [108]. The adsorption and desorption isotherms are then measured and BET equations are utilized to calculate the volume of nitrogen needed to form a monolayer on the sample. From this information, the actual surface area of the sample can be determined [109].

In the context of this work, BET was utilized to determine the surface area of the various catalysts synthesized including the ReO_x/CeO_2 and the ReO_x-Pd/CeO_2 and the ceria support. BET was also conducted to see if the synthesis methodology including the

impregnation of the metals significantly altered the surface area of the ceria. The surface area measurements were also used to determine density of rhenium particles per nm on the catalyst.

2.4 STATISTICAL METHODS

2.4.1 DESIGN OF EXPERIMENTS

Design of experiments (DOE) is a statistical method that investigates the effects that various input factors/features have on specific responses and is a powerful tool to help identify significant factor to response relationships and optimize a system or process. DOE has been a popular approach for optimization for decades [110] and was originally developed by Ronald Fisher in the 1920s and 30s [111], [112]. DOE had several innovations in the 1950s with response surface methodology being developed [113] and in 1960s with the Taguchi methods and designs being developed [114]. The designs utilize various regression models and statistical analyses to determine which input factors are significant, and to model the responses as a function of these significant input factors. The general DOE process is shown in Figure 2.2. First, the factors and responses must be determined, and the number of levels for each factor must be set, based on the experimental throughput capabilities of the system of interest. Then the type of design must be selected, which is often based on throughput capabilities and the type of interactions that are expected [115]. Once the type of design is determined, the design is then constructed, and the experiments are conducted. The experimental data collected is then analyzed in software, and a regression model and factor significance are determined. Then the insignificant factors can be removed from the regression, the model is then verified, and optimum conditions are evaluated.

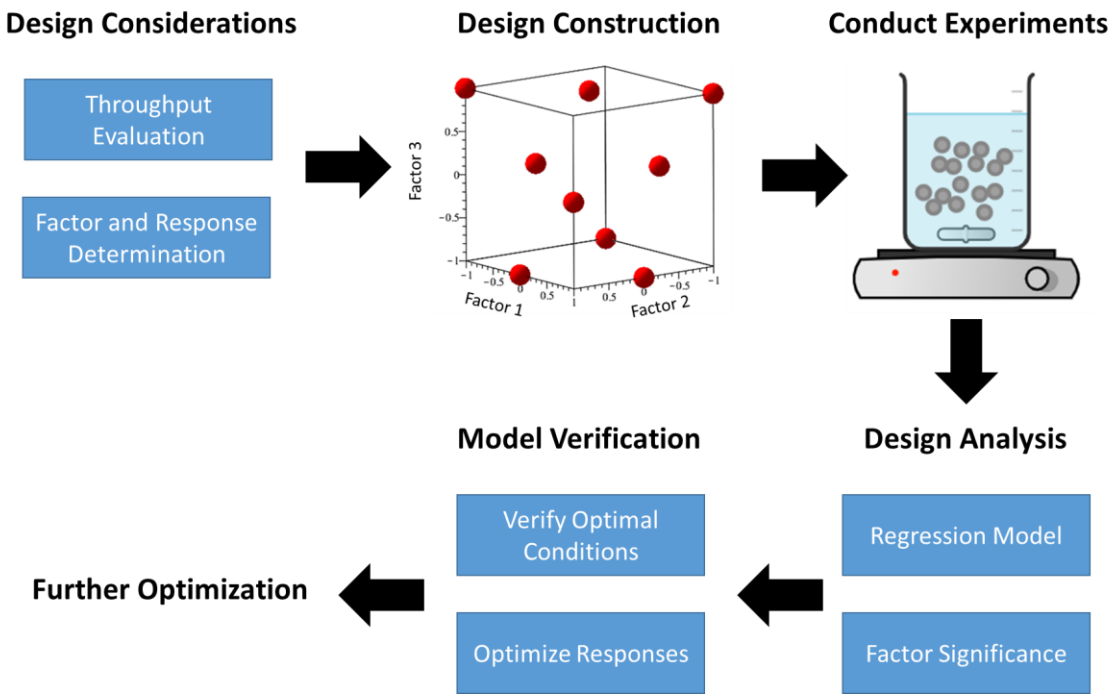

Figure 2.2. Design of Experiments process cycle.

Due to the relationships that the DOE can establish, it has been widely utilized in catalysis to probe important factors such as reaction conditions, including temperature, pressure, flow rates and reaction time, and catalyst synthesis parameters such as active and promoter metal loadings, and calcination or reduction temperature and time [69], [116]–[119]. The designs have shown that significant relationships and optimizations can be elucidated with a relatively low number of experiments [69], [118], [120], [121].

The designs tend to scale with the relationship of $levels^{factors}$. The factors are the input factors that the user specifies, and the levels are how many points each factor is evaluated at. Here, experimental throughput is of utmost importance. Using a high-throughput system with multiple reactors in parallel will allow for more complex designs with more factors and levels to be used. However, if you only have a single reactor or system, throughput to knowledge gained becomes a significant consideration, and a more

well-tuned design space must be constructed. It is essential to pre-screen factors, e.g., by utilizing a linear screening design [122], to make sure that they are important in your system before including them in your design to save time and costs by reducing the design space to as few factors of interest as possible.

DOE has several benefits but also has some drawbacks. DOE in catalytic design spaces has demonstrated to be powerful in determining specific relationships between factors and responses such as reaction conditions to conversion and selectivity [69], [123]–[125] or catalyst synthesis parameters to catalyst activity [116], [126], [127]. The ability to elucidate a regression that can be applied to your system and determine optimal settings for a process is a crucial advantage of DOE. DOE has been utilized to optimize a wide variety of catalytic processes, including biomass upgrading [69], [128], biodiesel synthesis [129]–[131], hydrogenation [125], and oxidation [116] reactions. However, DOE has several limitations and drawbacks. DOE can't easily model various elemental factors, which can be complex and hard to vary evenly. Another limitation to DOE is the fact that they only model within the design space specified and should not be used for extrapolation outside of the design space. Although the statistical analysis on the DOE tells the significance of the factors, it does not provide any fundamental insight into why they are important. For catalytic design spaces, there are a multitude of factors in the form of composition parameters, reaction parameters and synthesis parameters that affect desired responses, such as conversion or selectivity. However, time and cost limitations may necessitate a reduction in the number of factors studied. There has been evidence that simplistic designs, such as Taguchi designs, can significantly reduce the number of experiments needed while still optimizing catalytic systems [69], [117], [120], [129]. These

types of designs can be utilized as quick screening and optimization tools leading to further advancement.

There are several different types of DOEs ranging from robust to complex designs that are commonly utilized in catalysis. These include Taguchi, Response Surface, and Factorial designs. Taguchi designs are robust designs that utilize orthogonal arrays to reduce significantly the number of experiments needed while still estimating the optimum process settings and maximizing signal-to-noise ratios [69], [123], [132]. However, these designs only give linear correlations to the desired responses and do not capture cofactor interaction or potential higher-order terms. Response Surface designs develop quadratic functions for processes, investigate cofactor interactions, and slightly reduce the experimental runs needed from the $levels^{factors}$ relationship, but only continuous factors can be utilized [115]. Factorial designs determine interactions between variables and directly investigate the effects of single variable manipulation [116], [124]. However, they require more experiments than Taguchi designs or Response Surface designs since the number of experiments is determined directly by the $levels^{factors}$ [115].

In this work, several DOEs were used for process and reaction condition optimization. Several Taguchi designs were used to elucidate optimal conditions with a significant reduction in the experimental throughput requirement, and a Box-Behnken design was also utilized to optimize a reaction. The Box-Behnken design was also used to compare and contrast the results of a Taguchi design to directly compare the knowledge to experimental through put ratio and to see if a more complex design led to different results.

CHAPTER 3

REACTION OPTIMIZATION OF HYDRODEOXYGENATION OF SUGAR ALCOHOLS

3.1 MOTIVATION AND EXPERIMENTAL

3.1.1 MOTIVATION

Lignocellulosic biomass is derived from cell walls and can be reformed into liquid phase and upgraded into sugars that contain hydroxyl groups, such as 1,4-anhydroerythritol (AHERY) [17], [133], [134]. The liquid phase reforming produces glucose and can be fermented into erythritol. Erythritol can then go through an acid catalyzed dehydration to form AHERY [29]. These sugars can either undergo deoxydehydration (DODH) to form double bonds or hydrodeoxygenation (HDO) to remove vicinal hydroxyl groups [38]. The removal of the hydroxyl groups allows for the biomass derived sugars to be utilized as an alternative feedstock for fuel and platform chemical production [135]. The deoxydehydration typically uses a ReO_x-Au/CeO_2 catalyst, and the HDO uses either a WO_x-Pd/ZrO_2 catalyst to remove a single hydroxyl group or a ReO_x-Pd/CeO_2 catalyst to simultaneously remove two vicinal hydroxyl groups [29], [38], [42]–[44], [136]. The latter reaction is a simultaneous hydrodeoxygenation (S-HDO) and proceeds via deoxydehydration followed by a hydrogenation step that allows for the simultaneous removal of two vicinal hydroxyl groups. Re based catalysts have been utilized for DODH due to their high reaction rates and selectivity [137]. Deoxydehydration of methyl glycosides over these Re based catalysts has been achieved at low H_2 pressures with high

yields [136]. Literature has shown that ReO_x-Pd/CeO_2 is a better catalyst for the S-HDO of AHERY as compared to ReO_x-Pd on other oxide supports [45]. The S-HDO of AHERY, producing tetrahydrofuran (THF), was used as a model reaction for S-HDO since it has two vicinal cis-hydroxyl groups. AHERY is ideal to use for a model reaction for S-HDO since it can only occur once on this compound. For other compounds containing more than two vicinal cis-hydroxyl groups the hydroxyl groups that the S-HDO selectively removes first dictates the possible products that can be formed. The AHERY S-HDO reaction is shown in Figure 3.1.

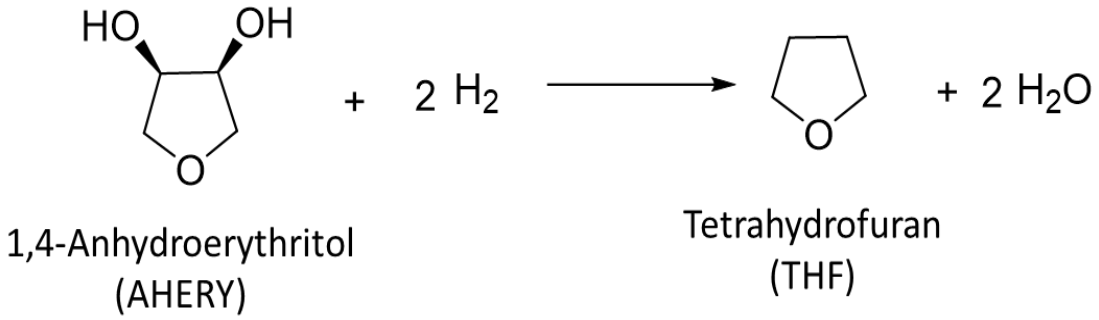

Figure 3.1. Simultaneous hydrodeoxygenation of 1,4-anhydroerythritol to tetrahydrofuran. [69]

HDO reactions have been conducted over a wide range of conditions, including pressures that exceed 75bar H_2 and temperatures over 350°C [48]–[60], [138]. One of the issues that arises with HDO reactions is that the conditions involve either high pressure, high temperature or both high pressure and temperature. These harsh conditions challenge the scaling of aqueous-phase HDO reactions for commercial viability and has resulted in a bottleneck for further development of these processes [139]. Elucidating milder conditions in terms of temperature and pressure for these HDO reactions would make the process more economically favorable for pilot scale and beyond, due to the reduction in cost of

materials, heating energy required, and potential gas compressors. The S-HDO of AHERY has been evaluated in literature at 80 bar H_2 and 180 °C in a small scale batch reactor [45]. For a batch process, these conditions would pose major problems at an industrial level regarding economic viability. A pressure of 80 bar H_2 greatly surpasses the safety rating for many commonly used industrial batch reactors and would require high rated gas compressors. In this work, we investigated the feasibility of running this reaction at milder conditions by utilizing a Taguchi design of experiments to probe milder temperature and pressure conditions while optimizing catalyst loading. The goal of this work was to determine the main effects of pressure, temperature, and catalyst loading on the yield of S-HDO products and to elucidate potential scalable operating conditions. These HDO reactions conducted at milder conditions could allow for scaling from the lab scale to the pilot scale and beyond to be easier and more economic by being able to utilize exisiting infastructure without the need for specilized equipment and thus reduce potential costs. The ability to reduce heating and feedstock costs can directly improve the economic viability of these processes and create a potentially viable path for the renewable generation of platform chemicals.

Xylitol is a five carbon long sugar alcohol that is widely utilized as a common sugar substitute. Xylitol is derived from lignocellulosic biomass, which is a renewable resource, and is already produced on a large commercial scale. Lignocellulosic biomass can go through a hemicellulose extraction to obtain xylan which can then go through hydrolysis to form xylose [140]. The xylose can then be fermented [141]–[144] or hydrogenated [145], [146] into xylitol. Xylitol contains five vicinal hydroxyl groups which can undergo an HDO. The xylitol S-HDO reaction is shown in Figure 3.2. The S-HDO of xylitol can

produce 1,2-dideoxypentitol and 1,2,5-pentanetriol if one pair of vicinal hydroxyl groups are removed. Both 1,2-dideoxypentitol and 1,2,5-pentanetriol are considered value-added products and are used as chemical building blocks for various reactions. These products that are initially formed range between 300-5000 times more valuable than the initial xylitol on a per mass basis. If another S-HDO occurs, the 1,2-dideoxypentitol and 1,2,5-pentanetriol are converted to either 1-pentanol or 3-pentanol. The 1-pentanol and 3-pentanol are widely used industrial chemicals, however, these are of low value when compared to the current production price of xylitol. The pentanols are on the order of 1.2 to 3.3 times as valuable as the initial xylitol and require a longer reaction time to form which would increase the associated operating costs of the reaction.

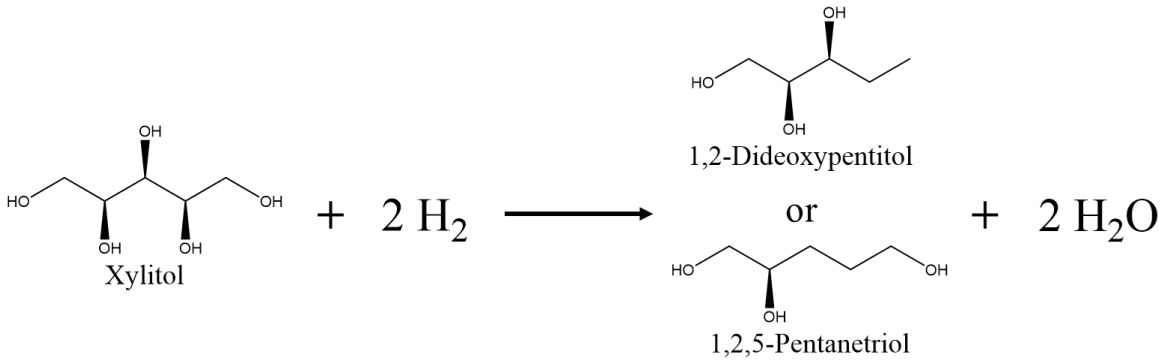

Figure 3.2. Simultaneous hydrodeoxygenation of xylitol to 1,2-dideoxypentitol or 1,2,5-pentantetriol.

Xylitol S-HDO has been conducted in literature at 160°C and 80bar H_2 [45]. The reaction was conducted for 24 hours and mainly produced 1-pentanol and 3-pentanol due to the long reaction time. Since the goal is to find economically favorable conditions, the 1,2-dideoxypentitol and 1,2,5-pentanetriol were targeted in this work due to the significant value potential created. Thus, a shorter time scale will be used for evaluation and comparison between experimental runs to focus on the significant value-added products. In this work, we have determined mild and scalable reaction conditions for xylitol S-HDO

to the value-added products 1,2-dideoxypentitol and 1,2,5-pentanetriol through the use of design of experiments.

3.1.2 CHEMICALS

The various chemicals used in this study are listed below along with their purity and supplier in Table 3.1. In the reactions, 1,4-dioxane was used as the solvent, and 1,4-anhydroerythritol, xylitol, and hydrogen were used as the reactants. AHERY, xylitol, tetrahydrofuran, 1,2,5-pentanetriol, 1,2-pentanediol, 1-pentanol, and 3-pentanol were used to make calibration standards for analysis in the gas chromatograph to be used for reaction analysis. The ammonium perrhenate and palladium (II) nitrate and cerium oxide were used in the synthesis of the ReO_x-Pd/CeO_2 catalysts.

Table 3.1. Chemical list including purity and their supplier. [69]

Compound	**Purity in %**	**CAS No.**	**Supplier**
1,4-Dioxane	99.9	123-91-1	Fischer Chemical
1,4-Anhydroerythritol (AHERY)	>98.0	4358-64-9	TCI
Tetrahydrofuran (THF)	≥99.9	109-99-9	Sigma-Aldrich
Xylitol	≥99	87-99-0	Sigma-Aldrich
1,2,5-Pentanetriol	97	14697-46-2	Combi-Blocks
1,2-Pentanediol	96	5343-92-0	Sigma-Aldrich
1-Pentanol	≥99	71-41-0	Sigma-Aldrich
3-Pentanol	98	584-02-1	Sigma-Aldrich
Ammonium perrhenate	≥99	13598-65-7	Sigma-Aldrich
Palladium (II) nitrate solution (10wt% in 10wt% nitric acid)	99.999	MDL: MFCD00011169	Sigma-Aldrich
Cerium (IV) oxide	-	1306-38-3	Daiichi
Hydrogen (UHP)	99.999	1333-74-0	Praxair

3.1.3 CATALYST PREPARATION

The various ReO_x-Pd/CeO_2 catalysts used in this work were prepared via wet impregnation using the synthesis procedure reported by Ota et al [38]. The CeO_2 support, which was donated by Daiichi Kigenso Kagaku Kogyo Co., Ltd. Osaka, Japan, was first calcined at 600 °C for 3 h. The ReO_x was then impregnated onto the CeO_2 support with an aqueous solution of ammonium perrhenate (NH_4ReO_4) with the corresponding amount of Re needed for the desired nominal loading. Catalysts were prepared with 2, 3, and 4 wt% nominal loadings of Re. Following the impregnation of Re, the catalyst was then dried at 110 °C for 12 h. The Pd was then impregnated with an aqueous solution of palladium (II) nitrate ($Pd(NO_3)_2$) with the corresponding amount of Pd needed for the desired nominal loading. Once the Pd was impregnated the solution was then dried in air at 110 °C for 12 h. Following the drying, the catalysts were calcined in air at 500 °C for 3 h. After calcination, the catalysts were ground into a powder using a mortar and pestle. The molar ratio between Pd and Re was kept constant at Pd/Re = 0.25 (which corresponds to the weight percent ratio of Pd/Re = 0.15) for the various catalyst loadings, as it was previously reported to be optimal [38], [147].

3.1.4 CATALYST CHARACTERIZATION

The 2, 3, and 4 wt% Re ReO_x-Pd/CeO_2 catalysts were characterized using X-ray diffraction (XRD), inductively coupled plasma optical emission spectroscopy (ICP-OES), and temperature-programmed reduction (TPR).

XRD was conducted with a Rigaku MiniFlex II with CuKα source radiation (α=1.5406) scanning between 2θ of 10°-80° at a rate of 2°/min. The XRD patterns for the various catalysts are shown in Figure 3.3. The XRD patterns for the catalysts match the

patterns for cerianite reported previously in literature [45]. No solid Re or Pd peaks were observed in the XRD, which implies our Re and Pd particles are well dispersed on our catalyst surface and likely monomeric species rather than oligomers.

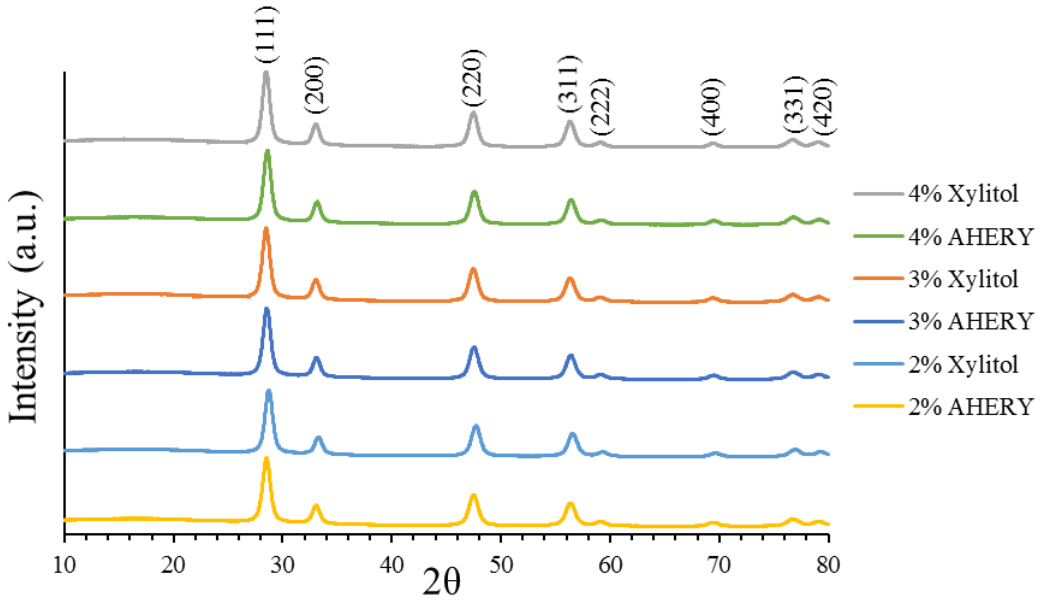

Figure 3.3. X-ray diffraction patterns of ReO_x-Pd/CeO_2 catalysts used in the design of experiments for AHERY and xylitol S-HDO. [69]

To determine the actual Re weight loadings of our catalysts, ICP-OES was conducted on a PerkinElmer Optima 2000 DV Optical Emission Spectrometer. The catalysts were dissolved using hydrochloric acid with a 110 °C digestion for 12 h. The actual Re loadings of the catalysts were 1.53, 2.51, and 3.30 wt% respectively, as shown in Table 3.2. The errors for the measurements were quite large potentially signaling inconsistent mixing of the sample or an incomplete digestion. The actual loadings were slightly lower than anticipated and shows that a stronger acid may be needed to fully digest the Re off of the catalyst. In the future aqua regia, more volume of acid, and longer digestion times should be explored to determine if they pay a role in the digestion of Re.

However, there was a significant difference between the different weight loading of catalysts which will allow for the effect of Re loading to be probed sufficiently.

Table 3.2. ICP-OES analysis of Re loading of various ReO_x-Pd/CeO_2 catalysts. [69]

Nominal Re Loading (wt%)	**Actual Loading (wt%)**	**Error (wt%)**
2	1.528	0.106
3	2.508	0.168
4	3.304	0.144

Hydrogen TPR was conducted on a Micrometrics AutoChem II Chemisorption Analyzer that used a moisture removal step. The moisture removal was conducted by ramping from room temperature to 120 °C in a He atmosphere using a ramping rate of 10 °C/min. When the temperature reached 120 °C, it was then held isothermally for 1 hour. After the isothermal hold, the sample was cooled to 40 °C at a rate of 10 °C/min. Once the temperature was stabilized at 40 °C, the gas environment was then switched to a 10% H_2 in Ar mixture and held for 30 minutes. After the 30 minutes the TPR experimentation was started by ramping from 40 °C to 800 °C at a rate of 5 °C/min with the detector recording a data point every second (one point per every 0.083 °C). After the program was completed the gas flow was switched to He to purge the H_2 mixture and the tube and furnace were cooled to 25 °C at a rate of 20 °C/min. The TPR profiles for the ReO_x-Pd/CeO_2 catalysts are shown in Figure 3.4. The 2 and 3 wt% catalysts showed two distinct reduction peaks in the TPR patterns, with the 3 wt% catalyst used in the AHERY design having the lowest reduction temperatures of the catalysts evaluated. The 4wt% catalysts have broader reduction peaks in the TPR spectra which are at slightly higher temperatures relative to the

distinct reduction peaks seen in the 2 wt% catalysts. In all of the catalysts, two distinct reduction events are seen, which are attributed to the partial reduction of the ReO_x species [38].

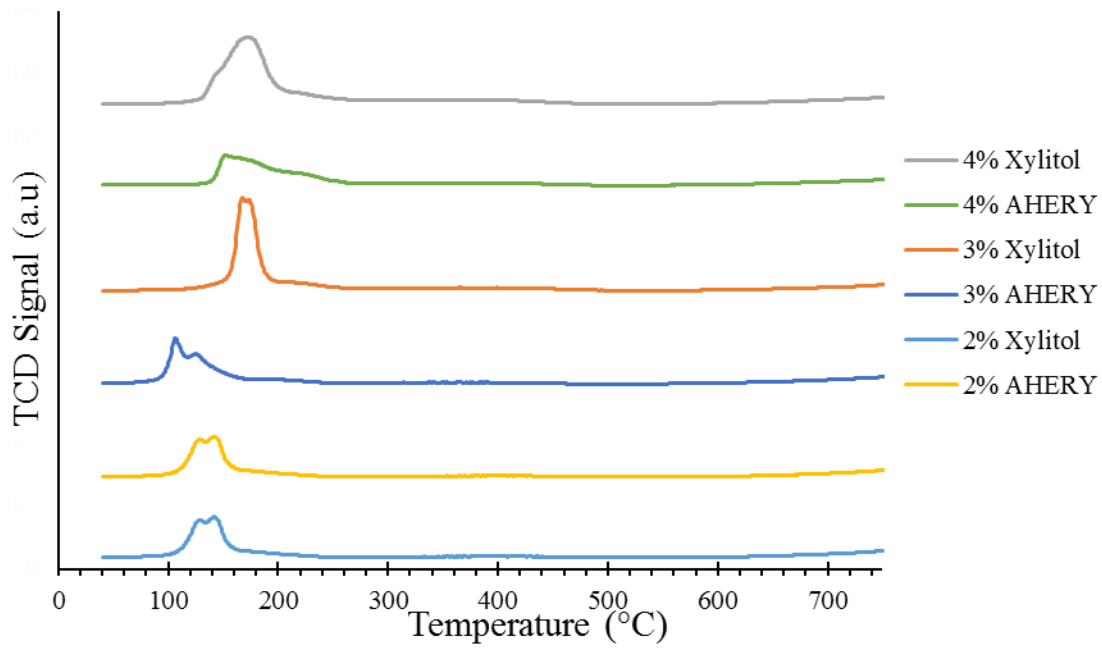

Figure 3.4. Temperature program reduction profiles of ReO_x-Pd/CeO_2 catalysts used in the design of experiments for AHERY and xylitol S-HDO. [69]

3.1.5 DESIGN OF EXPERIMENTS

To investigate the effects of temperature, pressure and catalyst loading on the yield of the AHERY S-HDO and to elucidate the optimum settings for the reaction, a design of experiments was conducted. An L9 Taguchi design was selected due to its ability to drastically reduce the number of necessary experiments while being able to probe a large design space. A Taguchi design is a type of statistical design of experiment that aims to maximize a certain response based on the input variables it is given. For this work we used

the input variables of temperature, pressure, and Re loading to try and maximize the yield of the S-HDO reactions. Each input variable utilized three evenly spaced levels to ensure the design was valid. Based on the number of input variables and the number of levels tested the Taguchi design will elucidate how many experimental runs are necessary. A major benefit of a Taguchi design is that it drastically reduces the necessary experimental runs and associated costs [132]. The Taguchi design reduces the experimental runs due to the utilization of orthogonal arrays. Since the design utilizes orthogonal arrays, one of the potential drawbacks of a Taguchi design is that it gives only linear correlations for the various factors. However, the linear model equations fit our data quite well.

To determine the various ranges of temperature, pressure and catalyst loading to evaluate, factor screening and literature evaluation were conducted. For temperature a large range was desirable since the goal was to try and evaluate milder reaction conditions and lowering reaction temperature as much as possible could substantially improve the economics of the reaction. However, the reduction in heating cost could cause the reaction rate to lower substantially due to classic/Arrhenius kinetics. Thus an 80 °C range was chosen since the literature had only evaluated a 20 °C range between 140-160 °C [38], [45]. For pressure the reactions were previously evaluated at 80 bar H_2. We chose to reduce the pressure up to a factor of 2 down to 40 bar H_2 to evaluate if pressure had a significant impact on conversion or selectivity over a large range. In the literature a volcano plot was previously reported for the Re weight loading vs S-HDO conversion and selectivity. From the volcano plot the 2 wt% point was determined to be optimal, but there were large gaps between the 2 wt% point and its next lower and higher points which were 0.5 and 4 wt% respectively. To investigate the gaps between 0.5 and 4 wt%, several screening experiments

were conducted. Reaction were conducted at 180 °C and 80 bar H_2 for 4h for a 1, 2, and 3 wt% Re ReO_x-Pd/CeO_2 (0.15, 0.30, 0.45 wt% Pd respectively) catalyst to determine which point was optimal. The AHERY S-HDO conversion and selectivity for the 1, 2, and 3wt% catalysts are shown in Table 3.3.

Table 3.3. Re loading parameter screening at 180 °C and 80 bar H_2 for 4 h.

Catalyst Loading Re wt%	Conversion %	THF Selectivity %
3	100	97.2
2	56.1	96.2
1	35.6	94.7

The 3 wt% catalyst significantly outperformed the other catalysts in terms of S-HDO conversion. To ensure that this effect was seen at other reaction temperatures, and to test if a higher loading was optimal, reactions for a 2, 3 and 4wt% catalyst were conducted at 140 C and 80 bar H2 for 4h. The results of these reactions are shown in Figure 3.5.

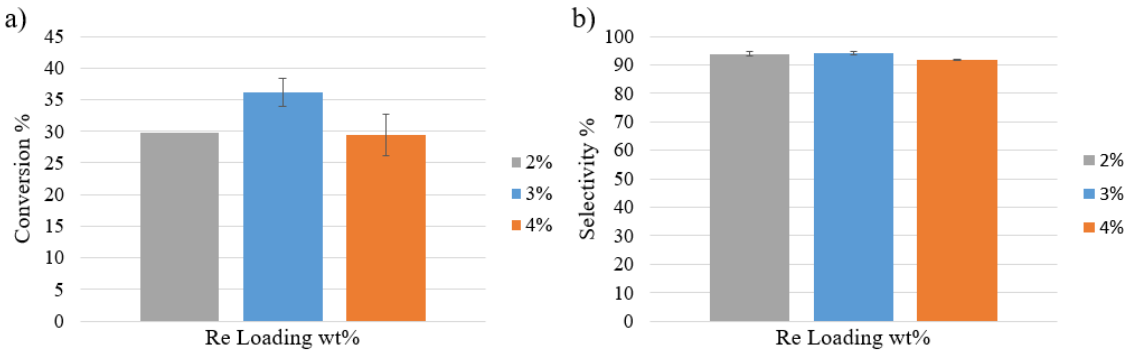

Figure 3.5. Re weight loading screening of AHERY S-HDO at 140 °C and 80 bar H_2 for 4 h. a) S-HDO conversion b) S-HDO selectivity to tetrahydrofuran (THF)

The error of the experimental runs was calculated based off of 2 experimental runs for each weight loading point. The standard error of conversion was determined to be 2.22 and 3.31% for the 3 and 4 wt% points respectively. The 3 wt% catalyst was still found to be the most active catalyst within the parameter range evaluated, while the selectivity's of the catalysts were largely comparable. Thus we made the 3 wt% catalyst the midpoint of

the experimental design since we found it to the optimal in our screening studies. After the literature and experimental screening, The L9 Taguchi design that contains three levels and three factors, was constructed to probe temperatures of 100, 140, and 180°C, pressures of 40, 60, and 80bar H_2, and Re loadings of 2, 3, and 4wt%. The full design layout can be seen in Table 3.4.

Table 3.4. L9 Taguchi design of experiments used for AHERY S-HDO

Run #	**Pressure (bar)**	**Temperature (°C)**	**Re wt% Loading**
1	40	100	2
2	40	140	3
3	40	180	4
4	60	100	3
5	60	140	4
6	60	180	2
7	80	100	4
8	80	140	2
9	80	180	3

From the results of the AHERY S-HDO Taguchi design and various pressure sweeps, a similar 3 factor 3 level Taguchi design was constructed and evaluated for xylitol S-HDO. The design tested temperatures of 140, 160, and 180°C, pressures of 5, 7.5, and 10bar H_2, and Re loadings of 2, 3, and 4wt%. The full L9 Taguchi design layout can be is shown in Table 3.5.

Table 3.5. L9 Taguchi design of experiments used for xylitol S-HDO

Run #	**Pressure (bar)**	**Temperature (°C)**	**Re wt% Loading**
1	5	140	2
2	5	160	3
3	5	180	4
4	7.5	140	3
5	7.5	160	4
6	7.5	180	2
7	10	140	4
8	10	160	2
9	10	180	3

3.1.6 REACTOR SETUP

For the chemical reactions conducted, a homebuilt 150 ml stainless steel high-pressure batch reactor was utilized, as previously described in this dissertation. The 150 ml reactor was machined from 316 SS and with a base that had a 2” diameter drilled out of a 3” diameter rod, leaving a 0.5” wall and bottom. Six holes were tapped in the top of the vessel for a bolted closure, and a groove was made for proper placement of an O-ring, to ensure the sealing of the reactor. The lid assembly was designed to permit both liquid and gas sampling through respective valves with stems going into different depths of the reactor accordingly. The gas and liquid sampling valves allow for the various phases to be sampled during the reaction without the need to cool down or depressurize the reactor. The sampling valves allowed for time on stream measurements as opposed to just initial and final measurements. The lid assembly was machined from a 0.5” thick 316 SS disk having a 4” diameter, and the disk was tapped with 0.25” National Pipe Tapered (NPT) fittings. A pressure gauge was connected to one of the NPT taps to monitor the pressure within the reactor over the course of the reaction. The other connections were made using bore through adapters with 0.25” male NPT and 0.125” male tube fittings. The various

connections include a gas sampling/venting tube, liquid sampling tube, gas inlet valve, and thermocouple well. The reactor was placed in an oil bath for heating coupled with a PID controller to maintain temperature throughout the reaction. The internal reaction temperature is monitored with a K-type thermocouple that is inserted in the thermocouple well. The internal temperature of the reactor was used as the reaction temperature since it best reflected the temperature within the reaction solution. A stir plate and 1.5" magnetic stir bar within the reactor were used for mixing. The reactor was pressure tested up to 100 bar and temperatures in excess of 180 °C. The gas sampling tube is equipped with a check valve to prevent air from entering the reactor after it has been purged. As a safety measure, a spring actuated pressure release valve was attached to the gas inlet. The spring was adjusted based on the desired reaction pressure to ensure that if the reaction or inlet gas over pressurized the reactor, that the system would vent.

3.1.7 REACTOR MASS TRANSFER EVALUATION

To validate our homebuilt reactor and ensure that the stirring method utilized was not mass transfer limited, a model reaction was chosen for validation. The model reaction selected was the hydrogenation of 2-Methyl-3-butyn-2-ol (MBY) using a Lindlar catalyst, since it is a well-studied and modeled reaction in literature [148]–[150]. The MBY is hydrogenated to 2-methyl-3-buten-2-ol (MBE), which is further hydrogenated to 2-methyl-2-butanol (MBA), as shown in Figure 3.6.

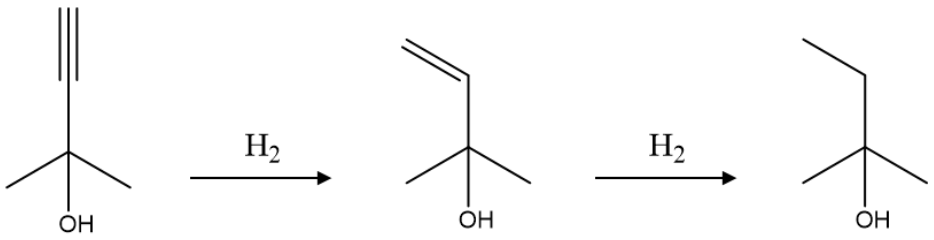

Figure 3.6 Reaction schematic of the hydrogenation of MBY to MBE and MBA.

To evaluate external mass transfer, stirring rates ranging from 250-800 RPM were evaluated under 9 bar_g H_2 at 333 K for comparison to the rate constants, product profiles, and models proposed in the literature [148]. The study used as a benchmark for comparison utilized a gas entrainment impeller for mixing and gas introduction. Our reactor setup utilizes a simplistic magnetic stir bar for mixing and a gas inlet stream for the introduction of gas into the reactor, relying on diffusion of the gas through the liquid phase. In each reaction, the ratio of catalyst to liquid reactant was kept constant at 0.175 wt% as reported in literature, where a rate of 5.8×10^{-2} mol/L/min was measured. For our reactor, following the procedure reported in literature, the average reaction rate obtained was $5.8\times10^{-2} \pm 0.002$ mol/L/min, which is consistent with the previously reported values. The reaction rates as a function of stirring rate are shown in Figure 3.7. For stir rates of 700 RPM and above, only 30% of the reactions were successful due to the stir bar losing the magnetic coupling with the stir plate. Thus, stirring rates above 700 RPM were not considered for reactions going forward. For stir rates of 250-450 RPM the reaction rate was lower than the previously reported reaction rate, indicating that external mass transfer limitations were present in this stirring regime. The reactions conducted between 550 and 750 RPM exhibited a plateau in reaction rate indicating that there were no mass transfer limitations in this region [151]. Thus the optimal range to conduct reactions in our reactor is between

550 and 650 RPM since the reaction rate stabilized at its maximum, and the stir bar did not lose its coupling within this range. For reactions in future discussion throughout this dissertation, a stir rate of 550 RPM was utilized since it was a point that was directly evaluated and confirmed to not have associated mass transfer limitations.

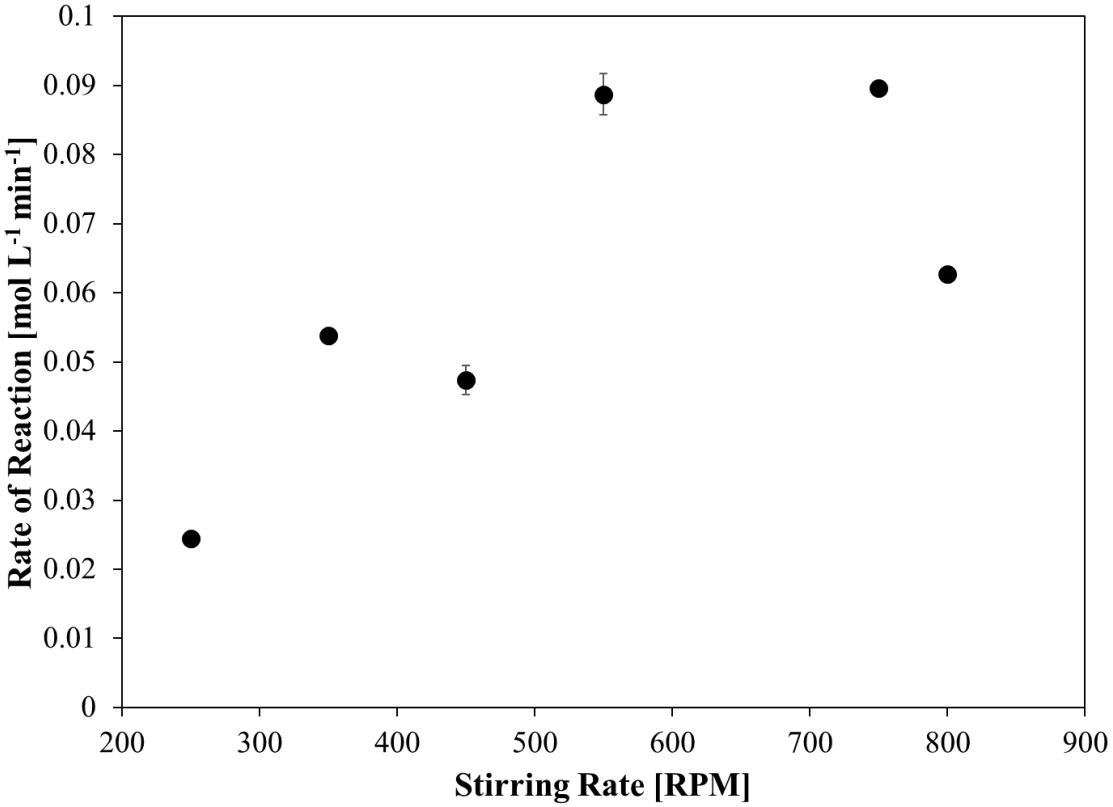

Figure 3.7. Reaction rate as a function of stirring rate for the hydrogenation of MBY.

The reaction profiles for the hydrogenation of MBY to MBE and MBA are shown in Figure 3.8, along with the model for reaction concentration from the literature [148]. The experimental results that were obtained were consistent with the model results from literature, further indicating that the homebuilt reactor can reproduce literature results and is absent of mass transfer limitations at the evaluated conditions. From the reactor evaluation study using the MBY hydrogenation as a model reaction, it can be concluded

that the reproducibility of the reaction rates, and concentration profiles were consistent with previously reported literature, validating that our reactor is not controlled by external mass transfer limitations for stir rates of 550 RPM and above.

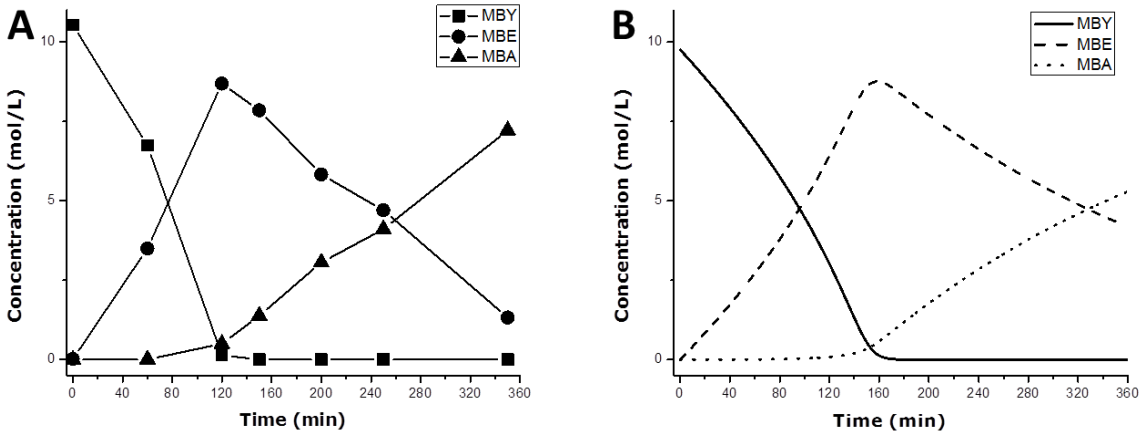

Figure 3.8. Mass transfer evaluation of the homebuilt reactor via the hydrogenation of MBY. A: MBY hydrogenation reaction profile with stir rate of 550 RPM. B: Model results from literature [148] using P=9 bar gauge, T=333K, and catalyst to reactant ratio=0.175 wt%. [69]

3.1.8 ACTIVITY MEASUREMENTS

AHERY S-HDO was used as a model reaction for sugar alcohol S-HDO since it has two vicinal cis hydroxyl groups. The removal of a singular hydroxyl group rather than both groups or a DODH occurring instead of an S-HDO can be easily monitored, calibrated and accounted for. The hydrogen was added initially at room temperature based on the ideal gas law to the reactant, solvent and catalyst mixture, which was then heated to the desired temperature. The reaction time was started once the reactor reached the desired temperature. Each reaction contained 50 ml of 1,4-dioxane (solvent), 3.15 ml (4 g) of AHERY, and 0.60 g of ReO_x-Pd/CeO_2 catalyst. The ratio of catalyst to reactant previously reported in literature to be optimal of 1g AHERY : 0.15 g ReO_x-Pd/CeO_2 catalyst was

utilized in this work [38]. Liquid samples were taken at the initial and final points of the reaction for evaluation. Taking only two samples allowed for the maximum amount of hydrogen pressure to be kept within the reactor and allow for the reaction to stay as close to reaction pressure as possible. The reaction samples were diluted in methanol to $\frac{125}{3}$ their original volume and analyzed in a Shimadzu GC-2010 Plus. The GC utilized an FID detector, an RTX-1701 column (column length of 30 m, an inner diameter of 0.32 mm, and a film thickness of 1.00 μm**)**, and an AOC-5000 auto-injector. The GC was calibrated for AHERY and THF to determine the concentrations of each respectively in each sample. The 11 point calibrations were made using external standards ranging from 84-1348 ppm and 132-2105ppm for AHERY and THF respectively. For the AHERY S-HDO, conversion is based on the final and initial concentrations of AHERY. The selectivity to THF was calculated based on moles of THF produced with respect to the total moles of products produced. The only other product that was observed in the GC analysis was trans-AHERY. The yield of the AHERY S-HDO was calculated by taking the product of the AHERY conversion and the THF selectivity.

For the Xylitol S-HDO reactions, the reactor was filled with the reaction mixture (solvent, xylitol, and catalyst) and heated to the desired temperature. After the desired temperature was reached, constant hydrogen pressure was introduced and maintained within the reactor. Each reaction contained 50 ml of 1,4-dioxane (solvent), 2 g of xylitol, and 0.60 g of ReO_x-Pd/CeO_2 catalyst, again following literature [45]. Liquid samples were taken at the initial, mid, and final points of the reaction to monitor the reaction as a function of time. The samples were again diluted to $\frac{\mathbf{125}}{\mathbf{3}}$ their original volume and analyzed by GC and avoid saturating the FID detector. The GC was calibrated for xylitol, 1,2-

dideoxypentitol, 1,2,5-pentanetriol, 3-pentanol, 1-pentanol, and 1,2-pentanediol to monitor the possible products over the reaction by making an 8-point calibration curve using external standards. The external standards ranged from 82-17,240 ppm for the various calibrations. Xylitol S-HDO conversion was calculated based on the concentration of the products formed and their theoretical maximums. The selectivity of 1,2-dideoxypentitol and 1,2,5-pentanetriol (1 S-HDO products) was calculated based on the moles of the 1 S-HDO products produced with respect to the total moles of all products formed. The yield of the 1 S-HDO products was calculated by taking the product of the xylitol conversion and the 1 S-HDO selectivity.

Both the AHERY and xylitol reaction samples were analyzed using the same GC methodologies, with the only difference being the respective concentration curves. For each sample that was analyzed in the GC, 1 μL of the GC sample was collected by the injection needle and was then injected into the system for evaluation. The injection port was set to 250 °C and utilized a split injection mode. A split ratio of 1:10 with a column flow of 2.5 mL/min, a purge flow of 3 mL/min, and a total flow of 30.5 mL/min were used, with He as the carrier gas. The column pressure was set to 77.0 kPa and the linear velocity in the column was 38.9 cm/s. The FID was set to 260 °C, with a sampling rate of 40 ms. The FID utilized a makeup flow of 30.0 mL/min, a hydrogen flow of 40.0 mL/min, and an air flow of 400 mL/min. Post injection, the auto sampler was programmed to wash the injection needle in acetone and methanol to clear any contaminants from the needle and prepare it for the next injection. The GC oven was programmed to increase the separation of the various products for analysis. The program first utilized a 3 min isothermal hold at 40 °C. Following the hold, the oven was heated by 10 °C/min to 260 °C. Once 260 °C was

maintained an isothermal hold was conducted for 20 min. Once the hold was completed, the detector stopped recording and the oven was cooled to 40 °C in preparation of the next sample.

3.2 RESULTS AND DISCUSSION

3.2.1 AHERY S-HDO TAGUCHI DESIGN

The reactions of the L9 Taguchi design for the AHERY S-HDO were con ducted in a random order to help reduce bias in the experimental runs. The results from each experimental run of the Taguchi design are shown in Table 3.6.

Table 3.6. AHERY model reaction DOE results. [69]

Pressure (bar)	**Temperature (°C)**	**Re wt% Loading**	**Conversion %**	**THF Selectivity %**
40	100	2	14.5	75.0
40	140	3	30.7	95.5
40	180	4	99.9	99.7
60	100	3	3.93	99.9
60	140	4	21.3	99.9
60	180	2	99.9	98.0
80	100	4	3.63	99.9
80	140	2	21.7	99.9
80	180	3	75.0	99.9

To ensure the results were reproducible, a center point of the design with the conditions of 60 bar H_2, 140 °C, and a 4 wt% Re catalyst was repeated in triplicate. As shown in Table 3.7, the standard errors between runs were 0.97 % and 0.20 % for conversion and selectivity, respectively. The standard errors for conversion, selectivity, and yield were calculated using the following formula $SE = \frac{\sigma}{\sqrt{n}}$, where SE is standard error, σ is the standard deviation of the three experimental data points and n is the population size which was 3 in these cases.

Table 3.7. AHERY reproducibility results conducted at 60 bar H_2, 140 °C, and a 4 wt% ReO_x-Pd/CeO_2 catalyst.

Experimental run	Conversion	Selectivity	Yield
1	0.213	0.999	0.213
2	0.205	0.999	0.215
3	0.237	0.993	0.236
Standard Error	0.010	0.002	0.009

The main effects plot shows how the factors in the design affect the desired responses. The strength of the affect shows how significant the factors are. The larger the slope of the line the more statistically significant the factor. Temperature is the most significant factor in this process and has the strongest effect on the yield of the reaction, according to its slope shown in Figure 3.9. This effect is understandable due to the direct relationship expected between temperature and reaction rate from Arrhenius kinetics. Catalyst loading was determined to be mildly significant over the space tested. Catalyst loading had a very small relative effect on the reaction in comparison to temperature. However, the pressure of the reaction was statistically insignificant, since there was no obvious correlation between the data points and the slope of the lines were very small. The lack of dependence on pressure suggests that we have a zero order relation on hydrogen pressure for this reaction. Zero order or near zero order relations with hydrogen pressure have been reported in the literature for various HDO reactions [38], [152]. Thus, some part of the deoxydehydration step of this reaction is likely the rate-limiting step since the decrease in hydrogen concentration does not affect the activity. The deoxydehydration of AHERY produces 2,5-dihydrofuran [153], which is not observed during our analysis. The Pd on the surface of the CeO_2 catalyzes hydrogen dissociation, and spillover on the CeO_2 which allows for the regeneration of the catalyst [154]. Thus, the surface of the catalyst

may be saturated with hydrogen and the hydrogenation step proceeds as soon as the deoxydehydration step is completed, as suggested by a previously proposed mechanism [45].

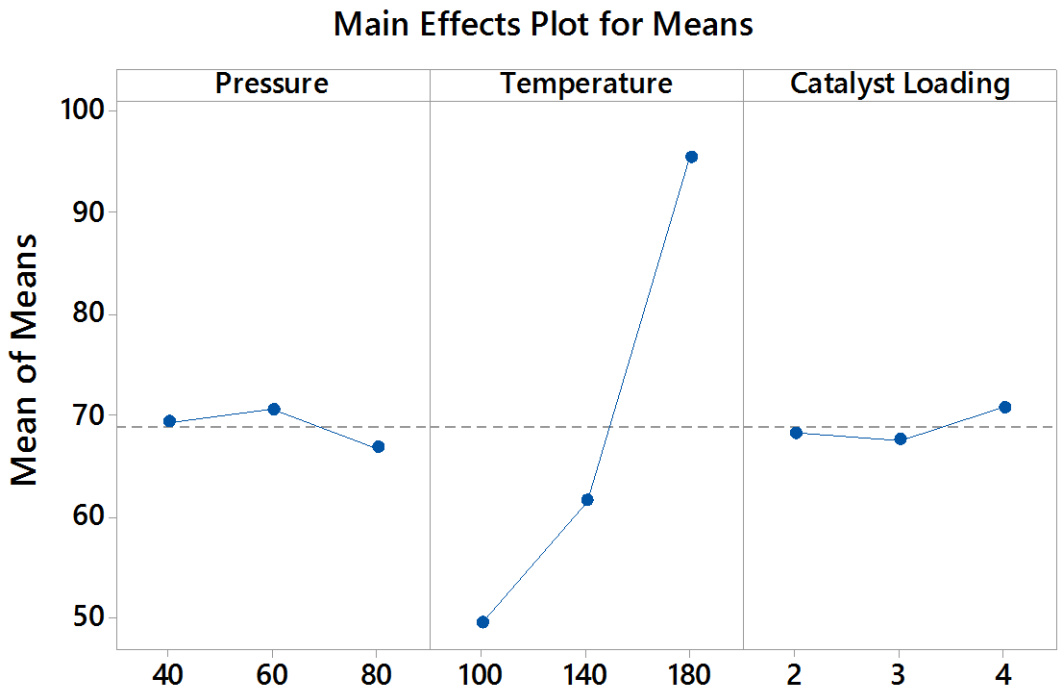

Figure 3.9. Correlation between design factors and responses resulting from L9 Taguchi design of experiments. [69]

Since the Taguchi design creates linear models, it is important to look at the proportionality of the factors and investigate if there are regions where certain conditions are more favorable. When looking at the yield of this reaction, the individual factors can affect conversion and selectivity differently. The varying proportionality can result in regions that are more favorable for higher yield. The proportionality of the various factors is shown in the various contours created by the regression of the Taguchi model shown in Figure 3.10. The temperature of the reaction is directly related to both conversion and selectivity. Thus temperature is directly related to the yield of the AHERY S-HDO reaction

and should be feasibly maximized to increase the yield of the reaction. The pressure was found to be inversely related to conversion, but directly related to selectivity.

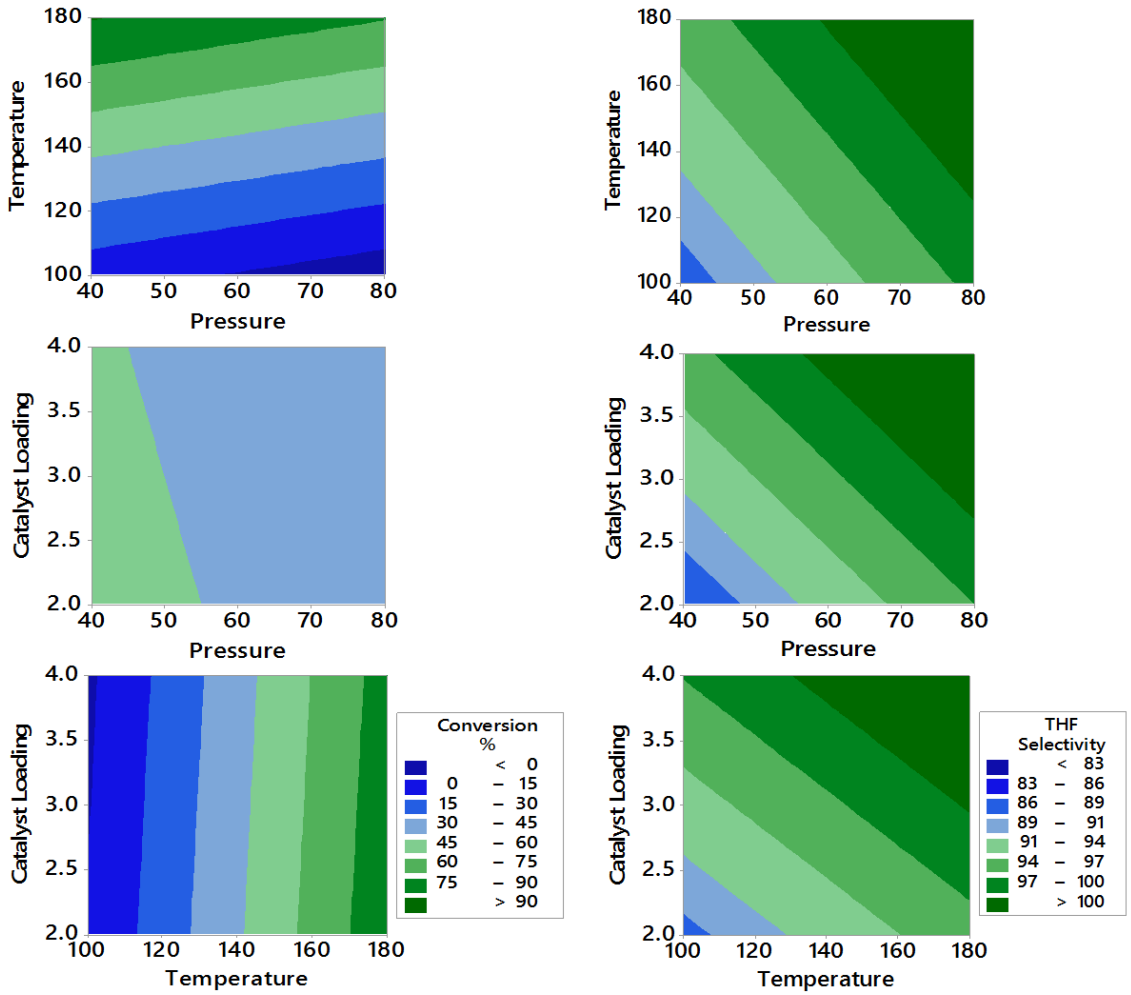

Figure 3.10. Taguchi model regression contours for conversion and selectivity for AHERY S-HDO. [69]

In order to see where the varying proportionality of pressure is most favorable, a yield contour over varying pressures was investigated using the Taguchi model equations. The model equations are shown in Table 3.8, in which conversion refers to the conversion of AHERY and selectivity refers to the selectivity to THF.

Table 3.8. L9 Taguchi design of experiments model equations for AHERY S-HDO

Model Equations
$Conversion = -\frac{78.2}{100} - \frac{0.374}{100} \times \mathrm{P} + \frac{1.054}{100} \times \mathrm{T} - \frac{1.89}{100} \times \mathrm{C}$
$Selectivity = \frac{55}{100} + \frac{.248}{100} \times P + \frac{.0944}{100} \times T + \frac{4.45}{100} \times C$
P is pressure in bar, T is temperature in °C and C is catalyst weight loading in wt%

The Taguchi model equations were used to create a 3D yield contour by fixing catalyst loading at the midpoint of 3 wt% Re to reduce the dimensionality of the design space so that it could be visualized. Catalyst loading was chosen as the dimension to reduce since it was found to have small impact on the yield, and the goal of the design was to find milder reaction conditions. The center point of catalyst loading, 3wt% was chosen to ensure the model equations would not be skewed. The resulting 3D yield contour over the experimental design space is shown in Figure 3.11. Reducing the pressure to 40 bar from 80 bar slightly improves the yield of the reaction. The pressure effects on conversion and selectivity seem to be negligible in the higher temperature region of our design but can become somewhat significant at lower temperatures. This adds further support to the reduction of pressure having negligible effects on the yield of AHERY S-HDO. However, the smaller change in yield at the higher temperature region is likely due to the reaction kinetics. The model equations suggest that pressure has an inverse relation with conversion but direct relation with selectivity. However, the conversion equation is largely controlled by the temperature term which has a constant and a design value which are both an order of magnitude large than the pressure terms. This gives further supports the main effects

plot in establishing temperature as the most significant factor in the constructed design space. From the Taguchi model equations, and the resulting 3D yield contour, the optimal reaction conditions within the design space for AHERY S-HDO was determined to be 40 bar and 180 °C. This finding is significant due to the fact that hydrogen pressure can be reduced by a factor of 2 and lead to higher yields.

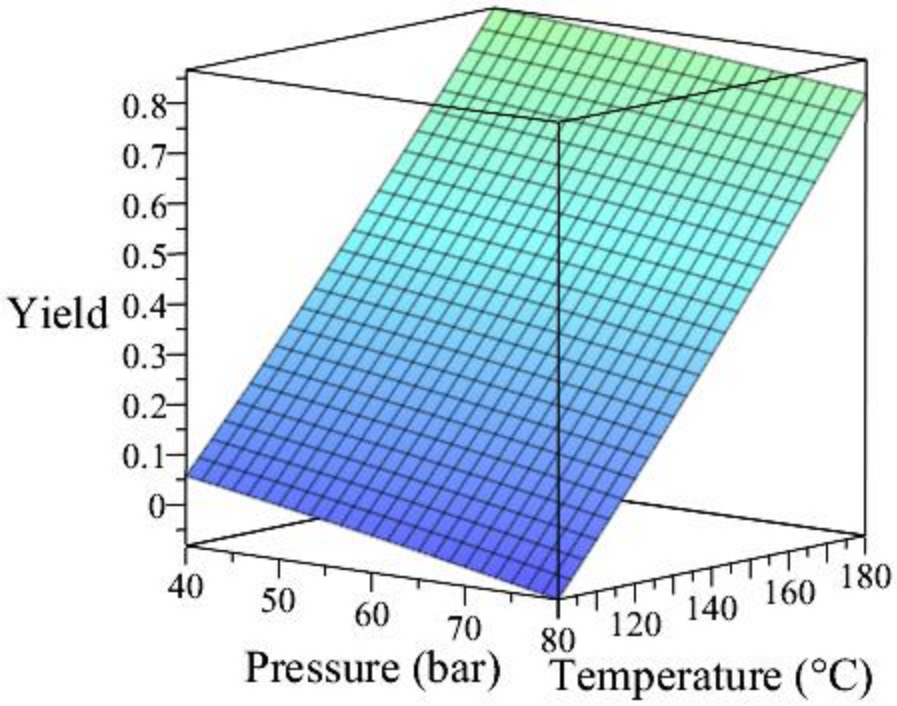

Figure 3.11. 3D yield contour for the S-HDO of AHERY using a 3wt% ReO_x-Pd/CeO_2 catalyst using the Taguchi model equations. [69]

Even though the yield contour results from linear model equations, it captures the general trends of the design space, as shown in Figure 3.12. The general trends over the design space are captured and there are no significant outliers present. The relatively close fitting of the data points further confirms the validity of the Taguchi model equations resulting from the AHERY S-HDO. This further supports the ability to drastically reduce the reaction pressure for this reaction while achieving comparable yields.

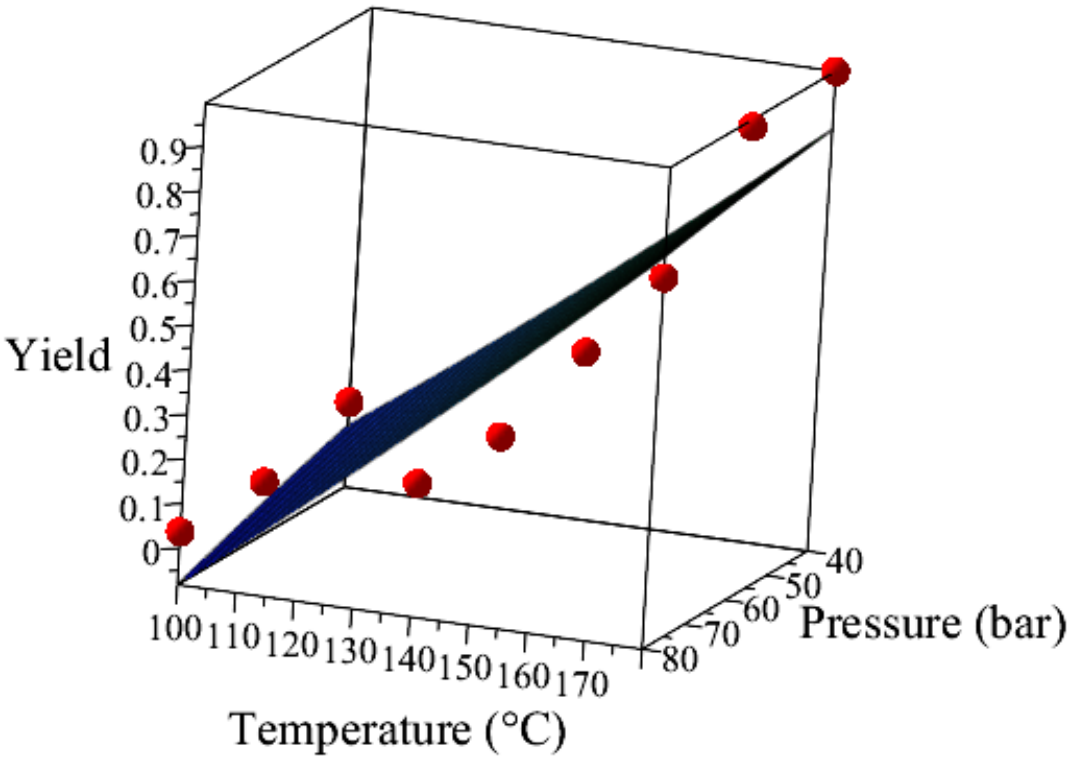

Figure 3.12. Yield contour overlaying the experimental data points from the AHERY Taguchi design. [69]

From the AHERY S-HDO L9 Taguchi design, it was demonstrated that milder reaction conditions for the S-HDO of AHERY are feasible with respect to pressure, and the ability to reduce pressure significantly without causing a decline in yield has been demonstrated. This reaction can serve as a model for other lignocellulosic biomass derived sugar alcohol S-HDO reactions and suggests that reducing the pressure might not have a significant effect on yield. Since the temperature has a significant effect on yield, it would be optimal to run S-HDO reactions at higher temperatures than previously reported, if feasible for the reactors being utilized. To see if these statements hold for another sugar alcohol, we performed a similar design of experiments for xylitol.

3.2.2 PRESSURE EFFECTS ON XYLITOL S-HDO

For the AHERY S-HDO, the pressure region above 40 bar was shown to have a zero-order dependence on S-HDO yield. Pressures of 40 bar and below were investigated for the xylitol S-HDO to investigate the threshold in which pressure starts to affect this reaction. Pressures of 40, 10, 7.5 and 5 bar H_2 were evaluated using a 4 wt% ReO_x-Pd/CeO_2 catalyst at 160 °C. For 10 bar and below, the pressure was a constant reaction pressure since the reactor gas inlet was left open so that the pressure would remain constant. The reactor was loaded with catalyst, solvent, and reactant and then brought to the desired reaction temperature before H_2 was introduced. This was possible since the flashback arrestor on the hydrogen regulator was rated to slightly over 10 bar, and pressuring of the reactor due to ideal gas law was not needed. The results from these reactions are shown in Table 3.9. The most significant change occurred within the 5-10 bar region. The calculated yield refers to the most valuable products 1,2-dideoxypentitol and 1,2,5-pentanetriol, which are formed through one S-HDO. The selectivity to 1,2-dideoxypentitol and 1,2,5-pentanetriol for the 40 bar and 10 bar reactions were the same within experimental error. However, the conversion for the 10 bar reactions were significantly higher thus resulting in a higher yield. Below 10 bar, there is a significant drop in activity for the xylitol S-HDO. The reactions at 7.5 bar and 5 bar had conversion fall by over a factor of 3, but the selectivity increased, which is in agreement with the AHERY Taguchi model equations. To further investigate this change in yield with respect to pressure, the L9 Taguchi design for the xylitol S-HDO included the factor of pressure with levels between 5 and 10bar H_2. By probing the range of pressures that varies both conversion and selectivity significantly, the design of experiment should be able to model the other factor interactions more accurately and the design space. This will also test if temperature is still as significant of a

factor at lower pressures, or if elevated temperature could increase the conversion at the milder pressure conditions to a level that is comparable and potentially more economically favorable for scaling.

Table 3.9. Pressure effects on the xylitol S-HDO conducted at 160 °C with a 4 wt% ReO_x-Pd/CeO_2 catalyst

H_2 Pressure	Conversion %	Selectivity %	Yield
40 bar	60.7	89.8	0.545
10 bar	74.1	89.3	0.662
10 bar	74.9	85.5	0.640
7.5 bar	20.8	95.8	0.199
5 bar	12.5	99.9	0.125

3.2.3 XYLITOL S-HDO L9 TAGUCHI DESIGN

The results from each experimental run of the Taguchi design for xylitol S-HDO are shown in Table 3.10.

Table 3.10. Xylitol reaction DOE results. [69]

Pressure (bar)	Temperature (°C)	Re wt% Loading	Conversion %	1 S-HDO Selectivity %
5	140	2	26.5	99.9
5	160	3	25.8	99.9
5	180	4	0	0
7.5	140	3	33.9	99.9
7.5	160	4	39.7	68.2
7.5	180	2	33.0	99.9
10	140	4	56.6	88.3
10	160	2	56.3	93.7
10	180	3	32.1	99.9

To ensure the results were reproducible, a center point of the design with conditions of 7.5 bar H_2, 140 °C, and a 3 wt% Re catalyst was repeated in triplicate to determine the standard error of the reactions. As shown in Table 3.11, the standard errors between the

runs were 4.71 % and 1.77 % for xylitol conversion and selectivity to the one S-HDO products (1,2-dideoxypentitol, and 1,2,5-pentanetriol), respectively. The yield of one S-HDO products for the reactions had a standard error of 3.86 %. The standard errors were calculated as previously described in the AHERY design. The standard errors for the xylitol S-HDO were significantly higher than for the AHERY S-HDO reaction. However, the reactions went to higher conversions and there were more possible products that could be produced in the reaction, leading to more possible variability in the results. The selectivity error was low, while the conversion error was more significant due to a likely outlier in the third experimental run.

Table 3.11. Xylitol reproducibility results conducted at 7.5 bar H_2, 140 °C, and a 3 wt% ReO_x-Pd/CeO_2 catalyst. [69]

Experimental run	Conversion %	Selectivity %	Yield
1	33.9	99.9	0.339
2	34.8	99.9	0.348
3	48.5	94.7	0.459
Standard Error	4.71	1.77	0.039

The main effect plots for the conversion of xylitol and the selectivity to the products which have undergone one S-HDO, are shown in Figure 3.13. For both conversion and selectivity, pressure exhibits a direct relation. However, both temperature and catalyst loading have inverse relations with conversion and selectivity within the design space. Although the relations agree, the scale of the relations are different. The factors affect selectivity significantly more than they affect conversion. The relations of the factors for the xylitol design vary from the model AHERY design. The most significant difference is in the relation of temperature. Not only is temperature suggested to be inversely related,

but it is no longer the most significant factor, as it was in the AHERY design. This effect is not expected since from a kinetics standpoint we would expect temperature to be directly related to conversion and to have a strong correlation with conversion as shown in the AHERY design. However, the design equations could be picking up on a potential limitation by the hydrogen pressure in which the surface may no longer be fully saturated with hydrogen which could limit the reduction of the ReO_x, which has been suggested to be a crucial step in the proposed S-HDO reaction mechanisms [38], [62]. The inability for the ReO_x to reduce could explain why pressure is the most significant factor, and why temperature isn't as significant in the design space probed. It is also important to note that the range of temperature probed for the xylitol design was 40 °C smaller than the AHERY design. For xylitol S-HDO, a stronger effect of catalyst loading on conversion and selectivity was exhibited. The selectivity of the reaction was significantly dependent on the Re loading of the catalyst, as where the conversion was only slightly effected. This could be due to the presence of different ReO_x sites in the higher loading catalyst or the ReO_x forming more oligomeric species rather than the monomeric ReO_x species which have been proposed to be the active sites for the reaction. The 2 wt% ReO_x-Pd/CeO_2 catalyst was superior to the 3 and 4 wt% catalysts in terms of both conversion and selectivity in the xylitol S-HDO.

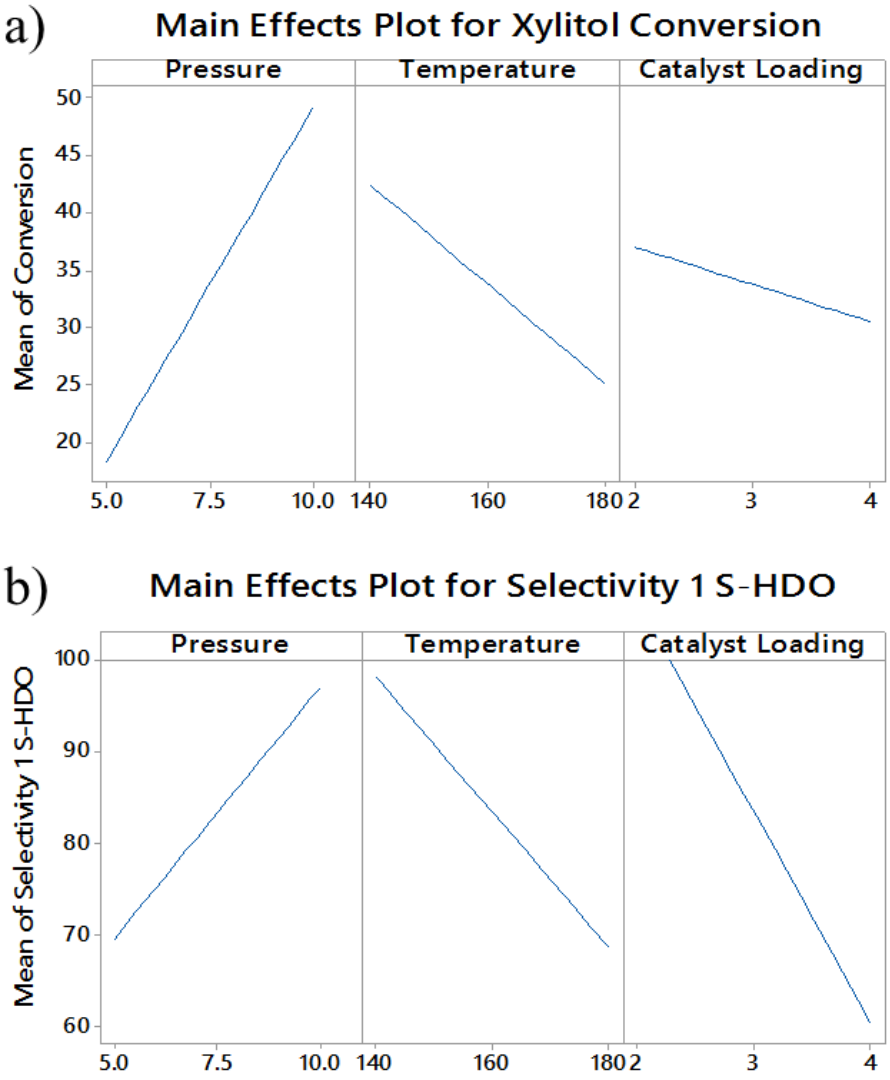

Figure 3.13. Correlation between design factors and responses resulting from the xylitol L9 Taguchi design of experiments. a) Conversion correlations b) Selectivity to 1,2-dideoxypentitol and 1,2,5-pentanetriol correlations.

In the conversion and selectivity contour plots for the xylitol S-HDO, shown in Figure 3.14, it is further displayed that the relations of the various factors follow the same proportionality as suggested in the main effects plots.

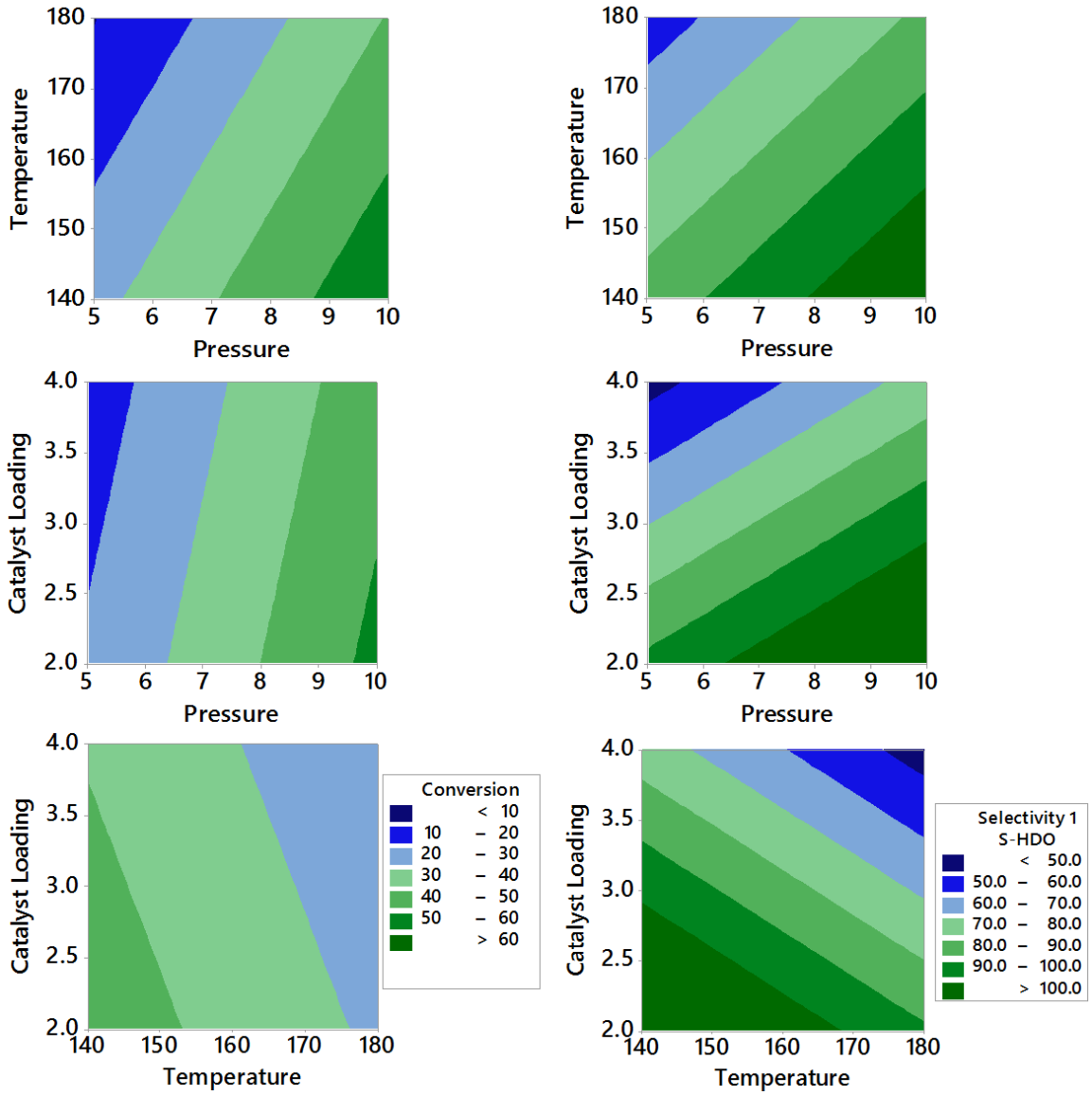

Figure 3.14. Taguchi model regression contours for the conversion and selectivity for xylitol S-HDO. [69]

In order to visually see how the factors, affect the yield of the xylitol S-HDO, a 3D yield contour plot was constructed, as shown in Figure 3.15. The 3D yield contour was constructed using the Taguchi model equations which are shown in Table 3.12. The 3D yield contour was constructed by reducing a dimension, as previously mentioned for the AHERY S-HDO contour. Catalyst loading was the dimension reduced, and the center point of 3 wt% was chosen so that reaction conditions could be evaluated. The model equations

suggest that pressure has a relatively similar effect on both conversion and selectivity. The catalyst loading affects the selectivity of the reaction an order of magnitude more than it affects the conversion of the reaction. The slight inverse relationship between temperature and conversion should be investigated further to see if there is truly an inverse relationship, or if there is something more complex occurring that the robust model cannot accurately model.

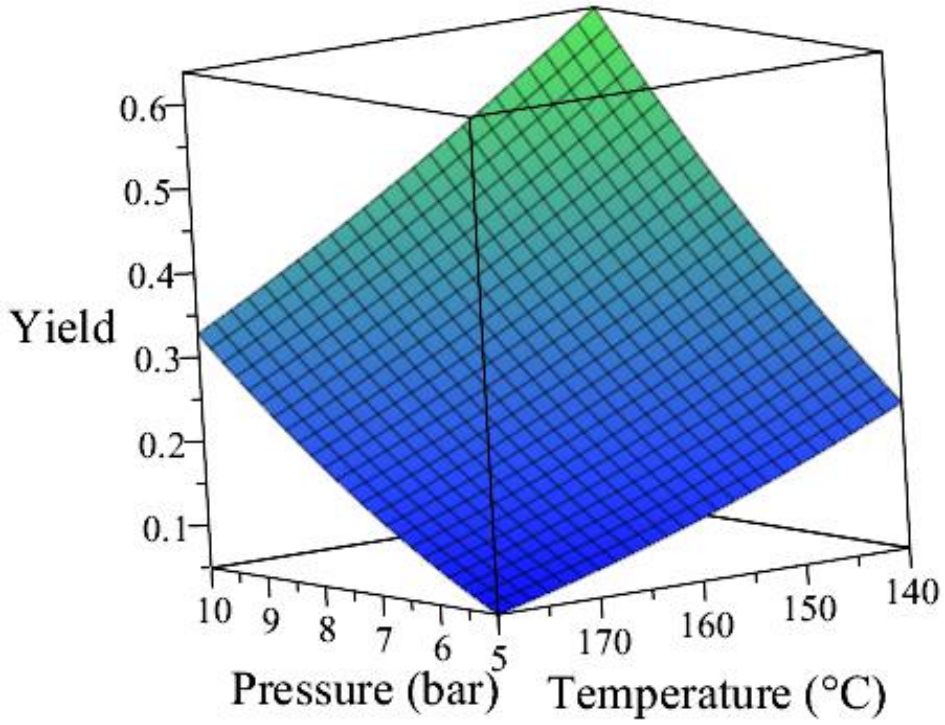

Figure 3.15. 3D yield contour for the S-HDO of xylitol via a 3wt% ReO_x-Pd/CeO_2 catalyst using the Taguchi model equations. [69]

The yield contour suggests that the optimal reaction conditions for the xylitol S-HDO are 140 °C and 10 bar within the design space tested. These optimal conditions are significantly milder then the previously reported literature conditions of 160 °C and 80 bar [45]. These milder reaction conditions would allow for the pressure to be reduced by a

factor of 8 and the temperature to be reduced by 20 °C. This could allow for significant savings in terms of heating costs and gas compression if the reaction was to be scaled.

Table 3.12. L9 Taguchi design of experiments model equations for xylitol S-HDO.

Model Equations
$Conversion = \frac{33}{50} + \frac{6.17}{100} \times P - \frac{.434}{100} \times T - \frac{3.25}{100} \times C$
$Selectivity = \frac{228.7}{100} + \frac{5.46}{100} \times P - \frac{.735}{100} \times T - \frac{22.9}{100} \times C$
P is pressure in bar, T is temperature in °C and C is catalyst weight loading in wt%

The yield contour was overlaid with the experimental data points, as shown in Figure 3.16 to visually illustrate how the model equations fit the data. The Taguchi model equations fit the experimental points well for a linear model but do not completely capture the trends in the studied parameter space. The contour shown in not the exact fit of the data since catalyst loading is also significant and was fixed at the mid-point for graphing. However, the general trends still stand and the simplistic Taguchi design was able to capture the design space utilizing only nine experimental runs. However, one of the drawbacks of a Taguchi design is that it will not capture higher order interactions between factors, which might lead to the observed difference between the model and the experimental data points [155], [156]. In the region probed, pressure could have a nonlinear relation with the responses since the hydrogen could be causing mass transfer limitations within the reaction. The mass transfer effects on the xylitol S-HDO reaction in terms of

both xylitol and hydrogen concentration should be evaluated to investigate potential limitations further.

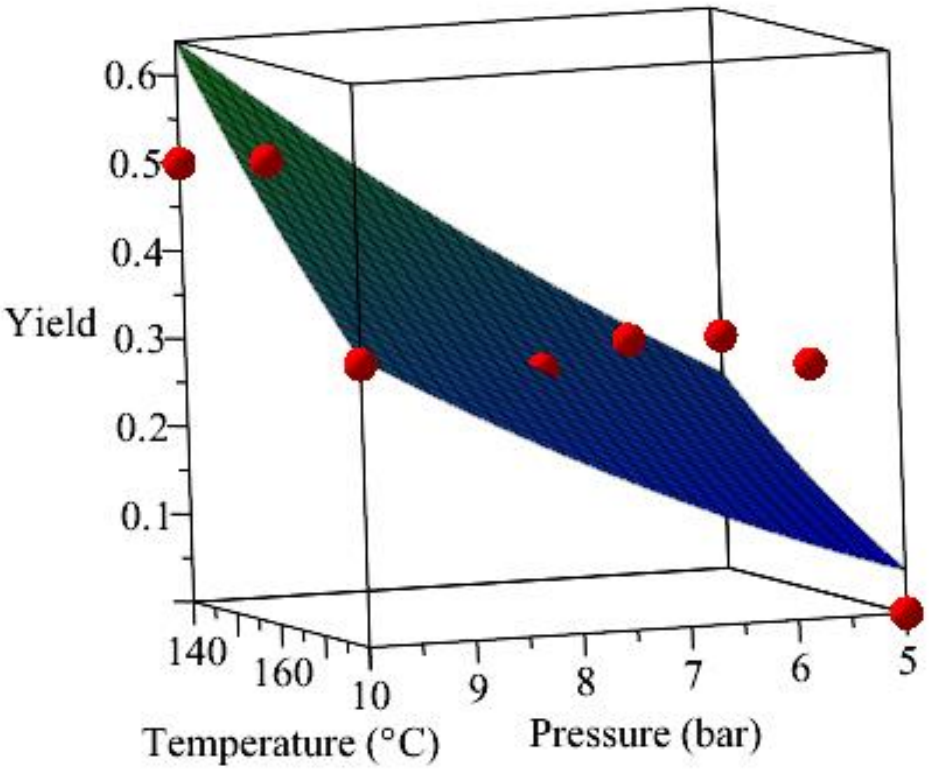

Figure 3.16. Yield contour overlaying the experimental data points from the xylitol Taguchi design. [69]

3.3 CONCLUSIONS

The investigation of milder reaction conditions for the S-HDO of AHERY using a Taguchi design of experiments elucidated that the reduction of pressure could be substantially reduced from 80 bar to 40 bar H_2 while maintaining a comparable yield of THF using a ReO_x-Pd/CeO_2 catalyst. Temperature was found to be the most significant factor for AHERY S-HDO in the design space probed. The negligible changes to the responses caused by pressure and catalyst loading showed that pressure and Re loading

could be utilized at their low points of the design to save on materials costs, and could be potentially reduced further outside of the design space tested if probed further in another study.

For the Xylitol S-HDO, yield was found to have a zero-order relation for pressures as low as 10bar based on a pressure sweep performed. This allowed for pressure to be reduced for the xylitol S-HDO from 80 bar to 10 bar H_2, a factor of 8 reduction, and allowed for the pressure to be constantly maintained in the reactor by keeping the system safely opened to the gas inlet. From the Taguchi design for xylitol S-HDO, the optimal conditions were found to be 140 °C and 10 bar H_2 within the design space, conditions that are substantially lower than those previously reported in literature [45]. These optimal and milder reaction conditions allow for 1,2-dideoxypentitol and 1,2,5-pentanetriol to be produced in a more economically feasible approach, allowing for the production of platform and value-added chemicals from a renewable feedstock. However, the inverse relationship between temperature and conversion that was suggested by the Taguchi design is not the expected relation according to Arrhenius kinetics. This relation should be further investigated to determine if it is truly an inverse relation, if temperature is not significant over the range evaluated, or if there is a more complex phenomena occurring that the robust Taguchi model couldn't not accurately model.

CHAPTER 4

KINETIC STUDY OF XYLITOL HYDRODEOXYGENATION

4.1 MOTIVATION AND EXPERIMENTAL

4.1.1 MOTIVATION

Lignocellulosic biomass is a promising renewable feedstock which can be utilized to produce various sugars from the various components of the biomass. These biomass derived sugar alcohols can be further upgraded to value-added chemicals or fuels via the removal of oxygen from the sugar [17], [133]–[135]. The Oxygen is largely in the form of hydroxyl groups on the sugar alcohols. Xylitol, which is a commonly used artificial sweetener is a promising sugar alcohol which contains 5 cis vicinal hydroxyl groups which can be removed for upgrading. Xylitol is derived from the hemicellulose portion of biomass and is produced through a multi-step process which converts the hemicellulose to xylan, which then goes through a hydrolysis to xylose, which is then fermented into xylitol [140], [141], [157], [158]. An effective way to remove hydroxyl groups from xylitol is simultaneous hydrodeoxygenation (S-HDO) [38], [69], [71], [147]. The S-HDO of xylitol, shown in Figure 4.1, produces 1,2-dideoxypentitol and 1,2,5-pentanetriol if one pair of vicinal hydroxyl groups is removed from either cleaving the C_1-C_2 or C_2-C_3 hydroxyl groups respectively. 1-pentanol can be produced from a subsequent S-HDO of either 1,2-dideoxypentitol or 1,2,5-pentanetriol. 3-pentanol can be formed if the C_2-C_3 hydroxyl

groups of 1,2-dideoxyhexitol are cleaved in the subsequent S-HDO. 1,2-dideoxypentitol and 1,2,5-pentanetriol show promise as target platform chemicals due to their economic value. 1,2-dideoxypentitol and 1,2,5-pentanetriol are value-added chemical building blocks that are between 300 to 5000 times more valuable than xylitol on a per mass basis [69]. 1,2,5-pentanetriol has an established use as an intermediate in the production of tetrahydrofurfuryl alcohol and 3-hydroxytetrahydropyran through dehydration [159], [160]. However, 1,2,5-pentanetriol has also been produced from D-ribose [161], but xylitol offers a potentially economic and scalable path for 1,2,5-pentanetriol and 1,2-dideoxypentitiol production via S-HDO due to the current large-scale production of xylitol. Xylitol has a current production of 242 thousand metric tons, which is expected to increase to over 266.5 thousand metric tons by 2022 [162]. The market for xylitol is expected to rise to over $1.37 billion by 2025, up from its current annual sales of $823.6 million [163]. In contrast, D-ribose annual production is only roughly 2,000-3,000 tonnes and is made through a fermentation process [164]. Thus the supply and promise of xylitol as a feedstock is significantly more advantageous due to its growing market and large scale production.

The S-HDO reaction consists of two steps, a deoxydehydration (DODH) step, followed by a hydrogenation step, shown in Figure 4.1. The DODH removes two vicinal cis hydroxyl groups and forms a double bond between the carbons previously containing the hydroxyl groups. For xylitol S-HDO, the C_1-C_2 or C_2-C_3 hydroxyl groups and undergo the DODH resulting in pent-4-ene-1,2,3-triol, and pent-3-ene-1,2,5-tiol respectively. The hydrogenation of the pentenetriols then occurs, and the double bond is hydrogenated to a single bond, resulting in the production of 1,2-dideoxypentitol, and 1,2,5-pentanetriol. The

state-of-the-art catalyst for this reaction is a ReO_x-Pd/CeO_2 catalyst, which utilizes the Re to catalyze the DODH step [38], [69], [71], [147], [154] and the Pd to facilitate hydrogen dissociation on the surface of the catalyst to catalyze the hydrogenation step [154]. The dissociation of hydrogen on the surface of the catalyst is catalyzed by the Pd, and also allows for the ReO_x to reduce during the proposed reaction mechanisms [147], [154]. The state-of-the-art ReO_x-Pd/CeO_2 catalyst has been shown to be over 99% selective to the S-HDO products while achieving high rates of conversion [38], [69], [71], [147]. A large parameter space has been probed in trying to elucidate active materials for the S-HDO reaction including active metals such as Re, W, Mo, Cr, Nb, Mn, and V, additives including Co, Ni, Cu, Ru, Rh, Pd, Ir, and Pt, and supports including CeO_2, SiO_2, C, activated carbon, Al_2O_3, ZrO_2, TiO_2, MgO, CaO, La_2O_3, and Y_2O_3 [38], [147]. From this parameter screening, the combination of ReO_x-Pd/CeO_2 (2 wt% Re and 0.30 wt % Pd) had the highest selectivity and conversion for the S-HDO reaction.

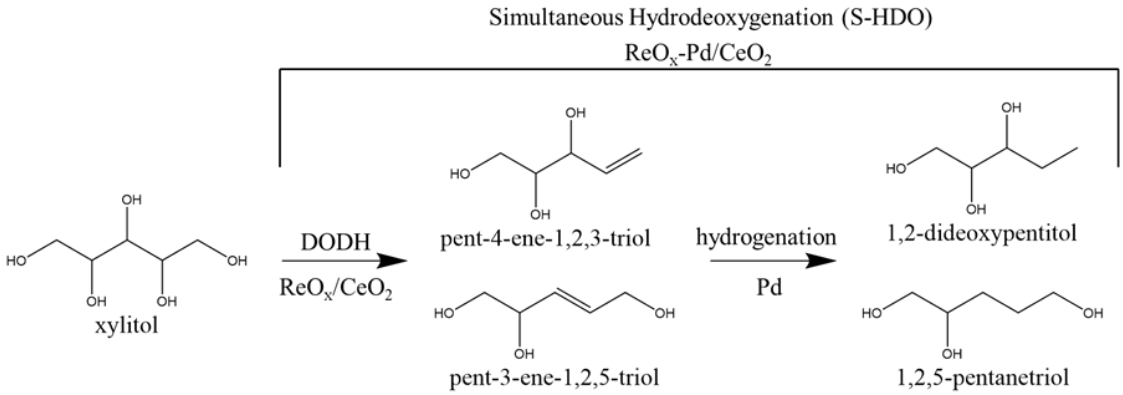

Figure 4.1. Reaction schematic of xylitol simultaneous hydrodeoxygenation. [71]

The Re and Pd loadings of the ReOx-Pd/CeO2 catalyst has been previously optimized [38], and it was determined that 2.0 wt% Re and 0.30 wt% Pd were optimal for the S-HDO reaction. Two different reaction mechanisms for S-HDO have been proposed

in the literature with different species of the ReOx (mono-oxo and di-oxo) being proposed as the active species [38], [154]. However, the general kinetics of xylitol S-HDO has not been investigated, and fundamental information such as activation energy, reaction orders, and mass transfer have not been experimentally evaluated. The DODH of various similar substrates has been investigated utilizing Re [38], [147], [152], [165] based and Mo [166] based catalysts in the literature, and a variety of activation energies has been reported. Table 4.1 shows the various reactions, activation energies, and method of determination for similar DODH reactions as reported in the literature. Density Functional Theory (DFT) calculations have been the predominant method for activation energy evaluations, with predictions ranging from 65–153 kJ/mol for the DODH over various catalyst using a sugar alcohol substrate. However, recently Cao et al. [152] performed both DFT and experimental Arrhenius calculations for the DODH of methyl α-L-rhamnopyranoside and methyl α-L-fucopyranoside over a ReO_x-Pd/CeO_2 catalyst. They were able to elucidate the activation energies for the reaction in which the predicted (DFT) and observed (Arrhenius) activation energies were within error of each other. The activation energies reported in the study were on the lower end of the activation energies previously proposed in the literature for similar substrates. The experimental determination of activation energy showed that similar reactants can have much lower activation energies than the DFT predictions have previously suggested, showing a possible over prediction of DODH activation energies, or potentially inaccurate reaction mechanisms.

Table 4.1. Literature activation energies for similar deoxydehydration (DODH) reactions. [71]

Reaction/Catalyst	Activation Energy	Method	Reference
DODH of 1,4-anhydroerythritol over ReO_2/CeO_2	153 kJ/mol	DFT	Ota et al., 2016 [46]
DODH of 1,4-anhydroerythritol over ReO/CeO_2	109 kJ/mol	DFT	Xi et al., 2018 [154]
DODH of 1,4-anhydroerythritol over $ReO\text{-}Pd/CeO_2$	111 kJ/mol	DFT	Xi et al., 2018 [154]
DODH of 1,4-anhydroerythritol over $ReO_2(2O)/TiO_2(101)$	71.4 kJ/mol	DFT	Xi et al., 2020 [166]
DODH 1,4-anhydroerythritol over $MoO_2(2O)/TiO2(101)$	160.2 kJ/mol	DFT	Xi et al., 2020 [166]
DODH of 3-Butene-1,2-diol over CH_3ReO_2	118.8 kJ/mol	DFT	Wu et al., 2016 [165]
DODH of 3-Butene-1,2-diol over $CH_3ReO(OH)_2$	79.9 kJ/mol	DFT	Wu et al., 2016 [165]
DODH of methyl α-L-rhamnopyranoside over $ReO_x\text{-}Pd/CeO_2$	65, 63 kJ/mol	DFT, Arrhenius	Cao et al., 2020 [152]
DODH of methyl α-L-fucopyranoside over $ReO_x\text{-}Pd/CeO_2$	77, 73 kJ/mol	DFT, Arrhenius	Cao et al., 2020 [152]

The previous work reported in this dissertation investigated the effects of temperature, pressure, and catalyst loading on xylitol S-HDO conversion and selectivity, utilized parameter sweeps and a design of experiment to find optimal conditions and elucidate factor to response relationships [69]. H_2 pressure was found to exhibit a zero-order relation with the conversion for xylitol S-HDO down to 10 bar for our standard reaction conditions within our homebuilt high pressure batch reactor. However, the linear L9 Taguchi design that we conducted suggested that temperature had an inverse with conversion. In terms of classic kinetics, this relationship wasn't expected due to the Arrhenius equation and the direct relationship that temperature and reaction rate should exhibit. Therefore, to investigate this phenomenon further and to determine if the inverse relationship was accurate or if there was something more complex in the design space that the Taguchi design couldn't model, a general kinetics study of xylitol S-HDO was

conducted. This study was the first experimental study investigating the kinetics of xylitol simultaneous hydrodeoxygenation. The goal of the study was to determine the reaction order of xylitol, the reaction rate dependence on temperature, the activation energy, the effects of xylitol concentration on reaction rate, and to evaluate internal and external mass transfer limitations in our system. This work served to address the knowledge gap in the literature on the kinetics of simultaneous hydrodeoxygenation on non-cyclic sugar alcohols and substrates that have more than three hydroxyl groups.

4.1.2 CHEMICALS

The following chemicals were used in this work for reactions, calibrations, and catalyst synthesis. Xylitol (CAS No. 87-99-0) ≥ 99%, 1,4-Dioxane (CAS No. 123-91-1) 99.9%, 1,2,5-Pentanetriol (CAS No. 14697-46-2) 97%, 1,2-Pentanediol (CAS No. 5343-92-0) 96%, 1-Pentanol (CAS No. 71-41-0) ≥ 99%, 3-Pentanol (CAS No. 584-02-1) 98%, Ammonium perrhenate (CAS No. 13598-65-7) ≥ 99%, Palladium (II) nitrate (10 wt% in 10 wt% nitric acid) (MDL: MFCD00011169) 99.999%, Cerium (IV) oxide (CAS No. 1306-38-3), and Ultra High Purity (UHP) Hydrogen (CAS No. 1333-74-0) 99.999%, were used in this study. The cerium (IV) oxide was donated by Daiichi Kigenso Kagaku Kogyo Co., Ltd. Osaka, Japan. The UHP hydrogen was obtained from Praxair, the 1,2,5-Pentanetriol was obtained from Combi-Blocks, the 1,4-Dioxane was obtained from Fisher Chemical, and all remaining above-mentioned chemicals were obtained from Sigma-Aldrich.

4.1.3 CATALYST SYNTHESIS

The ReO_x-Pd/CeO_2 (2 wt% Re, 0.30 wt% Pd) catalysts used and characterized in this study were prepared via wet impregnation following the procedures previously

reported in this dissertation [69], [70]. The CeO_2 support (donated from Daiichi Kigenso Kagaku Kogyo Co., Ltd. Osaka, Japan) was calcined in air at 600 °C for 3 h with a ramping rate of 10 °C/min. Following the calcination of the CeO_2 support, the ReO_x was then impregnated onto the CeO_2 via wet impregnation using the desired amount of ammonium perrhenate (NH_4ReO_4) dissolved in an aqueous solution that was mixed on a stir plate at an agitation rate of 300 rpm. Once the solution was adequately mixed and all of the precursor was dissolved, the solution was dried at 110 °C for 12 h to evaporate the excess water and leave the ReO_x/CeO_2 as a solid powder. The ReO_x/CeO_2 powder was then removed from the beaker and stored in a weight boat while the palladium solution was prepared. Then the palladium was impregnated via wet impregnation using an aqueous solution of the desired amount of palladium (II) nitrate ($Pd(NO_3)_2$) in the same manner as the ReO_x was impregnated. Once the solution was well mixed, the ReO_x/CeO_2 powder was added to the beaker containing the palladium solution. The solution was then dried at 110 °C for 12 h so that the ReO_x-Pd/CeO_2 could be extracted from the excess water. The ReO_x-Pd/CeO_2 powder was calcined in air at 500 °C for 3 h with a ramping rate of 10 °C/min. Following the calcination, the ReO_x-Pd/CeO_2 catalyst was ground into a fine powder with a mortar and pestle. All of the ReO_x-Pd/CeO_2 catalysts used in this study were made with a nominal loading of 2 wt% Re and 0.30 wt% Pd, respectively to ensure that the molar ratio of Pd to Re was Pd/Re = 0.25, as it was previously reported to be optimal [46].

4.1.4 ACTIVITY AND KINETIC MEASUREMENTS

The homebuilt 150 mL high-pressure batch reactor that was machined from 316 stain-less steel that was previously described in this dissertation was utilized for the kinetic measurements in this study. This reactor system allows for time on-stream samples to be

taken which allowed for kinetic data to be analyzed using concentrations of reactants and products from a single reaction at multiple time points. The reaction solution within the reactor was mixed using a magnetic stir bar and a stir plate, which was previously shown to be free of mass transfer limitations for the hydrogenation of 2-methyl-3-butyn-2-ol [69]. The reactor was heated using an oil bath coupled to a PID controller to maintain the set temperature over the course of the reaction.

For each xylitol S-HDO reaction, the reactor was loaded with the proper amount of catalyst, xylitol, and solvent (1,4-dioxane) along with a magnetic stir bar. The reactor was then sealed with an O-ring, and the reactor bolts were tightened until it the reactor was pressure tight. To test if the reactor was pressure tight, the reactor was pressurized with helium (an inert) to 10 bar over the reaction set point, and a leak detector was used to ensure that no gas was leaking from the reactor. After the reactor passed the pressure checks, it was then flushed of any residual air in the reactor with helium by pressurizing and venting the reactor three separate times. Following the purge of the helium, the reactor was then heated to the specified reaction temperature using the PID controller and oil bath. The temperature inside of the reactor was monitored using a K type thermocouple in the temperature probe well previously described in the reactor schematic. Once the desired temperature within the reactor (measured by thermocouple) was reached, the reactor was kept at this temperature for at least 30 min to ensure the reactor temperature was stable. Once the temperature stability was verified, the hydrogen gas was added to the reactor, and the line to the tank was left open to ensure the reactor maintained a constant pressure of 10 bar. Once the hydrogen was added, the reaction time was started, and the first sample was taken to ensure that no reactions occurred during the heating of the reaction solution.

Samples were taken every 30 min of the reactions for 4 h or until the volume of the reaction solution was too low to sample to provide an accurate assessment of the reaction over time, and allow for concentration based kinetic calculations to be utilized.

The reaction samples collected throughout each experiment were analyzed with Gas Chromatography (GC) to determine the concentration of xylitol, 1,2,5-pentanetriol, 1,2-dideoxypentitol, 3-pentanol, 1-pentanol, and 1,2-pentanediol. The GC system utilized a Shimadzu GC 2010 Plus along with an AOC-5000 autoinjector. Within the GC an RTX-1701 column with a column length of 30 m, an inner diameter of 0.32 mm, and a film thickness of 1.00 μm was used for product separation, and the system utilized a Flame Ionization Detector (FID) for quantitative analysis. The reaction samples were diluted by a factor of $\frac{125}{3}$ ($\frac{solvent}{reactant}$) times their original volume in methanol to ensure that the FID would not saturate, and to make analyze the components within the made calibration ranges. For each run in the GC, 1 μL of the GC sample was injected into the system using a split ratio of 1:10 with a column flow of 2.5 mL/min and a total flow of 30.5 mL/min. Following the injection, the injection needle was washed three times in acetone and then three times in methanol to ensure that any residual reactants or products were removed and that the needle was cleaned. The GC oven methodology included a 40 °C starting temperature with a 3 min hold, which was followed by a heating ramp of 10 °C/min to 260 °C, which was then held for 20 min. Upon the completion of the program, the column was cooled to 40 °C in preparation for the next sample. Once the system was stable at 40 °C, the next reaction sample was then injected into the GC and the same methodology was followed. Xylitol, 1,2,5-pentanetriol, 1,2-dideoxypentitol, 3-pentanol, 1-pentanol, and 1,2-pentanediol were calibrated by making an 8-point calibration curve with known

concentration standards to allow for accurate concentration determinations. Over the scope of reaction times and temperatures utilized, 3-pentanol, 1-pentanol, and 1,2-pentanediol were not seen in significant concentration. The absence of then pentanols shows that only one S-HDO of xylitol was occurring over these reaction times and temperatures. It also indicates that the concentration of xylitol on the surface of the catalyst was likely higher and more favorable to react than the pentanols. The lack of 1,2-pentanediol production indicates that singular removal of hydroxyl groups was not occurring in a substantial manner, but rather the S-HDO was occurring.

Reaction order determination and activation energy elucidation (Arrhenius and non-Arrhenius) reactions were conducted at temperatures between 120 to 170 °C. Each reaction utilized 0.60 g of ReO_x-Pd/CeO_2 catalyst, 2.0 g of xylitol, and 50 mL of solvent (1,4-dioxane). For mass transfer evaluations with respect to xylitol concentration, the reaction temperature, solvent volume, and the ratio of ReO_x-Pd/CeO_2 catalyst to xylitol were fixed at 160 °C, 50 ml, and a 0.3:1.0 wt. ratio of catalyst to xylitol respectively, while the total concentration of xylitol and catalyst were varied. The 0.3:1.0 ratio was previously reported to be an optimal condition in the literature [147].

To investigate any external mass transfer limitations, a mixing evaluation study was conducted and the stirring rate was varied from between 150 and 700 rpm for separate reactions while fixing the reaction temperature, catalyst, xylitol, and solvent amounts at 160 °C, 0.60 g, 2.0 g, and 50 mL respectively for each individual reaction. To investigate internal mass transfer, the Weisz–Prater criterion was also evaluated. The effect of reactant concentration was also investigated by varying xylitol concentration from 0.5–8 g while keeping the solvent concentration (50 mL), and catalyst to reactant ratio constant (0.30 g

catalyst: 1 g xylitol) while conducting each reaction at 160 °C. All experiments conducted in this kinetics study utilized a constant hydrogen pressure of 10 bar H_2 to ensure that the H_2 reaction order was zero order as previously shown in this dissertation.

4.2 RESULTS AND DISCUSSION

4.2.1 CATALYST CHARACTERIZATION

The ReO_x-Pd/CeO_2 catalysts used in this kinetics study were characterized using Scanning Electron Microscopy (SEM), X-ray Diffraction (XRD), Temperature Programmed Reduction (TPR), X-ray Fluorescence Spectroscopy (XRF), Inductively Coupled Plasma—Optical Emission Spectrometry (ICP-OES), and Raman Spectroscopy.

SEM was conducted to determine the particle size of the CeO_2 of the ReO_x-Pd/CeO_2 catalyst used for the kinetic evaluations. The SEM was conducted on a Zeiss Gemini 500 Field Emission Scanning Electron Microscope with a Type II Secondary Electron Detector (SE2) and a voltage of 5 keV. SEM images and the respective particle size distribution histograms of the CeO_2 support that underwent the same pre and post treatments as the ReO_x-Pd/CeO_2, and the ReO_x-Pd/CeO_2 catalyst are shown in Figure 4.2. From the SEM that was conducted, it was determined that the morphology of the particles does not change during the synthesis of the ReO_x-Pd/CeO_2 catalyst using the synthesis methodology reported. However, some changes in the distribution of the size of the particles between the support and the catalyst were observed. The distribution of particle sizes for the CeO_2 and the ReO_x-Pd/CeO_2 are shown in Figure 4.2c, d, respectively.

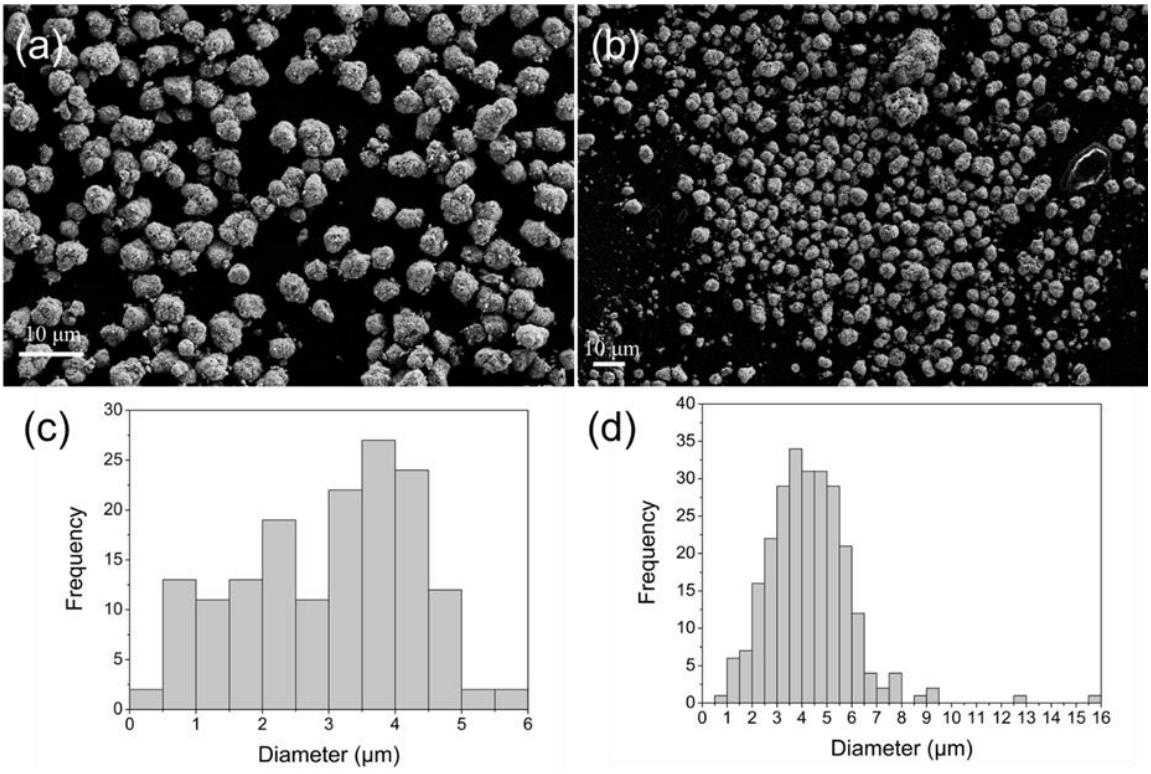

Figure 4.2. SEM of CeO_2 support and ReO_x-Pd/CeO_2 catalyst. (a) CeO_2 1280 x magnification (b) ReO_x-Pd/CeO_2 629 x magnification (c) CeO2 particle size histogram (d) ReO_x-Pd/CeO_2 particle size histogram. [71]

The particle sizes (diameter) were determined using ImageJ, by evaluating the area of each particle and assuming a circular particle size to calculate the radius of the particles from the respective areas. The average particle size (diameter) measured for the CeO_2 and ReO_x-Pd/CeO_2 were 3.00 and 4.30 µm, respectively, determined from 158 and 254 particles respectively. The distribution of the particle sizes exhibited a slightly skewed left distribution for CeO_2 particles with the largest group of particles being between 3.5-4 µm. For the ReO_x-Pd/CeO_2 particles, the distribution exhibited a unimodal slightly skewed right distribution with the largest group of particles also being between 3.5-4 µm. However, the ReO_x-Pd/CeO_2 catalyst particles, on average, are more likely to be larger in size than the CeO_2 support, which shows that the synthesis parameters and environment are causing a

small agglomeration of the CeO_2 particles, or that the impregnated metals are making the particles larger. Low (134-150x) and high (3540-4400x) magnification SEM images of the CeO_2 and ReO_x-Pd/CeO_2 are shown in Figure 4.3. The CeO_2 particles are homogeneous in size and morphology as shown in Figure 4.3a. However, the ReO_x-Pd/CeO_2 catalyst particles, shown in Figure 4.3b, have a few large agglomerations with the majority of the particles being much smaller and homogenous. These large agglomerates could be the result of inconsistent grinding of the catalyst powder using the mortar and pastel, or that the synthesis parameters including, exposure to excess water, and the addition of metal precursors, causes the CeO_2 particles to agglomerate. When the particles of the CeO_2 and ReO_x-Pd/CeO_2 are compared under a high magnification, shown in Figure 4.3c, d, the particles look very similar. There is no noticeable difference between the particles, indicating that the Re and Pd are either very well dispersed on the CeO_2 surface, in the pores of the CeO_2 or a combination of both. The lack of large growths of Re or Pd observed on the catalyst surface gives more evidence to the Re being dispersed enough to have monomeric sites which have been proposed to be the active site [46], [154], and observed in Raman spectroscopy [70], [71].

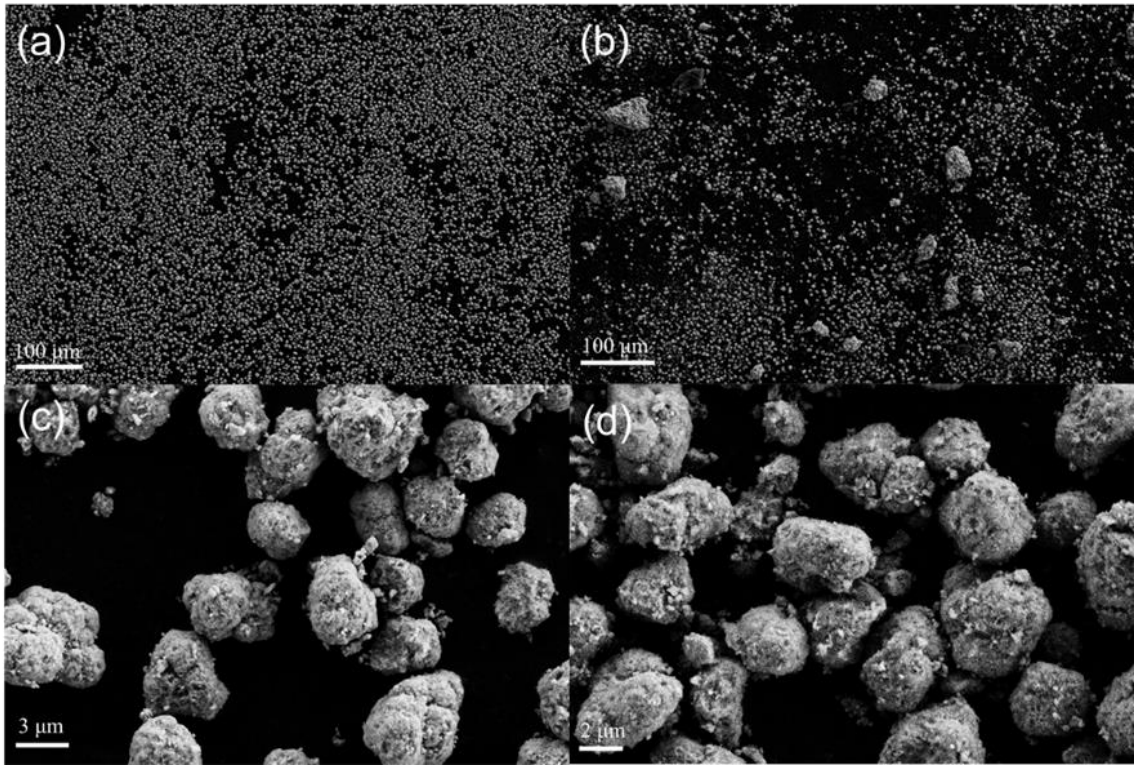

Figure 4.3. SEM of CeO_2 support and 2 wt% ReO_x-Pd/CeO_2 catalyst. (a) CeO_2 134 x magnification, (b) ReO_x-Pd/CeO_2 150 × magnification, (c) CeO_2 3540 × magnification, (d) ReO_x-Pd/CeO_2 4400 × magnification.[71]

XRD was utilized to determine if there was any long range ordering of the Re or Pd supported on the CeO_2 and to make sure that there weren't an impurities present in the catalyst. It was also used to make sure that the different batches of ReO_x-Pd/CeO_2 were uniform. The XRD was conducted using a Rigaku MiniFlex II with Cu Kα source radiation (α = 1.5406 Å). Each sample was scanned between a 2θ of 10° to 80° using a 2°/min scanning rate with a 0.02° step size. The resulting diffraction patterns for all three batches of ReO_x-Pd/CeO_2 using in the kinetic evaluations are shown in Figure 4.4. All three patterns matched the reference patterns for CeO_2 and previously reported ReO_x-Pd/CeO_2 catalyst diffraction patterns [69], [70]. Since no diffraction patterns were observed for Re or Pd, it is further evidence that they are well dispersed on the CeO_2 support. This also give further support for the Re being in mostly monomeric species as the cross-linked oligomer species

of ReO_x would exhibit long range ordering and thus exhibit a diffraction pattern if in high enough of concentration.

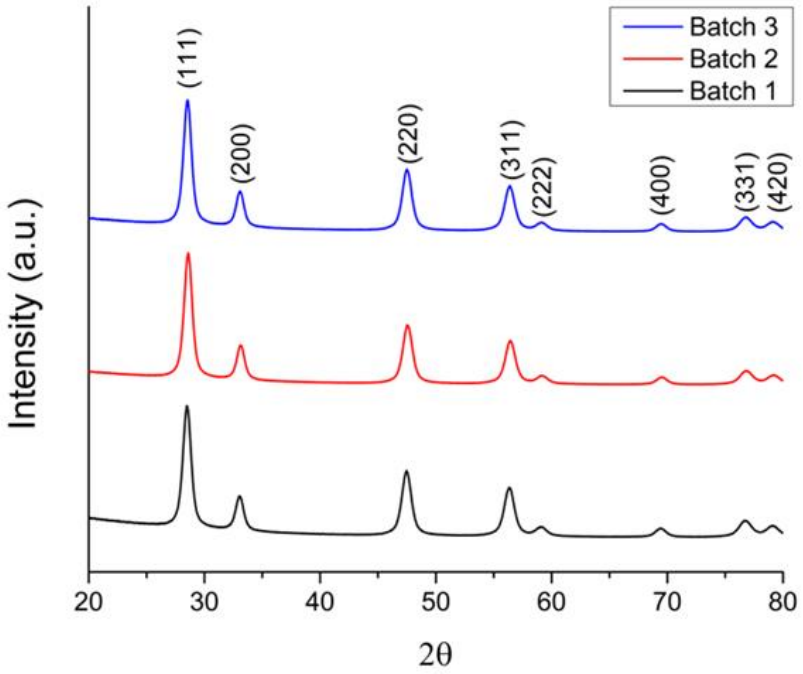

Figure 4.4. XRD patterns of 2 wt% ReO_x-Pd/CeO_2 catalysts at a scanning rate of 2°/min with a step size of 0.02°. [71]

TPR was conducted to determine the temperature at which reduction events would occur, and to determine the number of reduction events for the ReO_x-Pd/CeO_2. The TPR was conducted on a Micrometrics AutoChem II chemisorption analyzer and utilized H_2 for the reduction. The sample was first subjected to a moisture removal step to ensure that any moisture from the air, in the analysis tube, or from the storage of the catalyst was removed. The moisture removal was conducted by having the sample heat from room temperature to 120 °C in a He environment at 10 °C/min and hold isothermally at 120 °C for 1 h. Following the isothermal hold, the sample was then cooled to 40 °C maintaining a 10 °C/min cooling rate under a He environment. Once 40 °C was reached and was stabilized,

the gas environment was switched from He to a 10% H_2 in Ar mixture. The H_2 environment was maintained and held for 30 min. Following this hold, the TPR experimentation was conducted by heating from 40 °C to 800 °C at 5 °C/min. During the experiment, a data point was recorded every second, corresponding to a data point every 0.083 °C. Once the sample reached the final temperature of 800 °C, the detector stopped recording data and gas flow was switched to He to purge the H_2 and Ar mixture from the sample tube and system. The sample was then cooled to 25 °C at a cooling rate of 20 °C/min. The batches of catalyst showed similar results in the TPR, and a representative TPR profile of the ReO_x-Pd/CeO_2 catalysts are shown in Figure 4.5. In the TPR pattern, there were two distinct reduction events that occurred, one at 147 °C and the other at 183 °C. These reduction events have been previously reported in TPR profiles for a 2 wt% ReO_x-Pd/CeO_2 (0.30 wt% Pd) catalyst [46], [69]. The reduction events correspond to the partial reduction of ReO_x, as previously shown in the literature using XPS [46]. The Pd substantially reduces the temperature of the reduction events corresponding to the partial reduction of ReO_x. The CeO_2 has been shown to partially reduce above 700 °C between 730-1000 °C [46]. In our TPR profiles we started to see a reduction event occurring at around 750 °C, but since our methodology only went up to 800 °C, we did not see the full reduction event. However, no reductions of ReO_x are expected above this range.

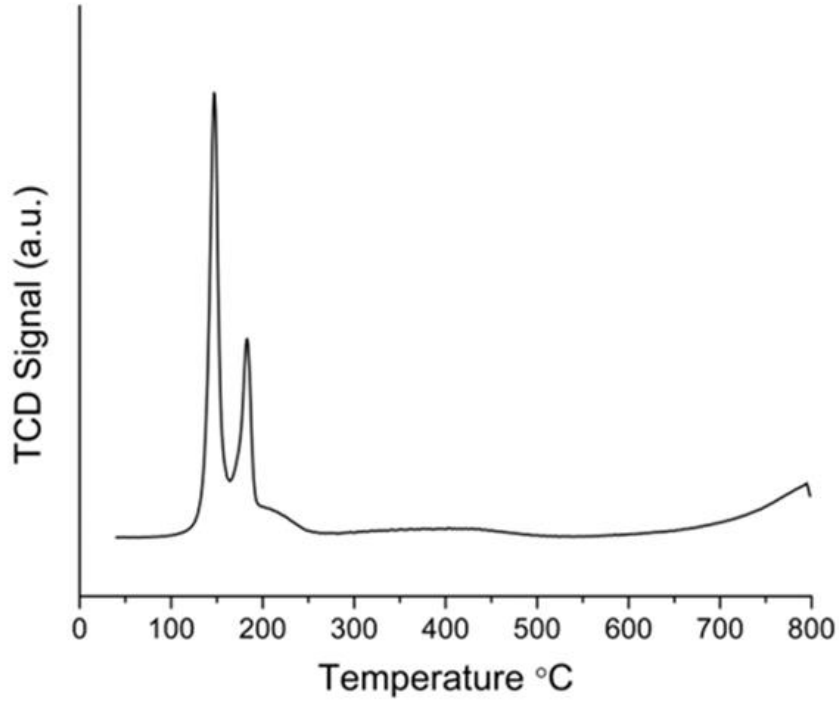

Figure 4.5. Representative H2 TPR profile of 2 wt% ReO_x-Pd/CeO_2 catalyst.

XRF was conducted on the ReO_x-Pd/CeO_2 catalyst samples to ensure that the Re and Pd were uniformly distributed within the catalyst and to make sure that there was no significant difference between various batches of the catalysts. XRF was conducted on a Fischerscope XDAL system utilizing a 0.30 mm collimator size and an 80 s measurement time. The XRF was used in standard free mode, and thus the percentages reported are not exact values but can still give insight into the distribution of the elements. ICP-OES was conducted to determine calibrated loadings of Re and Pd respectively and will be discussed later. For analysis, the ReO_x-Pd/CeO_2 catalyst powder was placed in an XRD sample holder (diameter of 24 mm and a depth of 2 mm) and the powder was flattened using a glass slide. Once the sample was focused on in the instrument, 11 random points away from the edges were selected for subsequent scanning and the software was programmed to scan for Re, Pd, and Ce. The respective concentrations of Re, Pd, and Ce were then reported for each

scan. XRF on the ReO_x-Pd/CeO_2 catalyst showed that both the Re and Pd were uniformly distributed with standard deviations of 0.075 wt% and 0.054 wt%, respectively. The relatively low standard deviations for the Re and Pd show that that the metals are well dispersed and homogeneous throughout the catalyst. Pd had a higher coefficient of variation percentage (ratio between standard deviation and mean) of 7.17%, suggesting a higher variation in the distribution. However, a very low nominal load (0.30 wt%) was used in making these catalysts which can skew the coefficient of variation since the mean value is an order of magnitude lower for the Pd as compared to the Re. The Re and Pd XRD composition contours are shown in Figure 4.6. The various X-Y scans showed that the regions of higher Re concentration also had a higher concentration of Pd. Likewise, the regions of lower Re concentration also have a lower concentration of Pd, suggesting that the ratio of Re:Pd is relatively uniform throughout the sample. This could also be due to uneven packing within the sample holder, but the ratio of Re:Pd being relatively uniform gives further evidence that there is not significant localization of the metals within the catalyst.

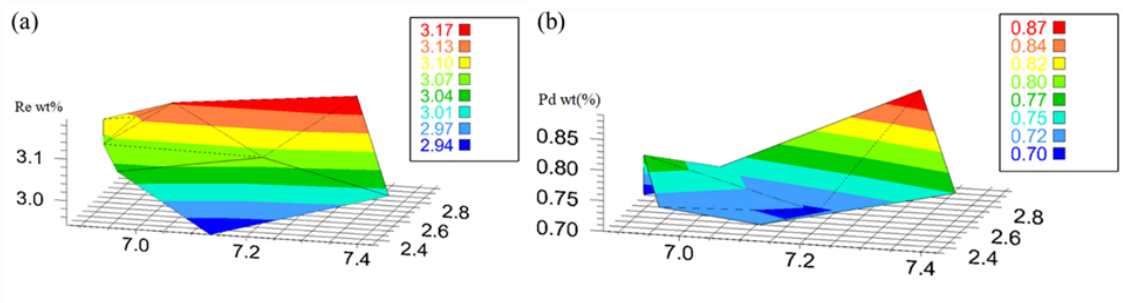

Figure 4.6. XRF X-Y position (in cm) composition contour of ReO_x-Pd/CeO_2 catalyst (a) Re contour, (b) Pd contour. [71]

ICP-OES was conducted to determine the actual loadings of Re and Pd in the ReO_x-Pd/CeO_2 catalysts. The experimentation and data collection were performed on a Perkin Elmer Avio 200 which was equipped with an S10 autosampler. Freshly prepared aqua regia was used for the digestion of the catalysts, and the solutions were allowed to digest for 12 h at 120 °C following the procedure used in MacQueen et al. [70]. The three batches of catalyst used in this study were analyzed for both Re and Pd, which had a nominal loading of 2.0 wt% Re and 0.30 wt% Pd respectively. Three runs of each sample were analyzed in the ICP-OES and the errors presented are the standard deviation of the runs. The batches were determined to have an actual loading of 1.86 ± 0.02 wt%, 1.89 ± 0.01 wt%, and 1.90 ± 0.02 wt% of Re, respectively, and 0.217 ± 0.003 wt%, 0.204 ± 0.002 wt%, and 0.202 ± 0.001 wt% of Pd, respectively. Thus, all of the Re loadings were within error of each other. Two of the Pd loadings were within error of each other with only 1 batch having a slightly higher loading. However, since Pd just facilitates the dissociation of hydrogen on the surface of the catalyst, this small difference in actual loading should not affect the activity of the catalyst significantly. Thus all of the catalyst used in this study were homogenous and lead to similar kinetic results.

In-situ Raman was conducted to investigate what structures of ReO_x were present under reaction conditions. The in-situ Raman spectroscopy was conducted with a Horiba XploRA Plus Raman microscope that utilizes a 30 mW excitation source, a 638 nm diode laser, and a Horiba Scientific charge-coupled device detector. The laser was calibrated using a polystyrene standard, and the detector was thermoelectrically cooled to −50 °C. A Linkam THMS600PS in-situ Raman cell was used for the experimentation. All spectra taken utilized a laser power of 50%, and the vibrational bands were monitored throughout

the experimentation to ensure that there wasn't degradation of the sample. For the experiment, an ambient spectrum was first taken, and then the sample was heated to 550 °C at 50°/min while flowing 20 sccm of ultra-high purity O_2 (99.9993% O_2) and held at 550 °C for 30 min. The calcination was conducted to follow the methodology previously reported [70], which was done to clean off the surface of the catalyst and ensure that any moisture or impurities from the storage of the catalyst were removed before analysis. Following the calcination, the cell was purged of O_2 with Ar and then reduced in 20 sccm of a 1:1 volume mixture of H_2 and Ar for 10 min. A spectrum was then taken to endure that the ReO_x vibrational bands had fully reduced. Following the reduction, the cell was again purged with Ar and then exposed to an O_2 environment (20 sccm O_2) at 550 °C to reoxidize the sample for 10 min. A spectrum was then taken to ensure that the Re had reoxidzed and the ReO_x vibrational bands were present. Following the re-oxidation, the cell was purged with Ar and then cooled to 100 °C while flowing 20 sccm of Ar. Spectra were then collected at every 10 °C from 100 °C to 180 °C. The resulting spectra from the ambient, calcined, reoxidized, and temperature scans are shown in Figure 4.7. The ambient spectrum showed a much broader vibrational bands as compared to the calcined and reoxidzed bands. However, there was no substantial difference between the calcined and the reoxidized spectra, indicating that the Re had been oxidized back to ReO_x post reduction. There was a significant difference in the ReO_x vibrational bands observed between the 100 °C and 180 °C spectra. To investigate the difference further the 100 °C, 140 °C, and 180 °C spectra were fitted and analyzed.

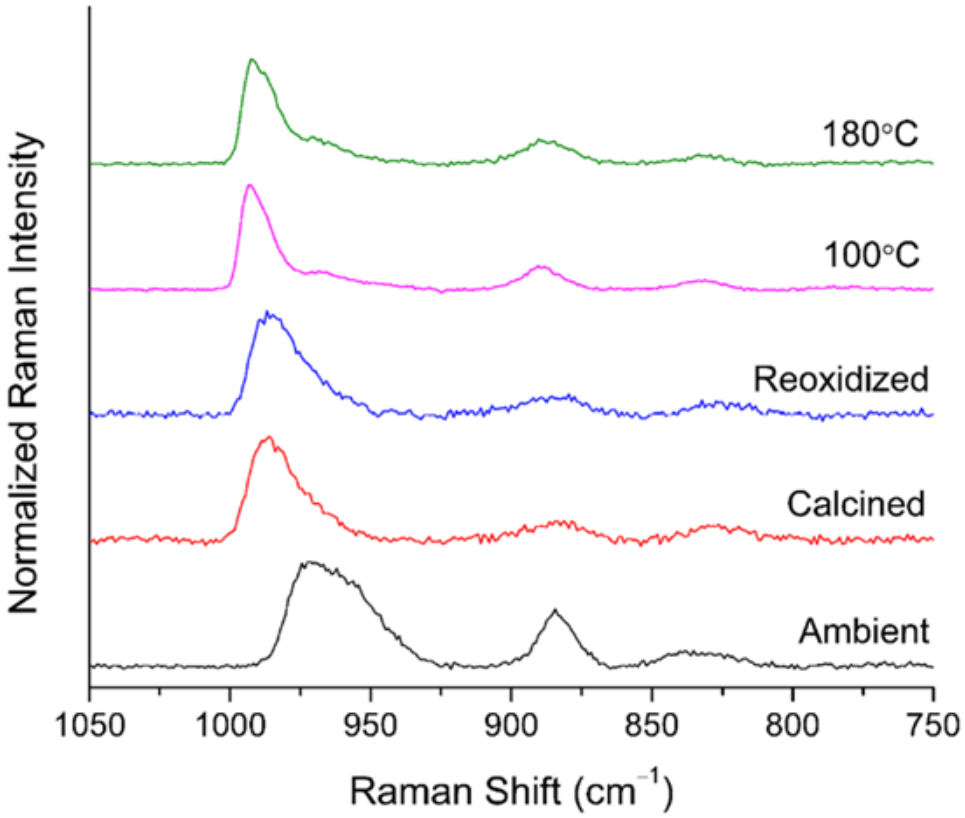

Figure 4.7. *In-situ* Raman spectra of 2 wt% ReO_x-Pd/CeO_2 catalyst. [71]

The 100 °C, 140 °C, and 180 °C fitted spectra are shown in Figure 4.8. The mono-oxo (Re=O), di-oxo (O=Re=O), oligomeric crosslinked (O-Re-O), and hydroxyl (Re-OH) structures were present in the sample, as assigned by MacQueen et al. [70]. The mono-oxo vibrational band is located at 994 cm^{-1}. The di-oxo bands are located at 988 and 972 cm^{-1} for the symmetric and asymmetric stretches, respectively. The oligomeric crosslinked band was located at 888 cm^{-1}, and the hydroxyl band was located at 832 cm^{-1}. The full-width half maximums were fixed for each respective band across spectra, and the areas of the symmetric and asymmetric stretch bands of the di-oxo species were constrained to be equivalent during fitting. As the temperature is increased, the relative area of the di-oxo species bands increases, and the mono-oxo bands decrease. The increase in the concentration of the di-oxo species can be attributed to an increase in oxygen migration

from the ceria support as the temperature is increasing, which has previously been reported in other ceria systems in the literature [167]. Ceria is able to store and release oxygen due to the stability of Ce^{3+} and Ce^{4+}, which allows for the ceria to shift between CeO_2 and CeO_{2-x} [168]–[171], thus allowing for the oxygen migration to the Re to occur. The area of the hydroxyl band also slightly decreases as the temperature is increased, which could be due to the hydroxyl species further oxidizing from the oxygen migration from the support. However, no new vibrational bands are formed while the temperature is increased. Thus at higher reaction temperatures, there is more di-oxo ReO_x available to participate in the reaction.

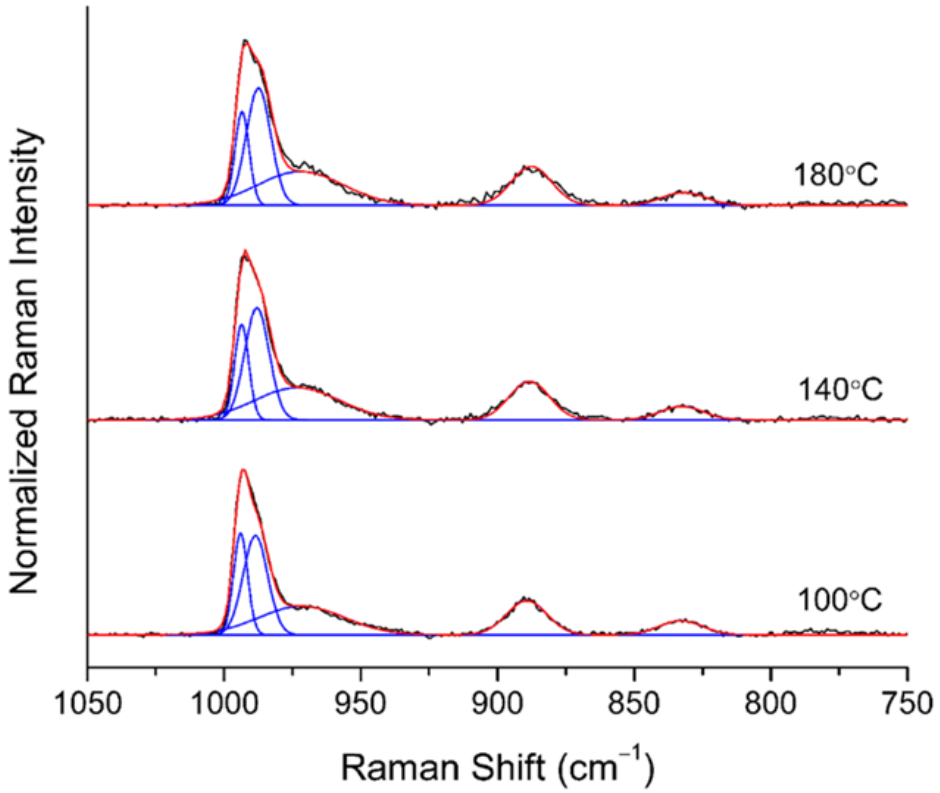

Figure 4.8. *In-situ* Raman spectra of a 2 wt% ReO_x-Pd/CeO_2 catalyst at 100 °C, 140 °C, and 180 °C under an Ar environment. [71]

4.2.2 REACTION ORDER DETERMINATION

The reaction order with respect to xylitol concentration of the xylitol S-HDO over the ReO_x-Pd/CeO_2 catalyst was determined by conducting reactions at various temperatures ranging from 120 °C and 170 °C. The resulting reactant and product concentrations as a function of time were and evaluated and fit to respective reaction order fittings. Zero, first, and second-order fittings were applied to the data for evaluation of the reaction order of xylitol. It was determined that the xylitol S-HDO was a zero-order reaction, with the zero order fitting consistently having the best fit over the 120-170 °C temperature range. The reaction concentration profiles of the reactant and products and the zero-order fit for the 160 °C reaction are shown in Figure 4.9. The S-HDO reaction using other substrates has been reported as zero-order with respect to the reactant in the literature [152]. The volume of the reaction solution remains virtually constant throughout the entirety of the reaction. Only a negligible (~300 μL) amount of volume is removed for sampling for analysis for each data point. As shown in the 160 °C reaction, shown in Figure 4.9, the selectivity to 1,2-dideoxypentitol was slightly higher than to 1,2,5-pentanetriol, which was previously reported in the literature [69]. The reaction order fitting for the zero-order case showed significantly better fit and higher R^2 values of 0.997 for xylitol and 0.998 and 0.993 for 1,2-dideoxypentitol and 1,2,5-pentanetriol, respectively. This trend was exhibited at all reaction temperatures, but the first-order fitting was comparable to the zero-order fit at some reaction temperatures. However, when comparing the product fits, the reaction in all cases is clearly zero-order. Since in all cases, the zero-order fitting was consistently the best fit, the reaction of xylitol S-HDO over the ReO_x-Pd/CeO_2 was

determined to be a zero-order reaction, and thus there was no effect of xylitol concentration on the reaction rate during the reaction.

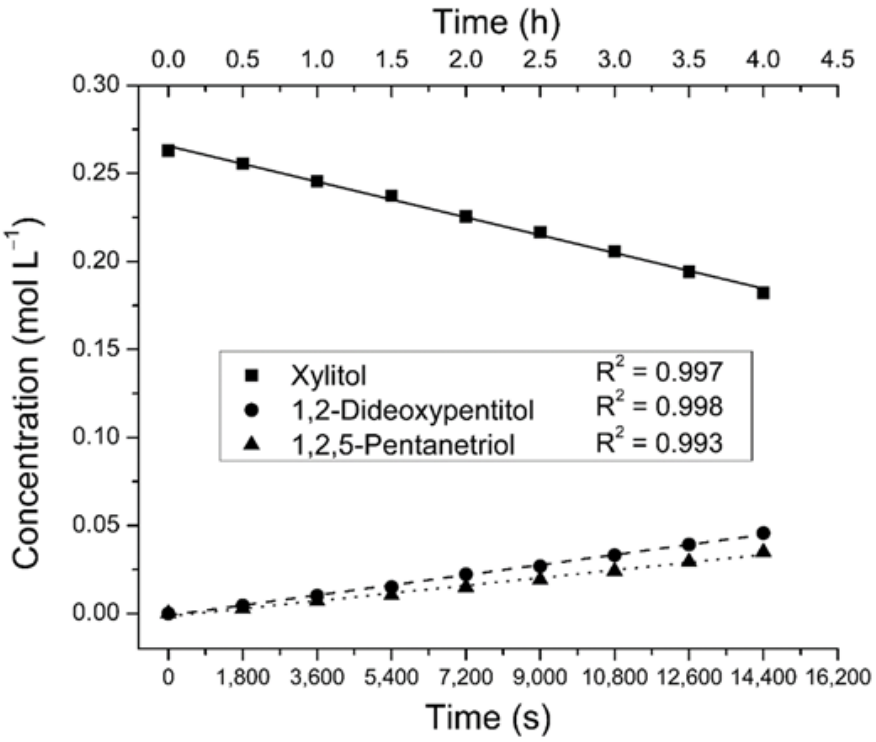

Figure 4.9. Reaction order fittings for the simultaneous hydrodeoxygenation (S-HDO) of xylitol over ReO_x-Pd/CeO_2 at 160 °C. [71]

In previous work in this dissertation, it was reported that over a wide range of H_2 reaction pressures down to 10 bar, the reaction hydrogen pressure exhibited a zero-order relation for the S-HDO of 1,4-anhydroerythritol and xylitol [69]. The pressure reaction order has been determined to be near zero for other reactants for the S-HDO reaction over ReO_x-Pd/CeO_2 [152]. Thus, the general reaction equation is determined to be the following:

$$C_5H_{12}O_5 + 2\,H_2 \rightarrow C_5H_{12}O_3 + 2\,H_2O \qquad (4.1)$$

$$Rate = k[C_5H_{12}O_5]^0[H_2]^0 = k \quad (4.2)$$

In the S-HDO reaction, xylitol and hydrogen are consumed to form 1,2-dideoxypentitol and 1,2,5-pentanetriol and water, as shown in Equation (4.1). The reaction rate equation, shown in Equation (4.2), is dependent on the xylitol and hydrogen reaction orders. Since they were both determined to exhibit a zero-order relationship, the reaction rate is equal to k and there is no dependence on the reactant concentrations.

4.2.3 ACTIVATION ENERGY DETERMINATION

To evaluate the activation energy of the xylitol S-HDO, reactions between 150 and 170 °C were evaluated and analyzed using Arrhenius kinetics. The resulting reaction rates from the tested temperature range were then plotted in an Arrhenius plot, as shown in Figure 4.10. Below 150 °C, the reaction rates were significantly lower and had a lower Arrhenius slope, which resulted in a lower activation energy. The increasing concentration of the di-oxo species (O=Re=O) at higher temperatures seen in the Raman could explain the higher reaction rates seen above 140 °C. If the di-oxo species is the active species for S-HDO as previously proposed in Ota et al. [38], then along with the temperature effects on reaction rate, having a higher concentration of the di-oxo species could also significantly increase the reaction rate. However, Xi et al. [154] proposed that the mono-oxo species could be the active site of the reaction. However, since the activity increases as the concentration of the di-oxo species increases, it is likely that the active site is the di-oxo species, if the reaction rate is being affected by the ReO_x structure. The lower reaction rates observed below 150 °C can also be attributed to the ReO_x species not reducing since the first significant reduction event occurred at 147 °C in TPR. Thus, only temperatures above 150 °C were considered.

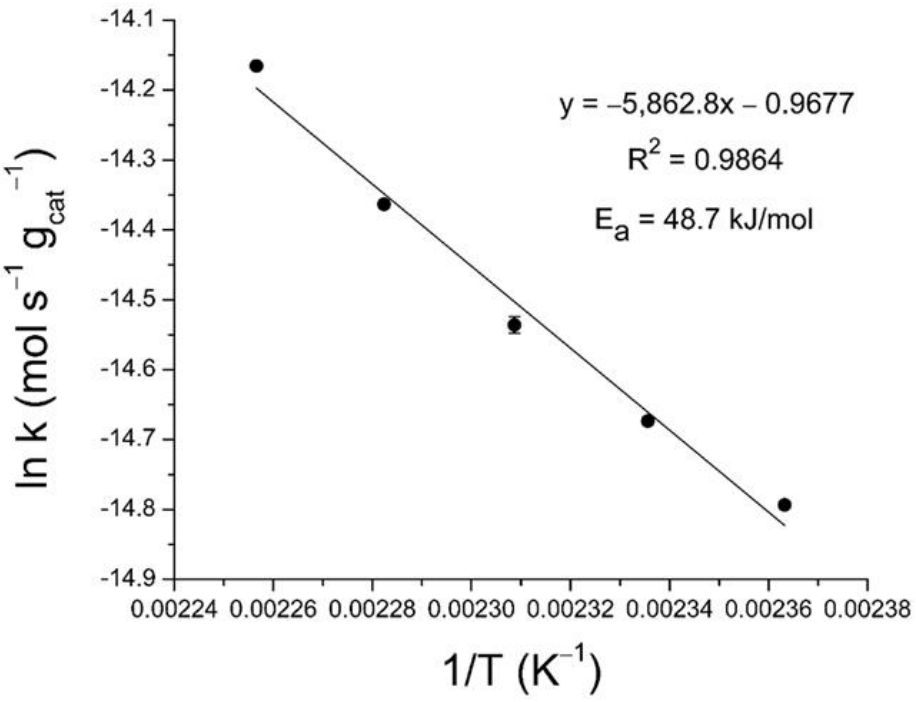

Figure 4.10. Arrhenius plot for the S-HDO of xylitol. [71]

The Arrhenius plot linear fit had an R^2 value of 0.9864, with respective data points having a standard error of 0.0116. The slope of the Arrhenius plot is equal to the $-E_a/R$, in which E_a is the apparent activation energy and R is the universal gas constant. From the Arrhenius plot, the apparent activation energy was determined to be 48.7 ± 10.5 kJ/mol, and the pre-exponential constant was determined to be 0.38 mol s^{-1} g_{cat}^{-1}. The activation energy error was determined using 95% confidence intervals for the slope coefficient from the linear regression. The resulting Arrhenius equation for this reaction is as follows:

$$k = Ae^{-\mathrm{E_a}/RT} \tag{4.3}$$

$$k = 0.38\frac{mol}{s \times g_{cat}}\ e^{-(48.7\frac{kJ}{mol})/(8.314\frac{J}{mol \times K} \times T)} \tag{4.4}$$

Since the reaction rates seemed to exhibit a non-linear trend at lower temperatures, non-Arrhenius kinetic parameter determination was conducted utilizing reaction temperatures of 120–170 °C. It has been reported in the literature that for sub-Arrhenius

and super-Arrhenius relations, the activation energy is dependent on temperature and can be accounted for by an additional quadratic term in the rate equation [172]–[175], as shown in Equation (4.5). The quadratic parameter C determines the curvature and thus if the curve is concave (positive C value) in the case of a sub-Arrhenius relation or convex (negative C value) in the case of a super-Arrhenius relation. This additional term results in E_a being dependent linearly on 1/T [173], [174]. Activation energy is thus equal to the partial derivative of the natural log of *k* with respect to 1/RT, in which $(\frac{\partial \ln k}{\partial \frac{1}{RT}})$ of Equation (4.5) results in Equation (4.6).

$$\ln k = \ln A + \frac{B}{RT} + \frac{C}{(RT)^2} \tag{4.5}$$

$$\mathrm{E_a} = -B - \frac{2C}{RT} \tag{4.6}$$

The resulting non-Arrhenius behavior plot resulting from reaction temperatures of 120–170 °C is shown in Figure 4.11, and the associated kinetic parameters are shown in Table 4.2. The C value was positive in this case leading to a concave curve characteristic for sub-Arrhenius behavior. The quadratic fitting of the sub-Arrhenius behavior improved the R^2 value to 0.99 over the entire temperature range evaluated in this work. The 95% confidence intervals were calculated for the respective kinetic parameters and are reported in Table 4.2.

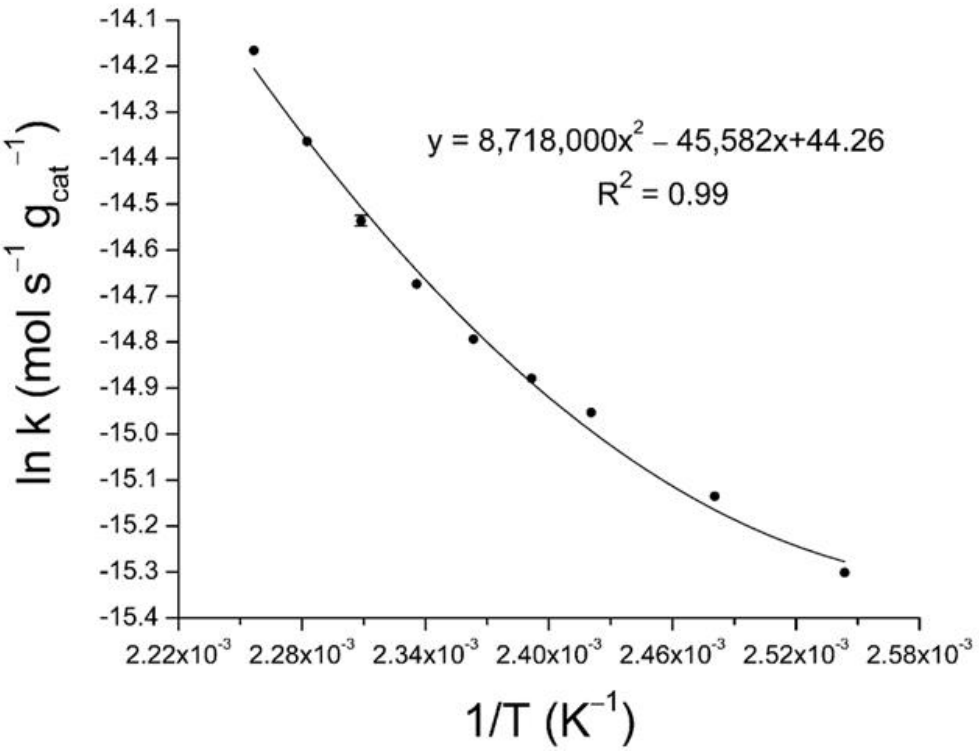

Figure 4.11. Sub-Arrhenius behavior plot for the S-HDO of xylitol. [71]

Table 4.2. Kinetic parameters for sub-Arrhenius behavior. [71]

Kinetic Parameter	Value	95% CI
A	44 mol s^{-1} g_{cat}^{-1}	(23, 65)
B	-3.79×10^5 J mol^{-1}	$(-5.76 \times 10^5, -2.34 \times 10^{-5})$
C	6.03×10^8 J^2 mol^{-2}	$(3.52 \times 10^8, 8.53 \times 10^8)$

The resulting activation energies over the temperature range tested are reported in Table 4.3. Over the temperature range tested, the activation energy ranged from 10.2–51.8 kJ/mol. At the lower range of temperatures tested, the sub-Arrhenius activation energies greatly differ from the Arrhenius activation energy. However, at and above 155 °C, the Activation energies are within error of the Arrhenius calculated activation energy. The improved fit over the expanded temperature range strongly supports that sub-Arrhenius

behavior is present, and thus, E_a is a function of temperature for xylitol S-HDO in the temperature range tested in this study.

Table 4.3. Temperature-dependent activation energies from sub-Arrhenius behavior.

Temperature (K)	Activation Energy (kJ/mol)
393.15	10.2
403.15	19.4
413.15	28.1
418.15	32.3
423.15	36.4
428.15	40.4
433.15	44.3
438.15	48.1
443.15	51.8

The sub-Arrhenius relationship is indicative of quantum tunneling occurring within the reaction [172]. Quantum tunneling allows particles to bypass the energy barrier by tunneling though the energy barrier without the need for the kinetic energy. This violates the principles of classic mechanics, but has been observed experimentally in various processes [176]–[179]. This phenomenon has been proven through the use of different hydrogen isotopes, such as deuteron and triton, to show that the transmission probability, reaction rate, etc., changes with the respective mass of the proton and exhibits the sub-Arrhenius relationship [179], [180]. Quantum tunneling is often seen in proton-involved reactions where the proton undergoes the tunneling. Xylitol S-HDO has hydrogen which is a proton on the surface of the catalyst once it dissociates, which could undergo the tunneling. It is likely that in the reaction mechanism, one of the highest energy barriers is proton/hydrogen related, which would explain why the tunneling would occur with the hydrogen. The previously mentioned proposed S-HDO mechanisms suggest that the desorption/extrusion step in which the alkene is the rate limiting step of the reaction [38]. However, hydrogen is not directly involved in this proposed step, but rather in the

coordination of the substrate directly beforehand [38], [154]. Thus it is likely that either the coordination of the substrate, which involves either hydrogen to reduce the ReO_x or to eliminate a Re-OH bond to form water, is limiting in the proposed mechanism. It is also likely that the current proposed mechanisms are not fully accurate and thus can't model the tunneling. However, regardless of the reaction mechanism, from the sub-Arrhenius behavior, we can accurately model the quantum tunneling that occurs via the barrier height (E_0), the deformation parameter (d), and the penetration frequency v^* [172]. By using the quadratic equations from the non-Arrhenius kinetics, the barrier height, deformation parameter, and penetration frequency can be calculated. The apparent activation energy is related to the barrier height and deformation parameter as follows:

$$\frac{1}{\mathrm{E_a}} = \frac{1}{E_0} - d\frac{1}{RT} \tag{4.7}$$

where the deformation parameter (d) is dependent on Planck's constant (h), the penetration frequency v^*, and the barrier height (E_0), as described by Bell's tunneling theory shown in Equation (4.8).

$$d = -\frac{1}{3}\left(\frac{\mathrm{h}v^*}{2E_0}\right)^2 \tag{4.8}$$

Using the activation energies and the respective reaction temperatures from Table 3, E_0 was determined to be −2608 J/mol, and v^* was determined to be 1.648×10^{37} mol^{-1} s^{-1}. These values are on the same order of magnitude as similar quantum tunneling for non-Arrhenius behavior reported in the literature [181], [182]. The deformation parameter can then be calculated using the values for E_0 and v^* as shown in Equation (4.9).

$$\frac{1}{\mathrm{E_a}} = \frac{1}{-2608\ \frac{J}{mol}} - \frac{-\frac{1}{3}\left(\frac{6.626 \times 10^{-34}\ J \times s\ \times 1.648 \times 10^{37}\ \frac{1}{mol \times s}}{2 \times -2608\frac{J}{mol}}\right)^2}{8.314\frac{J}{K \times mol} \times T} \quad (4.9)$$

The deformation parameter was determined to be $d = -1.461$. The value of d is negative which is further indicative of sub-Arrhenius behavior. E_0 and d can be plugged into Equation (4.7) which results in the following:

$$\frac{1}{\mathrm{E_a}} = \frac{1}{-2608\ \frac{J}{mol}} - \frac{-1.461}{8.314\frac{J}{K \times mol} \times T} \quad (4.10)$$

Euler's celebrated limit can then be used to describe the sub-Arrhenius behavior in terms of the deformed Arrhenius equation [172] as shown in Equation (4.11). Using the kinetic parameter, A from the sub-Arrhenius fitting, the deformation parameter, and the barrier height, the resulting rate equation based on Euler's celebrated limit is shown in Equation (4.12).

$$k(T) = A\left[1 - d\frac{E_0}{RT}\right]^{\frac{1}{d}} \quad (4.11)$$

$$k = 44\frac{mol}{s \times g_{cat}}\left[1 - (-1.461\frac{-2608\frac{J}{mol}}{8.314\frac{J}{mol \times K} \times T})\right]^{\frac{1}{-1.461}} \quad (4.12)$$

The activation energies elucidated for xylitol S-HDO in the case of Arrhenius and sub-Arrhenius kinetics are lower than reported literature values for other compounds previously discussed [152], [165], [166]. Recently, Cao et al. reported theoretical and experimental activation energies that were also significantly lower than previously reported activation energies for similar reactions [152]. Cao et al. evaluated the S-HDO reaction for several methyl glycosides over ReO_x-Pd/CeO_2 and used DFT to model the reaction

mechanisms. They found the reaction order with respect to the substrate concentration and hydrogen to be almost zero. This result suggests that the active site is almost saturated with methyl glycosides during the reaction. It also suggests that the rate-determining step is not the coordination of the substrate to the Re species or the hydrogenation reaction, but rather that the desorption step is the rate-determining step. Similarly, the desorption step is possibly the rate limiting step for xylitol S-HDO due to the similar reaction orders seen with the methyl glucosides. However, since there is tunneling occurring in the reaction and the proposed mechanisms don't have hydrogen involved in the desorption step, the rate limiting step likely another intermediate or the coordination of the substrate which involves hydrogen. There could also be a limitation due to a reaction between the adsorbed pentene-triols with hydrogen on the catalyst surface. This occurs when the equilibrium is completely shifted to the right for hydrogenation as reported in other systems in the literature [183], [184]. Further modeling and DFT calculations would be needed to investigate this potential limitation and the potential impacts on the reaction mechanism. Cao et al. evaluated methyl α-l-rhamnopyranoside and methyl α-l-fucopyranoside, which are stereoisomers, as model compounds for methyl glycosides. They found a near 5-fold difference in the reactivity of the methyl glycosides with the methyl α-l-rhamnopyranoside having the higher reaction rate, suggesting that geometric orientation of the OH functional groups plays a significant role in the activity. This relationship was also seen in the Arrhenius plots which showed that the methyl α-l-rhamnopyranoside (63 kJ/mol) had an activation energy that was 10 kJ/mol lower than methyl α-l-fucopyranoside (73 kJ/mol). Cao et al. also attributed the activation energy difference between the methyl glycosides to

the substrates having either different transition states or adsorption states due to their differing geometry.

The activation energy for xylitol S-HDO we report is lower than reported by Cao et al. for the methyl glycosides over a similar temperature range, but is much closer to their reported experimental values than previous theoretical calculations in the literature (shown in Table 4.1). There are several possibilities why the activation energy for xylitol S-HDO is lower than the other reported reactions. First, the structure of xylitol is more simplistic than many of the other reported compounds modeled in the fact that it is linear, and has only cis hydroxyl groups, which could explain the disparity. Xylitol has five cis-vicinal hydroxyl groups, which could make it more likely for the xylitol to adsorb to the ReO_x since there are multiple pairs of hydroxyl groups that have the possibility of adsorbing to the catalyst. As seen by the two products, 1,2-dideoxypentitiol and 1,2,5-pentanetriol, the C_1-C_2 or C_2-C_3 hydroxyl groups can be adsorbed and undergo the S-HDO. It has been shown for other sugars in similar reactions that the reaction rate was dependent on the stereochemical configuration and strongly influenced the adsorption and activation energy [185]. It has also been shown that for the S-HDO of methyl glycosides that only the cis-vicinal OH groups can be selectively removed and that the trans-vicinal OH groups can still be adsorbed on the active site but suppresses the reaction [186]. The possible suppression of the reaction and blocking of active sites would not occur for the xylitol S-HDO due to the presence of only cis vicinal hydroxyl groups in xylitol. However, the additional hydroxyl groups could potentially cause steric hindrance. It has also been shown for the hydrogenolysis of glycerol that due to steric reasons, the primary hydroxyl group is cleaved more readily as compared to secondary hydroxyl groups [187]. This could explain

the higher selectivity to 1,2-dideoxypentitiol, which is formed from the cleavage of a primary and a secondary hydroxyl group as compared to 1,2,5-pentanetriol, which forms due to the cleavage of two secondary hydroxyl groups. However, the selectivity difference observed between 1,2-dideoxyhexitol and 1,2,5-pentantetriol was not drastic, suggesting that the potential steric effects likely aren't the key reason the activation energy is lower. Xylitol has two primary hydroxyl groups, which can also potentially be a reason why the activation energy is lower as compared to the other substrates, such as 1,4-anhydroerythritol and methyl α-l-rhamnopyranoside, which contain only secondary hydroxyl groups. For the DODH of methyl α-l-rhamnopyranoside and methyl α-l-fucopyranoside, as shown in Cao et al., reactants had three vicinal hydroxyl groups, and the resulting reaction had a lower activation energy than for compounds such as 1,4-anhydroerythritol [152], [154], which have two vicinal hydroxyl groups. There may be a relation between the number of available vicinal hydroxyl groups and the activation energy of the reaction. If a relationship did exist, it could further explain the lower activation energy seen for the xylitol S-HDO. In the literature, it has been reported that the reaction rate of dehydration in sugar alcohols is correlated to the strength of the C-O bond [188], [189]. It has been reported that the C-O bond strength has an inverse relationship with the number of hydroxyl groups on the alcohol. This relationship implies that the more OH groups the alcohol contains, the lower the C-O bond strength, which results in a higher reaction rate. The lower C-O bond strength could be a substantial reason why the xylitol S-HDO activation energy is lower, since xylitol has five hydroxyl groups. It is also possible that there could be a significant difference between the activation energies for cyclic molecules and xylitol, which is a straight chain. This could be due to steric hindrance, or

differences in the strength of the C-O bond for linear and cyclic molecules. However, more work needs to be performed to fully investigate why the activation energy is lower in comparison and to incorporate tunneling into the reaction mechanisms.

4.2.4 MASS TRANSFER EVALUATIONS

To determine if there were any internal diffusion limitations present in the reaction, the Weisz–Prater criterion was for both reactants (xylitol and hydrogen). The criterion was calculated from the following equation:

$$C_{WP} = \frac{-r_A(obs) \times \rho_c \times R^2}{D_e \times C_{AS}} \tag{4.13}$$

In Equation 4.13, the reaction rate observed is r_A, ρ_c is the density of ceria, R is the radius of the ReO_x-Pd/CeO_2 particles, which was determined from SEM, D_e is the effective diffusivity, and C_{AS} is the reactant concentration at the particle surface. For the liquid–liquid diffusion, D_e is estimated/assumed to be on the order of 10^{-9} m^2/s based on similar reactions reported in the literature [190]–[193]. However, to be conservative and to allow for deviation and error in our estimations, we are estimating D_e to be on the order of 10^{-10}.

For xylitol, the lowest concentration a reaction point in this study was used for C_{AS} to be conservative, which was at the final time point of the 160 C and 0.5 g xylitol run discussed later in this section. With the resulting terms in Equation 4.13 for xylitol plugged in, the result is as follows:

$$C_{WP} = \frac{7.04 \times 10^{-4} \left(\frac{mol}{kg \times s}\right) \times 7220 \left(\frac{kg}{m^3}\right) \times (2.15 \times 10^{-6})^2 \, (m^2)}{10^{-10} \left(\frac{m^2}{s}\right) \times 51 \left(\frac{mol}{m^3}\right)} \tag{4.14}$$

$$C_{WP} = 4.61 \times 10^{-3}, C_{WP} \ll 1 \tag{4.15}$$

Since the Weisz–Prater criterion is much less than 1 for xylitol, it can be assumed that no internal diffusion limitations are present for xylitol diffusion in the reaction.

For hydrogen diffusing in the solvent, the D_e and C_{AS} values change from Equation 4.14. For hydrogen, D_e has been reported to be on the order of 10^{-9} m^2/s in 1,4-dioxane in the literature [190]. However, to be conservative, we are using a D_e value of 10^{-10} to make sure that at a worst case scenario there wouldn't be any limitations. C_{AS} was estimated by using Henry's law and solubility data for H_2 in 1,4-dioxane from the literature [194]. Based on the enthalpy, entropy, and mole fraction solubility data presented, a Henry's law constant (k_H) of 3.89×10^{-4} mol kg^{-1} bar^{-1} was calculated. This value is reasonable considering that the Henry's law constant for hydrogen in water is on the same order of magnitude when using data from the NIST database. C_{AS} was calculated based on 10 bar H_2 pressure with H_2 being the only gas in the reactor. The result resulting concentration of hydrogen in the solvent was 4.01 mol/m^3. With the resulting terms for hydrogen, the result is as follows:

$$C_{WP} = \frac{7.04 \times 10^{-4} \left(\frac{mol}{kg \times s}\right) \times 7220 \left(\frac{kg}{m^3}\right) \times (2.15 \times 10^{-6})^2 \, (m^2)}{10^{-10} \left(\frac{m^2}{s}\right) \times 4.01 \left(\frac{mol}{m^3}\right)} \tag{4.16}$$

$$C_{WP} = 5.86 \times 10^{-2}, C_{WP} \ll 1 \tag{4.17}$$

Since the Weisz–Prater criterion is much less than 1 for hydrogen, as shown in Equations 4.16 and 4.17, it can be safely assumed that no internal diffusion limitations are present for hydrogen diffusion in the reaction. Thus there are no internal diffusion limitation for either reactants used in this kinetic study.

To determine if there were any external mass transfer limitations present in the reaction, a mixing evaluation study was conducted by varying the stirring rate of the

magnetic stir bar within the reactor over a wide range (150-700 rpm). Stir rates of 150–700 rpm were evaluated for the xylitol S-HDO at 160 °C and 10 bar H_2 at the reaction concentrations previously discussed. The S-HDO reaction rates as a function of the stirring rate are shown in Figure 4.12. Over the stirring range tested, there was no significant difference between any of the reactions conducted, as all of the reaction rates were within experimental error of each other. The standard error for the 550 rpm reaction was calculated from three separate reactions at the same condition and was determined to be 9.81×10^{-9} mol s^{-1} g_{cat}^{-1} (2.02%). Since there was no significant difference by varying the stirring rate, there is no evidence of external mass transfer limitations being present during the reactions.

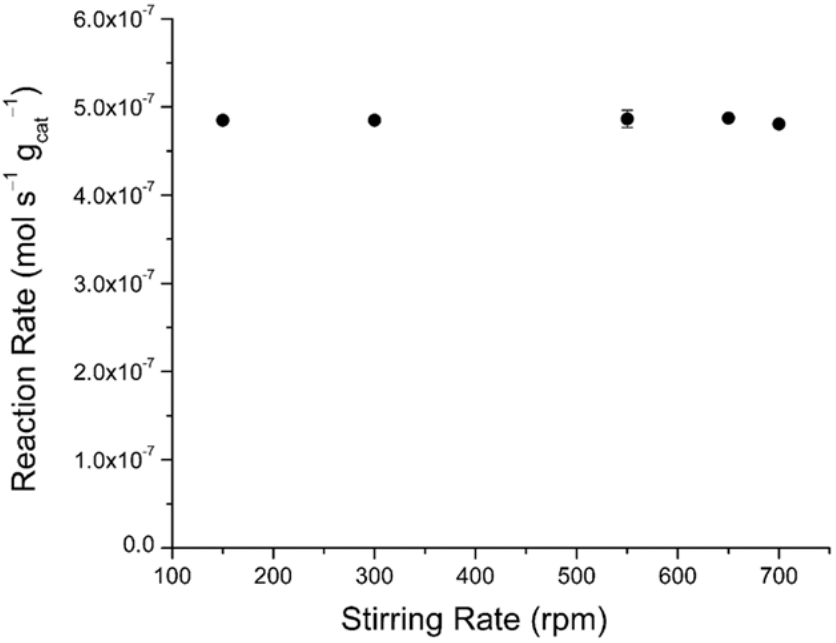

Figure 4.12. Evaluation of mixing and associated mass transfer. [71]

The effect of xylitol concentration on the reaction rate was investigated to evaluate concentration effects and determine optimal conditions. Reactions were conducted by varying the xylitol concentration from 0.962–13.4 wt% (0.5–8 g) while keeping the reactant to catalyst weight ratio constant (0.30 g catalyst: 1 g xylitol). By fixing the reactant

to catalyst ratio, the reaction rate on a per catalyst basis should be equivalent given the zero order relationship xylitol concentration was shown to exhibit. For each reaction, 50 mL of solvent (1,4-dioxane) was used, and the reaction temperature was fixed at 160 °C for direct comparison. The reaction rate as a function of xylitol concentration is shown in Figure 4.13. The reaction rate on a mol s^{-1} basis increases linearly in the 0.962–7.21 wt% region, as seen in Figure 4.13a, and as expected due to the zero order relationship of xylitol concentration previously found in the general kinetics investigation. Above the 7.21 wt% (4 g) point, the reaction rate still increases, but the increase in reaction rate is lower than expected based on a linear trend. It is likely that above 7.21 wt% of xylitol, significant solubility issues occur, and that the undissolved xylitol could be blocking the catalyst in the reaction mixture and preventing it from adsorbing dissolved xylitol. It has been shown in the literature that xylitol has a very high solubility in water, but for organic solvents the solubility can drop by several orders of magnitude [195], [196]. When the reaction rates were normalized to the mass of catalyst, the rates in the 0.962–7.21 wt% region were comparable, but the 3.74 wt% (2 g) rate was slightly higher, as shown in Figure 4.13b. The standard error of the 3.74 wt% reaction rate was 9.81×10^{-9} mol s^{-1} g_{cat}^{-1} (2.02%), based on three experimental runs. The slightly higher reaction rate at the 3.74 wt% point could be attributed to experimental error, but if the highest reaction rate is sought after, it is the optimal point tested in this study. However, since the 7.21 wt% point was comparable, if this process were to be scaled up, it would be optimal due to the higher amount of total reactant that could be utilized and upgraded. More investigation between the 7.21 and 13.4 wt% data points should be investigated to see at what concentration the drop off in activity

occurs to further optimize this process for scaling, and to investigate the solubility of xylitol in 1,4-dioxane.

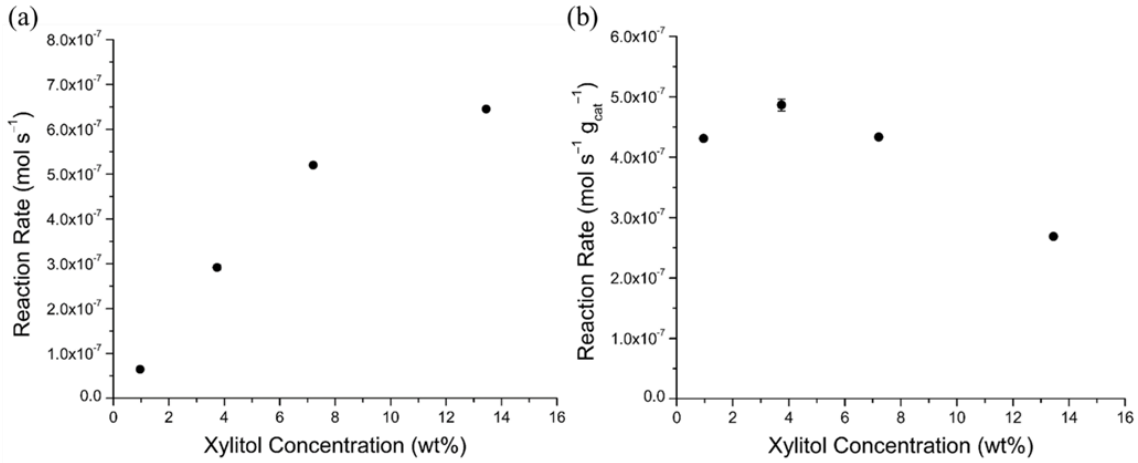

Figure 4.13. Xylitol concentration effect on reaction rate at 160 °C. (a) Rate in mol s^{-1}, (b) rate in mol s^{-1} $gcat^{-1}$. [71]

4.3 CONCLUSIONS

In conclusion, a comprehensive kinetics study of xylitol simultaneous hydrodeoxygenation was conducted, reaction orders were determined, activation energy was evaluated, and internal and external mass transfer and diffusion were investigated. The S-HDO of xylitol over ReO_x-Pd/CeO_2 was determined to be a zero-order reaction. The Arrhenius activation energy of the reaction was determined to be 48.7 ± 10.5 kJ/mol over the 150-170 °C temperature range. A sub-Arrhenius relation was found from 120–170 °C in which activation energy was temperature dependent and ranged from 10.2–51.8 kJ/mol. The sub-Arrhenius relationship indicated that there was quantum tunneling occurring in the reaction, likely involving the hydrogen. The tunneling of hydrogen in the reaction suggests that the proposed reaction mechanisms in the literature either are not accurate for

xylitol S-HDO or that they can't account for the tunneling phenomena. Since the hydrogen tunneling bypasses the energy barrier of the reaction, the hydrogen must be involved with the rate determining of the reaction, which is not currently suggested in the proposed mechanisms. More work needs to be done theoretically (using DFT) and experimentally (using in-situ spectroscopy techniques such as Raman or DRIFTS) to investigate the possible reaction mechanisms and intermediates that could help explain the tunneling observed through the sub-Arrhenius relationship for this reaction.

Various mass transfer evaluations were conducted to ensure that our results were not skewed by transport limitations or phenomena. The Weisz–Prater criterion was evaluated to investigate internal diffusion, and it was determined that no internal diffusion limitations were present for both reactants (xylitol and hydrogen) since the criterion was much less than 1 for both species. There were no external mass transfer limitations found when varying the stirring rate over a range of 150–700 rpm, as the reaction rates were within experimental error of each other over the entire range. It was further shown that no mass transfer limitations were present in our system since there was a sub-Arrhenius relationship present, and if limitations or transport phenomena were preset, we would expect to see a super-Arrhenius relationship.

From the characterization of the ReO_x-Pd/CeO_2 catalyst, insight into the active species in the reaction was elucidated. The di-oxo (O=Re=O) species of ReO_x was found to increase in concentration as temperature is increased in Raman spectroscopy, suggesting that it is likely the active species within the reaction. The shift in mono-oxo to di-oxo ReO_x suggests that there could be competing mechanisms in the reaction which could further explain the sub-Arrhenius relationship observed in this work. However, further

investigation via isolating the two structures and evaluating them separately experimentally and theoretically should be conducted to evaluate if there are truly competing mechanisms. It was also determined that the catalyst synthesis parameters and environment cause a small agglomeration of the CeO_2 particles. This slight agglomeration increases the average particle size from 3.00 to 4.30 μm.

CHAPTER 5

OPTIMIZATION OF SORBITOL HYDRODEOXYGENATION VIA DESIGN OF EXPERIMENTS

5.1 MOTIVATION AND EXPERIMENTAL

5.1.1 MOTIVATION

Sorbitol is a sugar alcohol that is commonly used as a sugar substitute commercially. Sorbitol can be produced from lignocellulosic biomass by first extracting cellulose, and then upgraded to sorbitol through a catalytic hydrogenation process [197]–[203]. The production of sorbitol is expected to increase to over 2.4 million tons by 2023 with a value of $4 billion dollars by 2023, up from 1.85 million tons in 2015 [200]. The large scale production of sorbitol offers a promising renewable feedstock that could be utilized for upgrading to other value products. Biomass derived sugar alcohols, like sorbitol, can be upgraded into various value added fuels and chemicals by removing hydroxyl groups from the sugar alcohol [17], [69], [133]–[135], [204]. A promising route for the removal of hydroxyl groups is the simultaneous hydrodeoxygenation (S-HDO), a reaction which cleaves two vicinal hydroxyl groups utilizing a state of the art ReO_x-Pd/CeO_2 catalyst [38], [69], [71], [147], [152]. The ReO_x-Pd/CeO_2 catalyst has been shown

to be a more active for the S-HDO reaction than other ReO_x, MoO_x, WoO_x, MnO_x, and VO_x, supported catalysts in the literature [147]. The S-HDO reaction consists of a deoxydehydration (DODH) step which cleaves the hydroxyl groups and forms a double bond, and a hydrogenation step which hydrogenates the double bond to a single bond. The ReO_x supported on the CeO_2 catalyzes the DODH step while the Pd catalyzes the hydrogenation step through hydrogen dissociation on the surface of the catalyst [38], [147], [154]. Sorbitol S-HDO can produce various dideoxyhexitols, hexanediols, and hexane, as shown in Figure 5.1. Hexanediols are commonly used as chemical additives, solvents, and for polymer production [205]–[207]. 1,6-hexanediol had a market size of $902 million in 2019 and is expected to grow to $1401 million by 2025 [206]. Similarly, 1,2-hexanediol had a market of $40 million in 2019 which is expected to reach $54 million by 2024 [205].

Sorbitol S-HDO to 1,2-, 1,4-, and 1,6-hexanediol could be a potentially renewable route to chemicals with large established markets, in which a drop-in strategy could be utilized [18]. The drop-in strategy takes advantage of existing value chains and infrastructure to capture a mature market by using a biomass resource to form a platform chemical for which existing intermediates can be obtained [18]. Using this methodology, the renewable biomass resource could replace or reduce the dependence on fossil resources for chemical production. This strategy has been utilized with corn biomass by fermenting the biomass into ethanol and then converting the ethanol into ethylene for use as an intermediate. 1,2-hexanediol and 1,6-hexanediol are roughly 40-49 times as valuable as sorbitol on a per mass basis and 1,4-hexanediol is up to 7,750 times as valuable on the same basis. This upgrading shows significant promise in terms of economic potential to upgrade

a renewable sugar alcohol to widely utilized chemicals with established infrastructures and value chains.

1,2-hexanediol can also be further converted to hexane, which can be used as fuel or solvent [208], [209]. However, there is an order of magnitude value loss on a per mass basis when converting 1,2-hexanediol to hexane, and it requires a much longer reaction time to produce. Thus, for this study we focus on the production of hexanediols as our target products since they have the most promising economic pathway. However, down the road sorbitol S-HDO could off a potentially economic manner to produce hydrocarbon fuels from a renewable resource by producing hexane.

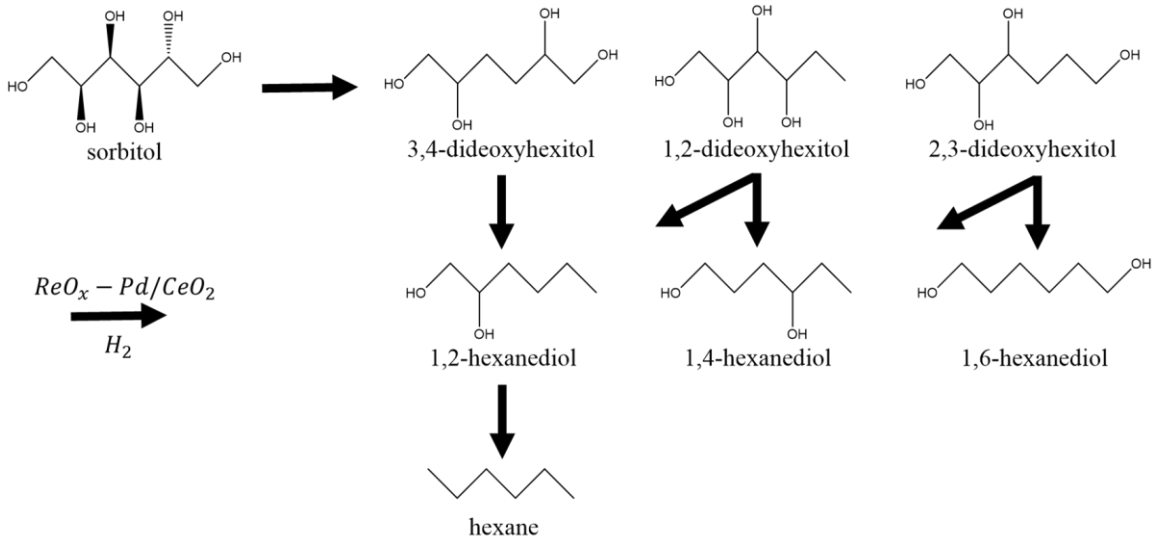

Figure 5.1. Sorbitol simultaneous hydrodeoxygenation schematic.

Sorbitol S-HDO was previously reported in the literature at 160 °C, 80 bar H_2, utilizing a 2 wt% ReO_x-Pd/CeO_2 catalyst, and a reaction time of 72 hours [147]. However, this reaction was not optimized and the various reaction parameters such as temperature, pressure, catalyst active metal loading, and reaction time were not probed. It has been previously reported that for 1,4-anhydroerythritol and xylitol S-HDO, that pressure, temperature, and Re loading can have a significant effect on S-HDO conversion, and

selectivity [69]. However, for sorbitol S-HDO, the effects of temperature, pressure, and Re loading on conversion and selectivity to hexanediols are unknown. In order to elucidate the relations, model the design space, and predict optimal conditions, an L9 Taguchi deign and a Box-Behnken design of experiments were utilized. The different designs were utilized to determine if a more simplistic design, such as a Taguchi design could elucidate the same relationships as a more complex design, such as a Box-Behnken design. Being able to elucidate and extract the most amount of knowledge while needing the fewest amount of experiments is ideal and can help fuel future discoveries.

5.1.2 CHEMICALS

D-Sorbitol (CAS No. 50-70-4) ≥ 98%, 1,4-Dioxane (CAS No. 123-91-1) 99.9%, 1,2,5-Pentanetriol (CAS No. 14697-46-2) 97%, 1,2-Hexanediol (CAS No. 6920-22-5) 98%, 1,6-Hexanediol (CAS No. 629-11-8) 99%, n-Hexane (CAS No. 110-54-3) 99%, Ammonium perrhenate (CAS No. 13598-65-7) ≥ 99%, Palladium (II) nitrate (10 wt% in 10 wt% nitric acid) (MDL: MFCD00011169) 99.999%, Cerium (IV) oxide (CAS No. 1306-38-3), and Ultra High Purity (UHP) Hydrogen (CAS No. 1333-74-0) 99.999%, were used in this study. The cerium (IV) oxide was donated by Daiichi Kigenso Kagaku Kogyo Co., Ltd. Osaka, Japan. The UHP hydrogen was obtained from Praxair, the 1,2,5-Pentanetriol was obtained from Combi-Blocks, the 1,4-Dioxane and n-Hexane were obtained from Thermo Fisher Scientific, and all remaining above-mentioned chemicals were obtained from Sigma-Aldrich.

5.1.2 CATALYST SYNTHESIS AND PREPARATION

The ReO_x-Pd/CeO_2 catalysts used in this study were made via wet impregnation using previously reported methodology [38], [69], [70]. The catalysts in this study were

made with a molar ratio of Pd to Re of Pd/Re = 0.25, which corresponds to a weight ratio of Pd/Re = 0.15. The nominal loadings of the catalysts used were 2.0 wt% Re and 0.30 wt% Pd, 3.0 wt% Re and 0.45 wt% Pd, and 4.0 wt% Re and 0.60 wt% Pd. The CeO_2 support was first calcined in air at 600 °C for 3 h and was then cooled to room temperature. The ReO_x was then impregnated onto the CeO_2 support via wet impregnation using an aqueous solution of ammonium perrhenate (NH_4ReO_4) with the desired Re concentration based on the target nominal loading. The solution was then dried at 110 °C for 12 h to allow for the water to evaporate from the solution and leave only the ReO_x/CeO_2 remaining. The palladium was then impregnated onto the ReO_x/CeO_2 using wet impregnation using an aqueous solution palladium (II) nitrate ($Pd(NO_3)_2$) with the desired Pd concentration based on the target nominal loading. The solution was then dried at 110 °C for 12 h and the ReO_x-Pd/CeO_2 powder was then removed. The ReO_x-Pd/CeO_2 was then calcined in air at 500 °C for 3 h with a ramping rate of 10 °C/min. After calcination, the sample was cooled to room temperature and the catalyst was then ground into a fine powder using a mortar and pestle.

5.1.3 CATALYST CHARACTERIZATION

The 2-4 wt% (nominal Re wt%) ReO_x-Pd/CeO_2 catalysts utilized in this study were characterized using X-ray Diffraction (XRD), X-ray Fluorescence Spectroscopy (XRF), Inductively Coupled Plasma—Optical Emission Spectrometry (ICP-OES), *in-situ* Raman Spectroscopy and Scanning Electron Microscopy (SEM).

X-ray Diffraction (XRD) was conducted on the ReO_x-Pd/CeO_2 catalysts using a Rigaku MiniFlex II with Cu Kα source radiation (α = 1.5406 Å). Each sample was scanned between a 2θ of 10° to 80° with a step size of 0.02° and a scanning rate of 2°/min. The

resulting diffraction patterns for the 2, 3, and 4 wt% Re catalysts are shown in Figure 5.2. All three diffraction patterns matched the reference patterns for CeO_2 and previously reported ReO_x-Pd/CeO_2 catalyst diffraction patterns [69], [71]. No Re or Pd diffractions were observed, implying that the Re and Pd particles are well dispersed on the catalyst surface.

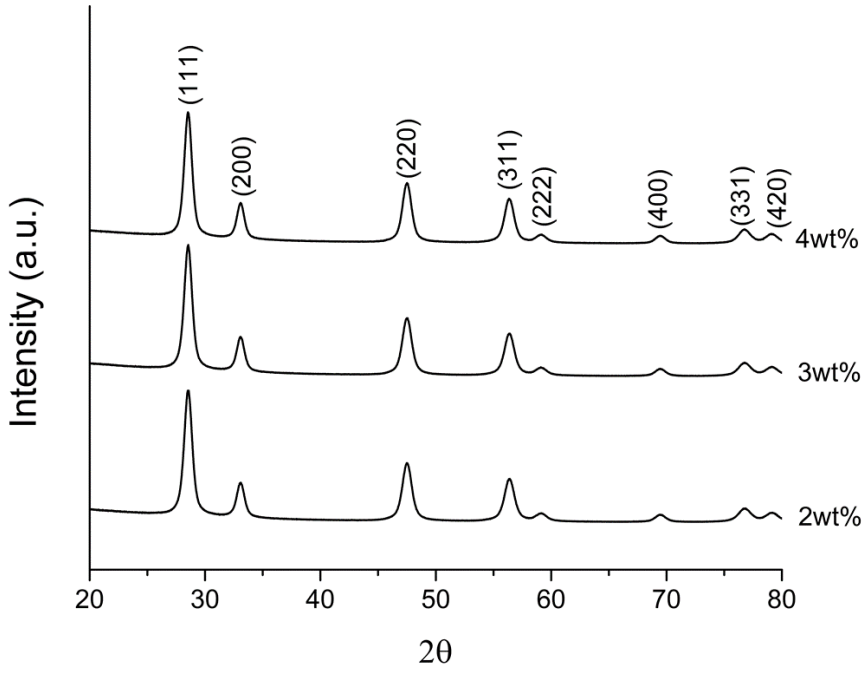

Figure 5.2. XRD patterns of 2, 3, and 4 wt% ReO_x-Pd/CeO_2 catalysts at a scanning rate of 2 °/min.

X-ray Fluorescence Spectroscopy (XRF) was conducted on the catalysts using a Fischerscope XDAL system utilizing a 0.30 mm collimator size. The catalyst powders were placed in XRD sample holders (diameter of 24 mm and a depth of 2 mm) and flattened for analysis. Samples were scanned at 9 equally spaced points away from the edges of the sample holder. Each point was subjected to an 80 s scan for analysis. The XRF was used

in standard free mode, which allows for a qualitative measure of the distribution of the elements being scanned. The resulting XRF compositional scans of the ReO_x-Pd/CeO_2 catalysts for Re and Pd are shown in Figure 5.3.

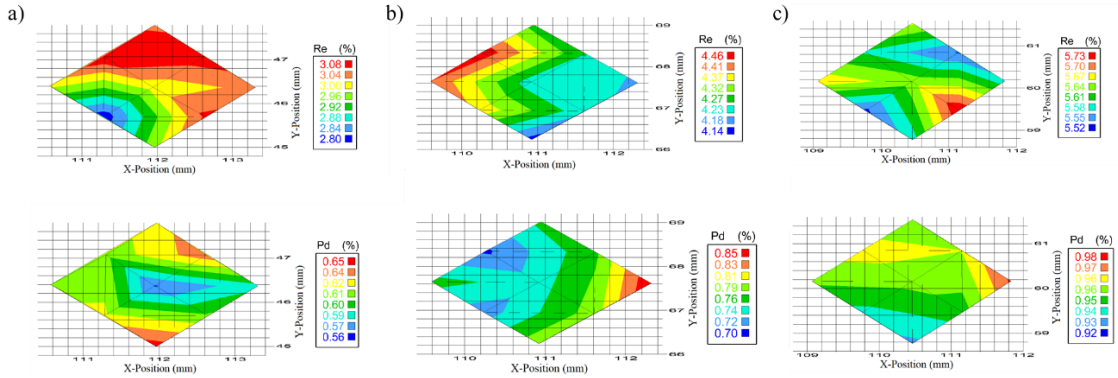

Figure 5.3. XRF composition scans of design of experiments catalysts. a) 2 wt% Re 0.3 wt% Pd b) 3 wt% Re 0.45 wt% Pd c) 4 wt% Re 0.60 wt% Pd

The mean, standard deviation and the coefficient of variation of the scans for the respective catalysts are shown in Table 5.1. The catalyst metal dispersions were similar between the samples. The 2 wt% ReO_x-Pd/CeO_2 sample showed some localization in the Re and Pd scans, but the coefficient of variation was only roughly 3% and 4% for the Re and Pd respectively. The coefficient of variation is the ratio of the standard deviation to the mean, and measures relative dispersion of the data. The 3 wt% ReO_x-Pd/CeO_2 sample showed the highest variation of the samples with respect to Pd, with a coefficient of variation of 5.7%. The 4 wt% ReO_x-Pd/CeO_2 sample showed the lowest variation in terms of both Re and Pd and suggests that this catalyst could be the most uniformly distributed. However, the lower coefficient of variance and standard deviation observed could be due to the fact that there is a significantly higher loading of both Re and Pd in this sample. The higher nominal loadings increase the mean of the scans which can result in a reduction of

the coefficient of variation. All samples had similar standard deviations within the Re and Pd scans respectively as shown in Table 5.1.

Table 5.1. XRF sample statistics for design of experiments ReO_x-Pd/CeO_2 catalysts.

Sample (Re)	**2 wt%**	**3 wt%**	**4 wt%**
Mean (μ)	3.02	4.31	5.63
Stand. Dev. (σ)	0.09	0.11	0.07
C.O.V (σ/μ)	3.06%	2.57%	1.26%
Sample (Pd)	**0.30 wt%**	**0.45 wt%**	**0.60 wt%**
Mean (μ)	0.62	0.78	0.96
Stand. Dev. (σ)	0.03	0.04	0.01
C.O.V (σ/μ)	4.02%	5.69%	1.44%

Inductively Coupled Plasma—Optical Emission Spectrometry (ICP-OES) was performed on a Perkin Elmer Avio 200 equipped with an S10 autosampler. ICP-OES was conducted to determine the actual loading of Re and Pd in the various ReO_x-Pd/CeO_2 catalysts. The catalysts were digested in freshly prepared aqua regia. The samples were digested for 12 h at 120 °C following the procedure previously reported by MacQueen et al. [70], [71]. The catalysts used in this study were analyzed for both Re and Pd and had a nominal loading of 2.0, 3.0, and 4.0 wt% Re and 0.30, 0.45, and 0.60 wt% Pd, respectively. Each sample was analyzed three times in the ICP-OES and error was quantified via standard deviation. For Re the 221.42 and 227.53 nm wavelengths were used for analysis and in the Pd the 340.46 and 363.47 nm wavelengths were used. The catalysts were determined to have an actual Re loading of 1.93 ± 0.02 wt%, 2.88 ± 0.02 wt%, and 3.81 ± 0.02 wt%, respectively. The actual Pd loading of the catalysts were determined to bed 0.203 ± 0.007 wt%, 0.335 ± 0.005 wt%, and 0.461 ± 0.018 wt%, respectively.

In-situ Raman spectroscopy was conducted with a Horiba XploRA Plus Raman microscope that utilizes a 30 mW excitation source, a 638 nm diode laser, and a Horiba Scientific charge-coupled device detector. The detector was thermoelectrically cooled to -

50 °C. The 638 nm diode laser was calibrated using a silicon standard. A Linkam THMS600PS in-situ Raman cell that used recirculating water as a temperature control was utilized for the experimentation. We followed the procedure for pretreatment, and analysis previously reported by MacQueen et al. [71]. The sample was first loaded into the stage and the laser was focused and an ambient spectrum was taken. The sample was then calcined by flowing 20 sccm of ultra-high purity O_2 (99.9993% O_2) and heating the sample to 550 °C at a ramping rate of 50 °C/min. Once the sample reached 550 °C, the temperature was held constant for 30 min. The cell was then purged with Ar to remove all O_2 and was then reduced in a 1:1 volume mixture of H_2 and Ar with a total flow of 20 sccm for 10 min while maintaining a temperature of 550 C. After 10 min a spectrum was taken to ensure that the sample was fully reduced. After the reduction, the H_2 flow was turned off and the cell was purged with Ar to evacuate any remaining H_2. The Ar flow was then turned off and the sample was reoxidized in 20 sccm of O_2 for 10 min at 550 °C. Following the reoxidation a spectrum was taken to ensure that the Re had reoxidized to ReO_x. The cell was then purged using Ar and the cell was cooled to 100 °C and held for 10 min while flowing 20 sccm of Ar. The sample was then heated to 150 °C at a rate of 5 °C/min and spectra were collected at 150, 160, and 170 °C after an isothermal hold of 5 min at each temperature.

In-situ Raman spectroscopy was conducted to investigate the change in ReO_x structure as a function of temperature and catalyst loading under reaction conditions. It was previously reported that the structure of ReO_x shifted to a higher concentration of di-oxo ReOx (O=Re=O) from the mono-oxo species (Re=O) as temperature was increased over the range of 100 to 180 °C in a 2 wt% ReO_x-Pd/CeO_2 sample [71]. This effect was

investigated for the 2, 3, and 4 wt% catalysts at 150, 160, and 170 °C to see if the reaction temperatures used in this study could be shifting the catalyst active metal structure. The mono-oxo (Re=O), di-oxo (O=Re=O), and oligomeric crosslinked (Re-O-Re) structures were present in the samples. The band assignments were based on previously reported literature [70], [71], [210]. The mono-oxo vibrational band is located at 998 cm^{-1}. The di-oxo bands are located at 992 and 982 cm^{-1} respectively for the symmetric and asymmetric stretches. The cross linked oligomeric species band was located 893, 898, and 901 cm^{-1} for the 2, 3 and 4 wt% species respectively. The full-width half maximums were fixed for each respective band across spectra, and the areas of the symmetric and asymmetric stretch bands were constrained to be equivalent during fitting. To compare the mono-oxo and di-oxo structures the areas of the symmetric bands of each were compared by dividing the di-oxo area by the mono-oxo area. The mono-oxo and di-oxo areas and area ratios are shown in Table 5.2 for the various spectra.

Table 5.2. In-situ Raman mono-oxo and di-oxo band comparison.

2 wt%	**Mono-oxo area**	**Di-oxo area**	**Di-oxo : Mono-oxo**
170 °C	38.2	25	0.65
160 °C	41.2	25	0.61
150 °C	39.7	25.7	0.65
3 wt%	**Mono-oxo area**	**Di-oxo area**	**Di-oxo : Mono-oxo**
170 °C	36	24.7	0.69
160 °C	38.4	24.4	0.64
150 °C	43.4	22.7	0.52
4 wt%	**Mono-oxo area**	**Di-oxo area**	**Di-oxo : Mono-oxo**
170 °C	39.5	24.7	0.63
160 °C	42.2	22.3	0.53
150 °C	45.7	19.3	0.42

The 2 wt% and 3 wt% spectra are shown in Figure 5.4 and Figure 5.5 respectively. The 2 wt% sample showed no substantial difference in terms of area ratio over the temperature range tested. This indicates that during the various design temperatures

evaluated, the speciation of ReO_x (mono-oxo and di-oxo concentrations) remained fairly constant.

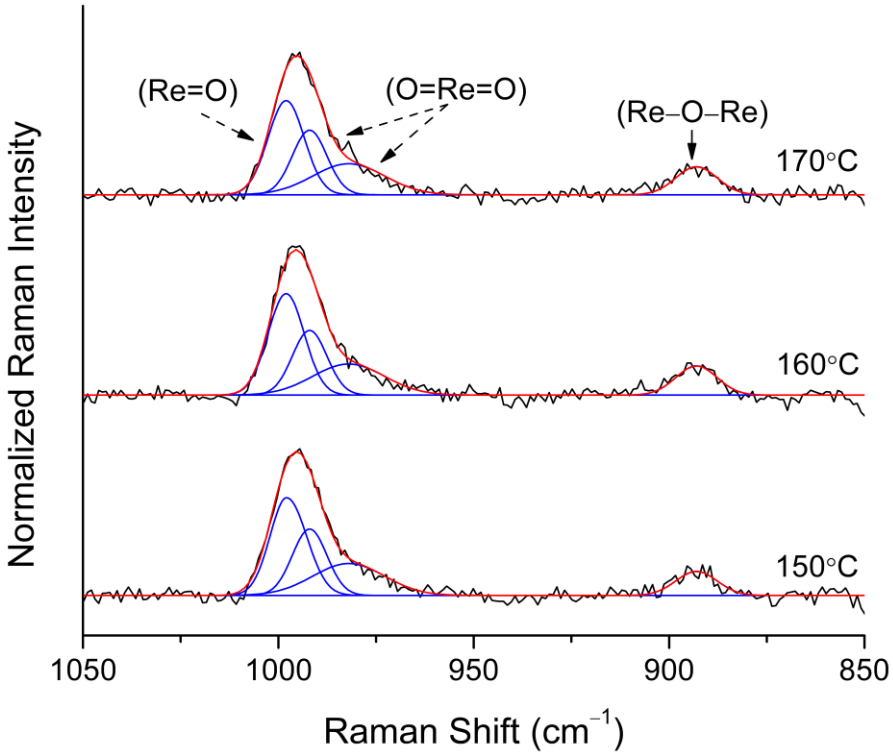

Figure 5.4. In-situ Raman spectroscopy of 2 wt% ReO_x-Pd/CeO_2 catalyst under Ar flow post calcination, reduction, and re-oxidation.

However, the 3 wt% (Figure 5.5) and 4 wt% (Figure 5.6) samples showed a significant increase in the di-oxo structure as a function of temperature. The 3 wt% sample had a significant increase in the di-oxo species area from 150 to 160 °C, with a significant decrease in the mon-oxo area. However, from 160 to 170 °C, the di-oxo species respective area increased only slight while the mono-oxo species still significantly decreased in area.

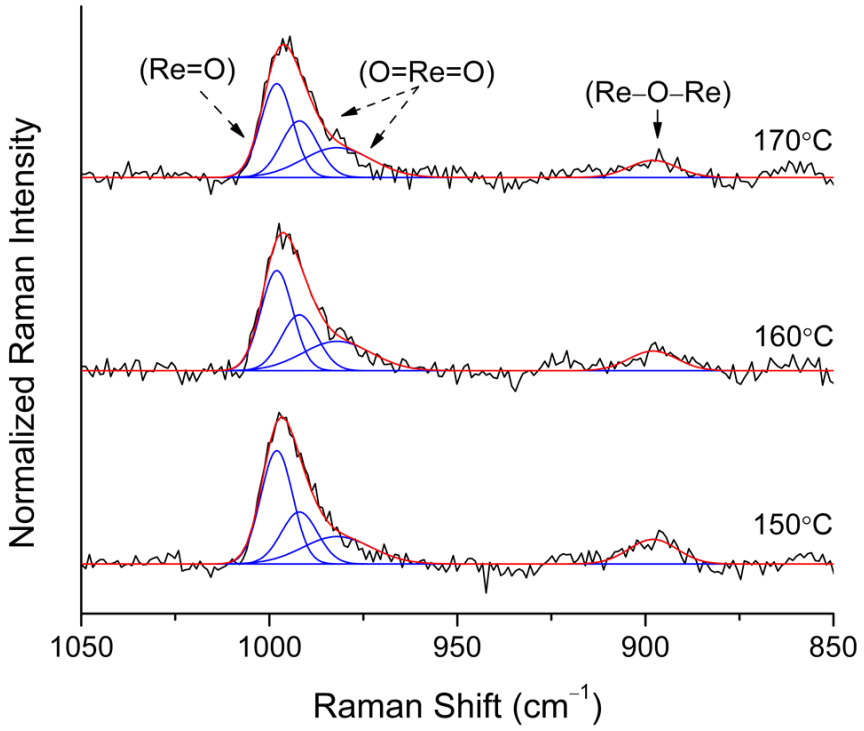

Figure 5.5. In-situ Raman spectroscopy of 3 wt% ReO_x-Pd/CeO_2 catalyst under Ar flow post calcination, reduction, and re-oxidation.

The 4 wt% sample showed the largest change in area ratio (0.42 to 0.63) over the temperature range tested and the spectra are shown in Figure 5.6. The increase in the concentration of the di-oxo species is likely due to oxygen migration from the ceria support [71], [167]–[171]. However, the degree of this oxygen migration seems to depend on the weight loading of the Re on the catalyst, with the higher Re concentration leading to a higher extent of oxygen migration.

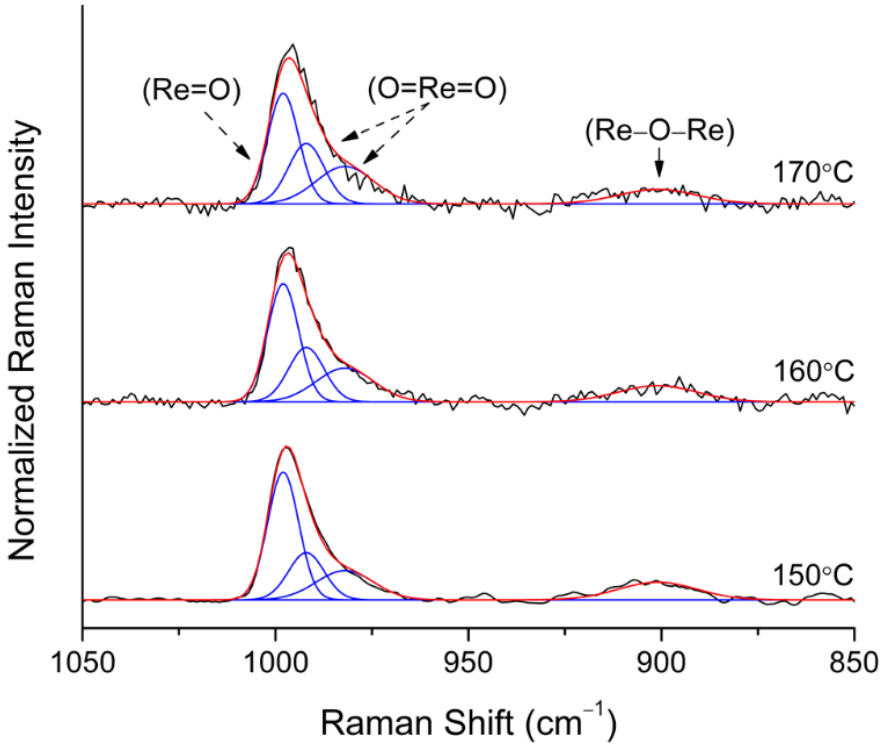

Figure 5.6. In-situ Raman spectroscopy of 4 wt% ReO_x-Pd/CeO_2 catalyst under Ar flow post calcination, reduction, and re-oxidation.

The 170 °C spectra of the 2, 3, and 4 wt% catalysts are shown in Figure 5.7. The area ratios only vary slightly between the spectra with the 3 wt% having a slightly higher di-oxo concentration compared to the other catalysts.

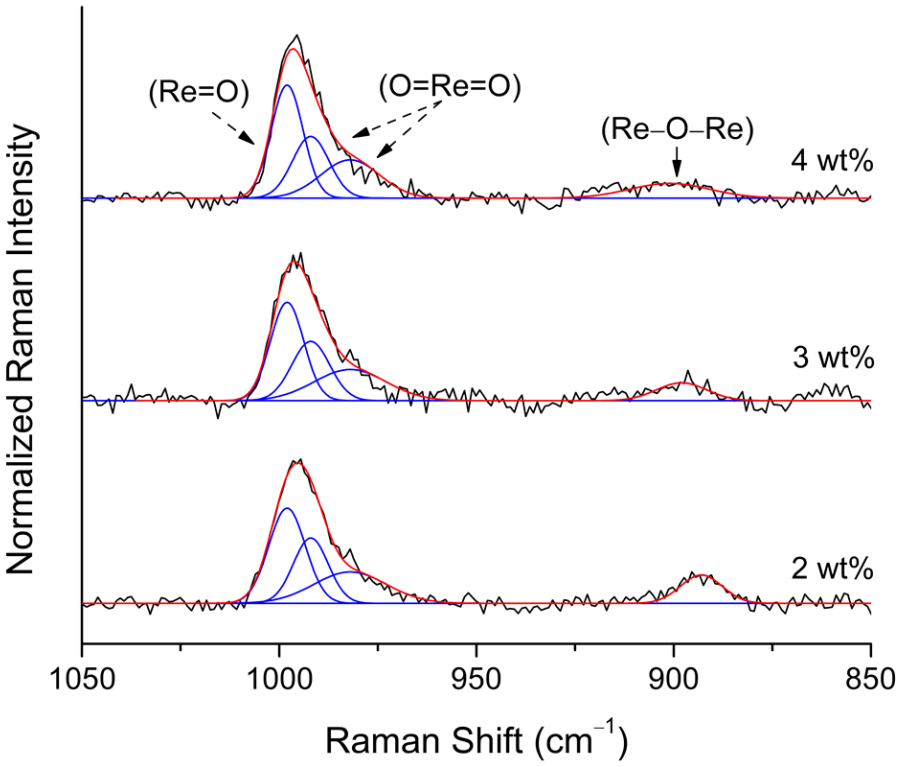

Figure 5.7. Comparison of design of experiments ReO_x-Pd/CeO_2 catalysts Raman spectra at 170°C under Ar flow post calcination, reduction, and re-oxidation.

Scanning Electron Microscopy (SEM) was performed on a Zeiss Gemini 500 Field Emission Scanning Electron Microscope with a Type II Secondary Electron Detector (SE2) and a voltage of 5.0 keV. A working distance of 6.4 mm was utilized for the microscopy. SEM was conducted to determine the particle size of the CeO_2 for the various weight loadings of ReO_x-Pd/CeO_2 catalysts used in this study. It has previously been shown that the morphology of the catalyst particles does not change during the synthesis methodology used to make these catalysts [71]. SEM images at 10,000 x magnification and particle size distributions of the 2, 3 and 4 wt% catalysts are shown in Figure 5.8.

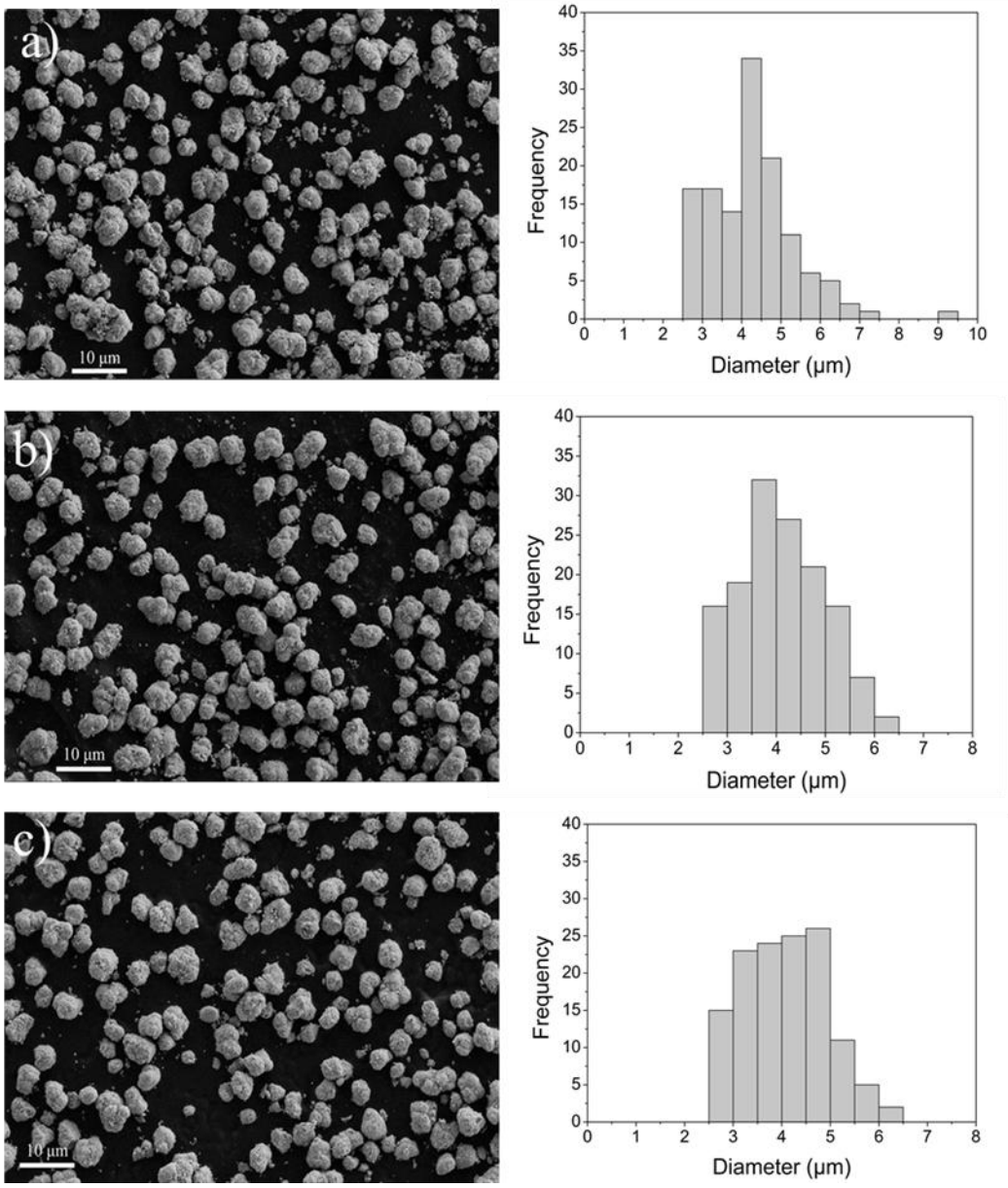

Figure 5.8. SEM images and particle size distribution of ReO_x-Pd/CeO_2 catalysts at 10,000 x magnification catalysts. a) 2 wt% ReO_x b) 3 wt% ReO_x c) 4 wt% ReO_x.

The average particle size (diameter) of CeO_2 for the 2, 3, and 4 wt% ReO_x-Pd/CeO_2 catalysts were 4.30, 4.12, and 4.07 µm respectively. The particle sizes were consistent with previously reported ReO_x-Pd/CeO_2 catalysts synthesized with the same support, precursors, and methodology [71]. There was no significant difference between the particles' morphologies at various weight loadings. The distribution in particle size

changed slightly between the samples but the average particle sizes were similar. The 2 wt% catalyst had the largest average particle size due to the presence of several larger particles present in the sample. These larger agglomerates are very few in number but were dispersed throughout the sample. SEM images of the various catalysts at 5000, 25,000, and 100,000 x magnifications are shown in Figure 5.9. At all magnifications, the morphology of the particles is consistent. At 100,000 x magnification, there appears to be some lighter small specs/particles on the catalyst which are likely the Re. However, without elemental mapping it is hard to determine if this is truly Re of if it is Ce. The Re is also likely impregnated in the pores of the CeO_2 which would not be visible unless elemental mapping was conducted.

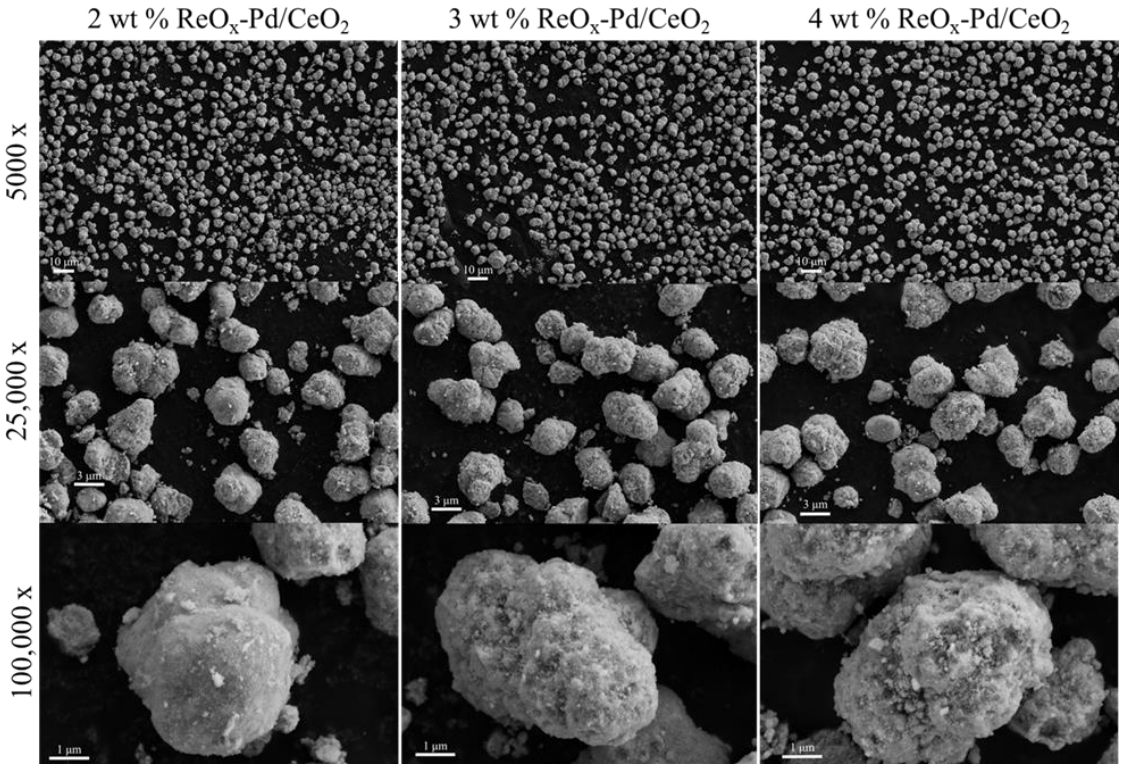

Figure 5.9. SEM images at various magnifications of 2, 3, and 4 wt% ReO_x-Pd/CeO_2 catalysts.

5.1.3 DESIGN OF EXPERIMENTS AND DESIGN SPACE

An L9 Taguchi design and a Box-Behnken Response Surface design of experiments were utilized to investigate the effects of temperature, pressure, and catalyst loading on the conversion, selectivity and yield of sorbitol S-HDO to hexanediols. The design of experiments was utilized to elucidate optimal reaction conditions within the design space as well as compare the throughput to knowledge gained benefit of the more complex Box-Behnken design to the robust Taguchi design. The designs were created and analyzed in Minitab.

Sorbitol S-HDO was previously reported at 160 °C, 80 bar H_2 and was conducted for 72 h [147]. However, our previous work has shown that for the S-HDO of 1,4-anhydroerythritol and xylitol, the pressure can be significantly reduced while maintaining comparable conversion and selectivity [69], [71]. Since the temperature, pressure, and Re loading of the catalyst have been shown to be significant for similar reactants, they were the factors selected for investigation in the design of experiments. For the designs, temperature was varied from 150 to 170 °C, pressure was varied from 5 to 10 bar, and Re loading was varied from 2-4 wt%. For temperature, we wanted to use the literature point as a mid-point to investigate if milder conditions could result in comparable yields or if higher temperatures would be optimal, as we would expect from kinetics. Pressure was varied from 5-10 bar to probe milder conditions and to see if the zero order relationship of hydrogen pressure, reported for xylitol S-HDO [69], [71], was seen at lower than 10 bar for the sorbitol S-HDO. Re loadings of 2-4 wt% Re were selected based on the optimal loadings previously reported for the ReO_x-Pd/CeO_2 catalyst in the literature [38], [147].

A 3 factor 3 level Taguchi design was constructed and tested for the sorbitol S-HDO reaction. Taguchi designs have been shown to be effective for reaction and catalyst optimization, while greatly reducing the experimental throughput for the elucidation of relationships of factors and responses [69], [117], [120], [129]. Taguchi designs aim to maximize the various responses, in our case conversion and selectivity, given the input variables (temperature, pressure, and Re loading) [123], [132]. The number of experiments needed for this statistical design scales with the number of factors and levels for each factor. The Taguchi design drastically reduces the necessary experimental runs through the use of orthogonal arrays [132], [211]. This can lead to a significant saving in time, experimental runs, and various associated costs by using this method as opposed to other more advanced statistical designs [132]. However, due to its design, the Taguchi design is limited to linear correlations of the responses to the input factors. Due to this limitation, co-factor interaction and higher order terms such as quadratic terms are not able to be modeled [155], [156]. However, if the Taguchi design can capture the design space as accurately as a more complex design, the savings in time, and costs would present it as a strong candidate as an optimization tool for similar design spaces and applications in the future. The full design layout of the L9 Taguchi design used in this study is shown in Table 5.3.

Table 5.3. L9 Taguchi Design of Experiments.

Run #	Temperature (°C)	Pressure (bar)	Re wt% Loading
1	150	5	2
2	150	7.5	3
3	150	10	4
4	160	5	3
5	160	7.5	4
6	160	10	2
7	170	5	4
8	170	7.5	2
9	170	10	3

A 3 factor 3 level Box-Behnken design utilizing 1 base block and 3 replicates of the center point was constructed and tested for the sorbitol S-HDO reaction. Box-Behnken designs model curvature and elucidate optimal factor setting within a design space. The design uses co-factor interaction terms and quadratic terms along with the standard linear terms to model the responses of the various factors [115]. Box-Behnken methodology has been shown to be slightly more efficient than central composite designs and significantly more efficient than full factorial designs [115]. However, the Box-Behnken design does not test the extremes of each factor by expanding past the specified design space as a typical response surface design would [212]. This testing of extremes can be helpful for probing outside of an experimental design space. However, for continuous factors, which we use in this study, it can suggest unfeasible reaction conditions or material synthesis if operating near the limits of your experimental system. In this study, we are probing the high end of feasible reaction temperatures for our reactor system, and thus we selected the Box-Behnken design to avoid testing higher reaction temperatures than our specified design space. Box-Behnken methodology has been used for catalytic and reaction condition optimization successfully in the literature [121], [213], [214]. This design was used to probe if temperature, pressure, or Re loading of the catalyst had any co-factor interaction and if the design space could be more accurately modeled using nonlinear equations. The full design layout of the Box-Behnken design used in this study is shown in Table 5.4.

Table 5.4. Box-Behnken Design of Experiments.

Run #	Temperature (°C)	Pressure (bar)	Re wt% Loading
1	150	5	3
2	150	7.5	2
3	150	7.5	4
4	150	10	3
5	160	5	2
6	160	5	4
7	160	7.5	3
8	160	7.5	3
9	160	7.5	3
10	160	10	2
11	160	10	4
12	170	5	3
13	170	7.5	2
14	170	7.5	4
15	170	10	3

5.1.4 ACTIVITY MEASUREMENTS AND CALIBRATIONS

For each sorbitol S-HDO reaction, the reactor was loaded with a magnetic stir bar, 1.0 g of sorbitol, 0.30 g of catalyst, and 50 mL of solvent (1,4-dioxane). The reactor was then sealed using an O-ring, and was tightened until it was pressure tight. To test the seal of the reactor, helium was used along with an electronic leak detector. Once it was determined to be pressure tight, the reactor was flushed three times with helium to evacuate any air remaining inside of the reactor. The reactor was then heated to the desired reaction temperature using an oil bath connected to a PID controller. When the desired reaction temperature was reached and stabilized, the hydrogen was added to the reactor, a constant pressure was maintained, and the reaction time was started. An initial sample was taken immediately after adding the hydrogen to ensure that no reactions had occurred in the heating process and to account for any conversion from the initial addition of hydrogen into the reactor. Samples were then taken at the 4 and 8 h reaction times for analysis.

The reaction samples were analyzed using Gas Chromatography (GC) to determine the concentrations of 1,2-dideoxyhexitol, 2,3-dideoxyhexitol, 3,4-dideoxyhexitol, 1,2-

hexanediol, 1,4-hexanediol, 1,6-hexanediol, and hexane present in the samples. Reaction samples were diluted by a factor of $\frac{125}{3}$ ($\frac{solvent}{reactant}$) times the original volume in methanol for analysis and to ensure the detector wouldn't saturate. Calibration curves for 1,2-hexanediol, 1,6-hexanediol, hexane, and 1,2,5-pentanetriol were made using known external standards and an 8-point calibration. The concentration of 1,4-hexanediol was estimated using the 1,2-hexanediol calibration and the concentration of the dideoxyhexitols was estimated using the 1,2,5-pentaetriol calibration, which is a similar compound produced in the S-HDO of xylitol [69], [71]. A Shimadzu GC 2010 Plus utilizing an AOC-5000 autoinjector and equipped with a Flame Ionization Detector (FID) was utilized. An RTX-1701 column with a column length of 30 m, an inner diameter of 0.32 mm, and a film thickness of 1.00 μm, was used for product separation. The injection port was set to 250 °C and the FID was set to 260 °C. 1 μL of sample was injected for each run, using a split ratio of 1:10 with a linear velocity of 38.9 cm/s, a column flow of 2.5 mL/min, and a total flow of 30.5 mL/min. Ultra high purity helium was used as the carrier gas for all samples and calibrations. The GC oven was programmed to start at 40 °C with a 3 min hold, followed by a ramp to 260 °C at 10 °C/min and a subsequent hold at 260 °C for 20 min. After the completion of each sample the column was cooled back to 40 °C while flowing carrier gas to prepare for the next sample. The injection needle was washed in acetone pre and post injection to prepare for the next sample.

5.2 RESULTS AND DISCUSSION

5.2.1 REACTION TIME DETERMINATION

To determine a reaction time at which meaningful comparisons could be made while minimizing reaction time for throughput considerations, a screening experiment was

conducted. A sorbitol S-HDO reaction was conducted for 22 h at 160 °C, and 10 bar H_2 utilizing a 2 wt% ReO_x-Pd/CeO_2 catalyst. The results of the reaction are shown in Figure 5.10, in which samples were taken every 2 h up to 10 h and then at 20 and 22 h. Initially, only the various dideoxyhexitols are formed in the reaction due to the S-HDO removing two vicinal hydroxyl groups from either the C_1-C_2, C_2-C_3, or C_3-C_4 hydroxyl groups. However, after 4 h 1,2-hexanediol and 1,4-hexanediol begin to be produced due to the dideoxyhexitols undergoing an S-HDO. The concentration of the dideoxyhexitols continues to increase up to the 20 h point. 1,6-hexanediol begins to be produced at the 8 h reaction point. Hexane production from the S-HDO of 1,2-hexanediol was not seen until the 22 h point in the reaction. Due to the various hexanediols being produced at the 8 h reaction point, it was determined that this was the best reaction time to make comparisons. After the 8 h point, the production to 1,2-hexanediol is much more selective than to the other hexanediol species. We would expect this trend to continue at longer reaction times. The 8 h reaction time also allowed for a reaction to be completed within one day allowing for a faster and more effective screening and probing of this reaction.

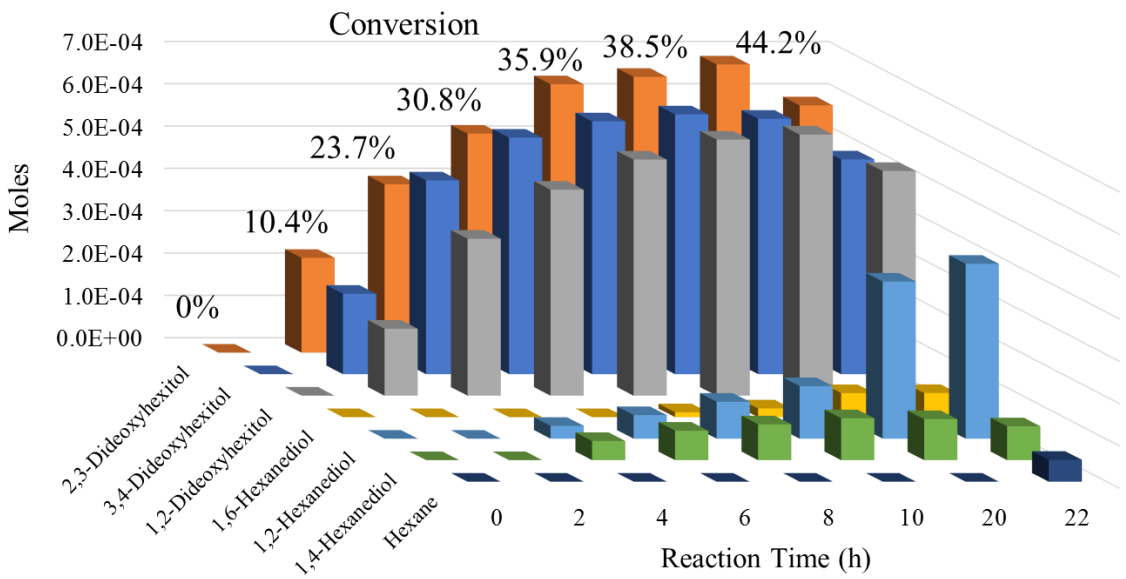

Figure 5.10. Sorbitol simultaneous hydrodeoxygenation product distribution as a function of time at 160 °C and 10 bar H_2.

5.2.2 TAGUCHI DESIGN

The reaction results from each run of the Taguchi design are shown in Table 5.5. The experimental standard error for the reaction points was determined to be 1.42 % and 0.43 % for conversion and selectivity respectively. The standard error was calculated based off of three separate experimental runs at the same conditions (160 °C, 7.5 bar H_2, 3 wt% Re loading), in which the standard error is equal to the standard deviation divided by the square root of the population size.

The correlations between temperature, pressure, catalyst Re loading and conversion and selectivity are shown in the main effects plot shown in Figure 5.11. The model suggests that temperature and pressure and directly related to conversion and selectivity and that Re loading is inversely related to the responses. Pressure is shown to be the most significant

factor in this design space. The model suggests a substantial drop in activity occurs when the pressure is reduced below 7.5 bar H_2.

Table 5.5. L9 Taguchi Design Reaction Results

Temperature (°C)	Pressure (bar)	Re wt% Loading	Conversion (%)	Selectivity to Hexanediols (%)
150	5	2	21.0	6.68
150	7.5	3	28.5	11.5
150	10	4	32.1	13.0
160	5	3	19.7	11.5
160	7.5	4	34.1	13.5
160	10	2	36.5	10.6
170	5	4	1.68	16.5
170	7.5	2	42.0	12.1
170	10	3	38.3	17.2

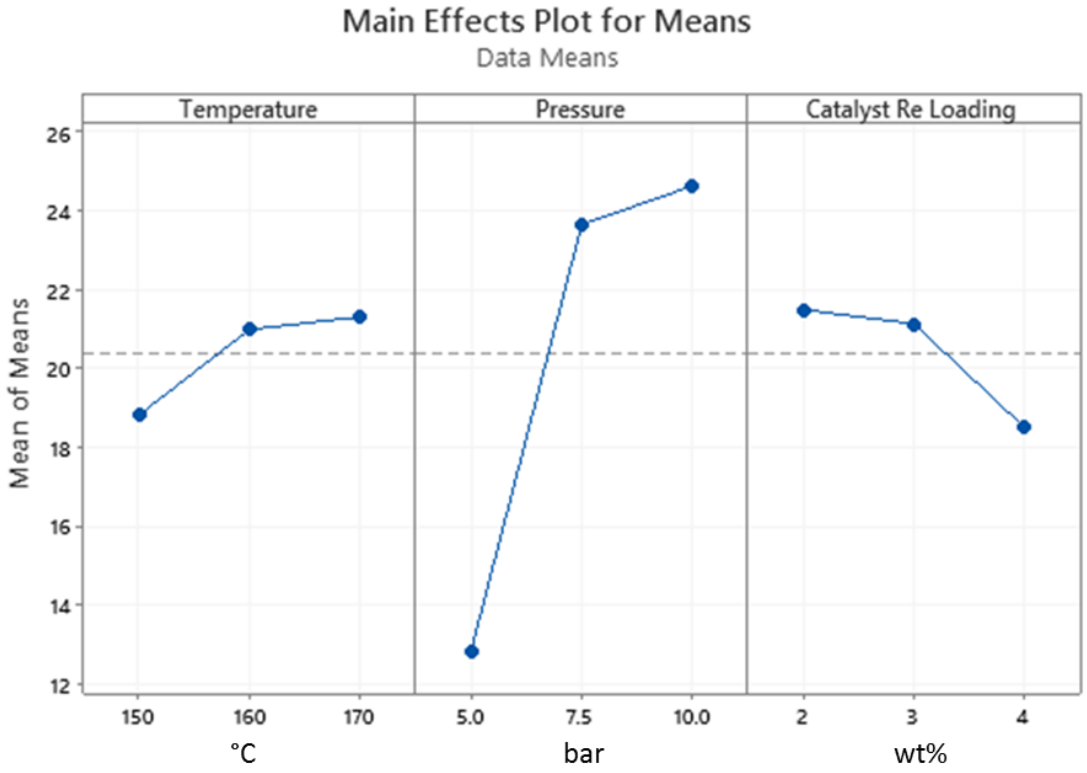

Figure 5.11. Main effects plot for Taguchi design for sorbitol conversion and selectivity to hexanediols.

To determine the exact effect of each parameter directly on conversion and selectivity, a linear regression was fit to the Taguchi design to model the design space. For

the regressions in this study, temperature, pressure, and catalyst Re loading were abbreviated as T, P, and C respectively. For conversion of sorbitol in the S-HDO reaction, the regression was determined to be the following:

$$Conversion = 10.9 + 4.30 \times P + 0.005 \times T - 5.27 \times C$$

However, the p-values for the constant, pressure, temperature, and catalyst Re loading terms were 0.860, 0.029, 0.988, 0.198 respectively. Thus assuming a significance level (α) of 0.05, only pressure is statistically significant for conversion. The regression equation was then updated to only include the pressure term and the pressure term constant was refit. The resulting regression is shown below.

$$Conversion = 3.798 \times P$$

The updated Taguchi conversion regression substantially improved the model fit as evident by the increase in the R^2, and the decrease in the standard error of the regression (S). The R^2 increase from 69.4 % in the original regression to 93.4 % in the updated regression. The standard error of regression is the standard deviation of the distance between the experimental data points and the predicated values from the model regression. S values are reported in the units of the corresponding response (conversion % or selectivity %). The standard error of regression decreased from 8.70 to 8.33 in the updated conversion regression. Conversion as a function of temperature and pressure, modeled by the updated Taguchi regression along with the experimental data points are shown in Figure 5.12. The conversion regression appears to capture the design space well, outside of two outliers at higher temperature (170 °C) and mid to low pressure (5, and 7.5 bar) points.

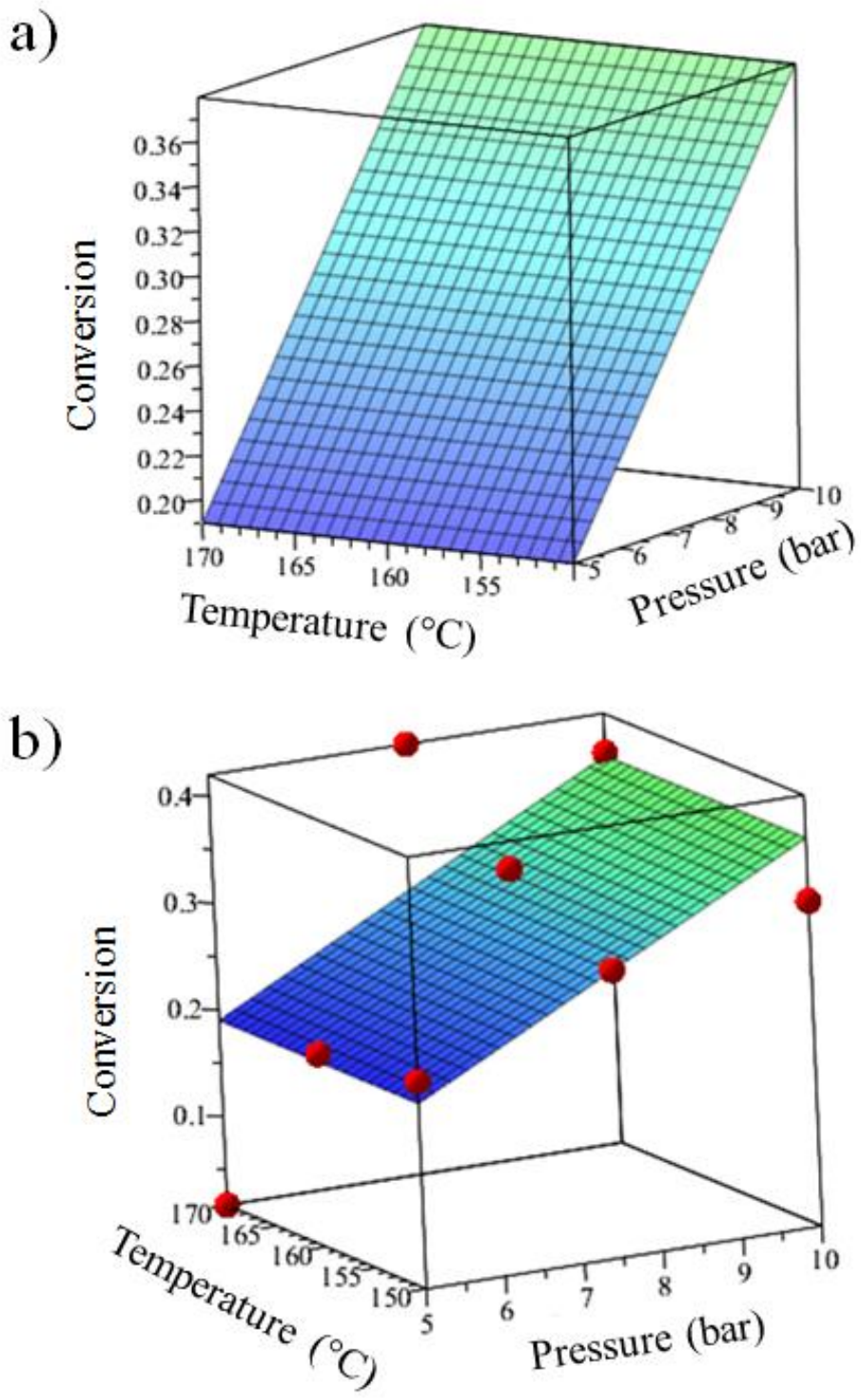

Figure 5.12. 3D conversion contour on a 0-1 scale using the updated Taguchi regression over the experimental design space. a) updated regression model b) experimental data points overlaid with model regression

For selectivity to hexanediols, the regression was determined to be the following:

$$Selectivity\ to\ Hexanediols = -36.28 + 0.410 \times P + 0.2429 \times T + 2.283 \times C$$

The p-values for the constant, pressure, temperature, and catalyst Re loading terms were 0.005, 0.073, 0.003, and 0.004 respectively. All terms except the pressure term were determined to be statistically significant since we assumed an α value of 0.05. The regression was then updated and refit by two different methods. A locked method was tested by locking all of the values from the original regression and allowing the constant to vary, and an unlocked method was tested by allowing all of the constants of the parameters to vary. It was determined that the locked methodology lead to a better fit. The updated regression is shown below.

$$Selectivity\ to\ Hexanediols = -33.196 + 0.2429 * T + 2.283 * C$$

The updated selectivity regression had a slight increase in the standard error of the regression from 1.11 to 1.25. This is likely due to the original model overfitting the data by using the pressure term which was found to be statistically insignificant. With pressure being significant for conversion, and temperature, and catalyst loading for selectivity, all factors in the design space were determined to be significant for a response (conversion or selectivity) in the Taguchi design.

5.2.3 BOX-BEHNKEN DESIGN

The reaction results from each run of the Box-Behnken design are shown in Table 5.6. The center point of the design (160 °C, 7.5 bar, 3 wt%) was conducted three times in the design. The standard error for these runs was determined to be 1.42 % for conversion and 0.43 % for selectivity.

Table 5.6. Box-Behnken Design Reaction Results

Temperature (°C)	Pressure (bar)	Re wt% Loading	Conversion (%)	Selectivity to Hexanediols (%)
150	5	3	24.9	11.7
150	7.5	2	32.9	11.0
150	7.5	4	32.2	17.7
150	10	3	29.6	9.85
160	5	2	20.2	9.29
160	5	4	24.6	19.8
160	7.5	3	32.7	16.8
160	7.5	3	31.5	17.0
160	7.5	3	36.2	18.1
160	10	2	36.5	10.6
160	10	4	32.0	18.3
170	5	3	6.21	5.95
170	7.5	2	42.0	12.1
170	7.5	4	33.3	17.1
170	10	3	38.3	17.2

For conversion of sorbitol in the S-HDO reaction, the Box-Behnken regression was determined to be the following:

$$Conversion = -69 + 1.66 \times T - 19.5 \times P + 22.0 \times C - 0.0097 \times T^2 - 1.237 \times P^2 + 2.60 \times C^2 + 0.2737 \times T \times P - 0.200 \times T \times C - 0.895 \times P \times C$$

The statistical significance of the factors for conversion are shown in the Pareto chart in Figure 5.13a. Using an α cutoff of 0.05, the factors that were statically significant for conversion are the constant, and the pressure, pressure^2, and temperature × pressure terms, which had p-values of 0.000, 0.005, 0.019, and 0.026 respectively. All of the insignificant factors were below the 0.05 α cutoff in terms of standardized effect which is represented by the red line at 2.571 standardized effect in the Pareto chart in Figure 5.13a.

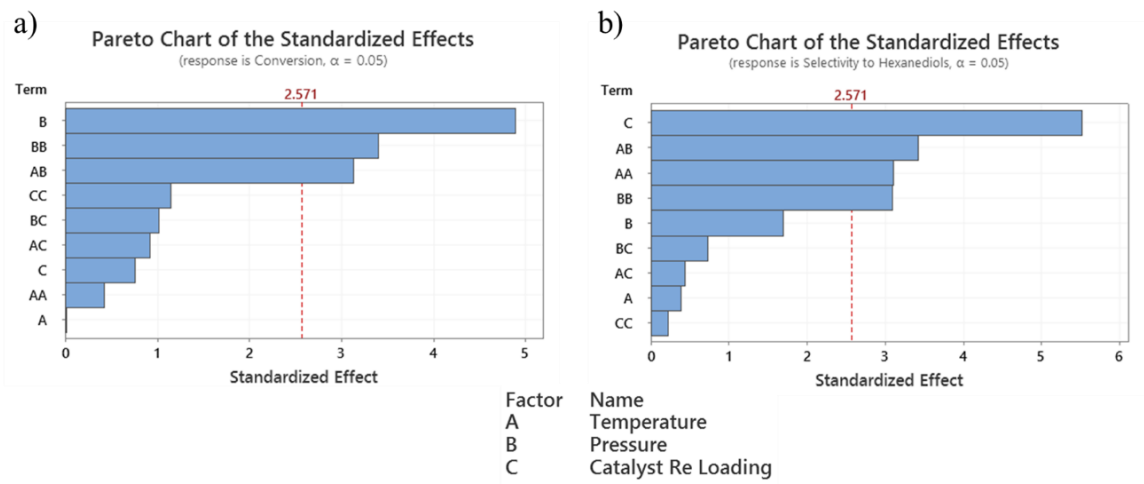

Figure 5.13. Pareto chart of the standardized effects of Box-Behnken factors. a) Conversion chart b) Selectivity to hexanediols chart

The Box-Behnken conversion regression was then updated via the methods previously described for the Taguchi selectivity regression. It was determined that unlocked methodology was optimal and it resulted in the following conversion equation:

$$Conversion = -58.93 + 19.49 \times P - 1.256 \times P^2 + 0.0148 \times T \times P$$

The updated conversion regression maintained a low standard error of regression (5.64) while drastically reducing the number of terms included in the regression. The standard error of regression did increase from the original regression (2.61) but avoids over fitting from the various statistically insignificant terms. Conversion as a function of temperature and pressure, modeled by the updated Box-Behnken regression along with the experimental data points are shown in Figure 5.14. The updated Box-Behnken conversion regression better captures the curvature in the data set as shown in Figure 5.14b, but still does not capture the outliers at low and mid pressures (5 and 7.5 bar) at high temperature (170 °C).

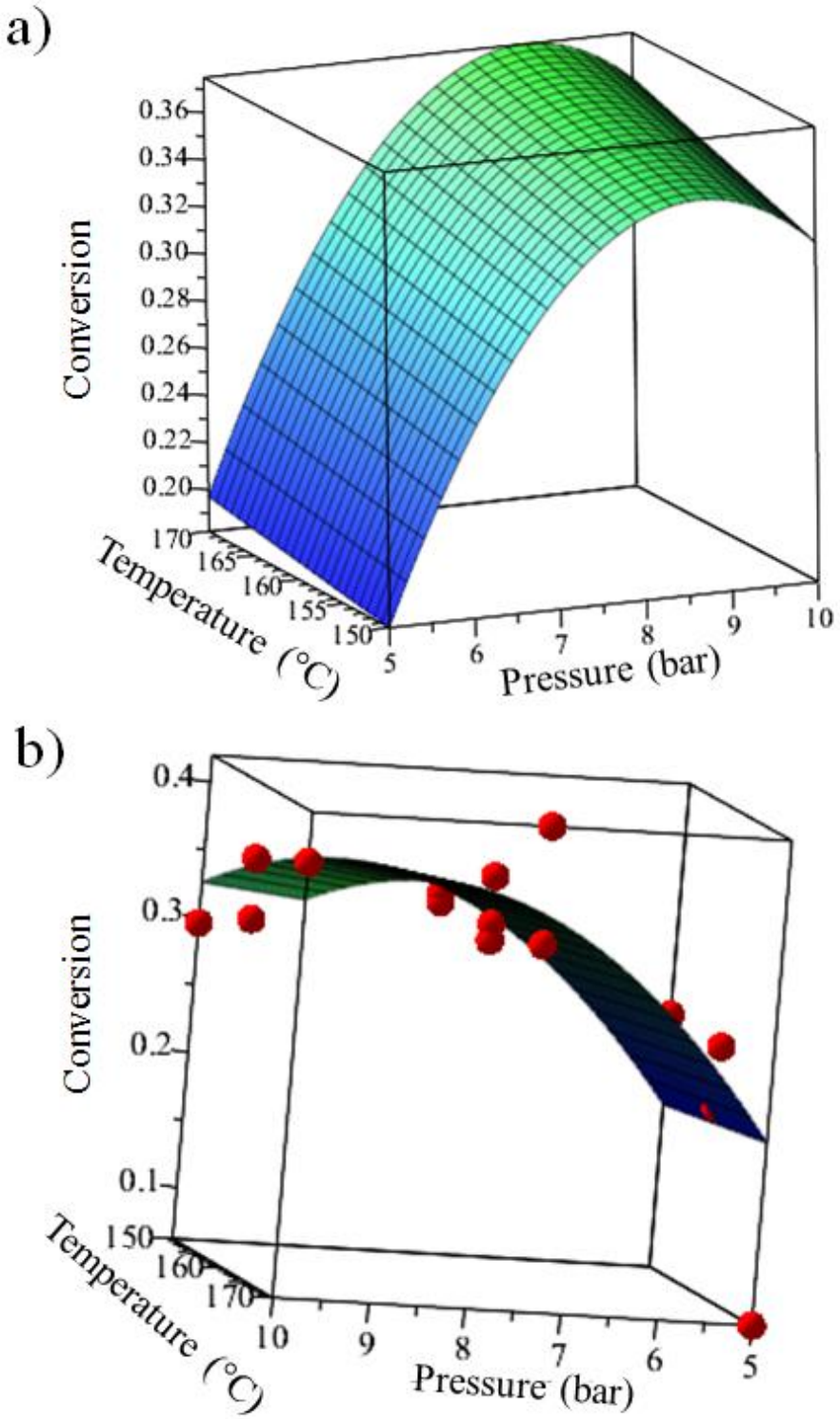

Figure 5.14. 3D conversion contour on a 0-1 scale using the updated Box-Behnken regression over the experimental design space. a) updated regression model b) experimental data points overlaid with model regression

For selectivity to hexandiols, the Box-Behnken regression was determined to be the following:

$$Selectivity\ to\ Hexanediols = -687 + 9.06 \times T - 12.26 \times P + 11.2 \times C - 0.0309 \times T^2 - 0.493 \times P^2 + 0.227 \times C^2 + 0.131 \times T \times P - 0.0418 \times T \times C - 0.281 \times P \times C$$

From the Pareto chart for selectivity shown in Figure 5.13b, it is determined that the constant, catalyst Re loading, temperature^2, pressure^2, and temperature × pressure are statistically significant with p values of 0.000, 0.003, 0.027, 0.027, and 0.019 respectively. Similar to the conversion regression, all other factors in the regression had p-values well above 0.05. Thus to avoid overfitting, the statistically insignificant terms were removed, and the regression was updated using unlocked methodology. The resulting updated selectivity regression is as follows:

$$Selectivity\ to\ Hexanediols = 1.480 + 3.732 \times C - 1.310 \times 10^{-3} \times T^2 - 0.5948 \times P^2 + 0.0588 \times T \times P$$

The updated selectivity regression had a slight increase in the standard error of regression from 1.14 in the original regression to 2.64. The updated regression suggests that all factors in the design space influence selectivity. This is the only updated equation from both models that incorporates all factors.

5.2.4 MODEL COMPARISONS

From the regression equations for conversion and selectivity, the optimal yield of hexanediols would be achieved at 170 °C, and 10 bar using a 4 wt% Re catalyst according to the Taguchi updated regression and at 170 °C, and 8.6 bar using a 4 wt% Re catalyst according to the updated Box-Behnken regression. Both models suggest that the highest

Re wt% catalyst is optimal. This could be due to more active sites being present on the higher loading catalyst, or it could be due to the higher di-oxo (O=Re=O) speciation of the 4 wt% catalyst at 170 °C, as seen in the in-situ Raman. The Taguchi updated regression predicts that at the suggested optimal conditions, conversion and selectivity would be 38.0 % and 17.2 % respectively, leading to a hexanediol yield of 0.065. The Taguchi updated regression optimal point was conducted and resulted in a conversion of 35.3 % and a selectivity to hexanediols of 22.8 %. This resulted in a yield of 0.081 which was slightly higher than the predicted value and was the highest of any reaction tested in this study. The optimal point suggested by the updated Box-Behnken regression was also evaluated. The predicted values for the Box-Behnken optimal were 37.5 % and 20.5 % for conversion and selectivity to hexanediols respectively, resulting in a yield of 0.077. The actual values were slightly lower than predicted at 35.5 % and 15.6 % for conversion and selectivity to hexanediols respectively. This results in a yield of hexanediols of 0.055.

When comparing the fit over the entire design space, the Box-Behnken updated conversion regression is more accurate than the updated Taguchi conversion regressions. The Box-Behnken updated conversion regression had a standard error of regression of 5.64 as compared to the updated Taguchi regression which was 8.33 respectively. However, for the updated selectivity regressions, the Taguchi model had a lower standard error of regression of 1.25 as compared the Box-Behnken S value of 2.64. For conversion, the reduction in S with the incorporation of higher order pressure terms shows the importance and non-linearity of the hydrogen pressure for S-HDO conversion. However, The Taguchi design was able to extract that hydrogen pressure was the most important factor for conversion. The Taguchi design didn’t suggest that temperature was also an important

factor as the Box-Behnken design did by suggesting a co-factor interaction between temperature and pressure. However, this term is the smallest contributor in terms of magnitude to the regression over the design space. Thus, the Taguchi design did a decent job of modeling the design space without the use of complex terms. This is more evident with the suggested maximum points of the models. The Box-Behnken maximum point had a more accurate prediction in terms of conversion, but the Taguchi maximum point resulted in a higher conversion. Since pressure was the only factor varied between these maximum points, it suggests that the higher pressure lead to increased conversion. This gives more evidence to the predictive power of the Taguchi design even though it had a higher S value.

For selectivity, the more simplistic Taguchi regression more accurately modeled the design space. The Taguchi design also avoids potential overfitting in mostly linear systems since it does not predict higher order or interaction terms. The updated Taguchi regression suggested that only temperature and catalyst Re loadings were significant as compared to the dependence on T^2, P^2 and a temperature and pressure interaction as suggested by the updated Box-Behnken regression. The increased model accuracy with only linear terms suggests that the higher order terms might be over fitting the data. This is also evident when comparing the p-values of the various factors. The p-values of the T^2, P^2, and $T \times P$ terms were an order of magnitude higher in value than the linear terms in the Taguchi model. This further suggests that the Taguchi design has significant predictive power given the limited data it required.

As a whole the Box-Behnken design more accurately modeled the design space but required a higher experimental throughput due to the additional experimental data points it required. The superior fit over the design space is more accurately shown when all

experimental points from both designs are fit against the respective regression models shown in Figure 5.15. The Taguchi regression (Figure 5.15a) captured the edges of the design space well, outside of outliers, but did not capture the center of the design space well. In contrast, the Box-Behnken regression (Figure 5.15b) captured all regions of the design space outside of the initial outliers on the edge of low pressure and high temperature.

The ability of the Box-Behnken regression to completely capture the design space gives more credibility to the relationships between the input factors and responses suggested by the model. While the additional data points and more complex regression and analysis did help the Box-Behnken model elucidate and establish co-factor interactions and higher order terms, it was not able to predict optimal conditions within the design space. However, the more robust and simplistic Taguchi design was not only able predict optimal conditions within the design space, it did so with less experimental data points, and a more simplistic model. The reduction in experiments when utilizing the Taguchi design can lead to significant time and experimental cost savings. This can lead to an efficient and fast optimization of reaction conditions and other factors of interest. The Taguchi design shows promise of being a way to quickly determine factor statistical importance, build simplistic models, and predict optimal conditions, especially for systems with limited throughput capabilities. However, the Taguchi design has limitations on how well it can accurately model the design space as a whole, since systems are not always linearly correlated. If capturing the design space as a whole the Box-Behnken design is likely the better option if the experimental throughput needed is available. However, if predicting and elucidating optimal conditions is the goal, the Taguchi design shows strong promise to be able to do so in a faster, cheaper, and more efficient manner.

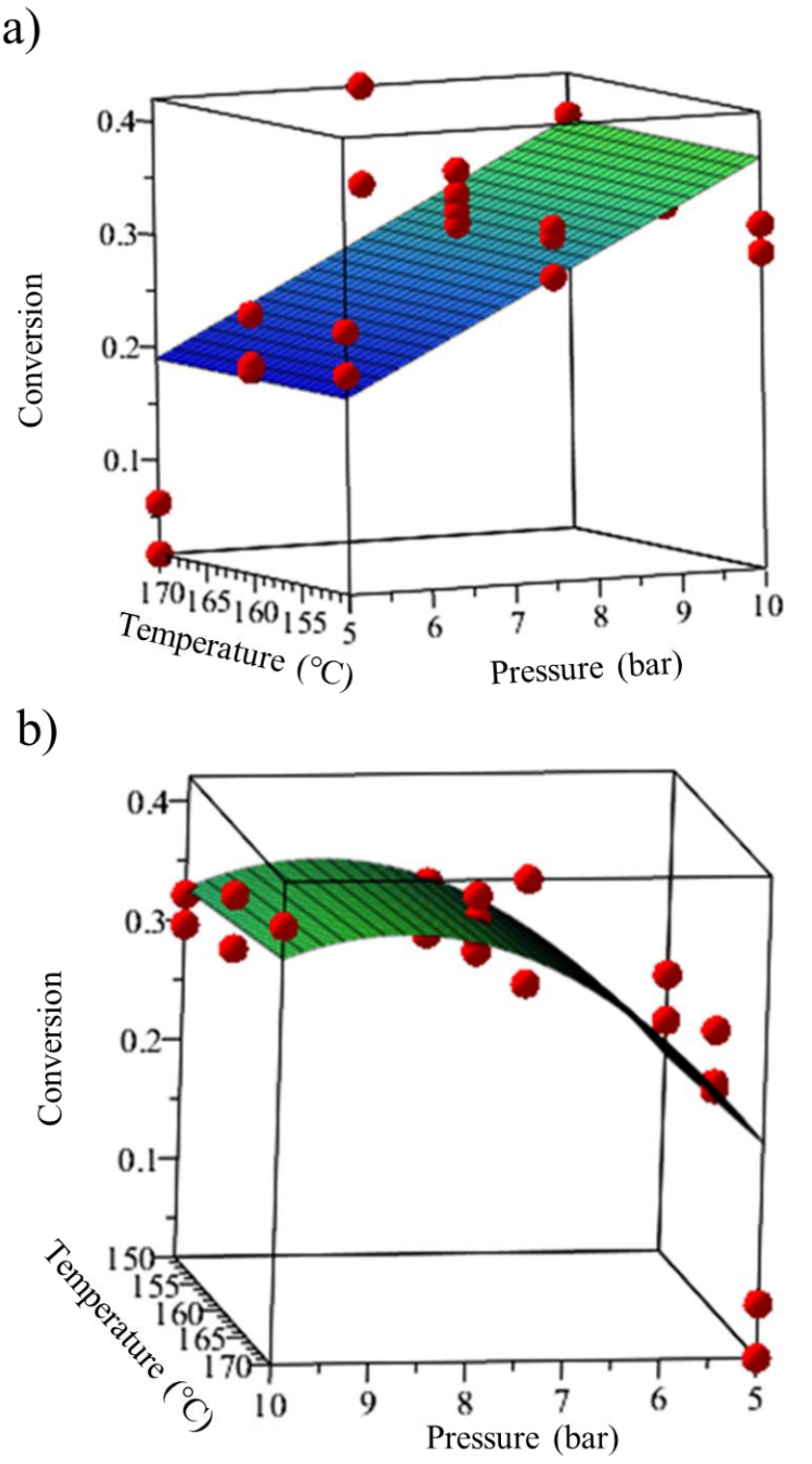

Figure 5.15. 3D conversion contours on a 0-1 scale using the updated Taguchi and Box-Behnken regressions with all experimental data from both designs included. a) Taguchi regression b) Box-Behnken regression

5.3 CONCLUSIONS

In conclusion, it was demonstrated that Taguchi design of experiments show promise in being able to accurately model catalytic design spaces utilizing less experiments and more simplistic regressions than Box-Behnken design of experiments. The Taguchi design compromised on the fit of the regressions, but was able to predict optimal conditions within the design space. The Box-Behnken design showed its strengths in being able to accurately model the entire design space and elucidate co-factor interaction. The maximum yield of hexanediols from sorbitol simultaneous hydrodeoxygenation was achieved at 170 °C, 10 bar, using a 4 wt% Re catalyst, as predicted by the Taguchi design regressions. The Box-Behnken regression suggested that a slightly lower pressure (8.6 bar) would lead to the optimal yield. The optimal points lead to comparable conversions of sorbitol, but the higher pressure lead to a substantial increase in the selectivity to hexanediols. This suggests that the Box-Behnken regression is likely over estimating the effects of pressure within the higher end of the design space. In terms of knowledge to throughput ratio, the Taguchi design was superior in being able to predict the optimal conditions. This trend would likely be more drastic in a more complex design space with either more factors and/or more than three levels. This work served as a base level proof of concept that the Taguchi designs can compete with the more complex design of experiments for these catalytic design spaces. However, more work will need to be done with a more complex design space to see if our findings hold merit and test the effectiveness of the Taguchi design methodology in scenarios in which experimental throughput capabilities are more limiting.

From the In-situ Raman spectroscopy, it was observed that the 4 wt% ReO_x-Pd/CeO_2 catalyst had the largest change in speciation from mono-oxo (Re=O) to di-oxo

(O=Re=O) as temperature increased within the design space. The 2 wt% sample remained fairly constant over the temperature range, while the 3 wt% sample changed similarly to the 4 wt% sample but not as drastically. From the SEM of the various samples, the 2-4 wt% ReO_x-Pd/CeO_2 particles have consistent particle size and morphology. Thus the main differences in the catalyst tested, outside of Re loading, is the ratio of the various ReO_x species present on the catalyst.

CHAPTER 6

STRUCTURAL INVESTIGATIONS OF ReO_X IN ReO_X/CeO_2

6.1 MOTIVATION AND EXPERIMENTAL

6.1.1 MOTIVATION

The surface structure of ReO_x supported on CeO_2 has not been confirmed in detail via vibrational spectroscopic methods and is currently debated in the literature. Several theoretical studies [38], [154] suggest that there are three likely structures that the isolated monomeric ReO_x species could form: mono-oxo, di-oxo, and tri-oxo [215], as shown in Figure 6.1.

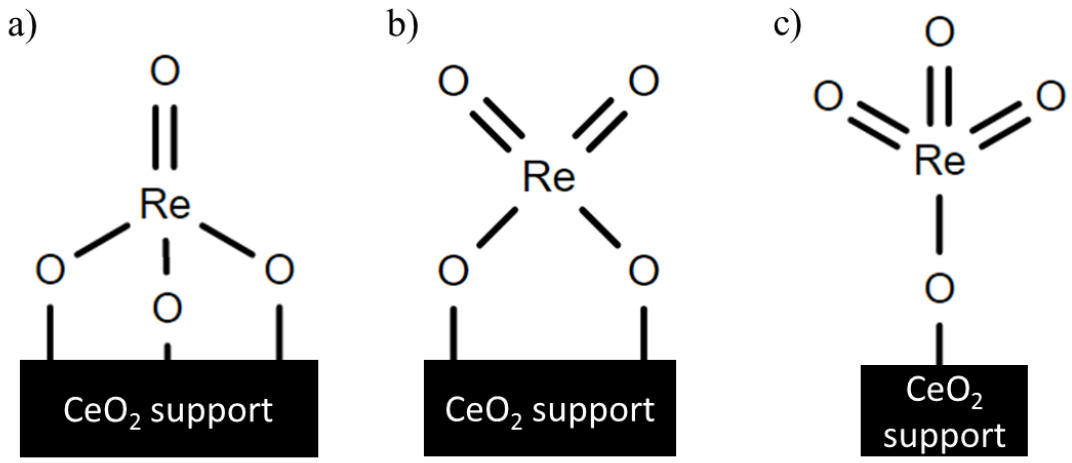

Figure 6.1. Structures of isolated Re sites in ReO_x/CeO_2 catalyst. a) mono-oxo structure, b) di-oxo structure, c) tri-oxo structure. [70]

The structures shown in Figure 6.1 are for isolated monomeric Re sites that can be present in sub monolayer coverages of Re on CeO_2. Once the Re weight loading increases, the possibility for the formation of an oligomeric cross-linked structure increases. The CeO_2 typically has a surface area between 80 and 150 m^2/g, which depends on the synthesis method and post treatment [216]–[222]. The theoretical total number of Re sites that can be occupied on the CeO_2 corresponds to a 20 wt% loading of Re [38]. However, cross-linking has been experimentally observed in a 3 wt% Re_2O_7/ZrO_2 catalyst [63] as well as proposed for a 2 wt% ReO_x-Pd/CeO_2 catalyst [38]. In order to reduce the possibility of having cross-linkage and to maximize the amount of isolated Re sites, a relatively low weight loading of 1 wt% (nominal) Re on CeO_2 was chosen for this study. This loading would also allow us to spectroscopically monitor the Re=O bonds with sufficient signal-to-noise ratio during isotopic exchange experiments.

Isotope exchange is a common technique used in conjunction with vibrational spectroscopy techniques as a means of identifying the number and types of vibrations in a material system [64], [223]–[226]. In literature, there have been multiple isotope exchange experiments performed on ReO_x on various supports such as Al_2O_3, ZrO_2, TiO_2, Cr_2O_3, and SiO_2 to determine the speciation of the ReO_x on the surface [63]–[67]. However, the same set of experiments has not been performed on ReO_x supported on CeO_2. These experiments, in conjunction with previous information on the ReO_x vibrational modes [227], [228], show the speciation of the catalyst from the number of bands that appear post-isotope exchange. With respect to the potential ReO_x species seen in Figure 1, the mono-oxo could show two bands post isotope exchange (stretching of Re=^{16}O and Re=^{18}O), the di-oxo could show six bands (symmetric and asymmetric stretching of ^{16}O=Re=^{16}O,

$^{18}O=Re=^{16}O$, and $^{18}O=Re=^{18}O$), and the tri-oxo could show eight bands (symmetric and asymmetric stretching of the $^{16}O=Re(=^{16}O)=^{16}O$, $^{18}O=Re(=^{16}O)=^{16}O$ $^{18}O=Re(=^{18}O)=^{16}O$, and $^{18}O=Re(=^{18}O)=^{18}O$). The total number of band present from the di-oxo and tri-oxo species also depends on the extent of exchange, since there are partially substituted and fully substituted species that can show different vibrational bands. If the isotope exchange is facilitated for a long time span and at a high enough temperature, the area of the partially substituted bands will likely be much lower than the fully substituted bands. It has been shown that multiple different species can form on the surface instead of any one speciation, leading to increasing complexity of the spectral analysis post-exchange. Thus the possibility of having multiple speciation's of ReO_x supported on the CeO_2 must be considered. Andriopoulou *et al.* showed mono-oxo and di-oxo configurations of ReO_x were present on TiO_2 at 350 °C [67]. Additionally, Weckhyusen *et al.* showed that mono-oxo metal oxide species co-exist with crosslinked metal oxide species on a ZrO_2 support [63]. Thus, any single or co-existing monomeric or oligomeric ReO_x species can been determined through isotopic exchange vibrational spectroscopy experimentation.

ReO_x/CeO_2 holds significant value in its superior ability to remove oxygen containing groups from various compounds through deoxydehydration (DODH) [42], [43], [136], [186], [229]–[231], and through hydrodeoxygenation (HDO) when supported with Pd [38], [69], [147]. ReO_x-Pd/CeO_2 is the state-of-the-art catalyst for the simultaneous hydrodeoxygenation (S-HDO) of sugar alcohols in which two vicinal hydroxyl groups are removed at the same time [38], [69], [147]. The S-HDO is comprised of two steps, a DODH step which removes two vicinal hydroxyl groups and forms a double bond, followed by a hydrogenation step which hydrogenates the double bond to a single bond. The ReO_x/CeO_2

is responsible for the DODH step and has been utilized for a variety of substrates such as glycerol, 1,4-anhydroerythritol, and methyl glycosides [42], [43], [136], [186], [229]–[231]. The palladium catalyzes hydrogen dissociation and is responsible for hydrogen spillover onto the surface, which promotes the hydrogenation step [62]. A previously proposed reaction mechanism by Ota *et al.* [38] for the ReO_x-Pd/CeO_2 catalyzed S-HDO starts with an isolated Re^{VI} species. This theoretical study used Re atoms randomly dispersed among all of the possible sites of a $Ce_{70}O_{140}$, CeO_2 (111), (87 m^2 g^{-1}) support surface [38]. The S-HDO reaction mechanism calculated from Density Functional Theory (DFT) starts with a tri-oxo species (Figure 6.1c) that is then reduced to a di-oxo structure (Figure 6.1b) which changes oxidation state from a Re^{IV} to a Re^{VI} species once the 1,4-anhydroerythritol attaches to the ReO_x. The resulting Re^{VI} species remains di-oxo but has one Re-O bond from the CeO_2, two terminal Re=O bonds, and two Re-O bonds from the substrate. The reduction from the Re^{VI} to Re^{IV} was proposed to be promoted by the Pd which dissociated the hydrogen on the surface of the catalyst allowing for the reduction. After forming the di-oxo species with the 1,4-anhydroerythritol attached, the S-HDO is proposed to occur via the DODH followed by the hydrogenation of the alkene. The ReO_x species is in a tri-oxo structure after the formed Tetrahydrofuran (THF) desorbs but is then reduced back to the di-oxo structure, which is catalyzed by the Pd, resulting in a regenerative cycle.

Another reported mechanism by Xi *et al.* [62] has the isolated Re species starting as a mono-oxo structure with one terminally double-bonded oxygen atom and three single-bonded oxygen atoms that are bonded to the ceria support (Figure 6.1a). This study utilized a fully hydroxylated CeO_2 (111) support surface with four O-Ce-O trilayers, which resulted

in the mono-oxo structure being the most energetically favorable structure under reaction conditions [62]. After the 1,4-anhydroerythritol adsorbs, the DODH then occurs leaving the Re species in a di-oxo structure, which is then reduced back to the mono-oxo structure through a regenerative hydrogen migration process [62]. The starting surface structure of the Re in the reaction mechanism differs in the DFT calculations in the literature which results in varying proposed mechanisms for the S-HDO [38], [62].

Since the two major DFT studies suggest different starting structures for the ReO_x, the resulting proposed reaction mechanisms also vary. However, each calculated mechanism predicts differing regeneration cycles which utilize the hydrogen dissociated on the surface of the catalyst to reduce the ReO_x and include a specific isolated ReO_x surface structure on which the sugar alcohol adsorbs. In order to experimentally confirm the surface structure of ReO_x on CeO_2 and gain insight into the starting point of the reaction mechanism, this work utilized *in situ* isotopic oxygen exchange experiments in combination with Raman spectroscopy and Diffuse Reflectance Infrared Fourier Transform Spectroscopy (DRIFTS).

6.1.2 CHEMICALS

In this work, cerium (IV) oxide, ammonium perrhenate, oxygen, and oxygen-$^{18}O_2$ isotope were used. The cerium (IV) oxide CAS No. 1306-38-3 was supplied by Daiichi Kigenso Kagaku Kogyo Co., Ltd.. The ammonium perrhenate ≥99% purity, CAS No. 13598-5-7, and the Oxygen-$^{18}O_2$ isotope 99% purity, CAS No. 32767-18-3 were obtained from Sigma-Aldrich. The cerium oxide and ammonium perrhenate were used for the synthesis of the ReO_x/CeO_2, and the oxygen and isotope were used in the Raman studies to create gas environments.

6.1.3 ReO_x/CeO_2 SYNTHESIS

The ReO_x/CeO_2 (1 wt% Re) catalysts were prepared using the method previously described by Ota *et al*. and MacQueen *et al.* [38], [69]. The 1 wt% was selected as the Re loading since it would provide enough ReO_x on the surface for the Raman intensity to be sufficient for analysis while minimizing the potential for oligomeric species or solid Re clusters forming. Before the Re was impregnated, the CeO_2 support was calcined in air at 600 °C for 3 h. Following the support calcination, the ReO_x was impregnated on the CeO_2 via a wet impregnation using an aqueous solution of ammonium perrhenate (NH_4ReO_4) while mixing the solution at 300 rpm. The amount of ammonium perrhenate needed in the solution was calculated based on the 1 wt% nominal loading of Re and the mass of CeO_2 that was used. The solution containing the ammonium perrhenate and the ceria was dried at 110 °C for 12 h to ensure all the water has evaporated from the solution. The ReO_x/CeO_2 powder was then collected from the beaker and transferred to an oven where it was then calcined in air at 500 °C for 3 h. Post calcination, the ReO_x/CeO_2 was then ground into a fine powder using a mortar and pestle and was transferred into a glass vial for storage before experimentation and characterization.

6.1.4 *In-situ* ISOTOPIC EXCHANGE RAMAN SPECTROSCOPY

The 1 wt% ReO_x/CeO_2 catalyst sample was subjected to *in situ* Raman spectroscopy pre and post isotopic exchange to track and evaluate the vibrational bands resulting from the various Re to O bonds. Initial scans of the ReO_x/ CeO_2 were taken at room temperature in ambient air, with a Horiba XploRA Plus Raman microscope. The excitation source of the Raman was a 30 mW, 638 nm diode laser, which was calibrated using a polystyrene standard. The scattered light was detected using a HORIBA Scientific

charge-coupled device detector, thermoelectrically cooled to -50 °C. Once the laser was properly focused, calibrated and the intensity of the vibrational bands in the 800-1000 cm^{-1} region were sufficient, the sample was then heated to 550 °C at a rate of 50°C/min while flowing 20 sccm ultra-high purity O_2 (99.9993% O_2) in a Linkam *in situ* Raman cell. Once at temperature, the samples were isothermally held for 30 minutes to serve as a calcination in the O_2 environment. Following the calcination step, the O_2 environment in the Linkam cell was purged using Ar, and the samples were then reduced with 20 sccm H_2 utilizing an isothermal hold at 550 °C for 10 minutes to ensure the reduction of the ReO_x. A spectrum was taken following the reduction to ensure that the corresponding ReO_x vibrational bands fully reduced. The calcination and reduction treatments were repeated in cycles, and after the repeated reduction the system was purged, sealed, and a 25 cm^3 sample cylinder was attached to the cell that was pressurized with 2 bar of the ^{18}O isotope. Prior to being pressurized, the sample cylinders were purged at 200 °C using a roughing pump for 12 h to ensure all gas in the cylinder and any potential contaminates were evacuated. The ^{18}O isotope was then introduced into the Linkam stage by releasing the pressure from the sample cylinder to form the ^{18}O environment. For the ^{18}O environment, the Linkam cell was capped and allowed for a batch environment for the exchange to occur. The 1 wt% ReO_x/CeO_2 sample was then calcined in the ^{18}O environment for 30 minutes at 550 °C to ensure sufficient isotopic exchange occurred. The calcination temperature of 550 °C was utilized based on previous literature, which utilized calcination temperatures ranging from 450-550 °C for isotopic ^{18}O exchange [63], [64], [98]. Higher temperature allows for the faster kinetic exchange of the ^{18}O and therefore would allow for shorter calcination times to ensures sufficient exchange. Based on these principals and our experimental

observations, this temperature and calcination time were sufficient for isotopic exchange to occur, and the corresponding vibrational bands to be measured. The ReO_x/CeO_2 catalyst was then reduced again in the same H_2 conditions as prior, and recalcined within the ^{18}O isotope environment. Spectral measurements were taken after each individual calcination and reduction treatment step and were baseline corrected before analysis.

6.1.5 *In-situ* TIME-REOLVED ISOTOPE EXCHANGE DRIFTS

Diffuse Reflectance Infrared Fourier Transform Spectroscopy (DRIFTS) was conducted on the 1 wt% ReO_x/CeO_2 sample to be able to investigate the isotopic exchange in a time-resolved manner and to perform a complimentary technique to Raman which could further confirm the findings. The *in situ* DRIFTS were taken at near identical conditions to the Raman spectroscopy as to subject the sample to the same conditions for analysis. For the experimentation, a Bruker Vertex 70 FTIR spectrometer equipped with a Mercury Cadmium Telluride (MCT) detector and a KBr beam splitter was used. The 1 wt% ReO_x/CeO_2 sample was placed in a DRIFTS cell and was heated to 550 °C at a ramping rate of 50 °C/min while flowing 20 sccm N_2. The sample was then calcined using a 25 cm^3 sample cylinder that was attached to the DRIFTS cell with 20 psig $^{16}O_2$ for 30 minutes. Afterward, the sample was reduced with 20 sccm H_2 for 30 minutes. After purging the lines with N_2, a sample cylinder filled with 20 psig $^{18}O_2$ was attached for the isotope exchange, and time-resolved measurements were taken for 30 minutes. The ^{18}O exchange was repeated after an additional reduction in H_2 at 550 °C. The sample cylinders used for the DRIFTS experimentation were purged before pressurization with the $^{16}O_2$ and $^{18}O_2$ using the procedure explained in the Raman methodology (Section 6.2.3).

6.2 RESULTS AND DISCUSSSION

6.2.1 CATALYST CHARACTERIZATION

In addition to the Raman and DRIFTS, the 1 wt% ReO_x/CeO_2 catalyst was characterized using X-ray Diffraction (XRD), Brunauer-Emmett-Teller (BET) surface area analysis, Inductively Coupled Plasma Optical Emission Spectroscopy (ICP-OES), and Temperature-Programmed Reduction (TPR).

XRD was conducted to determine if there was any long range ordering of the ReO_x in the catalyst or if the Re was well dispersed on the CeO_2. XRD patterns were collected using a Rigaku Miniflex II (Rigaku, Japan) using a Cu K-α radiation source scanning from 20-80 ° 2θ at a rate of 0.5 °/min and a step size of 0.02 °. The obtained pattern, shown in Figure 6.2, matches reference patterns for CeO_2 with no peaks corresponding to any Re containing phase or other unidentified material. This serves as evidence that the Re is well dispersed on the CeO_2 since there are no corresponding Re peaks [69].

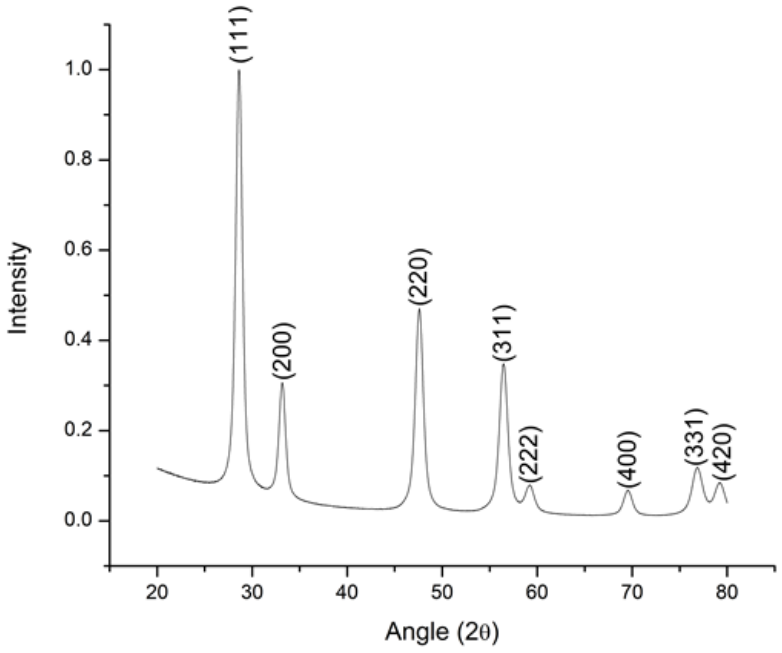

Figure 6.2. XRD pattern of 1 wt% ReO_x/CeO_2 at a scanning rate of 0.5°min. [70]

BET was conducted to determine the surface area of the support and the synthesized catalyst. BET surface area measurements were conducted using an ASAP 2020 (Micromeritics, USA) with nitrogen as the adsorbate gas. Surface area calculations were based upon a BET isotherm. The ceria support as provided by the manufacturer (Daiichi, Japan) without further treatment had a BET surface area of 84.7 m^2/g while the prepared catalyst had a surface area of 78.3 m^2/g, with an instrumental error of ± 3.2 m^2/g. These values are in close agreement with each other and suggest that that the catalyst preparation methodology does not greatly impact the physical properties of the supporting ceria.

ICP-OES was conducted to determine the actual loading of the nominal 1 wt% ReO_x/CeO_2 catalyst. ICP-OES was conducted by adding ~50mg of catalyst to aqua regia and digesting for 8 hours at 120 °C. A 1,000 ppm Ammonium Perrhenate standard was utilized to construct calibration curves (Ricca Chemical Company, USA). An Avio 200 (PerkinElmer, USA) equipped with a S10 autosampler was utilized for data collection. The untreated 1 wt% nominal Re catalyst had an actual weight loading of 1.02 ± 0.01 wt% Re and had a weight loading of 1.08 ±0.01 wt% after heat treating, attributable to experimental error. A previous batch of catalyst had a Re loading of 1.02 ± 0.02 wt% indicating good agreement between batches and excellent reproducibility with the catalyst synthesis methodology. The number of Re atoms per nm^2 was determined to be 0.422 ± 0.002 atoms/nm^2 based on the ICP-OES and BET results.

TPR was conducted to investigate the reducibility of the catalyst. The TPR was conducted on an AutoChem II 2920 (Micromeritics, USA) with an analysis gas consisting of 10% H_2 balanced in Argon. Experiments were carried out using a ramp rate of 5°C/min and an analysis gas flow rate of 50 sccm. Quantitative hydrogen uptake was calculated

utilizing a three-point calibration with known quantities of silver (II) oxide (Micromeritics, USA). To ensure accuracy, experiments were repeated in triplicate yielding a hydrogen uptake of 0.544 ± 0.037 mmol/g catalyst with a main reduction event with a maximum at ~408 °C, shown in Figure 6.3. Metal loading on the catalyst is approximately 0.056 ±0.001 mmol Re/g catalyst indicating a higher than stoichiometric hydrogen uptake even with Re existing in the highest feasible oxidation state. Therefore, this excess hydrogen uptake may be attributable to interactions and hydrogen spillover with the supporting ceria [38].

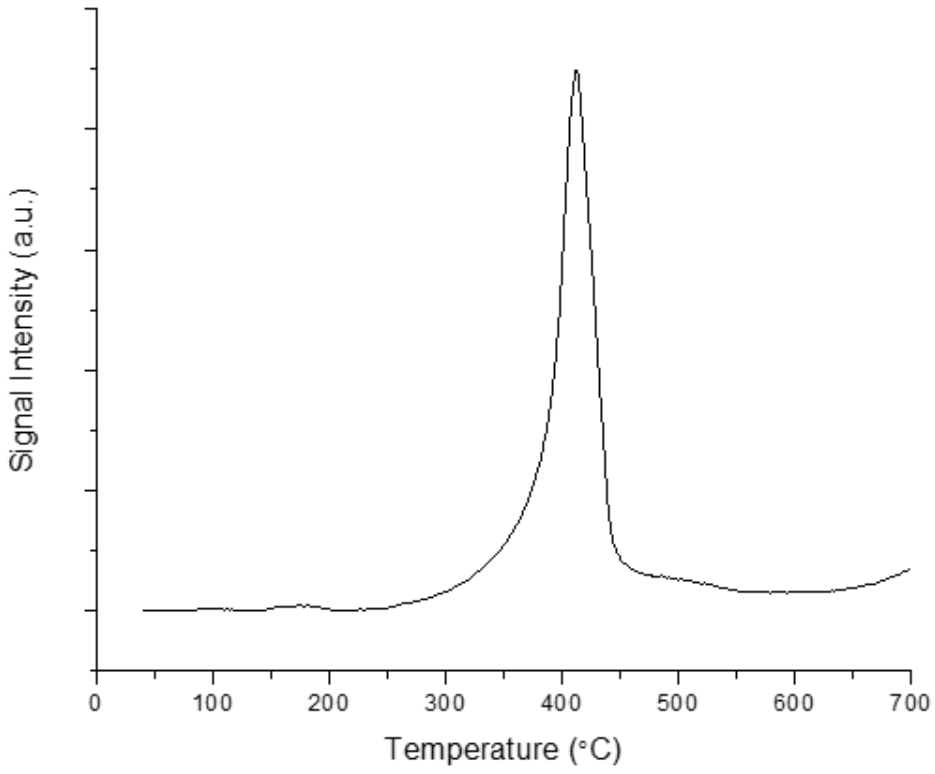

Figure 6.3. H_2 TPR spectrum of 1 wt% ReO_x/CeO_2. [70]

6.2.2 ^{18}O ISOTOPIC EXCHANGE RAMAN SPECTROSCOPY

The isotopic ^{18}O Raman spectra were collected with two ^{18}O exposure cycles following calcination cycles in ^{16}O to ensure sufficient isotope exchange [64], [66].The ^{16}O spectra served as baseline measurements for comparison with the isotopically exchanged spectra. This allowed for easier deconvolution of the vibrational bands and band assignment. The unsubstituted bands could then be assigned and any new bands which formed in the spectra be assigned to the potential isotopic bands. Each spectrum was normalized to the total area under its curve after baseline correction so that the spectrum had a total area of one [232], [233]. Figure 6.4 shows the normalized spectra of the 1 wt% ReO_x/CeO_2 catalyst after the sample was exposed to each oxidation step (^{16}O and ^{18}O) and heating step during the isotope exchange experiment.

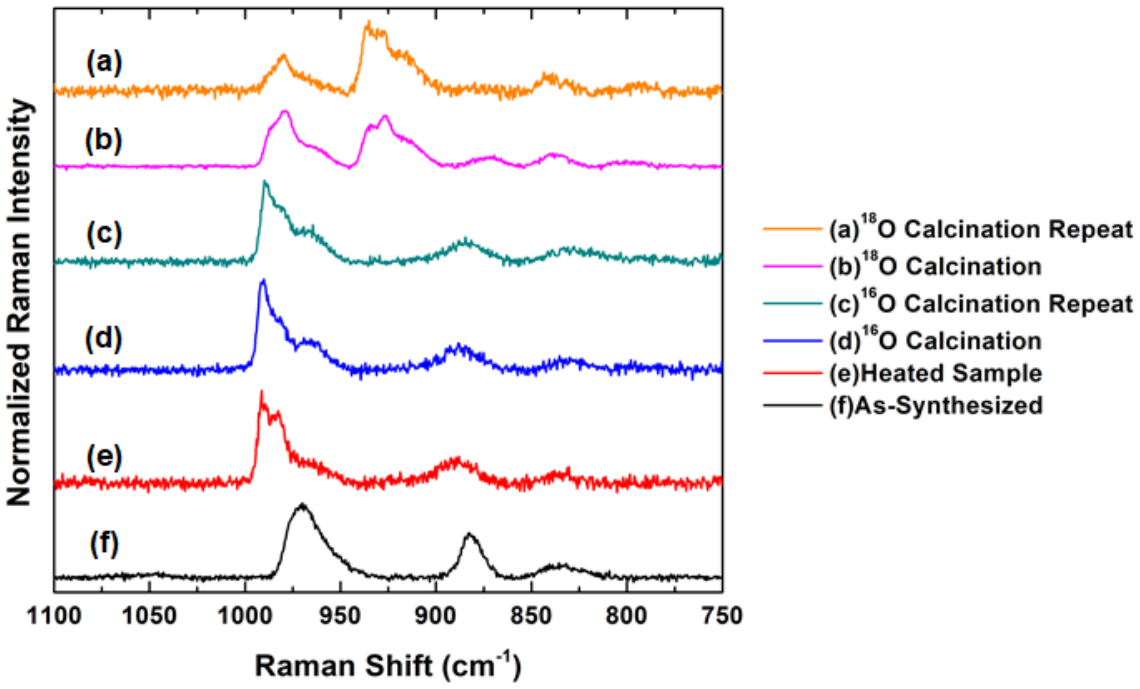

Figure 6.4. *In situ* Raman spectra of 1 wt% ReO_x/CeO_2 catalyst pre and post isotope exchange. The heated sample, (e), was taken at 550 °C in an Ar environment. The calcined sample spectra, (a-d), were obtained at 550 °C in the labeled gas environment. [70]

The as-synthesized 1 wt% ReO_x/CeO_2 sample spectrum is shown in Figure 6.4f. From the as-synthesized spectrum, three distinct ReO_x structures and the associated vibrational bands were deconvoluted and assigned. The symmetric and asymmetric stretches of di-oxo species $^{16}O=Re=^{16}O$ (972 and 961 cm^{-1}), the asymmetric stretch of an oligomer $Re-^{16}O-Re$ (881 cm^{-1}), and the bending mode of a hydroxyl species $Re-^{16}OH$ (834 cm^{-1}) were observed respectively. After the 1 wt% ReO_x/CeO_2 was heated to 550 °C in Ar, shifting and splitting of the ReO_x band (between 950-1000 cm^{-1}) was observed. The splitting of the ReO_x vibrational band revealed the presence of the mono-oxo species (Re=O) in addition to the di-oxo ReOx species (O=Re=O), seen in Figure 6.4e. After the reduction and recalcination of the samples, the band separation between the mono-oxo and di-oxo vibrations becomes more distinct, as shown in Figures 6.4d and 6.4c. However, no new chemical species were observed as a result of the reduction and recalcination. The reduction and recalcination did lead to the current species of ReO_x becoming more pronounced in the spectrum.

Once ^{18}O isotope exchange occurs, new vibrational bands begin to appear at lower wavenumbers (between 900-950 cm^{-1}), shown in Figure 6.4b, due to the redshift caused by the increase in mass [234]–[236]. After additional heating in an ^{18}O environment, shown in Figure 6.4a, the respective ^{16}O band intensities decrease, and the intensities of the redshifted bands associated with ^{18}O begin to increase to levels similar to the heated samples, shown in Figure 6.4e. The further increase in the intensity of the red shifting bands and the intensity of them respectively becoming larger than the unsubstituted bands indicates that ^{18}O exchange has been sufficiently facilitated. There was a significant difference in the signal-to-noise ratio (SNR) between the first and second ^{18}O calcination

spectra. The observed difference in the signal-to-noise ratio between Figure 6.4a (SNR = 12.0) and 6.4b (SNR = 31.8) was most likely due to slight variations in sample positions due to the experimental set-up, not from the volatility of ReO_x. When the sample gas was injected into the cell in the batch environment, the cell positioning can change slightly. This could cause the spot that the laser is focused on to slightly change from scan to scan after gas was added from the sample cylinders. The lack of volatility of the ReO_x was verified in the ICP-OES, where Re weight loading before heating was 1.01 ± 0.01 wt. % and after heating was 1.08 ± 0.01 wt. %. However, it can be reasonably assumed that the ReO_x distribution across the CeO_2 is constant. Additionally, Figure 6.5 shows a set of Raman spectra of the sample that has been unperturbed before and after calcination at 550 °C. The SNR, with respect to the band at 989 cm^{-1}, decreased from 51.5 to 45.3 after heating for 3 hours. This further supports that the SNR change seen after the various gas introductions were likely due to sample position movements rather than volatility.

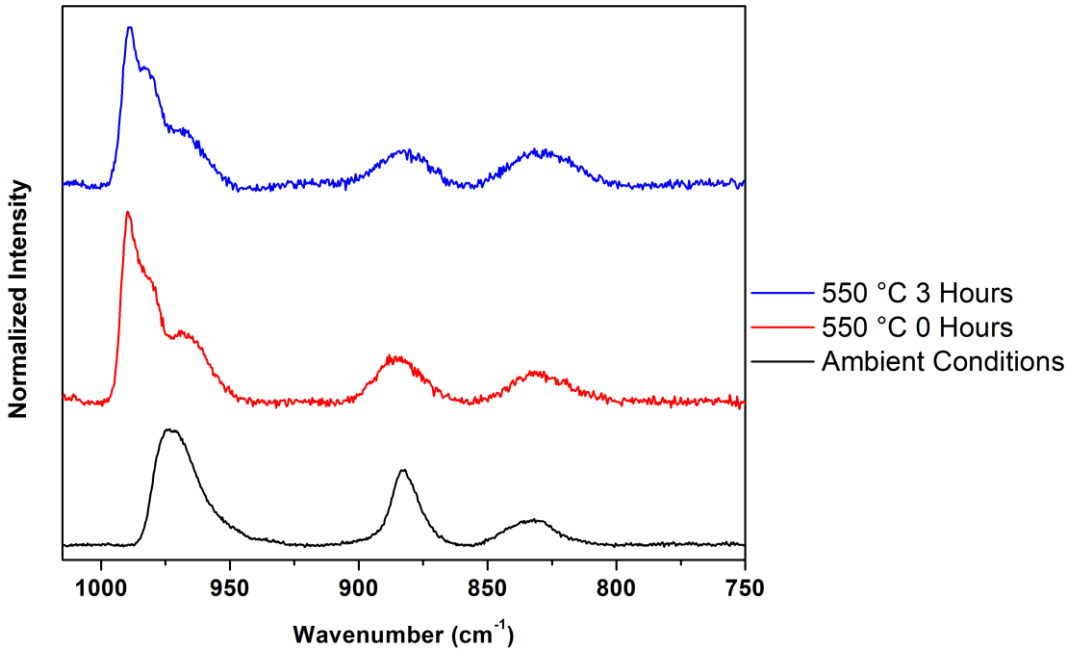

Figure 6.5. Raman spectra comparing the signal-to-noise of a 1 wt% ReO_x/CeO_2 catalyst heated at 550 °C for 0 h and after 3 h. [70]

Further inspection of the as-synthesized sample, shown in Figure 6.4f, shows that the highest wavenumber bands can be deconvoluted into two bands, as seen in Figure 6.6. These bands are fitted to 972 cm^{-1} and 961 cm^{-1} wavenumbers, using a Gaussian band shape [237] and were identified and assigned as the symmetric di-oxo (O=Re=O) and asymmetric di-oxo stretches, respectively [67], [227], [228]. The di-oxo (O=Re=O) ReO_x species present in the as-synthesized sample supports the reaction mechanism proposed by Ota *et al.* [38] for the S-HDO reaction due to the presence of the proposed surface species. Additionally, the spectrum shows a vibrational band at 881 cm^{-1}, which is indicative of the asymmetric stretch of the oxygen bridge between two rhenium atoms (Re-O-Re) [228]. This oxygen bridge corresponds to a cross-linked oligomeric ReO_x species, which has previously been proposed as inactive for S-HDO [38]. A final band at 834 cm^{-1} shows the in-plane bending of a hydroxyl group attached to the rhenium [228].

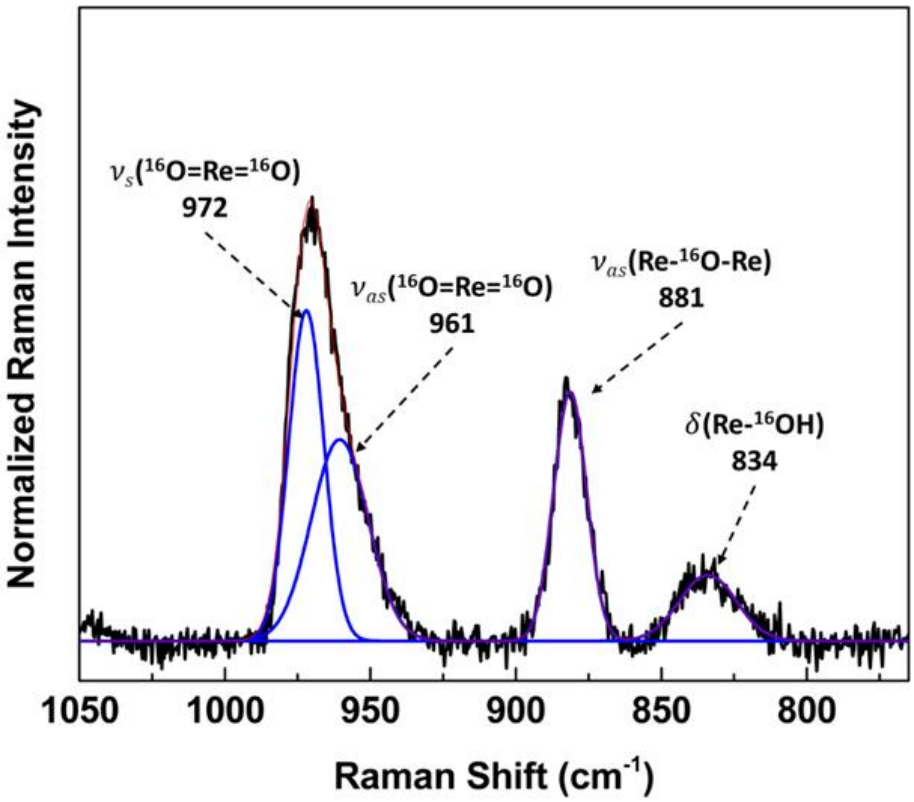

Figure 6.6. As-synthesized 1 wt% ReO_x/CeO_2 Raman spectrum at ambient conditions. [70]

In order to verify the presence of the hydroxyl species, additional spectra were taken at regions where the O-H vibration is present. While the known Re-OH stretch at 700 cm^{-1} was not observed in the Raman, a low intensity band is observed at the 3700 cm^{-1} Raman spectral region where O-H is visible [228]. The additional Re-OH investigations are show in Figure 6.7. The terminal hydroxyl group is likely attached to the Re in a mono-oxo structure, as previously proposed by Xi *et al*. [62]. The hydroxylated structure has not been proposed as a starting structure in a reaction mechanism. However, the hydroxylated structures can be reduced and the mono-oxo structures regenerated through a hydrogen migration process, which facilitates catalyst regeneration in the Xi *et al*. mechanism [62]. Thus, the hydroxylated species could still play a role in the S-HDO reaction when hydrogen is present to allow the reduction and regeneration of the ReO_x species. Alternatively, it is a possibility that the 834 cm^{-1} and could be from the Re-O-Ce bonding. This would explain why the 700 cm^{-1} band is not present and why the 3700 cm^{-1} band is of low intensity. However, this Re-O-Ce band has been reported in the literature at 874 cm^{-1}, 40 cm^{-1} higher than we observed in our study [210]. Thus the Re-OH assignment has more merit based on our observations.

The presence of multiple species within the spectrum of the as-synthesized sample (Figure 6.4f) shows that there is not a singular configuration for ReO_x. The presence of multiple configurations of ReO_x was also observed in previous works studying a ReO_x/TiO_2 catalyst [67] and with previous work done by Wachs *et al.* investigating ReO_x on various metal oxide supports excluding CeO_2 [66], [223], [238]. However, this has not been previously reported for ReO_x/CeO_2. The various ReO_x species present could have their own respective S-HDO reaction mechanisms, which could be competing or the

species could reduce or oxidize to the same starting speciation. However, it is not possible to discern which species is dominating in the reaction or which species are participating in the reaction without further studies into Re coverage effects and respective reaction data. If the distinct structures could be synthesized on the ceria individually on different samples, then the individual reaction rates and coverage effects could be elucidated. The formation of hydroxyl groups on the surface has not been typically seen in the experimental literature but has been theorized through DFT [62]. While the DFT showed that hydroxyl groups can be favorable to form, only a low intensity bending mode between Re and OH can be observed in our spectra at 834 cm^{-1}. Since the hydroxyl groups are likely reduced and removed through a hydrogen migration process under the reducing reaction conditions [38], [62], it should be unlikely to see these structures in a high concentration on the surface during reaction or under a reaction environment. Thus under S-HDO reaction conditions the ReO_x is likely only in the mono-oxo and di-oxo structures.

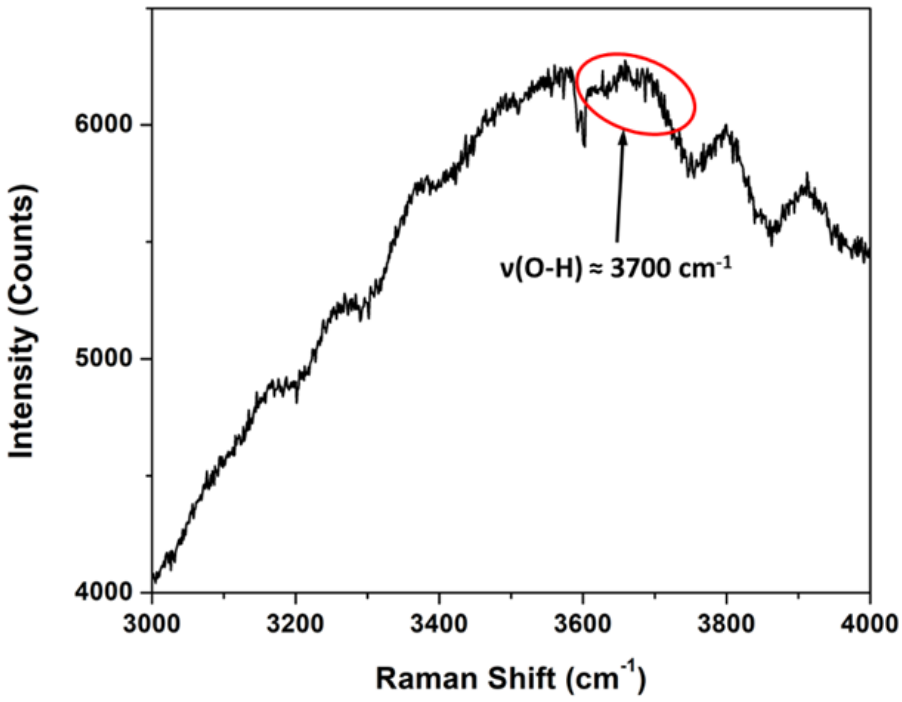

Figure 6.7. Raman spectrum of 1 wt% ReO_x/CeO_2 highlighting the O-H stretch. [70]

At elevated temperatures, a third band appears adjacent to the bands previously centered around 972 and 961 cm^{-1}, as seen in Figure 6.4e. Figure 6.8 compares the sample calcined in $^{16}O_2$ and the calcination of the sample in $^{18}O_2$ isotope conditions with the respective band fittings and assignments. From this spectrum, we can see four different ReO_x species present within the sample: the mono-oxo structure, di-oxo structure, cross-linked bridge, and hydroxyl bond.

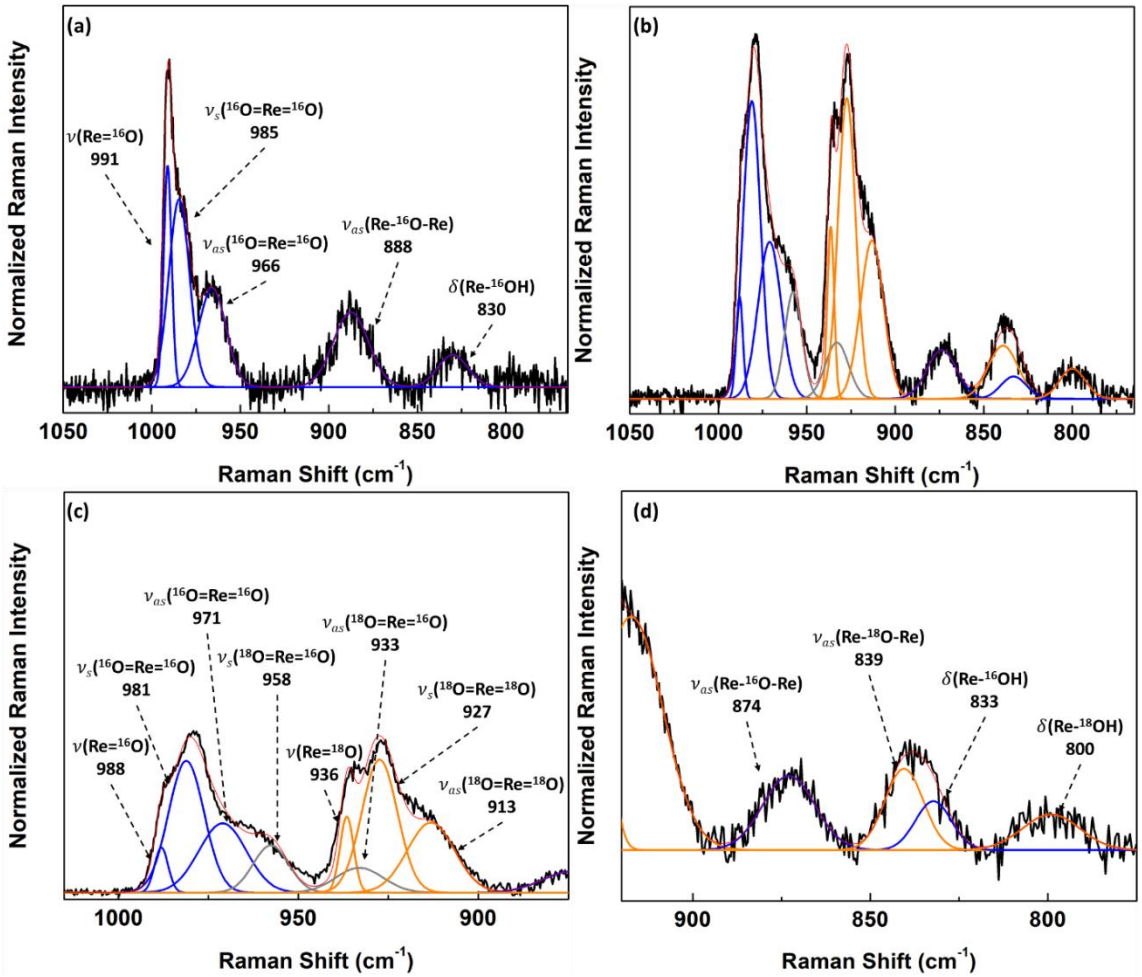

Figure 6.8. Raman spectra of 1.0 wt% ReO_x/CeO_2 after the first isotope exchange at 550 °C. (a) The heated sample calcined in flowing $^{16}O_2$ before the exchange. (b) The heated sample calcined in $^{18}O_2$. (c) Fitting and identification of the mono and di-oxo configuration [67]. (d) Fitting and identification of the bridge and hydroxyl group bands. [70]

The redshifting observed in the Raman spectra before and after isotope exchange seen in Figure 6.8 confirms the four different surface configurations of ReO_x. The bands assigned for the pre exchanged spectrum, shown in Figure 6.8a, all have a corresponding redshifted bands due to the isotopic exchange, shown in Figure 6.8b-d. Notably, the region for the ReO_x bands that correspond with the rhenium and oxygen double bond stretches shows spectroscopic evidence for two separate configurations (mono-oxo and di-oxo). Prior to isotope exchange, a band at 991 cm^{-1} is assigned with a mono-oxo termination configuration (Re=^{16}O), see Figure 6.9b. The mono-oxo ReO_x is the most stable and energetically favorable structure according to the calculations performed by Xi *et al.* [62]. The bands at 985 cm^{-1} and 966 cm^{-1} relate to the symmetric and asymmetric stretches, respectively, of the di-oxo termination of ReO_x (^{16}O=Re=^{16}O), see Figure 5a. The di-oxo structure is the active site for S-HDO proposed in the calculations performed by Ota *et al.* [38]. Additionally, the asymmetric stretch for the oxygen bridge between rhenium metal atoms (Re-^{16}O-Re) can be seen at 888 cm^{-1}, see Figure 6.9a, and the in-plane bending of the hydroxyl group (Re-^{16}OH) is labeled at 830 cm^{-1}, see Figure 6.9a. These bands shifted to slightly once the isotopic exchange occurred. The ^{16}O oxygen bridge shifted to 874 cm^{-1} and the ^{16}O hydroxyl group shifted to 833 cm^{-1}. The di-oxo, mono-oxo, and hydroxyl Re species that form are isolated monomeric species, see Figure 6.9a-c. However, when the crosslinked Re species is formed, see Figure 6.9d, it forms an oligomeric Re species.

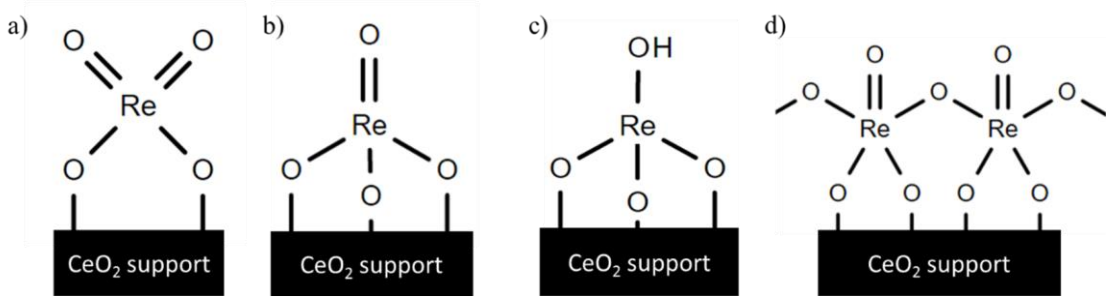

Figure 6.9. ReO_x species present on the surface of ReO_x/CeO_2. a) Di-oxo species. b) Mono-oxo species. c) hydroxyl species. d) crosslinked Re species. [70]

After a single oxidation in the ^{18}O isotope environment, exchange can be seen for each configuration present. The mono-oxo termination configuration is redshifted by 52 cm^{-1} to 936 cm^{-1}, and the bridge and hydroxyl oxygen's are similarly shifted to lower wavenumbers at 839 cm^{-1} and 800 cm^{-1} respectively. When both ^{16}O are exchanged with ^{18}O in the di-oxo structure (^{18}O=Re=^{18}O) the stretches are clearly visible at 927 cm^{-1} and 913 cm^{-1} for the symmetric stretch and asymmetric stretch respectively. However, the bands for the single isotope exchange for the same stretches (^{16}O=Re=^{18}O) were deconvoluted via fitting their locations based on their theoretical positions, shown in Table 6.1. The theoretical positions were calculated using the model for a simple rigid diatomic molecule, theoretical vibrational frequency ratios can be estimated for an isotope exchange. This isotopic ratio can be determined using the following expression [63], [234], [239], [240]:

$$\frac{\nu_{16_O}}{\nu_{18_O}} = \sqrt{\frac{\frac{1}{m_M}+\frac{1}{m_{16_O}}}{\frac{1}{m_M}+\frac{1}{m_{18_O}}}} \approx \sqrt{\frac{m_{18_O}}{m_{16_O}}}, m_M \gg m_{16_O}, m_{18_O}$$

In the expression, the vibrational frequencies of metal-^{16}O and metal-^{18}O isotope bond are represented by ν_{16_O} and ν_{18_O}, respectively. The atomic mass of the metal is m_M,

and the oxygen and isotope are m_{16_O} and m_{18_O} respectively. When the mass of the metal is much greater than the mass of the oxygen atoms, the equation can be simplified to the square root of the ratio between the mass of the ^{18}O and the mass of the ^{16}O. Typically, the diatomic model would only be used for mono-oxo constituents. However, it has been used before on the isotope exchange of the di-oxo speciation of Cr_2O_3/SiO_2 and on $CaCO_3$ [66], [239]. This model has been used as a first approximation to estimate the redshift from bond vibration dampening effect by the increase in mass. A more accurate theoretical estimate would require first principles computational techniques that are outside the scope of this work. Table 6.1 shows the theoretical vibrational shift versus the experimental shift for all band assignments made. The measured values are consistent with the theoretically calculated shift. The average difference in the redshift from the vibrational stretches was 3.16 cm^{-1}.

Utilizing the theoretical shifts and resulting band positions provided a better fit for all the spectra and allowed for position identification of the single exchanged symmetric stretch to be at 958 cm^{-1} and the asymmetric stretch to be at 933 cm^{-1} for the di-oxo species. All instances of band fitting in this study were performed with proper constraints to the full-width half-maximum of the Raman bands of the same species and a constraint to the area ratio of the symmetric and asymmetric stretches of the di-oxo ReO_x bands. By fixing the full-width half-maximum of the bands we ensure that the contribution from each species remains reasonable and prevents the fitting of singular broad peaks in the region of interest. By containing the areas of the symmetric and asymmetric bands to be equal, we ensure that the di-oxo species bands are being properly fit since the same species symmetric

and asymmetric vibrations should occur equally in terms of area. This also prevents the bands from fitting at different ratios which wouldn't make physical sense.

Table 6.1. Experimental and Theoretical Raman Shift for the Isotope Exchange. [70]

Raman Shifts (cm^{-1})				
	$^{18}O_2$ Theoretical		**$^{18}O_2$ Measured**	
Vibrational Mode	***Single Sub.***	***Double Sub.***	***Single Sub.***	***Double Sub.***
ν (Re=O)	**939**	**N/A**	**936**	**N/A**
ν_s (O=Re=O)	**955**	**933**	**958**	**927**
ν_{as} (O=Re=O)	**937**	**915**	**933**	**913**
ν_{as} (Re-O-Re)	**841**	**N/A**	**839**	**N/A**
δ(Re-OH)	**786**	**N/A**	**800**	**N/A**

The isotope exchange ratio can be seen in Table 6.2 and is determined by the fitted area of the bands that indicate single and double substituted modes divided by the fitted area of the unsubstituted ReO_x bands. The exchange ratio can indicate how much of the ^{18}O exchanged with each species, and which species exchanged faster than others. After the initial exposure to the ^{18}O environment, each species experienced at least fifty percent isotope exchange, which can be seen with the ^{18}O-^{16}O ratio being greater than 1 for each species. The mono-oxo ReO_x species has the highest exchange efficiency, with an exchange of approximately 62%. After an additional cycle, the mono-oxo species was 90% exchanged, and the di-oxo species was 70% exchanged. Interestingly, the crosslinked and hydroxyl species exchange to near completion, with the ^{16}O bands no longer visible within the spectra. The higher extent of exchange of the mono-oxo species, as compared to the di-oxo species, suggests that the mono-oxo ReO_x species is more reactive toward oxygen in the gas phase. This makes a shift in the oxidation state more likely to occur for the mono-oxo as compared to the di-oxo ReOx species. This also potentially suggests that the di-oxo

species is more stable and the Re=O bonds in the di-oxo species could potentially be stronger since it is harder for the isotope to exchange with the di-oxo species.

Table 6.2. Raman band area for the observed vibration modes. [70]

Raman Spectra Area		
	$^{18}O/^{16}O$ Ratio	
Vibrational Mode	^{18}O First Cycle	^{18}O Second Cycle
ν (Re=O)	1.68	9.86
ν_s (O=Re=O)	1.37	2.45
ν_{as} (O=Re=O)	1.37	2.45
ν_{as} (Re-O-Re)	1.09	Near Complete
δ(Re-OH)	1.36	Near Complete

6.2.3 ^{18}O ISOTOPIC EXCHANGE DRIFTS

Fourier Transform Infrared Spectroscopy (FTIR) was employed to provide a time resolved observation of the band formation from the isotope exchange. This allows for the extent of exchange and any preferential exchange to be observed as a function of time. The DRIFTS isotope exchange experiment was started with the 1 wt% ReO_x/CeO_2 sample surface oxidized with ^{16}O. The sample was then exposed to the ^{18}O isotope at 550 °C for 25 minutes, which was repeated for a second cycle. This procedure was utilized to try and closely replicate the environment the ReO_x/CeO_2 was exposed to during the Raman isotope exchange investigation. The first and second ^{18}O exposure cycles over 25 min are shown in Figure 6.10.

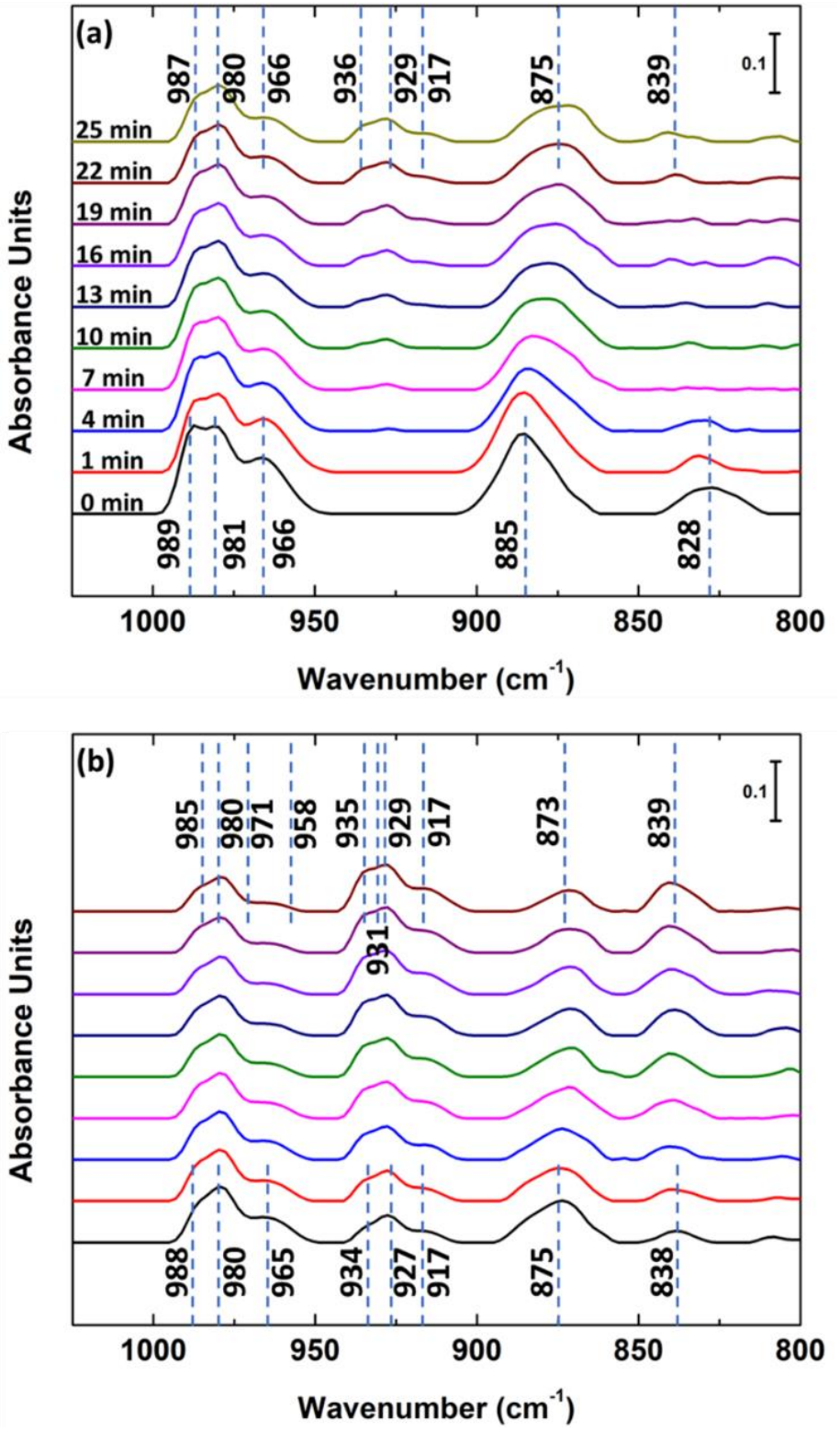

Figure 6.10. Time resolved FTIR spectra of reduced 1 wt% ReO_x/CeO_2 exposed to ^{18}O. (a) The sample was exposed to ^{18}O after reduction. (b) The sample was reintroduced to ^{18}O after a second reduction. [70]

The data complements the Raman spectra and shows the redshift of the Re=O and bridge vibrations. However, it is difficult to observe the hydroxyl isotope band formation as the adsorption of the ^{18}O occurs, which is potentially due to low intensity of Re-OH bending mode [228]. Additionally, initial analysis of the band intensities would imply that the asymmetric stretch of the di-oxo species is less than the intensity of the symmetric stretch, which violates the selection rules for IR. However, when accounting for the integrated intensity, we have found that the fitted area is near equivalent or greater than the integrated intensity of the symmetric stretch. Therefore, the selection rule has been satisfied [241]–[245]. Table 6.3 shows the integrated area comparisons of the symmetric and asymmetric stretches of the di-oxo species for Raman and FTIR respectively.

Table 6.3. Ration between the integrated intensities of the symmetric and asymmetric di-oxo stretches in the Raman and FTIR. [70]

Integrated Intensity			
	ν_s (O=Re=O)	ν_{as} (O=Re=O)	Sym/Asym Ratio
Raman	122.38	85.64	1.43
Raman (Isotope)	123.55	86.46	1.43
FTIR	0.374	0.377	0.99
FTIR (Isotope)	0.662	0.669	0.99

In the first ^{18}O exposure cycle, the mono-oxo vibrational band was initially observed at 989 cm^{-1} and shifted to 987 cm^{-1} after 25 min of exposure. The Fully substituted mono-oxo band was observed at 936 cm^{-1} (a red shift of 53 cm^{-1}) which is consistent with the red shifting observed in the Raman spectroscopy (52 cm^{-1}). The unsubstituted

symmetric and asymmetric stretches of the di-oxo species were observed at 981 cm^{-1} and 966 cm^{-1} respectively, while the fully substituted bands were observed at 929 cm^{-1} and 917 cm^{-1} respectively. The resulting red shifting observed was 52 cm^{-1} and 49 cm^{-1} for the symmetric and asymmetric bands respectively. The symmetric band red shifting seen in the DRIFTS was consistent with the Raman. However, the red shifting observed for the asymmetric band was significantly smaller in the DRIFTS than in the Raman (58 cm^{-1}). The shifting observed for the oligomeric oxygen bridge seen initially at 885 cm^{-1} and redshifted to 839 cm^{-1} was also consistent with the Raman isotope exchange spectroscopy.

Using the time resolved measurements, we can observe the amount of isotope that is exchanged per reduction and oxidation cycle. After about 15 minutes of exposure to the isotope at 550 °C, the exchange reaches a steady-state. The amount of actual exchange can be determined using the ratio of the band area of the ^{18}O sample and the band area of the ^{16}O sample., similar to the extent of exchange calculated and discussed in the isotopic Raman investigations. The spectra used after the second cycle of the isotope exchange, shown in Figure 6.10b, was used to calculate band areas. After two cycles of ^{18}O exposure, the area ratios show a similar trend in the change done to the ReO_x that was seen in the Raman spectra as shown in Table 6.4. After 25 minutes for the second exposure cycle, 60.5% of the ^{16}O in the sample was exchanged with ^{18}O, and the ratio of $^{18}O/^{16}O$ was 1.534. The second cycle showed a much greater extent of exchange as compared to the first cycle. Before reaching steady-state, the $^{18}O/^{16}O$ exchange rate was linear and was calculated based on the 1, 7, and 13-minute spectra. The $^{18}O/^{16}O$ exchange rate was calculated to be 2.29 % per minute, with the $^{18}O/^{16}O$ ratios being 0.308, 0.546, and 1.043 for the 1, 7, and 13-minute spectra, respectively for the second cycle. The symmetric and asymmetric di-

oxo stretch and the bridge band show further exchange in the IR, but the mono-oxo stretch shows less exchange than in a single exposure in the Raman. However, this could simply be a result of a different measurement technique used in the analysis. The ratios of ^{18}O exchange for the IR results in differences are not nearly as drastic as seen in the Raman. The relative similarity in the mono-oxo and di-oxo $^{18}O/^{16}O$ exchange ratios relative to the Raman supports that the species might be more similar in their ability to react with the environment.

Table 6.4. FTIR spectra band area for the visible modes in the spectra after 25 minutes of ^{18}O exposure. [70]

FTIR Spectra Area		
	$^{18}O/^{16}O$ Ratio	
Vibrational Mode	^{18}O First Cycle	^{18}O Second Cycle
ν (Re=O)	0.243	1.467
ν_s (O=Re=O)	0.350	1.873
ν_{as} (O=Re=O)	0.350	1.873
ν_{as} (Re-O-Re)	0.148	1.298

6.2.4 Re WEIGHT LOADING EFFECTS

To further investigate the dispersion of ReO_x and the formation of oligomeric ReO_x (Re_2O_7), ReO_x/CeO_2 samples ranging from 1 to 20 wt% Re supported on CeO_2 were synthesized and evaluated in XRD. The diffraction patterns for the various samples are shown in Figure 6.11. Up to 4 wt% ReO_x, no diffraction patterns from ReO_x were observed. Once the Re loading was increased to 8 wt%, some diffraction patters corresponding to the orthorhombic structure of Re_2O_7 became noticeable. The ReO_x diffractions due to long

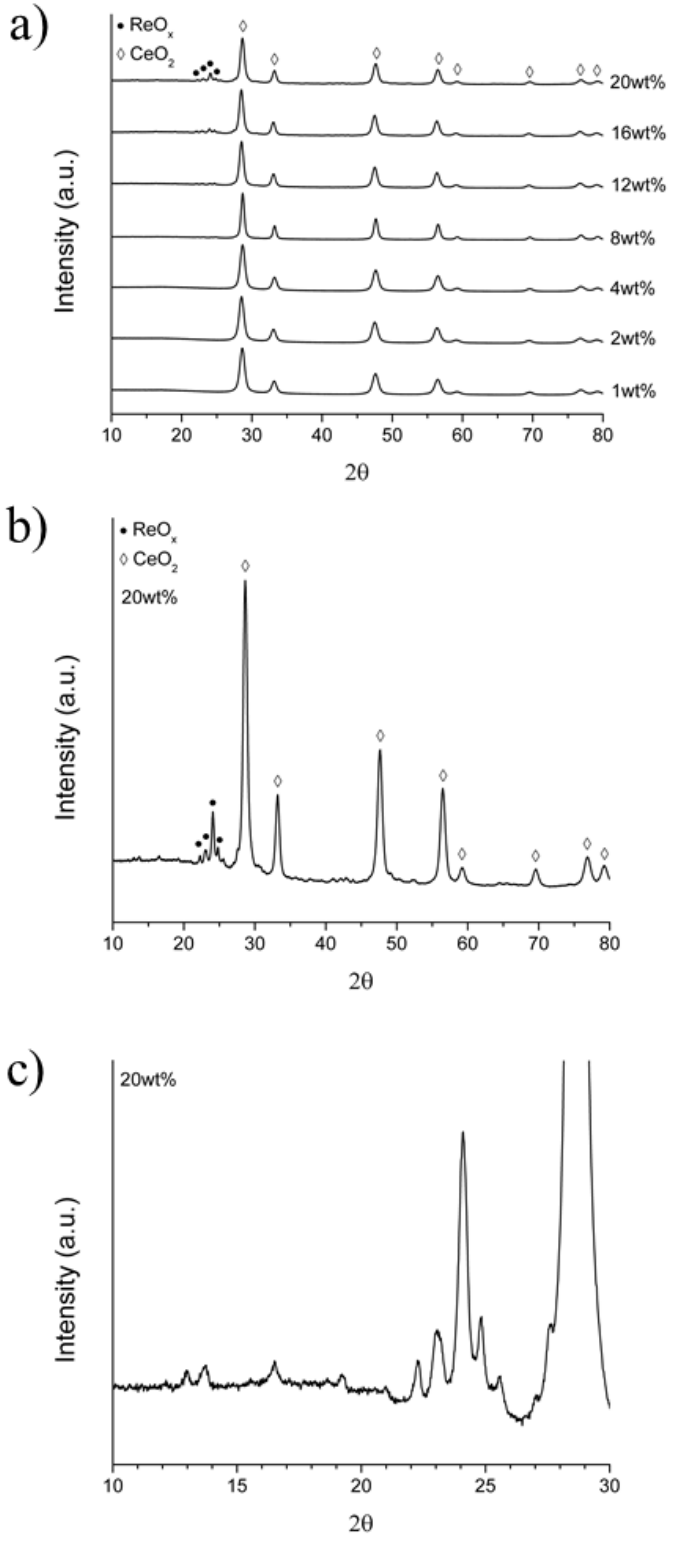

Figure 6.11. XRD diffraction patterns for ReO_x/CeO_2 catalysts of varying Re loadings. a) 1 to 20 wt% Re patterns b) 20 wt% Re pattern from 10-80 2θ c) 20 wt% Re zoomed in pattern from 10 to 30 2θ.

range ordering of ReO_x became significant as the weight loading was increased up to 20 wt%, which approaches a theoretical monolayer of coverage. These diffractions are shown in Figure 6.11 b and c. The diffractions observed in the 8 to 20 wt% Re samples corresponding to Re_2O_7 were observed at roughly 22, 23, 24, and 24.5° 2θ corresponding to the diffractions from the (121), (004), (122), and (113) planes respectively. Since diffraction patterns resulting from large clusters of Re_2O_7 were not observed until roughly 8 wt%, it can be assumed that for weight loadings of 4 wt% Re and lower, the ReO_x is well dispersed on the CeO_2 support and is in mostly monomeric isolated ReO_x structures or small oligomeric species.

6.3. CONCLUSIONS

Utilizing *in situ* ^{18}O isotopic exchange Raman spectroscopy and DRIFTS, the structures of ReO_x supported on CeO_2 have been determined to be three monomeric species including a di-oxo (O=Re=O), mono-oxo (Re=O) and mono-oxo with a hydroxyl group (Re-OH), as well as an oligomierc crosslinked (Re-O-Re) species. These species were identified and assigned, via their respective redshifted bands, which helped deconvolute the spectra and allow for accurate band fitting. The Raman and IR data showed that the extent of exchange after cycling ^{18}O was approximately 60 %, while the time resolved IR showed that the $^{18}O/^{16}O$ exchange rate was 2.29% per minute. The spectral results show that there are multiple structures of ReO_x present when supported CeO_2. The presence of multiple monomeric structures is quite unique for ReO_x since on most other oxide supports ReO_x exits as a singular monomeric structure. The presence of multiple ReO_x structures could lead to varying reaction mechanisms or potentially competing mechanisms when ReO_x/CeO_2 is used as a catalyst. However, due to the oxygen mobility capabilities of ceria,

more work would be needed to investigate the structures of ReO_x at specific conditions and in a simulated reaction environment to make further insights into the speciation of ReO_x under reaction conditions.

From our investigations into the effects of Re loading on the structure of the ReO_x, it was determined that for weight loadings below 4 wt% Re, the ReO_x was well dispersed and mostly in monomeric ReO_x structures as previously shown in the *in situ* Raman. At weight loadings above 8 wt%, significant diffraction patterns resulting from the formation of orthorhombic Re_2O_7 were observed.

CHAPTER 7

CONCLUSIONS AND FUTURE WORK

The body of this work focused on the upgrading of biomass derived sugar alcohols to platform chemicals via the simultaneous hydrodeoxygenation reaction over a ReO_x-Pd/CeO_2 catalyst. Reaction optimization was explored using design of experiments for 1,4-anhydroerythritol, xylitol, and sorbitol as substrates. The general kinetics and mass transfer were investigated for the xylitol S-HDO reaction to give further insight into the S-HDO reaction. The catalyst structure was also investigated and the structures of ReO_x supported on CeO_2 were elucidated.

The work in Chapter 3 focused on determining the relationship between pressure, temperature, and catalyst Re loading on the conversion and selectivity of the S-HDO reaction. In this work it was determined that hydrogen pressure had a zero-order relationship with yield for both the AHERY and xylitol S-HDO reactions over the ReO_x-Pd/CeO_2 catalyst down to 10 bar H_2. This zero-order relationship allows for the reaction to be conducted in a safer manner and potentially use cheaper compressors if scaled to a larger scale or into a flow system. Temperature was found to be highly significant, as expected due to thermodynamics. However, for xylitol S-HDO it was suggested by the Taguchi model that temperature exhibited an inverse relation with conversion. The Taguchi design

delivered quick and efficient optimizations for the simple catalytic design spaces and allowed for factor importance for the S-HDO reactions to be elucidated. The homebuilt high pressure batch reactor system was also evaluated for mass transfer limitations and was found to not exhibit any limitations utilizing the hydrogenation of MBY as a model reaction.

The future work that can be investigated for Chapter 3 could focus on evaluating if the relationships elucidated hold for other more complex sugar alcohols and evaluating if they still hold under different types of reactors. There are several other sugar alcohols such as methyl glycosides which are more complex in terms of sterics and structure. The glycosides also contain trans hydroxyl groups which have been proposed to suppress the S-HDO reaction. Determining if the hydrogen pressure still exhibits a zero-order relation for these more complex molecules would give further insight into the reaction. If the zero-order relation holds for these more complex molecules would also allow for the reactions to be conducted in the same reactors interchangeably in the same reactors under milder conditions. These reactions should be investigated in flow systems such as plug flow reactors, continuous stirred tank reactors, etc. to evaluate if the elucidated temperature, pressure, and catalyst loading relations still hold. Also investigating these types of reactors and the associated kinetics would allow for the potential scaling of this reaction. The design space evaluated for the Taguchi designs should also be expanded on both the high and low ends to see if the relations elucidated still hold under harsher or milder reaction conditions. Expanding the design space could lead to more optimal conditions to be found or could elucidate points in which limitations or other phenomena could be present and thus should be avoided.

The work in Chapter 4 focused on investigating the general kinetics and mass transfer of xylitol S-HDO over the ReO_x-Pd/CeO_2 catalyst and determining if the inverse relationship of temperature with conversion suggested in Chapter 3 was valid. It was determined that xylitol concentration was zero-order in the reaction. It was also determined that there were no internal or external mass transfer limitation within the system for all kinetic points that were evaluated. It was determined that temperature was directly related to xylitol conversion. However, the relationship was not a linear Arrhenius relation, but rather a sub-Arrhenius relationship was present. This relationship shows that activation energy is a function of temperature and ranged from 10.2-51.8 kJ/mol over the 120-170 °C temperature range evaluated. The sub-Arrhenius relationship is indicative of quantum tunneling occurring in the reaction, which can significantly impact the amount of energy required for the reaction to proceed. It was also determined through in-situ Raman that concentration of the di-oxo (O=Re=O) species of ReO_x was directly related to temperature. As temperature was increased, it was observed that the mono-oxo (Re=O) species of rhenium oxide oxidizes to the di-oxo species likely due to oxygen migration from the CeO_2 support as temperature is increased.

The future work that can be investigated for Chapter 4 involves further investigating the quantum tunneling or potential competing reaction mechanisms using both further kinetic and spectroscopic evaluations. Since the curvature seen in the kinetics data could be attributed to quantum tunneling or potentially competing reaction mechanisms between the di-oxo and mono-oxo species, it is important to determine which is occurring. To determine if the quantum tunneling is occurring, the xylitol S-HDO reaction should be conducted at several temperatures while using deuterium and/or tritium

instead of hydrogen as the gas reactant to see the mass effect on the reaction. If quantum tunneling is occurring, the sub-Arrhenius relation should still be seen and can be modeled by the increase in mass of the reactant. However, if the expected change in reaction rates is not observed based on the models used to capture and describe the quantum tunneling, then it is further evidence that there are likely competing mechanism occurring. Work should be done to try and synthesize or pretreat the catalysts to be able to isolate the mono-oxo and di-oxo species on separate catalysts to evaluate them individually and see which species is more active. Then further in-situ spectroscopy can be conducted to investigate the possible reaction mechanisms and intermediates that could help explain the tunneling observed through the sub-Arrhenius relationship for this reaction. This can be accomplish using an in-situ system and introducing both hydrogen and a model reactant such as AHERY or a simple sugar alcohol (through a heated line so that it is in the gas phase) to a reaction cell which contains the ReO_x-Pd/CeO_2 catalyst. During the reaction, the vibrational bands can be monitored under more realistic reaction conditions. This could also give further insight into the S-HDO reaction mechanisms.

The work in Chapter 5 focused on the optimization of sorbitol S-HDO using two different design of experiments to determine the pressure, temperature, and Re weight loading (in the catalyst) effects on the conversion and selectivity (to hexanediols) of the reaction. The Chapter also focused on the direct comparison of the simplistic Taguchi design vs the more complex Box Behnken design. This was done to evaluate if the more simplistic design could deliver comparable results with significantly fewer experiments and more simplistic regression models. It was determined that the simplistic Taguchi design was able to predict the optimal conditions within the design space at 170 °C, 10 bar,

using a 4 wt% Re catalyst. It was also determined that the 4 wt% ReO_x-Pd/CeO_2 catalyst had the largest change in speciation from mono-oxo (Re=O) to di-oxo (O=Re=O) as temperature increased within the design space. This change in speciation over the temperature range could be why the 4 wt% catalyst is the most active and selective catalyst that was tested.

The future work that can be investigated for Chapter 5 involves further evaluations of Taguchi designs against response surfaces and factorial designs, and further spectroscopic investigations into the ReO_x-Pd/CeO_2 catalysts. While the findings of the studies conducted in Chapter 5 are promising, it is important to test other systems and designs factors to see if the Taguchi designs still hold their weight. It would be critical to test a system that has a more complex reaction to see if the linear regressions can still capture a system that is more complex. The ReO_x-Pd/CeO_2 catalysts should also be further investigated to determine the number of active sites present of the various weight loadings of the catalyst. By determining the number of active sites through temperature programmed desorption, the turn over frequency could be determined. This could then give further insight into whether the 4 wt% catalyst is more active due to having more active sites or having more di-oxo sites. Once this is determined that catalyst can be further optimized and more insight into which of the rhenium oxide species is more active.

The work in Chapter 6 focused on determining the structure of ReO_x supported on CeO_2 and investigating the effects of Re loading on the speciation of ReO_x. From in situ isotopic ^{18}O exchange Raman and DRIFTS, it was determined that four species of rhenium oxide were present on the ReO_x/CeO_2 catalyst. Three monomeric species and one oligomeric species were elucidated and the associated bands were assigned. The isolated

monomeric species included a di-oxo (O=Re=O), a mono-oxo (Re=O) and a mono-oxo with a hydroxyl group (Re-OH). The oligomer was seen due to the asymmetric (Re-O-Re) band. These findings were similar to ReO_x/TiO_2 which had several structures or ReO_x observed on the catalyst surface as well. However, this was the first study directly elucidating the structures of ReO_x supported on CeO_2 using vibrational spectroscopy.

The future work that can be investigated for Chapter 6 includes further investigations into the effect of Re loading on the rhenium oxide speciation distribution and the effects of reducing and oxidizing environments on the structure of the rhenium oxide at different temperatures. Evaluating a large range of Re loadings would give a further knowledge base for future material design and optimization. Investigating the catalyst in both reducing and oxidizing environments can give further insight into catalyst stability and will provide further knowledge for this catalyst to be used in other reactions. Elemental mapping using SEM Energy Dispersive Spectroscopy (EDS) should also be conducted on the catalysts to be able to determine where the ReO_x is primarily located, and to determine if the oligomers can be seen on the CeO_2 surface. This can give more insight into the oligomer size and the metal dispersion on the CeO_2 support.

REFERENCES

[1] J. C. Védrine, *Fundamentals of heterogeneous catalysis*. Elsevier, 2018.

[2] M. Campanati, G. Fornasari, and A. Vaccari, "Fundamentals in the preparation of heterogeneous catalysts," *Catal. Today*, vol. 77, no. 4, pp. 299–314, 2003.

[3] Y. Matsuo, A. Yanagisawa, and Y. Yamashita, "A global energy outlook to 2035 with strategic considerations for Asia and Middle East energy supply and demand interdependencies," *Energy Strateg. Rev.*, vol. 2, no. 1, pp. 79–91, 2013.

[4] R. O. Afolabi and E. O. Yusuf, "Nanotechnology and global energy demand: challenges and prospects for a paradigm shift in the oil and gas industry," *J. Pet. Explor. Prod. Technol.*, vol. 9, no. 2, pp. 1423–1441, 2019.

[5] J. Popp, S. Kovács, J. Oláh, Z. Divéki, and E. Balázs, "Bioeconomy: Biomass and biomass-based energy supply and demand," *N. Biotechnol.*, vol. 60, no. October 2020, pp. 76–84, 2021.

[6] M. Stöcker, "Biofuels and biomass-to-liquid fuels in the biorefinery: Catalytic conversion of lignocellulosic biomass using porous materials," *Angew. Chemie - Int. Ed.*, vol. 47, no. 48, pp. 9200–9211, 2008.

[7] E. Environ, J. C. Serrano-ruiz, and J. A. Dumesic, "Catalytic routes for the conversion of biomass into liquid hydrocarbon transportation fuels," *Energy Environ. Sci.*, vol. 4, pp. 83–99, 2011.

[8] C. J. Barrett, Z. Y. Liu, and J. A. Dumesic, "Production of dimethylfuran for liquid fuels from biomass-derived carbohydrates," *Nature*, vol. 447, no. June, pp. 982–986, 2007.

[9] M. J. C. Van Der Stelt, H. Gerhauser, J. H. A. Kiel, and K. J. Ptasinski, "Biomass upgrading by torrefaction for the production of biofuels : A review," *Biomass and Bioenergy*, vol. 35, no. 9, pp. 3748–3762, 2011.

[10] J. Li, A. Brzdekiewicz, W. Yang, and W. Blasiak, "Co-firing based on biomass torrefaction in a pulverized coal boiler with aim of 100 % fuel switching," *Appl. Energy*, vol. 99, pp. 344–354, 2012.

[11] W. Chen, J. Peng, and X. T. Bi, "A state-of-the-art review of biomass torrefaction , densi fi cation and applications," *Renew. Sustain. Energy Rev.*, vol. 44, pp. 847–866, 2015.

[12] J. S. Tumuluru, S. Sokhansanj, J. R. Hess, C. T. Wright, and R. D. Boardman, "A review on biomass torrefaction process and product properties for energy applications," *Ind. Biotechnol.*, vol. 7, no. october, pp. 384–401, 2011.

[13] A. Corma, G. W. Huber, L. Sauvanaud, and P. O. Connor, "Biomass to chemicals : Catalytic conversion of glycerol / water mixtures into acrolein , reaction network,"

J. Catal., vol. 257, pp. 163–171, 2008.
[14] X. Tong, Y. Ma, and Y. Li, “General Biomass into chemicals : Conversion of sugars to furan derivatives by catalytic processes,” *"Applied Catal. A, Gen.*, vol. 385, no. 1–2, pp. 1–13, 2010.
[15] P. Gallezot and C. Pinel, “Conversion of Biomass into Chemicals over Metal Catalysts,” *Chem. Rev.*, vol. 114, pp. 1827–1870, 2014.
[16] A. Corma, S. Iborra, and A. Velty, “Chemical Routes for the Transformation of Biomass into Chemicals,” *Chem. Rev.*, vol. 107, pp. 2411–2502, 2007.
[17] D. M. Alonso, S. G. Wettstein, and J. A. Dumesic, “Bimetallic catalysts for upgrading of biomass to fuels and chemicals,” *Chem. Soc. Rev.*, vol. 41, no. 24, pp. 8075–8098, 2012.
[18] P. N. R. Vennestrøm, C. M. Osmundsen, C. H. Christensen, and E. Taarning, “Beyond Petrochemicals : The Renewable Chemicals Industry **,” *Angew. Chemie - Int. Ed.*, pp. 10502–10509, 2011.
[19] P. G. Levi and J. M. Cullen, “Mapping Global Flows of Chemicals: From Fossil Fuel Feedstocks to Chemical Products,” *Environ. Sci. Technol.*, vol. 52, no. 4, pp. 1725–1734, 2018.
[20] V. G. Yadav, G. D. Yadav, and S. C. Patankar, “The production of fuels and chemicals in the new world: critical analysis of the choice between crude oil and biomass vis-à-vis sustainability and the environment,” *Clean Technol. Environ. Policy*, vol. 22, no. 9, pp. 1757–1774, 2020.
[21] C. H. Zhou, X. Xia, C. X. Lin, D. S. Tong, and J. Beltramini, “Catalytic conversion of lignocellulosic biomass to fine chemicals and fuels,” *Chem. Soc. Rev.*, vol. 40, no. 11, pp. 5588–5617, 2011.
[22] S. G. Wettstein, D. Martin Alonso, E. I. Gürbüz, and J. A. Dumesic, “A roadmap for conversion of lignocellulosic biomass to chemicals and fuels,” *Curr. Opin. Chem. Eng.*, vol. 1, no. 3, pp. 218–224, 2012.
[23] C. Espro, B. Gumina, T. Szumelda, E. Paone, and F. Mauriello, “Catalytic Transfer Hydrogenolysis as an Effective Tool for the Reductive Upgrading of Cellulose, Hemicellulose, Lignin, and Their Derived Molecules,” *Catalysts*, vol. 8, no. 8, p. 313, 2018.
[24] C. Wen, E. Barrow, J. Hattrick-Simpers, and J. Lauterbach, “One-step production of long-chain hydrocarbons from waste-biomass-derived chemicals using bi-functional heterogeneous catalysts,” *Phys. Chem. Chem. Phys.*, vol. 16, no. 7, pp. 3047–3054, 2014.
[25] L. Jiang, N. Wu, A. Zheng, A. Liu, Z. Zhao, F. Zhang, F. He, and H. Li, “Comprehensive Utilization of Hemicellulose and Cellulose to Release Fermentable Sugars from Corncobs via Acid Hydrolysis and Fast Pyrolysis,” *ACS Sustain. Chem. Eng.*, vol. 5, no. 6, pp. 5208–5213, 2017.
[26] T. D. Matson, K. Barta, A. V. Iretskii, and P. C. Ford, “One-pot catalytic conversion of cellulose and of woody biomass solids to liquid fuels,” *J. Am. Chem. Soc.*, vol. 133, no. 35, pp. 14090–14097, 2011.
[27] A. Herbst and C. Janiak, “MOF catalysts in biomass upgrading towards value-added fine chemicals,” *CrystEngComm*, vol. 19, no. 29, pp. 4092–4117, 2017.
[28] K. G. Childers, S. D. Dreher, J. Lee, and J. M. Williams, “A practical and scaleable preparation of 1,4-anhydroerythritol,” *Org. Process Res. Dev.*, vol. 10,

no. 5, pp. 934–936, 2006.
[29] Y. Amada, N. Ota, M. Tamura, Y. Nakagawa, and K. Tomishige, “Selective hydrodeoxygenation of cyclic vicinal diols to cyclic alcohols over tungsten oxide-palladium catalysts,” *ChemSusChem*, vol. 7, no. 8, pp. 2185–2192, 2014.
[30] H. Luo and M. M. Abu-Omar, “Lignin extraction and catalytic upgrading from genetically modified poplar,” *Green Chem.*, vol. 20, no. 3, pp. 745–753, 2018.
[31] W. Schutyser, T. Renders, S. Van Den Bosch, S. F. Koelewijn, G. T. Beckham, and B. F. Sels, “Chemicals from lignin: An interplay of lignocellulose fractionation, depolymerisation, and upgrading,” *Chem. Soc. Rev.*, vol. 47, no. 3, pp. 852–908, 2018.
[32] V. F. Wendisch, Y. Kim, and J. H. Lee, “Chemicals from lignin: Recent depolymerization techniques and upgrading extended pathways,” *Curr. Opin. Green Sustain. Chem.*, vol. 14, pp. 33–39, 2018.
[33] S. Dutta, S. De, B. Saha, and M. I. Alam, “Advances in conversion of hemicellulosic biomass to furfural and upgrading to biofuels,” *Catal. Sci. Technol.*, vol. 2, no. 10, pp. 2025–2036, 2012.
[34] V. Aidinopoulou and D. G. Sampson, “An action research study from implementing the flipped classroom model in primary school history teaching and learning,” *Educ. Technol. Soc.*, vol. 20, no. 1, pp. 237–247, 2017.
[35] F. Ben Chaabane and R. Marchal, “Upgrading the Hemicellulosic Fraction of Biomass into Biofuel,” *Oil Gas Sci. Technol. – Rev. d’IFP Energies Nouv.*, vol. 68, no. 4, pp. 663–680, 2013.
[36] N. Li, G. A. Tompsett, T. Zhang, J. Shi, C. E. Wyman, and G. W. Huber, “Renewable gasoline from aqueous phase hydrodeoxygenation of aqueous sugar solutions prepared by hydrolysis of maple wood,” *Green Chem.*, vol. 13, no. 1, pp. 91–101, 2011.
[37] N. Li, G. A. Tompsett, and G. W. Huber, “Renewable high-octane gasoline by aqueous-phase hydrodeoxygenation of C5and C6carbohydrates over Pt/zirconium phosphate catalysts,” *ChemSusChem*, vol. 3, no. 10, pp. 1154–1157, 2010.
[38] N. Ota, M. Tamura, Y. Nakagawa, K. Okumura, and K. Tomishige, “Performance, Structure, and Mechanism of ReO_x–Pd/CeO_2 Catalyst for Simultaneous Removal of Vicinal OH Groups with H_2,” *ACS Catal.*, vol. 6, no. 5, pp. 3213–3226, 2016.
[39] S. Vkuturi, G. Chapman, I. Ahmad, and K. M. Nicholas, “Rhenium-catalyzed deoxydehydration of glycols by sulfite,” *Inorg. Chem.*, vol. 49, no. 11, pp. 4744–4746, 2010.
[40] N. N. Tshibalonza and J. C. M. Monbaliu, “The deoxydehydration (DODH) reaction: a versatile technology for accessing olefins from bio-based polyols,” *Green Chem.*, vol. 22, no. 15, pp. 4801–4848, 2020.
[41] W. Jin, L. Pastor-Pérez, J. Yu, J. A. Odriozola, S. Gu, and T. R. Reina, “Cost-effective routes for catalytic biomass upgrading,” *Curr. Opin. Green Sustain. Chem.*, vol. 23, pp. 1–9, 2020.
[42] S. Tazawa, N. Ota, M. Tamura, Y. Nakagawa, K. Okumura, and K. Tomishige, “Deoxydehydration with Molecular Hydrogen over Ceria-Supported Rhenium Catalyst with Gold Promoter,” *ACS Catal.*, vol. 6, no. 10, pp. 6393–6397, 2016.
[43] T. Wang, S. Liu, M. Tamura, N. Hiyoshi, K. Tomishige, and Y. Nakagawa, “One-

pot catalytic selective synthesis of 1,4- butanediol from 1,4-anhydroerythritol and hydrogen," *Green Chem.*, pp. 2547–2557, 2018.
[44] M. Tamura, N. Yuasa, J. Cao, Y. Nakagawa, and K. Tomishige, "Transformation of Sugars into Chiral Polyols over a Heterogeneous Catalyst," *Angew. Chemie - Int. Ed.*, pp. 8058–8062, 2018.
[45] N. Ota, M. Tamura, Y. Nakagawa, K. Okumura, and K. Tomishige, "Hydrodeoxygenation of vicinal OH groups over heterogeneous rhenium catalyst promoted by palladium and ceria support," *Angew. Chemie - Int. Ed.*, vol. 54, no. 6, pp. 1897–1900, 2015.
[46] N. Ota, M. Tamura, Y. Nakagawa, K. Okumura, and K. Tomishige, "Performance, Structure, and Mechanism of ReO x –Pd/CeO 2 Catalyst for Simultaneous Removal of Vicinal OH Groups with H 2," *ACS Catal.*, vol. 6, no. 5, pp. 3213–3226, 2016.
[47] Y. Lee, S. W. Lee, Y. F. Tsang, Y. T. Kim, and J. Lee, "Engineered rice-straw biochar catalysts for the production of value-added chemicals from furan," *Chem. Eng. J.*, vol. 387, no. January, p. 124194, 2020.
[48] C. Zhao, J. He, A. A. Lemonidou, X. Li, and J. A. Lercher, "Aqueous-phase hydrodeoxygenation of bio-derived phenols to cycloalkanes," *J. Catal.*, vol. 280, no. 1, pp. 8–16, 2011.
[49] O. İ. Şenol, T.-R. Viljava, and A. O. I. Krause, "Hydrodeoxygenation of methyl esters on sulphided NiMo/γ-Al2O3 and CoMo/γ-Al2O3 catalysts," *Catal. Today*, vol. 100, no. 3–4, pp. 331–335, 2005.
[50] A. Gutierrez, R. K. Kaila, M. L. Honkela, R. Slioor, and A. O. I. Krause, "Hydrodeoxygenation of guaiacol on noble metal catalysts," *Catal. Today*, vol. 147, no. 3–4, pp. 239–246, 2009.
[51] C. Zhao, Y. Kou, A. A. Lemonidou, X. Li, and J. A. Lercher, "Hydrodeoxygenation of bio-derived phenols to hydrocarbons using RANEY® Ni and Nafion/SiO2 catalysts," *Chem. Commun.*, vol. 46, no. 3, pp. 412–414, 2010.
[52] A. Centeno, E. Laurent, and B. Delmon, "Influence of the support of CoMo sulfide catalysts and of the addition of potassium and platinum on the catalytic performances for the hydrodeoxygenation of carbonyl, carboxyl, and guaiacol-type molecules," *Journal of Catalysis*, vol. 154, no. 2. pp. 288–298, 1995.
[53] C. R. Lee, J. S. Yoon, Y. W. Suh, J. W. Choi, J. M. Ha, D. J. Suh, and Y. K. Park, "Catalytic roles of metals and supports on hydrodeoxygenation of lignin monomer guaiacol," *Catal. Commun.*, vol. 17, pp. 54–58, 2012.
[54] T. Prasomsri, T. Nimmanwudipong, and Y. Rom??n-Leshkov, "Effective hydrodeoxygenation of biomass-derived oxygenates into unsaturated hydrocarbons by MoO3 using low H2 pressures," *Energy Environ. Sci.*, vol. 6, no. 6, pp. 1732–1738, 2013.
[55] B. Saha, C. M. Bohn, and M. M. Abu-Omar, "Zinc-assisted hydrodeoxygenation of biomass-derived 5-hydroxymethylfurfural to 2,5-Dimethylfuran," *ChemSusChem*, vol. 7, no. 11, pp. 3095–3101, 2014.
[56] D. D. Laskar, M. P. Tucker, X. Chen, G. L. Helms, and B. Yang, "Noble-metal catalyzed hydrodeoxygenation of biomass-derived lignin to aromatic hydrocarbons," *Green Chem.*, vol. 16, no. 2, pp. 897–910, 2014.
[57] M. Grilc, G. Veryasov, B. Likozar, A. Jesih, and J. Levec, "Hydrodeoxygenation

of solvolysed lignocellulosic biomass by unsupported MoS2, MoO2, Mo2C and WS2catalysts," *Appl. Catal. B Environ.*, vol. 163, pp. 467–477, 2015.
[58] Q. Bu, H. Lei, A. H. Zacher, L. Wang, S. Ren, J. Liang, Y. Wei, Y. Liu, J. Tang, Q. Zhang, and R. Ruan, "A review of catalytic hydrodeoxygenation of lignin-derived phenols from biomass pyrolysis," *Bioresour. Technol.*, vol. 124, pp. 470–477, 2012.
[59] H. Ren, W. Yu, M. Salciccioli, Y. Chen, Y. Huang, K. Xiong, D. G. Vlachos, and J. G. Chen, "Selective hydrodeoxygenation of biomass-derived oxygenates to unsaturated hydrocarbons using molybdenum carbide catalysts," *ChemSusChem*, vol. 6, no. 5, pp. 798–801, 2013.
[60] Y. Nakagawa, S. Liu, M. Tamura, and K. Tomishige, "Catalytic Total Hydrodeoxygenation of Biomass-Derived Polyfunctionalized Substrates to Alkanes," *ChemSusChem*, vol. 8, no. 7, pp. 1114–1132, 2015.
[61] M. Shiramizu and F. D. Toste, "Deoxygenation of biomass-derived feedstocks: Oxorhenium-catalyzed deoxydehydration of sugars and sugar alcohols," *Angew. Chemie - Int. Ed.*, vol. 51, no. 32, pp. 8082–8086, 2012.
[62] Y. Xi, W. Yang, S. C. Ammal, J. Lauterbach, Y. Pagan-Torres, and A. Heyden, "Mechanistic study of the ceria supported, re-catalyzed deoxydehydration of vicinal OH groups," *Catal. Sci. Technol.*, vol. 8, no. 22, pp. 5740–5752, 2018.
[63] B. M. Weckhuysen, J.-M. Jehng, and I. E. Wachs, "In Situ Raman Spectroscopy of Supported Transition Metal Oxide Catalysts: $^{18}O_2 - ^{16}O_2$ Isotopic Labeling Studies," *J. Phys. Chem. B*, vol. 104, no. 31, pp. 7382–7387, 2000.
[64] B. M. Weckhuysen and I. E. Wachs, "*In Situ* Raman Spectroscopy of Supported Chromium Oxide Catalysts: $^{18}O_2 - ^{16}O_2$ Isotopic Labeling Studies," *J. Phys. Chem. B*, vol. 101, no. 15, pp. 2793–2796, 1997.
[65] S. Lwin, C. Keturakis, J. Handzlik, P. Sautet, Y. Li, A. I. Frenkel, and I. E. Wachs, "Surface ReOx sites on Al2O3 and their molecular structure-reactivity relationships for olefin metathesis," *ACS Catal.*, vol. 5, no. 3, pp. 1432–1444, 2015.
[66] E. L. Lee and I. E. Wachs, "In situ Raman spectroscopy of SiO2-supported transition metal oxide catalysts: An isotopic 18O-16O exchange study," *J. Phys. Chem. C*, vol. 112, no. 16, pp. 6487–6498, 2008.
[67] C. Andriopoulou and S. Boghosian, "Molecular structure and termination configuration of Oxo-Re(VII) catalyst sites supported on Titania," *Catal. Today*, no. June, pp. 1–13, 2019.
[68] S. R. Bare, S. D. Kelly, F. D.vila, E. Boldingh, E. Karapetrova, J. Kas, G. E. Mickelson, F. S. Modica, N. Yang, and J. J. Rehr, "Experimental (XAS, STEM, TPR, and XPS) and theoretical (DFT) characterization of supported rhenium catalysts," *J. Phys. Chem. C*, vol. 115, no. 13, pp. 5740–5755, 2011.
[69] B. MacQueen, E. Barrow, G. Rivera Castro, Y. Pagan-Torres, A. Heyden, and J. Lauterbach, "Optimum Reaction Conditions for 1,4-Anhydroerythritol and Xylitol Hydrodeoxygenation over a ReOx-Pd/CeO2 Catalyst via Design of Experiments," *Ind. Eng. Chem. Res.*, vol. 58, no. 20, pp. 8681–8689, 2019.
[70] B. MacQueen, B. Ruiz-Yi, M. Royko, A. Heyden, Y. J. Pagan-Torres, C. Williams, and J. Lauterbach, "In-Situ Oxygen Isotopic Exchange Vibrational Spectroscopy of Rhenium Oxide Surface Structures on Cerium Oxide," *J. Phys.*

Chem. C, vol. 124, no. 13, pp. 7174–7181, 2020.
[71] B. MacQueen, M. Royko, B. S. Crandall, A. Heyden, Y. J. Pagán-Torres, and J. Lauterbach, "Kinetics Study of the Hydrodeoxygenation of Xylitol over a ReOx-Pd/CeO2 Catalyst," *Catalysts*, vol. 11, no. 1, p. 108, Jan. 2021.
[72] A. L. Patterson, "The scherrer formula for X-ray particle size determination," *Phys. Rev.*, vol. 56, no. 10, pp. 978–982, 1939.
[73] J. I. Langford and J. C. Wilson, "Scherrer after Sixty Years: A Survey and Some New Results in the Determination of Crystallite Size," *J. Appl. Crystallogr.*, vol. 11, pp. 102–113, 1978.
[74] H. Karaca, J. Hong, P. Fongarland, P. Roussel, A. Griboval-Constant, M. Lacroix, K. Hortmann, O. V. Safonova, and A. Y. Khodakov, "In situ XRD investigation of the evolution of alumina-supported cobalt catalysts under realistic conditions of Fischer-Tropsch synthesis," *Chem. Commun.*, vol. 46, no. 5, pp. 788–790, 2010.
[75] K. Thamaphat, P. Limsuwan, and B. Ngotawornchai, "Phase Characterization of TiO2 Powder by XRD and TEM," *Nat. Sci.*, vol. 42, pp. 357–361, 2008.
[76] B. Akbari, M. P. Tavandashti, and M. Zandrahimi, "Particle size characterization of nanoparticles- a practicalapproach," *Iran. J. Mater. Sci. Eng.*, vol. 8, no. 2, pp. 48–56, 2011.
[77] S. Mourdikoudis, R. M. Pallares, and N. T. K. Thanh, "Characterization techniques for nanoparticles: Comparison and complementarity upon studying nanoparticle properties," *Nanoscale*, vol. 10, no. 27, pp. 12871–12934, 2018.
[78] P. Brouwer, *Theory of XRF*. 2010.
[79] S. Piorek, "Principles and applications of man-portable X-ray fluorescence spectrometry," *Trends Anal. Chem.*, vol. 13, no. 7, pp. 281–286, 1994.
[80] F. Li, L. Ge, Z. Tang, Y. Chen, and J. Wang, "Recent developments on XRF spectra evaluation," *Appl. Spectrosc. Rev.*, vol. 55, no. 4, pp. 263–287, 2020.
[81] V. Kröger, U. Lassi, K. Kynkäänniemi, A. Suopanki, and R. L. Keiski, "Methodology development for laboratory-scale exhaust gas catalyst studies on phosphorus poisoning," *Chem. Eng. J.*, vol. 120, no. 1–2, pp. 113–118, 2006.
[82] S. Togami, M. Takano, M. Kumazawa, and K. Michibayashi, "An algorithm for the transformation of XRF images into mineral-distribution maps," *Can. Mineral.*, vol. 38, no. 5, pp. 1283–1294, 2000.
[83] L. Mino, A. Agostino, S. Codato, and C. Lamberti, "Study of epitaxial selective area growth In1-xGaxAs films by synchrotron μ-XRF mapping," *J. Anal. At. Spectrom.*, vol. 25, no. 6, pp. 831–836, 2010.
[84] C. Li, L. Wong, L. Tang, N. V. Y. Scarlett, K. Chiang, J. Patel, N. Burke, and V. Sage, "Kinetic modelling of temperature-programmed reduction of cobalt oxide by hydrogen," *Appl. Catal. A Gen.*, vol. 537, pp. 1–11, 2017.
[85] S. Rajagopal, H. J. Marini, J. A. Marzari, and R. Miranda, "Silica-Alumina-Supported Acidic Molybdenum Catalysts-TPR and XRD Characterization," *J. Catal.*, vol. 147, pp. 417–428, 1994.
[86] V. Mazzieri, F. Coloma-Pascual, A. Arcoya, P. C. L'Argentière, and N. S. Fígoli, "XPS, FTIR and TPR characterization of Ru/Al 2 O 3 catalysts," *Appl. Surf. Sci.*, vol. 210, no. 3–4, pp. 222–230, 2003.
[87] C. Serre, F. Garin, G. Belot, and G. Maire, "Reactivity of Pt/Al2O3 and Pt-CeO2Al2O3 catalysts for the oxidation of carbon monoxide by oxygen. I. Catalyst

characterization by TPR using CO as reducing agent," *Journal of Catalysis*, vol. 141, no. 1. pp. 1–8, 1993.
[88] D. S. Su, B. Zhang, and R. Schlögl, "Electron microscopy of solid catalysts - Transforming from a challenge to a toolbox," *Chem. Rev.*, vol. 115, no. 8, pp. 2818–2882, 2015.
[89] D. Su, "Advanced electron microscopy characterization of nanomaterials for catalysis," *Green Energy Environ.*, vol. 2, no. 2, pp. 70–83, 2017.
[90] A. Mohammed and A. Abdullah, "Scanning Electron Microscopy (SEM): A Review," *Int. Conf. Hydraul. Pneum.*, vol. 7, no. January, pp. 1–9, 2018.
[91] A. K. Datye, "Electron microscopy of catalysts: Recent achievements and future prospects," *J. Catal.*, vol. 216, no. 1–2, pp. 144–154, 2003.
[92] P. L. Gai, "Developments of electron microscopy methods in the study of catalysts," *Curr. Opin. Solid State Mater. Sci.*, vol. 5, no. 5, pp. 371–380, 2001.
[93] J. W. Olesik, "Elemental Analysis Using ICP-OES and ICP/MS," *Anal. Chem*, vol. 63, no. 1, pp. 12–21, 2000.
[94] M. S. Wheal, T. O. Fowles, and L. T. Palmer, "A cost-effective acid digestion method using closed polypropylene tubes for inductively coupled plasma optical emission spectrometry (ICP-OES) analysis of plant essential elements," *Anal. Methods*, vol. 3, no. 12, pp. 2854–2863, 2011.
[95] T. W. Barnard, M. I. Crockett, J. C. Ivaldi, P. L. Lundberg, D. A. Yates, P. A. Levine, and D. J. Sauer, "Solid-State Detector for ICP-OES," *Anal. Chem*, vol. 64, no. 4, pp. 1231–1239, 1993.
[96] A. Goncalves, J. R. Domínguez, and J. Alvarado, "Determination of Pd, Pt and Rh in vehicles escape fumes by GF-AAS and ICP-OES," *Talanta*, vol. 75, no. 2, pp. 523–527, 2008.
[97] I. E. Wachs, "In situ Raman spectroscopy studies of catalysts," *Top. Catal.*, vol. 8, no. 1–2, pp. 57–63, 1999.
[98] M. A. Vuurman and I. E. Wachs, "In situ Raman spectroscopy of alumina-supported metal oxide catalysts," *J. Phys. Chem.*, vol. 96, no. 12, pp. 5008–5016, 1992.
[99] P. C. Stair, "Advances in Raman spectroscopy methods for catalysis research," *Curr. Opin. Solid State Mater. Sci.*, vol. 5, no. 5, pp. 365–369, 2001.
[100] I. E. Wachs and C. A. Roberts, "Monitoring surface metal oxide catalytic active sites with Raman spectroscopy," *Chem. Soc. Rev.*, vol. 39, no. 12, pp. 5002–5017, 2010.
[101] A. Urakawa, N. Maeda, and A. Baiker, " Space- and Time-Resolved Combined DRIFT and Raman Spectroscopy: Monitoring Dynamic Surface and Bulk Processes during NO x Storage Reduction ," *Angew. Chemie*, vol. 120, no. 48, pp. 9396–9399, 2008.
[102] D. Ferri, M. S. Kumar, R. Wirz, A. Eyssler, O. Korsak, P. Hug, A. Weidenkaff, and M. A. Newton, "First steps in combining modulation excitation spectroscopy with synchronous dispersive EXAFS/DRIFTS/mass spectrometry for in situ time resolved study of heterogeneous catalysts," *Phys. Chem. Chem. Phys.*, vol. 12, no. 21, pp. 5503–5513, 2010.
[103] X. Wang, H. Shi, J. H. Kwak, and J. Szanyi, "Mechanism of CO2 Hydrogenation on Pd/Al2O3 Catalysts: Kinetics and Transient DRIFTS-MS Studies," *ACS Catal.*,

vol. 5, no. 11, pp. 6337–6349, 2015.
[104] T. Armaroli, T. Bécue, and S. Gautier, “Diffuse reflection infrared spectroscopy (DRIFTS): Application to the in situ analysis of catalysts,” *Oil Gas Sci. Technol.*, vol. 59, no. 2, pp. 215–237, 2004.
[105] A. Cárdenas-Arenas, A. Quindimil, A. Davó-Quiñonero, E. Bailón-García, D. Lozano-Castelló, U. De-La-Torre, B. Pereda-Ayo, J. A. González-Marcos, J. R. González-Velasco, and A. Bueno-López, “Isotopic and in situ DRIFTS study of the CO2 methanation mechanism using Ni/CeO2 and Ni/Al2O3 catalysts,” *Appl. Catal. B Environ.*, vol. 265, no. November 2019, p. 118538, 2020.
[106] M. A. Bollinger and M. A. Vannice, “A kinetic and DRIFTS study of low-temperature carbon monoxide oxidation over Au-TiO2 catalysts,” *Appl. Catal. B Environ.*, vol. 8, no. 1, pp. 417–443, 1996.
[107] K. Sing, “The use of nitrogen adsorption for the characterisation of porous materials,” *Colloids Surfaces A Physicochem. Eng. Asp.*, vol. 187–188, pp. 3–9, 2001.
[108] M. Naderi, “Surface Area: Brunauer-Emmett-Teller (BET),” *Prog. Filtr. Sep.*, pp. 585–608, 2015.
[109] M. S. P. Francisco, V. R. Mastelaro, P. A. P. Nascente, and A. O. Florentino, “Activity and characterization by XPS, HR-TEM, Raman spectroscopy, and bet surface area of CuO/CeO2-TiO2 catalysts,” *J. Phys. Chem. B*, vol. 105, no. 43, pp. 10515–10522, 2001.
[110] A. C. Atkinson, “Developments in the design of Experiments,” *Int. Stat. Rev.*, vol. 50, no. 2, pp. 161–177, 1982.
[111] R. P. Niedz and T. J. Evens, “Design of experiments (DOE)—history, concepts, and relevance to in vitro culture,” *Vitr. Cell. Dev. Biol. - Plant*, vol. 52, no. 6, pp. 547–562, 2016.
[112] A. C. Atkinson and R. A. Bailey, “One hundred years of the design of experiments on and off the pages of Biometrika,” *Biometrika*, vol. 88, no. 1, pp. 53–97, 2001.
[113] T. J. Robinson, “Box – Behnken Designs,” in *Encyclopedia of Statistics in Quality and Reliability*, 2008.
[114] R. C. Van Nostrand, “Design of Experiments Using the Taguchi Approach: 16 Steps to Product and Process Improvement,” *Technometrics*, vol. 44, no. 3, pp. 289–289, 2002.
[115] S. L. C. Ferreira, R. E. Bruns, H. S. Ferreira, G. D. Matos, J. M. David, G. C. Brandão, E. G. P. da Silva, L. A. Portugal, P. S. dos Reis, A. S. Souza, and W. N. L. dos Santos, “Box-Behnken design: An alternative for the optimization of analytical methods,” *Anal. Chim. Acta*, vol. 597, no. 2, pp. 179–186, 2007.
[116] J. D. Jimenez, K. Mingle, T. Bureerug, C. Wen, and J. Lauterbach, “Statistically guided synthesis of MoV-based mixed-oxide catalysts for ethane partial oxidation,” *Catalysts*, vol. 8, no. 9, p. 370, 2018.
[117] T. S. Singh and T. N. Verma, “Taguchi design approach for extraction of methyl ester from waste cooking oil using synthesized CaO as heterogeneous catalyst: Response surface methodology optimization,” *Energy Convers. Manag.*, vol. 182, pp. 383–397, 2019.
[118] C. S. Latchubugata, R. V. Kondapaneni, K. K. Patluri, U. Virendra, and S. Vedantam, “Kinetics and optimization studies using Response Surface

Methodology in biodiesel production using heterogeneous catalyst," *Chem. Eng. Res. Des.*, vol. 135, pp. 129–139, 2018.
[119] N. D. Burrows, S. Harvey, F. A. Idesis, and C. J. Murphy, "Understanding the Seed-Mediated Growth of Gold Nanorods through a Fractional Factorial Design of Experiments," *Langmuir*, vol. 33, no. 8, pp. 1891–1907, 2017.
[120] M. Nazari and S. M. Alavi, "An investigation of the simultaneous presence of Cu and Zn in different Ni/Al2O3 catalyst loads using Taguchi design of experiment in steam reforming of methane," *Int. J. Hydrogen Energy*, vol. 45, no. 1, pp. 691–702, 2020.
[121] R. Rodríguez-Ramírez, I. Romero-Ibarra, and J. Vazquez-Arenas, "Synthesis of sodium zincsilicate (Na2ZnSiO4) and heterogeneous catalysis towards biodiesel production via Box-Behnken design," *Fuel*, vol. 280, p. 118668, 2020.
[122] R. J. Hendershot, W. Benjamin Rogers, C. M. Snively, B. A. Ogunnaike, and J. Lauterbach, "Development and optimization of NOx storage and reduction catalysts using statistically guided high-throughput experimentation," *Catal. Today*, vol. 98, no. 3 SPEC. ISS., pp. 375–385, 2004.
[123] Y. H. Tan, M. O. Abdullah, C. Nolasco-Hipolito, and N. S. Ahmad Zauzi, "Application of RSM and Taguchi methods for optimizing the transesterification of waste cooking oil catalyzed by solid ostrich and chicken-eggshell derived CaO," *Renew. Energy*, vol. 114, pp. 437–447, 2017.
[124] B. Nabgan, W. Nabgan, T. A. Tuan Abdullah, M. Tahir, Y. Gambo, M. Ibrahim, and W. Syie Luing, "Parametric study on the steam reforming of phenol-PET solution to hydrogen production over Ni promoted on Al2O3-La2O3catalyst," *Energy Convers. Manag.*, vol. 142, pp. 127–142, 2017.
[125] Y. Sun, G. Yang, C. Wen, L. Zhang, and Z. Sun, "Artificial neural networks with response surface methodology for optimization of selective CO2 hydrogenation using K-promoted iron catalyst in a microchannel reactor," *J. CO2 Util.*, vol. 24, no. November 2017, pp. 10–21, 2018.
[126] V. S. Chandane, A. P. Rathod, K. L. Wasewar, and S. S. Sonawane, "Synthesis of cenosphere supported heterogeneous catalyst and its performance in esterification reaction," *Chem. Eng. Commun.*, vol. 205, no. 2, pp. 238–248, 2018.
[127] R. Rezaei, G. Moradi, and S. Sharifnia, "Dry Reforming of Methane over Ni-Cu/Al2O3 Catalyst Coatings in a Microchannel Reactor: Modeling and Optimization Using Design of Experiments," *Energy and Fuels*, vol. 33, no. 7, pp. 6689–6706, 2019.
[128] Z. Yang, H. Lei, Y. Zhang, K. Qian, E. Villota, M. Qian, G. Yadavalli, and H. Sun, "Production of renewable alkyl-phenols from catalytic pyrolysis of Douglas fir sawdust over biomass-derived activated carbons," *Appl. Energy*, vol. 220, no. March, pp. 426–436, 2018.
[129] S. H. Dhawane, A. P. Bora, T. Kumar, and G. Halder, "Parametric optimization of biodiesel synthesis from rubber seed oil using iron doped carbon catalyst by Taguchi approach," *Renew. Energy*, vol. 105, pp. 616–624, 2017.
[130] U. Jamil, A. Husain Khoja, R. Liaquat, S. Raza Naqvi, W. Nor Nadyaini Wan Omar, and N. Aishah Saidina Amin, "Copper and calcium-based metal organic framework (MOF) catalyst for biodiesel production from waste cooking oil: A process optimization study," *Energy Convers. Manag.*, vol. 215, no. April, p.

112934, 2020.
[131] V. Narula, M. F. Khan, A. Negi, S. Kalra, A. Thakur, and S. Jain, “Low temperature optimization of biodiesel production from algal oil using CaO and CaO/Al2O3 as catalyst by the application of response surface methodology,” *Energy*, vol. 140, pp. 879–884, 2017.
[132] K. N. Ballantyne, R. A. van Oorschot, and R. J. Mitchell, “Reduce optimisation time and effort: Taguchi experimental design methods,” *Forensic Sci. Int. Genet. Suppl. Ser.*, vol. 1, no. 1, pp. 7–8, 2008.
[133] K. Melin and M. Hurme, “Evaluation of Lignocellulosic Biomass Upgrading Routes To Fuels and Chemicals,” *Cellul. Chem. Technol.*, vol. 44, no. 4–6, pp. 117–137, 2010.
[134] J. S. Luterbacher, D. Martin Alonso, and J. A. Dumesic, “Targeted chemical upgrading of lignocellulosic biomass to platform molecules,” *Green Chem.*, vol. 16, no. 12, pp. 4816–4838, 2014.
[135] M. Stalpaert and D. De Vos, “Stabilizing Effect of Bulky β-Diketones on Homogeneous Mo Catalysts for Deoxydehydration,” *ACS Sustain. Chem. Eng.*, vol. 6, pp. 12197–12204, 2018.
[136] J. Cao, M. Tamura, Y. Nakagawa, and K. Tomishige, “Direct Synthesis of Unsaturated Sugars from Methyl Glycosides,” *ACS Catal.*, vol. 9, pp. 3725–3729, 2019.
[137] J. Shakeri, H. Hadadzadeh, H. Farrokhpour, and M. Weil, “A comparative study of the counterion e ff ect on the perrhenate-catalyzed deoxydehydration reaction,” *Mol. Catal.*, vol. 471, no. December 2018, pp. 27–37, 2019.
[138] L. Wang, Y. Weng, P. Duan, X. Liu, X. Wang, and Y. Zhang, “Influence of acid pretreatment on the hydrodeoxygenation performance of carbon supported RuMo bimetallic catalysts on sorbitol conversion,” *SN Appl. Sci.*, vol. 1, no. 404, 2019.
[139] X. Jin, B. Yin, Q. Xia, T. Fang, J. Shen, L. Kuang, and C. Yang, “Catalytic Transfer Hydrogenation of Biomass-Derived Substrates to Value-Added Chemicals on Dual-Function Catalysts : Opportunities and Challenges,” *ChemSusChem*, vol. 12, pp. 71–92, 2019.
[140] L. Venkateswar Rao, J. K. Goli, J. Gentela, and S. Koti, “Bioconversion of lignocellulosic biomass to xylitol: An overview,” *Bioresour. Technol.*, vol. 213, pp. 299–310, 2016.
[141] L. M. F. Sena, C. G. Morais, M. R. Lopes, R. O. Santos, A. P. T. Uetanabaro, P. B. Morais, M. J. S. Vital, M. A. de Morais, M. A. Lachance, and C. A. Rosa, “D-Xylose fermentation, xylitol production and xylanase activities by seven new species of Sugiyamaella,” *Antonie van Leeuwenhoek, Int. J. Gen. Mol. Microbiol.*, vol. 110, no. 1, pp. 53–67, 2017.
[142] M. G. A. Felipe, D. C. Vieira, M. Vitolo, S. S. Silva, I. C. Roberto, and I. M. Manchilha, “Effect of acetic acid on xylose fermentation to xylitol by Candida guilliermondii,” *J. Basic Microbiol.*, vol. 35, no. 3, pp. 171–177, 1995.
[143] O. E. Borokhova and N. P. Mikhailova, “Microbial conversion of D-xylose,” *Mikrobiologiya*, vol. 65, no. 5, pp. 581–588, 1996.
[144] P. Kotter and M. Ciriacy, “Microbiology Biotechnology Xylose fermentation by Saccharomyces cerevisiae,” *Appl. Microbiol. Biotechnol.*, vol. 38, pp. 776–783, 1993.

[145] A. Sadier, D. Shi, A.-S. Mamede, S. Paul, E. Marceau, and R. Wojcieszak, "Selective aqueous phase hydrogenation of xylose to xylitol over SiO2-supported Ni and Ni-Fe catalysts: Benefits of promotion by Fe," *Appl. Catal. B Environ.*, vol. 298, p. 120564, 2021.
[146] B. W. Hoffer, E. Crezee, P. R. M. Mooijman, A. D. Van Langeveld, F. Kapteijn, and J. A. Moulijn, "Carbon supported Ru catalysts as promising alternative for Raney-type Ni in the selective hydrogenation of D-glucose," *Catal. Today*, vol. 79–80, pp. 35–41, 2003.
[147] N. Ota, M. Tamura, Y. Nakagawa, K. Okumura, and K. Tomishige, "Hydrodeoxygenation of vicinal OH groups over heterogeneous rhenium catalyst promoted by palladium and ceria support," *Angew. Chemie - Int. Ed.*, vol. 54, no. 6, pp. 1897–1900, 2015.
[148] S. Vernuccio, P. R. Von Rohr, and J. Medlock, "General Kinetic Modeling of the Selective Hydrogenation of 2-Methyl-3-butyn-2-ol over a Commercial Palladium-Based Catalyst," *Ind. Eng. Chem. Res.*, vol. 54, no. 46, pp. 11543–11551, 2015.
[149] A. Bruehwiler, N. Semagina, M. Grasemann, A. Renken, L. Kiwi-Minsker, A. Saaler, H. Lehmann, W. Bonrath, and F. Roessler, "Three-phase catalytic hydrogenation of a functionalized alkyne: Mass transfer and kinetic studies with in situ hydrogen monitoring," *Ind. Eng. Chem. Res.*, vol. 47, no. 18, pp. 6862–6869, 2008.
[150] M. Crespo-Quesada, M. Grasemann, N. Semagina, A. Renken, and L. Kiwi-Minsker, "Kinetics of the solvent-free hydrogenation of 2-methyl-3-butyn-2-ol over a structured Pd-based catalyst," *Catal. Today*, vol. 147, no. 3–4, pp. 247–254, 2009.
[151] B. L. Nogueira, J. Pérez, M. C. M. van Loosdrecht, A. R. Secchi, M. Dezotti, and E. C. Biscaia, "Determination of the external mass transfer coefficient and influence of mixing intensity in moving bed biofilm reactors for wastewater treatment," *Water Res.*, vol. 80, pp. 90–98, 2015.
[152] J. Cao, M. Tamura, R. Hosaka, A. Nakayama, J. Hasegawa, Y. Nakagawa, and K. Tomishige, "Mechanistic Study on Deoxydehydration and Hydrogenation of Methyl Glycosides to Dideoxy Sugars over ReOx-Pd/CeO2 Catalyst," *ACS Catal.*, vol. 10, pp. 12040–12051, 2020.
[153] L. Sandbrink, K. Beckerle, I. Meiners, R. Liffmann, K. Rahimi, J. Okuda, and R. Palkovits, "Supported Molybdenum Catalysts for the Deoxydehydration of 1,4-Anhydroerythritol into 2,5-Dihydrofuran," *ChemSusChem*, vol. 10, no. 7, pp. 1375–1379, 2017.
[154] Y. Xi, W. Yang, S. C. Ammal, J. Lauterbach, Y. Pagan-Torres, and A. Heyden, "Mechanistic study of the ceria supported, re-catalyzed deoxydehydration of vicinal OH groups," *Catal. Sci. Technol.*, vol. 8, no. 22, pp. 5740–5752, 2018.
[155] J. Engel and A. F. Huele, "TAGUCHI PARAMETER DESIGN BY SECOND-ORDER RESPONSE SURFACES," *Qual. Reliab. Eng. Int.*, vol. 12, pp. 95–100, 1996.
[156] J. M. Parks, "On stochastic optimization : Taguchi Methods □ demystified ; its limitations and fallacy clarified &," *Probabilistic Eng. Mech.*, vol. 16, pp. 87–101, 2001.
[157] R. S. Rao, R. S. Prakasham, K. K. Prasad, S. Rajesham, P. N. Sarma, and L. V.

Rao, “Xylitol production by Candida sp.: Parameter optimization using Taguchi approach,” *Process Biochem.*, vol. 39, no. 8, pp. 951–956, 2004.
[158] T. B. Granström, K. Izumori, and M. Leisola, “A rare sugar xylitol. Part II: Biotechnological production and future applications of xylitol,” *Appl. Microbiol. Biotechnol.*, vol. 74, no. 2, pp. 273–276, 2007.
[159] A. Yamaguchi, N. Hiyoshi, O. Sato, K. K. Bando, and M. Shirai, “Enhancement of cyclic ether formation from polyalcohol compounds in high temperature liquid water by high pressure carbon dioxide,” *Green Chem.*, vol. 11, no. 1, pp. 48–52, 2009.
[160] A. Yamaguchi, N. Hiyoshi, O. Sato, and M. Shirai, “Sorbitol dehydration in high temperature liquid water,” *Green Chem.*, vol. 13, no. 4, pp. 873–881, 2011.
[161] M. Tamura, N. Yuasa, J. Cao, Y. Nakagawa, and K. Tomishige, “Heterogeneous Catalysis Transformation of Sugars into Chiral Polyols over a Heterogeneous Catalyst Angewandte,” *Angew. Chemie - Int. Ed.*, vol. 57, pp. 8058–8062, 2018.
[162] Y. Delgado Arcaño, O. D. Valmaña García, D. Mandelli, W. A. Carvalho, and L. A. Magalhães Pontes, “Xylitol: A review on the progress and challenges of its production by chemical route,” *Catal. Today*, vol. 344, no. April 2018, pp. 2–14, 2020.
[163] A. Felipe Hernández-Pérez, P. V. de Arruda, L. Sene, S. S. da Silva, A. Kumar Chandel, and M. das G. de Almeida Felipe, “Xylitol bioproduction: state-of-the-art, industrial paradigm shift, and opportunities for integrated biorefineries,” *Crit. Rev. Biotechnol.*, vol. 39, no. 7, pp. 924–943, 2019.
[164] Z. Wei, J. Zhou, W. Sun, F. Cui, Q. Xu, and C. Liu, “Improvement of d-ribose production from corn starch hydrolysate by a transketolase-deficient strain bacillus subtilis UJS0717,” *Biomed Res. Int.*, vol. 2015, 2015.
[165] D. Wu, Y. Zhang, and H. Su, “Mechanistic Study on Oxorhenium-Catalyzed Deoxydehydration and Allylic Alcohol Isomerization,” *Chem. - An Asian J.*, vol. 11, no. 10, pp. 1565–1571, 2016.
[166] Y. Xi, J. Lauterbach, Y. Pagan-Torres, and A. Heyden, “Deoxydehydration of 1,4-anhydroerythritol over anatase TiO2(101)-supported ReOxand MoOx,” *Catal. Sci. Technol.*, vol. 10, no. 11, pp. 3731–3738, 2020.
[167] S. Shirbhate, A. K. Yadav, and S. Acharya, “Investigation of in-situ oxygen vacancies dissociation mechanism and associated atomic scale reshuffling during oxy-ion migration in nanostructured co-doped ceria,” *Solid State Ionics*, vol. 345, p. 115157, 2020.
[168] H. Cordatos, T. Bunluesin, J. Stubenrauch, J. M. Vohs, and R. J. Gorte, “Effect of Ceria Structure on Oxygen Migration for Rh / Ceria Catalysts,” *J. Phys. Chem.*, vol. 100, pp. 785–789, 1996.
[169] J. Varalda, C. A. Dartora, P. C. De Camargo, A. J. A. De Oliveira, and D. H. Mosca, “Oxygen diffusion and vacancy migration thermally-activated govern high-temperature magnetism in ceria,” *Sci. Rep.*, vol. 9, no. 4708, 2019.
[170] G. Balducci, M. S. Islam, J. Kaspar, P. Fornasiero, and M. Graziani, “Bulk reduction oxygen migration in the ceria-based oxides,” *Chem. Mater.*, vol. 12, no. 3, pp. 677–681, 2000.
[171] M. Nolan, J. E. Fearon, and G. W. Watson, “Oxygen vacancy formation and migration in ceria,” *Solid State Ionics*, vol. 177, no. 35–36, pp. 3069–3074, 2006.

[172] V. H. C. Silva, V. Aquilanti, H. C. B. De Oliveira, and K. C. Mundim, "Uniform description of non-Arrhenius temperature dependence of reaction rates, and a heuristic criterion for quantum tunneling vs classical non-extensive distribution," *Chem. Phys. Lett.*, vol. 590, pp. 201–207, 2013.
[173] A. P. H. Gregório, D. Borsato, I. Moreira, E. T. Silva, É. S. Romagnoli, and K. R. Spacino, "Apparent activation energy and relative protection factor of natural antioxidants in mixture with biodiesel," *Biofuels*, vol. 10, no. 5, pp. 607–614, 2019.
[174] M. Nishiyama, S. Kleijn, V. Aquilanti, and T. Kasai, "Temperature dependence of respiration rates of leaves, 18O-experiments and super-Arrhenius kinetics," *Chem. Phys. Lett.*, vol. 482, no. 4–6, pp. 325–329, 2009.
[175] D. G. Truhlar and A. Kohen, "Convex Arrhenius plots and their interpretation," *Proc. Natl. Acad. Sci. U. S. A.*, vol. 98, no. 3, pp. 848–851, 2001.
[176] J. P. Layfield and S. Hammes-Schiffer, "Hydrogen tunneling in enzymes and biomimetic models," *Chem. Rev.*, vol. 114, no. 7, pp. 3466–3494, 2014.
[177] J. Pu, J. Gao, and D. G. Truhlar, "Multidimensional tunneling, recrossing, and the transmission coefficient for enzymatic reactions," *Chem. Rev.*, vol. 106, no. 8, pp. 3140–3169, 2006.
[178] J. Joseph, C. Baker, S. Mukkamala, S. H. Beis, M. C. Wheeler, W. J. Desisto, B. L. Jensen, and B. G. Frederick, "Chemical shifts and lifetimes for nuclear magnetic resonance (NMR) analysis of biofuels," *Energy and Fuels*, vol. 24, no. 9, pp. 5153–5162, 2010.
[179] D. Der Naturwissenschaften, "Hydrogen Isotope Transport and Separation via Layered and Two- Dimensional Materials," no. April, 2021.
[180] F. O. Sanches-Neto, N. D. Coutinho, F. Palazzetti, and V. H. Carvalho-Silva, "Temperature dependence of rate constants for the H(D) + CH4 reaction in gas and aqueous phase: deformed Transition-State Theory study including quantum tunneling and diffusion effects," *Struct. Chem.*, vol. 31, no. 2, pp. 609–617, 2020.
[181] N. D. Coutinho, V. H. C. Silva, H. C. B. De Oliveira, A. J. Camargo, K. C. Mundim, and V. Aquilanti, "Stereodynamical origin of anti-arrhenius kinetics: Negative activation energy and roaming for a four-atom reaction," *J. Phys. Chem. Lett.*, vol. 6, no. 9, pp. 1553–1558, 2015.
[182] N. D. Coutinho, F. O. Sanches-Neto, V. H. Carvalho-Silva, H. C. B. de Oliveira, L. A. Ribeiro, and V. Aquilanti, "Kinetics of the OH+HCl→H2O+Cl reaction: Rate determining roles of stereodynamics and roaming and of quantum tunneling," *J. Comput. Chem.*, vol. 39, no. 30, pp. 2508–2516, 2018.
[183] T. Berglin and N. H. Schöön, "Selectivity Aspects of the Hydrogenation Stage of the Anthraquinone Process for Hydrogen Peroxide Production," *Ind. Eng. Chem. Process Des. Dev.*, vol. 22, no. 1, pp. 150–153, 1983.
[184] E. Santacesaria, M. Di Serio, R. Velotti, and U. Leone, "Kinetics, Mass Transfer, and Palladium Catalyst Deactivation in the Hydrogenation Step of the Hydrogen Peroxide Synthesis via Anthraquinone," *Ind. Eng. Chem. Res.*, vol. 33, no. 2, pp. 277–284, 1994.
[185] G. M. Lari, O. G. Grçninger, Q. Li, C. Mondelli, and P. Ø. Javier, "Catalyst and Process Design for the Continuous Manufacture of Rare Sugar Alcohols by Epimerization – Hydrogenation of Aldoses," *ChemSusChem*, vol. 9, pp. 3407–

3418, 2016.
[186] M. Tamura, N. Yuasa, J. Cao, Y. Nakagawa, and K. Tomishige, “Transformation of Sugars into Chiral Polyols over a Heterogeneous Catalyst,” *Angew. Chemie - Int. Ed.*, vol. 57, no. 27, pp. 8058–8062, 2018.
[187] A. M. Ruppert, K. Weinberg, and R. Palkovits, “Hydrogenolysis Goes Bio : From Carbohydrates and Sugar Alcohols to Platform Chemicals,” *Angew. Chemie - Int. Ed.*, vol. 51, pp. 2564–2601, 2012.
[188] L. Vilcocq, A. Cabiac, C. Especel, E. Guillon, and D. Duprez, “Transformation of Sorbitol to Biofuels by Heterogeneous Catalysis : Chemical and Industrial Considerations,” *Oil Gas Sci. Technol. - Rev. d’IFP Energies Nouv.*, vol. 68, no. 5, pp. 841–860, 2013.
[189] B. Peng, C. Zhao, I. Mejía-centeno, G. A. Fuentes, A. Jentys, and J. A. Lercher, “Comparison of kinetics and reaction pathways for hydrodeoxygenation of C3 alcohols on Pt/Al2O3,” *Catal. Today*, vol. 183, no. 1, pp. 3–9, 2012.
[190] C. Sievers, S. L. Scott, Y. Noda, L. Qi, E. M. Albuquerque, and R. M. Rioux, “Phenomena affecting catalytic reactions at solid−Liquid interfaces,” *ACS Catal.*, vol. 6, no. 12, pp. 8286–8307, 2016.
[191] H. Harju, G. Pipitone, and L. Lefferts, “Influence of the Catalyst Particle Size on the Aqueous Phase Reforming of n-Butanol Over Rh/ZrO2,” *Front. Chem.*, vol. 8, no. 17, pp. 1–13, 2020.
[192] J. Fu, X. Lu, and P. E. Savage, “Catalytic hydrothermal deoxygenation of palmitic acid,” *Energy Environ. Sci.*, no. 3, p. 253, 2010.
[193] S. Mukherjee and M. A. Vannice, “Solvent effects in liquid-phase reactions. I. Activity and selectivity during citral hydrogenation on Pt/SiO2 and evaluation of mass transfer effects,” *J. Catal.*, vol. 243, no. 1, pp. 108–130, 2006.
[194] E. Brunner, “Solubility of Hydrogen in 10 Organic Solvents at 298.15, 323.15, and 373.15 K,” *J. Chem. Eng. Data*, vol. 30, no. 3, pp. 269–273, 1985.
[195] S. Wang, Q. S. Li, Z. Li, and M. G. Su, “Solubility of xylitol in ethanol, acetone, N,N-dimethylformamide, 1-butanol, 1-pentanol, toluene, 2-propanol, and water,” *J. Chem. Eng. Data*, vol. 52, no. 1, pp. 186–188, 2007.
[196] A. C. Galvão, W. da Silva Robazza, P. F. Arce, A. Mocelin, and A. R. Paludo, “Experimental study and thermodynamic modeling of xylitol and sorbitol solubility in mixtures of methanol and ethanol at different temperatures,” *J. Mol. Liq.*, vol. 248, pp. 509–514, 2017.
[197] A. Romero, E. Alonso, and A. Nieto-m, “Conversion of biomass into sorbitol : Cellulose hydrolysis on MCM-48 and D -Glucose hydrogenation on Ru / MCM-48,” *Microporous Mesoporous Mater.*, vol. 224, pp. 1–8, 2016.
[198] L. Ding, A. Wang, M. Zheng, and T. Zhang, “Selective Transformation of Cellulose into Sorbitol by Using a Bifunctional Nickel Phosphide Catalyst,” *ChemSusChem*, no. entry 3, pp. 818–821, 2010.
[199] A. Negoi, K. Triantafyllidis, V. I. Parvulescu, and S. M. Coman, “The hydrolytic hydrogenation of cellulose to sorbitol over M (Ru , Ir , Pd , Rh) -BEA-zeolite catalysts,” *Catal. Today*, vol. 223, pp. 122–128, 2014.
[200] S. Kumar, H. Ali, S. K. Kansal, A. Pandey, and S. Saravanamurugan, “Chapter 9 - Sustainable production of sorbitol-a potential hexitol,” *Biomass, Biofuels, Biochem.*, no. Elsevier, Cambridge, pp. 259–281, 2020.

[201] H. Singh, A. Rai, R. Yadav, and A. K. Sinha, “Glucose hydrogenation to sorbitol over unsupported mesoporous Ni/NiO catalyst,” *Mol. Catal.*, vol. 451, no. January, pp. 186–191, 2018.
[202] P. Gallezot, N. Nicolaus, G. Flèche, P. Fuertes, and A. Perrard, “Glucose hydrogenation on ruthenium catalysts in a trickle-bed reactor,” *J. Catal.*, vol. 180, no. 1, pp. 51–55, 1998.
[203] B. Kusserow, S. Schimpf, and P. Claus, “Hydrogenation of Glucose to Sorbitol over Nickel and Ruthenium Catalysts,” *Adv. Synth. Catal.*, vol. 345, no. 1–2, pp. 289–299, 2003.
[204] S. Kim, E. E. Kwon, Y. T. Kim, S. Jung, H. J. Kim, G. W. Huber, and J. Lee, “Recent advances in hydrodeoxygenation of biomass-derived oxygenates over heterogeneous catalysts,” *Green Chem.*, vol. 21, no. 14, pp. 3715–3743, 2019.
[205] S. Chaudhari, H. T. Shin, S. Y. Choi, K. Y. Cho, M. Y. Shon, S. E. Nam, and Y. I. Park, “Hydrophilic and organophilic pervaporation of industrially important α,β and α,ω-diols,” *RSC Adv.*, vol. 11, no. 16, pp. 9274–9284, 2021.
[206] H. Kim, S. Lee, and W. Won, “System-level analyses for the production of 1,6-hexanediol from cellulose,” *Energy*, vol. 214, p. 118974, 2021.
[207] T. Buntara, S. Noel, P. H. Phua, I. Melián-Cabrera, J. G. De Vries, and H. J. Heeres, “From 5-hydroxymethylfurfural (HMF) to polymer precursors: Catalyst screening studies on the conversion of 1,2,6-hexanetriol to 1,6-hexanediol,” *Top. Catal.*, vol. 55, pp. 612–619, 2012.
[208] T. A. Phung Hai, N. Neelakantan, M. Tessman, S. D. Sherman, G. Griffin, R. Pomeroy, S. P. Mayfield, and M. D. Burkart, “Flexible polyurethanes, renewable fuels, and flavorings from a microalgae oil waste stream,” *Green Chem.*, vol. 22, no. 10, pp. 3088–3094, 2020.
[209] T. Muppaneni, H. K. Reddy, S. Ponnusamy, P. D. Patil, Y. Sun, P. Dailey, and S. Deng, “Optimization of biodiesel production from palm oil under supercritical ethanol conditions using hexane as co-solvent: A response surface methodology approach,” *Fuel*, vol. 107, pp. 633–640, 2013.
[210] B. Zhang and I. E. Wachs, “Identifying the Catalytic Active Site for Propylene Metathesis by Supported ReOx Catalysts,” *ACS Catal.*, vol. 11, no. 4, pp. 1962–1976, 2021.
[211] J. Antony, “Taguchi or classical design of experiments: A perspective from a practitioner,” *Sens. Rev.*, vol. 26, no. 3, pp. 227–230, 2006.
[212] A. R. Khataee, M. B. Kasiri, and L. Alidokht, “Application of response surface methodology in the optimization of photocatalytic removal of environmental pollutants using nanocatalysts,” *Environ. Technol.*, vol. 32, no. 15, pp. 1669–1684, 2011.
[213] R. Zeynolabedin and K. Mahanpoor, “Preparation and characterization of nano-spherical CoFe2O4 supported on copper slag as a catalyst for photocatalytic degradation of 2-nitrophenol in water,” *J. Nanostructure Chem.*, vol. 7, no. 1, pp. 67–74, 2017.
[214] C. C. Liao and T. W. Chung, “Optimization of process conditions using response surface methodology for the microwave-assisted transesterification of Jatropha oil with KOH impregnated CaO as catalyst,” *Chem. Eng. Res. Des.*, vol. 91, no. 12, pp. 2457–2464, 2013.

[215] I. E. Wachs, “Raman and IR studies of surface metal oxide species on oxide supports: Supported metal oxide catalysts,” *Catal. Today*, vol. 27, no. 3–4, pp. 437–455, 1996.
[216] A. Gómez-Cortés, Y. Márquez, J. Arenas-Alatorre, and G. Díaz, “Selective CO oxidation in excess of H2 over high-surface area CuO/CeO2 catalysts,” *Catal. Today*, vol. 133–135, no. 1–4, pp. 743–749, 2008.
[217] A. Bumajdad, M. I. Zaki, J. Eastoe, and L. Pasupulety, “Microemulsion-based synthesis of CeO2 powders with high surface area and high-temperature stabilities,” *Langmuir*, vol. 20, no. 25, pp. 11223–11233, 2004.
[218] H. F. Li, N. Zhang, P. Chen, M. F. Luo, and J. Q. Lu, “High surface area Au/CeO2 catalysts for low temperature formaldehyde oxidation,” *Appl. Catal. B Environ.*, vol. 110, pp. 279–285, 2011.
[219] M. F. Luo, Y. P. Song, J. Q. Lu, X. Y. Wang, and Z. Y. Pu, “Identification of CuO species in high surface area CuO-CeO2 catalysts and their catalytic activities for CO oxidation,” *J. Phys. Chem. C*, vol. 111, no. 34, pp. 12686–12692, 2007.
[220] P. Periyat, F. Laffir, S. A. M. Tofail, and E. Magner, “A facile aqueous sol-gel method for high surface area nanocrystalline CeO 2,” *RSC Adv.*, vol. 1, no. 9, pp. 1794–1798, 2011.
[221] P. Fornasiero, M. Graziani, and J. Kas, “Use of CeO2-Based Oxides in the Three-Way Catalysis,” *Catal. Today*, vol. 50, no. 2, pp. 1–14, 1999.
[222] X. Tang, B. Zhang, Y. Li, Y. Xu, Q. Xin, and W. Shen, “Carbon monoxide oxidation over CuO/CeO2 catalysts,” *Catal. Today*, vol. 93–95, pp. 191–198, 2004.
[223] I. E. Wachs and C. A. Roberts, “Monitoring surface metal oxide catalytic active sites with Raman spectroscopy,” *Chem. Soc. Rev.*, vol. 39, no. 12, pp. 5002–5017, 2010.
[224] Z. Wu, S. Dai, and S. H. Overbury, “Multiwavelength Raman spectroscopic study of silica-supported vanadium oxide catalysts,” *J. Phys. Chem. C*, vol. 114, no. 1, pp. 412–422, 2010.
[225] Z. Wu, A. J. Rondinone, I. N. Ivanov, and S. H. Overbury, “Structure of vanadium oxide supported on ceria by multiwavelength Raman spectroscopy,” *J. Phys. Chem. C*, vol. 115, no. 51, pp. 25368–25378, 2011.
[226] G. Tsilomelekis and S. Boghosian, “In situ raman and FTIR spectroscopy of molybdenum(VI) oxide supported on titania combined with 18O/16O exchange: Molecular structure, vibrational properties, and vibrational isotope effects,” *J. Phys. Chem. C*, vol. 115, no. 5, pp. 2146–2154, 2011.
[227] C. Andriopoulou, I. Anastasiou, and S. Boghosian, “Di-oxo and tri-oxo Re(VII)-oxosulfato complexes in the Re2O7-K2S2O7 molten system. Molecular structure, vibrational properties and temperature-dependent interconversion,” *Vib. Spectrosc.*, vol. 100, no. September 2018, pp. 14–21, 2019.
[228] I. R. Beattie, T. R. Gilson, and P. J. Jones, “ Vapor Phase Vibrational Spectra for Re 2 O 7 and the Infrared Spectrum of Gaseous HReO 4 . Molecular Shapes of Mn 2 O 7 , Tc 2 O 7 , and Re 2 O 7 ,” *Inorg. Chem.*, vol. 35, no. 5, pp. 1301–1304, 2002.
[229] Y. Nakagawa, S. Tazawa, T. Wang, M. Tamura, N. Hiyoshi, K. Okumura, and K. Tomishige, “Mechanistic Study of Hydrogen-Driven Deoxydehydration over

Ceria-Supported Rhenium Catalyst Promoted by Au Nanoparticles," *ACS Catal.*, vol. 8, no. 1, pp. 584–595, 2018.
[230] T. Wang, M. Tamura, Y. Nakagawa, and K. Tomishige, "Preparation of Highly Active Monometallic Rhenium Catalysts for Selective Synthesis of 1,4-Butanediol from 1,4-Anhydroerythritol," *ChemSusChem*, pp. 3615–3626, 2019.
[231] L. J. Donnelly, S. P. Thomas, and J. B. Love, "Recent Advances in the Deoxydehydration of Vicinal Diols and Polyols," *Chem. - An Asian J.*, vol. 14, no. 21, pp. 3782–3790, 2019.
[232] C. Andriopoulou and S. Boghosian, "Tuning the configuration of dispersed oxometallic sites in supported transition metal oxide catalysts: A temperature dependent Raman study," *Catal. Today*, no. January, pp. 1–10, 2019.
[233] E. Barrow, "Heterogeneous Catalysis for the Upgrading of Biomass Derived Chemicals via Hydrodeoxygenation," 2019.
[234] G. M. Zhang, X. P., Huang, S. J., Habermeier, H. U., Zhao, "Isotope effect on Raman spectra of polycrystalline La0.67Ca0.33MnO3," *J. Raman Spectrosc.*, vol. 32, no. 10, pp. 812–816, 2001.
[235] M. Chisanga, H. Muhamadali, D. McDougall, Y. Xu, N. Lockyer, and R. Goodacre, "Metabolism in action: Stable isotope probing using vibrational spectroscopy and SIMS reveals kinetic and metabolic flux of key substrates," *Analyst*, vol. 146, no. 5, pp. 1734–1746, 2021.
[236] H. N. Noothalapati Venkata and S. Shigeto, "Stable isotope-labeled raman imaging reveals dynamic proteome localization to lipid droplets in single fission yeast cells," *Chem. Biol.*, vol. 19, no. 11, pp. 1373–1380, 2012.
[237] M. S. Bradley and C. Bratu, "Vibrational line profiles as a probe of molecular interactions," *J. Chem. Educ.*, vol. 74, no. 5, pp. 553–555, 1997.
[238] D. S. Kim and I. E. Wachs, "Surface rhenium oxide-support interaction for supported Re2O7 catalysts," *J. Catal.*, vol. 141, no. 2, pp. 419–429, 1993.
[239] P. Gillet, P. McMillan, J. Schott, J. Badro, and A. Grzechnik, "Thermodynamic properties and isotopic fractionation of calcite from vibrational spectroscopy of 18O-substituted calcite," *Geochim. Cosmochim. Acta*, vol. 60, no. 18, pp. 3471–3485, 1996.
[240] G. Tsilomelekis and S. Boghosian, "In Situ Raman and FTIR Spectroscopy of Molybdenum (VI) Oxide Supported on Titania Combined with 18 O / 16 O Exchange : Molecular Structure , Vibrational Properties , and Vibrational Isotope Effects," *J. Phys. Chem. C*, vol. 115, no. 5, pp. 2146–2154, 2011.
[241] A. S. Wexler, "Integrated Intensities of Absorption Bands in Infrared Spectroscopy," *Appl. Spectrosc. Rev.*, vol. 1, no. 1, pp. 29–98, Jan. 1967.
[242] P. C. Painter, R. W. Snyder, M. Starsinic, M. M. Coleman, D. W. Kuehn, and A. Davis, "Concerning the Application of Ft-Ir To the Study of Coal: a Critical Assessment of Band Assignments and the Application of Spectral Analysis Programs.," *Appl. Spectrosc.*, vol. 35, no. 5, pp. 475–485, 1981.
[243] J. Fan and M. Trenary, "Symmetry and the Surface Infrared Selection Rule for the determination of the Structure of Molecules on Metal Surfaces," *Langmuir*, vol. 10, no. 10, pp. 3649–3657, 1994.
[244] R. G. Snyder, S. L. Hsu, and S. Krimm, "Vibrational spectra in the CH stretching region and the structure of the polymethylene chain," *Spectrochim. Acta Part A*

Mol. Spectrosc., vol. 34, no. 4, pp. 395–406, 1978.
[245] H. Hagemann, R. G. Snyder, A. J. Peacock, and L. Mandelkern, “Quantitative Infrared Methods for the Measurement of Crystallinity and Its Temperature Dependence. Polyethylene,” *Macromolecules*, vol. 22, no. 9, pp. 3600–3606, 1989.

APPENDIX A

COPYRIGHTS & PERMISSIONS

Figure A.1. Copyright permission for B. MacQueen, E. Barrow, G. Rivera Castro, Y. Pagan-Torres, A. Heyden, and J. Lauterbach, "Optimum Reaction Conditions for 1,4-Anhydroerythritol and Xylitol Hydrodeoxygenation over a ReOx-Pd/CeO2 Catalyst via Design of Experiments," *Ind. Eng. Chem. Res.*, vol. 58, no. 20, pp. 8681–8689, 2019.

Figure A.2. Copyright permission for B. MacQueen, B. Ruiz-Yi, M. Royko, A. Heyden, Y. J. Pagan-Torres, C. Williams, and J. Lauterbach, "In-Situ Oxygen Isotopic Exchange Vibrational Spectroscopy of Rhenium Oxide Surface Structures on Cerium Oxide," *J. Phys. Chem. C*, vol. 124, no. 13, pp. 7174–7181, 2020.

MDPI Open Access Information and Policy

All articles published by MDPI are made immediately available worldwide under an open access license. This means:

- everyone has free and unlimited access to the full-text of *all* articles published in MDPI journals;
- everyone is free to re-use the published material if proper accreditation/citation of the original publication is given;
- open access publication is supported by the authors' institutes or research funding agencies by payment of a comparatively low **Article Processing Charge (APC)** for accepted articles.

Permissions

No special permission is required to reuse all or part of article published by MDPI, including figures and tables. For articles published under an open access Creative Common CC BY license, any part of the article may be reused without permission provided that the original article is clearly cited. Reuse of an article does not imply endorsement by the authors or MDPI.

Figure A.3. Copyright permission for B. MacQueen, M. Royko, B. S. Crandall, A. Heyden, Y. J. Pagán-Torres, and J. Lauterbach, "Kinetics Study of the Hydrodeoxygenation of Xylitol over a ReO_x-Pd/CeO_2 Catalyst," *Catalysts*, vol. 11, no. 1, p. 108, Jan. 2021.